Dissertation zur Erlangung des Doktorgrades
der Fakultät für Chemie und Pharmazie
der Ludwig-Maximilians-Universität München

# Tackling the COF Trilemma: New Synthetic Approaches to Covalent Organic Frameworks

Johannes Maschita

aus

Wiesbaden, Deutschland

2022

## Erklärung

Diese Dissertation wurde im Sinne von § 7 der Promotionsordnung vom 28. November 2011 von Frau Professor Dr. Bettina V. Lotsch betreut.

## Eidesstattliche Versicherung

Diese Dissertation wurde eigenständig und ohne unerlaubte Hilfe erarbeitet.

Schwäbisch Gmünd, 01.09.2022

(Johannes Maschita)

| | |
|---|---|
| Dissertation eingereicht am: | 05.09.2022 |
| 1. Gutachterin: | Prof. Dr. Bettina Lotsch |
| 2. Gutachter: | Prof. Dr. Konstantin Karaghiosoff |
| Mündliche Prüfung am: | 25.10.2022 |

## *Acknowledgements*

First of all, I would like to express my sincere gratitude to my supervisor Prof. Bettina Lotsch for giving me the opportunity to do a PhD on an interesting and exciting topic in her group, for her supervision, support as well as the scientific freedom granted to me.

I would like to thank Prof. Konstantin Karaghiosoff for agreeing to be my second examiner for this thesis and my defense. In addition, I would like to thank the members of the doctoral committee Prof. Andreas Kornath, Prof. Christian Ochsenfeld, Prof. Knut Müller-Caspary, and Prof. Lena Daumann for their contribution.

I thank Frederick and Tanmay for their mentoring, whether in terms of lab techniques, helpful discussions, or writing scientific papers. I also thank Willi, Claudi, Viola, and Sigrid for their everyday, always warm, and often technical support as well as their organizational help.

I thank Marie and Alex for the great time I was allowed to spend with them in the office, for the many helpful discussions and mutual motivating support, Sebastian for being the best lab mate and his support in all synthetic questions and idea development, and Andi for his persistence in discussing electrochemical questions.

Furthermore, I would like to thank all former and current group members of the Lotsch group for the pleasant and productive working atmosphere, for the stimulating discussions, for the leisure time we spent outside the laboratory, and for those that have blessed me with their friendship.

I thank all my collaborators at MPI and elsewhere mentioned in this thesis for their constructive cooperation and for carrying out successful projects. I thank Luzia for her scientific drive and for always having time for my XRD questions, and Gökcen for his constant motivation and theoretical support.

I would like to thank the German Federal Ministry of Education and Research (BMBF), the German Research Foundation (DFG) and the Max Planck Society for their funding.

Last but not least, I would like to thank my family for their continuous support throughout all these years, which has enabled me to get to where I am today. This is especially true for Sophie, who has been with me through all the ups and downs of the PhD and kept me on track with her patience, advice and support.

Thank you all for everything.

## *Summary*

Covalent organic frameworks (COFs) are two- or three-dimensional extended networks formed by the assembly of molecular building blocks through reversible covalent bond formation. While formally belonging to the class of functional porous polymers, these materials differ from other porous polymers in their crystallinity and high degree of modularity, which enables a wide range of applications such as gas storage, gas separation, energy storage, and catalysis. Since their discovery in 2005, a variety of chemical reactions have been employed for the synthesis of well-defined COFs. The imidization reaction has been one of such developments. Imide-linked COFs (polyimide COFs, PI-COFs) are typically synthesized from amine- and anhydride-functionalized building blocks that form stable cyclic pyrrolidine-2,5-dione backbones, and are particularly characterized by their high thermal and chemical resistance as well as their redox-active backbones. However, due to the low reversibility of the imide ring formation reaction, the synthesis of PI-COFs is exceptionally challenging, and there are few synthetic strategies that can be used to obtain well-ordered COFs. The established synthetic protocol for the preparation of stable and crystalline PI-COFs is the solvothermal method, which requires the use of dry, high-boiling solvents, toxic catalysts, high reaction temperatures and often time-consuming solvent screening, making their synthesis expensive and environmentally harmful.

This thesis explores alternative synthesis methods for PI-COFs that are universally applicable and provide more environmentally friendly alternatives to the commonly used solvothermal method. Taking advantage of the high chemical stability of PI-COFs and other COF linkages, the suitability of COFs as nitric oxide (NO) adsorption scaffolds is investigated and chemical reactions of the adsorbent with the different adsorptives is elucidated.

### *Results*

With the aim of reducing the amount of solvents and toxic catalysts normally required for the synthesis of PI-COFs, an alternative ionothermal synthesis protocol has been developed (Chapter 4). The ionothermal synthesis allows the synthesis of PI-COFs in zinc chloride from their respective linker molecules by simply mixing the reactants and subsequent heating under inert conditions. This synthesis method does not require soluble precursor molecules, and the reaction time is significantly reduced to hours compared to standard solvothermal synthesis methods (up to 7 days). In addition, the use of expensive, high-boiling solvents and toxic catalysts is bypassed, as is the need for time-consuming solvent screening. In addition to applying the synthesis to already known imide COFs, a new perylene-based COF that could not be obtained by the classical solvothermal route has also been synthesized. However, the high reaction temperature of 280-300 °C required for ionothermal synthesis using pure $ZnCl_2$ as reaction medium limits the selection of suitable linker molecules, as they may decompose or carbonize under these harsh reaction conditions – a well-known problem in

the ionothermal synthesis of covalent triazine frameworks (CTFs). To avoid the decomposition of sensitive linker molecules, a eutectic salt mixture of $ZnCl_2$/NaCl/KCl has been identified that can be used for lowering the reaction temperature to 250 °C, which allows the ionothermal synthesis of PI-COFs from less stable building blocks.

In addition to the ionothermal method, an alcohol-assisted hydrothermal polymerization (aaHTP) approach has been explored for the synthesis of a wide range of crystalline and porous imide-linked COFs (Chapter 5). Taking advantage of the altered solvent behavior of water at high temperatures and pressures, this method provides access to new COFs and eliminates toxic solvents by up to 90% by replacing commonly used organic solvent mixtures with water and small amounts of n-alcohols. While the water in the reaction mixture serves as a good solvent for the anhydride linker and facilitates the reverse reaction according to Le Chatelier's principle, the n-alcohol increases the solubility of the water-insoluble precursor molecules and acts as a co-solvent, keeping the less polar imide dimers and oligomers longer in solution and thus accessible for the reaction. In addition to direct synthesis from the corresponding precursor molecules using aaHTP, an environmentally friendly COF-to-COF conversion of an imine-linked COF to a novel PI-COF by linker exchange has been demonstrated, which could not be prepared using published reaction conditions.

COFs have emerged as versatile platforms for the separation and storage of hazardous gases. At the same time, the synthetic toolkit to address the "COF trilemma" has been diversified to include topochemical linkage transformations and post-synthetic stabilization strategies. Using physisorption and solid-state nuclear magnetic resonance (ssNMR) spectroscopy on $^{15}$N-enriched COFs with different linkage types, the gas uptake capacity and selectivity of NO adsorption have been investigated and the interactions of NO with COFs have been deciphered (Chapter 6). Suitable linkages for adsorption of the highly reactive gas have been narrowed down to imide and thiazole linkages, since imine and amine linkages do not exhibit durable resistance to the gas. ssNMR spectroscopy revealed the clean deamination of terminal amine groups on the particle surfaces by NO, which represents a unique surface passivation strategy for COFs. In addition, the formation of a NONOate-linkage by the reaction of NO with an amine-linked COF has been described, which shows controlled release of NO under physiological conditions. NONOate COFs are therefore promising as tunable NO delivery platforms for bioregulatory NO release in biomedical applications.

# *Table of Contents*

1 General Introduction to Covalent Organic Frameworks - 1 -

1.1 Design Principles of Covalent Organic Frameworks - 4 -

1.1.1 Structural Diversity and Building Block Requirements for 2D Covalent Organic Frameworks - 5 -

1.1.2 Reversible COF Forming Reactions - 8 -

1.1.3 Solving the COF Trilemma - 12 -

1.2 Synthesis Strategies for Covalent Organic Frameworks - 17 -

1.2.1 Solvothermal Synthesis - 17 -

1.2.2 Irradiation-Assisted Synthesis - 18 -

1.2.3 Mechanochemical Synthesis - 19 -

1.2.4 Ionothermal Synthesis - 19 -

1.2.5 Synthesis of COF Thin Films - 20 -

1.3 Properties and Applications of Covalent Organic Frameworks - 20 -

1.4 Bibliography - 23 -

2 Imide-Linked Covalent Organic Frameworks - 35 -

2.1 Historical Overview of the Synthesis of Polyimides - 35 -

2.2 Synthesis of Imide-Linked Covalent Organic Frameworks - 40 -

2.2.1 Solvothermal Synthesis of PI-COFs - 40 -

2.2.2 High-Temperature Solid-State Approach - 42 -

2.2.3 Surfactant Supported Synthesis of a PI-COF Thin Film - 42 -

2.2.4 Synthesis in Ionic Liquids - 44 -

2.2.5 Linker-Exchange Strategy - 44 -

2.2.6 Hydrothermal Synthesis - 44 -

2.3 Challenges in the Synthesis of Imide-Linked COFs - 45 -

2.4 Properties and Applications of Imide-Linked Covalent Organic Frameworks - 46 -

2.4.1 Adsorption and Drug Delivery - 46 -

2.4.2 Sensing - 49 -

2.4.3 Energy Storage - 49 -

2.4.4 Catalysis - 51 -

2.5 Bibliography - 53 -

3 Research Objective - 59 -

4 Ionothermal Synthesis of Imide-Linked Covalent Organic Frameworks - 61 -

4.1 Introduction - 62 -

4.2 Results and Discussion - 63 -

4.3 Conclusion - 74 -

4.4 Bibliography - 75 -

5 Direct and Linker-Exchange Alcohol-Assisted Hydrothermal Synthesis of Imide-Linked Covalent Organic Frameworks - 77 -

5.1 Introduction - 78 -

5.2 Results and Discussion - 80 -

5.3 Conclusion - 89 -

5.4 Bibliography - 90 -

6 NO as a Reagent for Topochemical Framework Transformation and Controlled Nitric Oxide Release in Covalent Organic Frameworks - 93 -

6.1 Introduction - 94 -

6.2 Results and Discussion - 96 -

6.3 Conclusion - 104 -

6.4 Bibliography - 106 -

7 Conclusion - 109 -

7.1 Bibliography - 112 -

8 Appendix - 113 -

8.1 Abbreviations - 113 -

8.2 Supporting Information of Chapter 4.1 “Ionothermal Synthesis of Imide-Linked Covalent Organic Frameworks” - 116 -

8.2.1 Experimental Details - 116 -

8.2.2 Materials and Synthetic Procedures - 119 -

8.2.3 Supplementary Figures - 121 -

8.2.4 Supplementary Tables - 160 -

8.2.5 Bibliography - 166 -

8.3 Supporting Information of Chapter 4.2 “Direct and Linker-Exchange Alcohol-Assisted Hydrothermal Synthesis of Imide-Linked COFs” - 167 -

8.3.1 Experimental Details - 167 -

8.3.2 Materials and Synthetic Procedures - 168 -

8.3.3 Supplementary Figures - 170 -

8.3.4 Supplementary Tables - 184 -

8.3.5 Bibliography - 185 -

8.4 Supporting Information of Chapter 5 “NO as a Reagent for Topochemical Framework Transformation and Controlled Nitric Oxide Release in Covalent Organic Frameworks” - 186 -

8.4.1 Experimental Details - 186 -

8.4.2 Materials and Synthetic Procedures - 188 -

8.4.3 Supplementary Figures - 192 -

8.4.4 Supplementary Tables - 213 -

8.4.5 Bibliography - 214 -

8.5 List of Publications - 215 -

8.5.1 Publications that are part of this thesis - 215 -

8.5.2 Publications that are not part of this thesis - 215 -

# 1 General Introduction to Covalent Organic Frameworks

Polymers have undoubtedly been one of the most significant discoveries in chemistry in the last century and a half. Their discovery and development has enabled the realization of materials that impact virtually everything every day, making chemistry an integral part of our daily lives. While the word "polymer" was first introduced by the Swedish chemist J. J. Berzelius, who considered, for example, benzene ($C_6H_6$) to be a polymer of acetylene ($C_2H_2$),[1] the origin of modern polymer science can be traced back to the early 19th century when Henry Braconnot described the nitration of various cellulose compounds, thus laying the foundation of the first semi-synthetic plastic.[2] A semi-synthetic elastic polymer was discovered by Goodyear in 1839, who found that the vulcanization of rubber with sulfur improved the durability of the material and lead to superior properties.[3] In the 1860th, Parkes and Hyatt obtained a thermoplastic polymer, known as celluloid, by the addition of camphor to nitrocellulose.[4] While polymer chemistry in the 19th century was limited to the modification of naturally occurring polymers such as rubber or cellulose, the first fully synthetic polymer was synthesized by Baekeland in 1907. By reacting phenol with formaldehyde at precisely controlled temperatures and pressures, he obtained poly-phenol-formaldehyde (PF), better known as Bakelite.[5] Bakelite was commercialized a few years later and is credited with beginning the truly synthetic plastics age and industry.

Despite significant advances in the synthesis and characterization of polymers, it was not until the 1920s that a correct understanding of the molecular structure of polymers emerged. Until then, scientists believed polymers were clusters of small molecules of no specific molecular weights held together by an unknown force, a concept known as association theory. In 1920, Hermann Staudinger proposed that polymers consist of long chains of atoms held together by covalent bonds, an idea for which Staudinger was eventually awarded the Nobel Prize.[6-7] Further pioneering work in polymer chemistry was done by Wallace Carothers – known for the invention of nylon 66 and neoprene – who published the theory of polycondensation that led to the development of polyesters and polyamides. Carother also demonstrated that polymers could be synthesized rationally from their constituent monomers to modify their properties, leading to the rapid development of this field.[8-10] Important contributions to the synthesis of polymers have been made by Giulio Natta and Karl Ziegler, who won the Nobel Prize in 1963 for the development of the Ziegler-Natta catalyst enabling the room temperature synthesis of polyethylene (PE) and polypropylene (PP) – both among the most used polymers today.[11-13] Since then, numerous 1D polymers have been developed for countless applications. However, inspired by nature's ability to form discrete, macromolecular higher-order structures such as DNA and enzymes, towards the end of the 20th century, research interests shifted towards two- or three-dimensional (2D, 3D) macromolecular polymeric materials. Functional porous materials are an excellent example.

Porous materials are organic or inorganic solid-state materials featuring permanent porosity, created by accessible structural voids that can vary in size and shape. They can exhibit high surface areas and are classified according to their average pore diameter ranging from micropores (<2 nm), over mesopores (2-50 nm), to macropores (>50 nm).[14] These pores can be accessible for gaseous or solution-based guest molecules, rendering them promising candidates for many applications, such as gas storage/separation or heterogeneous catalysis, in which the size, shape, and pore wall characteristics strongly influence their properties.

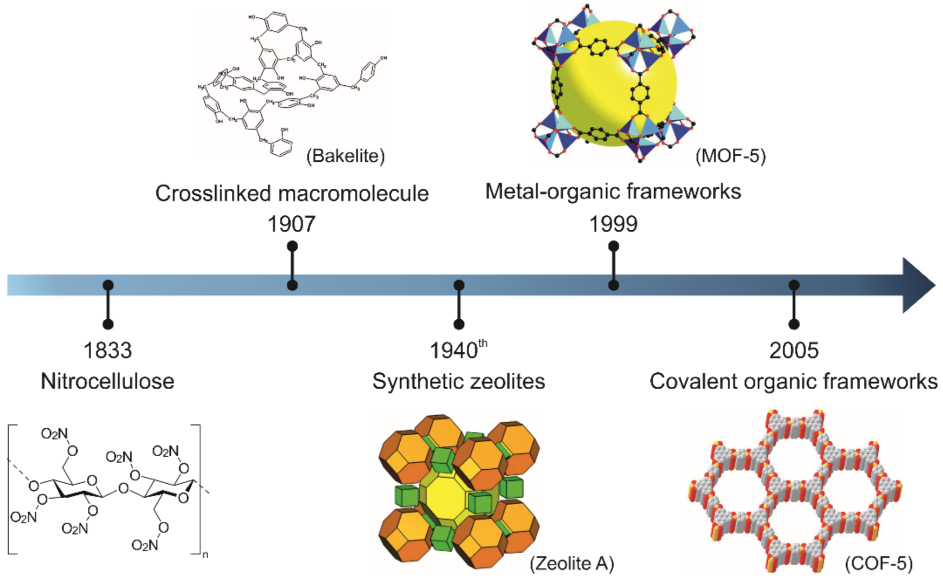

**Figure 1-1.** Timeline of the milestones in polymer chemistry showing the (schematic) structures of nitrocellulose, Bakelite reprinted from [15], Zeolite A reprinted and adapted from [16], MOF-5 reprinted and adapted from [17] and COF-5 reprinted and adapted from [18].

Naturally occurring inorganic porous materials are aluminosilicate-based zeolites consisting of silica and alumina tetra- and octahedra. This material class exhibits large surface areas, defined microporous voids, and shows high molecule specificity. Due to their confined environment and robustness, they are applied as excellent catalysts for the synthesis of branched hydrocarbons,[19] sorbents,[20-22] or molecular sieves on an industrial scale.[23] However, while zeolites have well-defined microporous structures, their pore-wall characteristics cannot be readily altered, rendering the modification of their properties difficult. A more versatile class of porous materials that addresses this impediment are metal-organic frameworks (MOFs), first introduced by Omar Yaghi and co-workers in 1999.[17] MOFs are (mostly) 3D coordination polymers and thus at the interface between inorganic and organic materials, as they are formed from inorganic clusters bridged by organic ligands. The combination of highly symmetric metal nodes, rigid ligands, and directional ligand-metal interactions enables the synthesis of materials with permanent porosity and structural order. The well-defined crystalline structures with openly accessible pores manifests in exceptionally high surface areas, up to 5640 $m^2/g$ for MOF-177.[24] Further, the low-temperature solvothermal synthesis of MOFs allows the use of highly functional and fragile ligands, and functional groups can thereby be relatively easily introduced into the framework. Similar to classical polymer science, the monomers (ligands) can be designed by conventional organic synthesis methods, which enables the targeted synthesis of MOFs for specific applications by using pre-designed ligands. These materials thus find a wide variety of applications in, e.g., gas storage,[25-26] sensing,[27] and heterogeneous catalysis.[28-29] However, the metal-ligand interactions forming the structure are relatively weak compared to covalent bonds, which makes MOFs prone to degradation.[30]

Amorphous, porous materials that are built entirely of covalent bonds are called porous polymer frameworks (PPFs) or porous organic polymers (POPs) and are strongly related to traditional organic polymers.[31] These materials consist of organic building blocks that are randomly interconnected through covalent bonds. Due to the random interconnection of the building units, accessible voids can thereby be generated, however, without distinct size and shape. Nevertheless, such materials have found considerable applications in gas storage and heterogeneous catalysis, owing primarily to the molecular tunability of their structure.[32-33]

Inspired by nature's ability to form ordered polymeric structures, such as DNA and enzymes, by shaping covalently bonded polymer chains in two or three dimensions through weak interactions like van-der-Waals forces and hydrogen bonding, a new class of porous materials was developed: In 2005, Omar Yaghi pushed the boundaries of modern polymer science with their synthesis of ordered 2D organic polymers entirely formed by covalent bonds.[18] The 2D polymer sheets form quasi 3D structures by stacking in the third dimension by virtue of out-of-plane π-π interactions and van-der-Waals forces. These so-called covalent organic frameworks (COFs) are lightweight as they are composed entirely of light elements (C, N, O, B, S), and they feature permanent porosity and crystallinity. In 2009, Yaghi and co-workers demonstrated that the formation of COFs *via* the formation of directional covalent bonds is also possible in 3D.[34]

In general, COFs are built of organic monomers, the so-called linkers or building blocks, which are connected *via* strong, but reversible covalent bonds (linkages) using reticular chemistry.[18, 35-36] The reversibility of the bond-forming reaction allows self-healing of defects through bond formation, breakage, and reformation. This concept is known as dynamic covalent chemistry (DCC).[37] In contrast to conventional organic polymer chemistry where usually kinetic disordered products are formed, the synthesis of COFs is carried out under equilibrium conditions yielding the thermodynamically most stable, and therefore crystalline product. Thus, COFs combine the advantages of two worlds: They share both the robustness typical of organic polymers and the porosity and functional diversity of MOFs. Equipped with these favorable properties, COFs have accelerated research in the field of porous materials in the last decade and continue to be intensively studied and further developed. The present thesis is a small addition in this direction.

In Section 1.1, an overview of the design principles of COFs, the various network topologies achieved, and a discussion of the different COF formation reactions is presented. Different strategies for the synthesis of well-oriented COFs are summarized in Section 1.2. The molecular composition of the COF framework opens up the possibility of modifying such systems for a variety of applications, some of which are summarized in Section 1.3.

## *1.1 Design Principles of Covalent Organic Frameworks*

COFs are highly functional materials as they are built of molecular organic building blocks. These building blocks can be individually customized to achieve specific properties required for the desired applications.[38] In order for the growth of a two- or three-dimensional framework to propagate in an ordered manner, the building blocks must meet a variety of requirements, such as appropriate rigidity, suitable functional groups, and appropriate symmetries. The structural diversity and the possible network topologies resulting from the specific combinations of linker molecules of the same or different geometries are presented in Section 1.1.1.

In addition to the choice of a suitable building block, the type of covalent bond linking these building blocks must be compatible with the principles of DCC to allow controlled growth of the polymer backbone in two or three dimensions. [18, 39] In contrast to classic organic chemistry, which generally employs kinetically controlled reactions to form irreversible chemical bonds,[40] reversible reactions, such as condensation reactions, are used in DCC to form the thermodynamically controlled product.[37] The variety of reversible reactions that have been used to form COFs are summarized in Section 1.1.2. By controlling the thermodynamics of the linkage reaction through precise adjustment of temperature and pressure, as well as by the use of appropriate catalysts, mismatched covalent bonds can be cleaved to cause continuous reassembly of the building blocks during COF formation, resulting in a self-healing of the structure (Figure 1-2).[18, 41] These error-control and proof-reading mechanisms are imperative to reduce defects in the structure that inevitably arise from the numerous reactive sites that simultaneously drive crystallite growth.

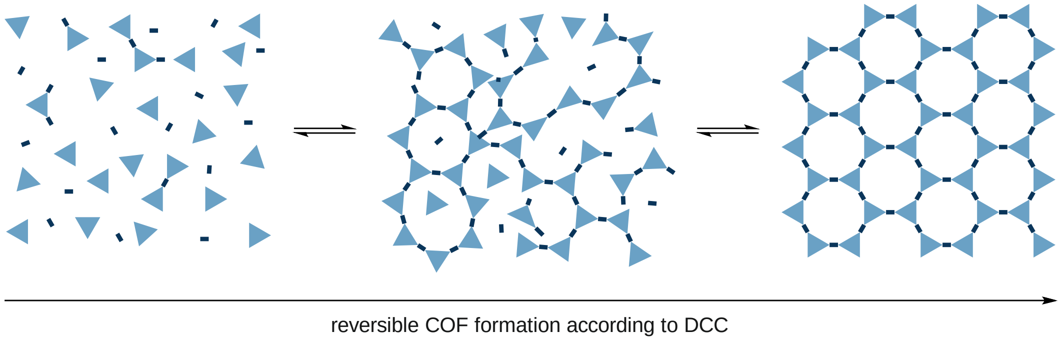

**Figure 1-2.** Schematic representation of the COF formation mechanism *via* reversible bond formation according to DCC.

To tune the properties of COFs for specific applications, complex building blocks with desired functional groups and electronic properties can be synthesized and subsequently incorporated into the framework. This precise tunability of the properties of COFs through the incorporation of specific building blocks represents a tremendous advantage of COFs over other porous materials such as porous carbons or zeolites. However, complex linker molecules can only be used if the linkages are much weaker than any other bonds in the building block and are cleaved in a discriminatory manner to allow reversibility of the linking reaction without destruction of the linker functional groups.[42] As the bonds become more stable, their reversibility decreases, so that harsher reaction conditions are required to initiate the self-healing processes. However, the use of harsh reaction conditions may limit the choice of linker molecules, as they may decompose before reversibility is achieved.[42] This so-called COF trilemma and approaches to circumvent this phenomenon by using alternative synthetic strategies are described in Section 1.1.3.

### *1.1.1 Structural Diversity and Building Block Requirements for 2D Covalent Organic Frameworks*

2D-COFs are formed by the combination of rigid planar building blocks that create 2D layers with voids of certain polygonal geometries in the molecular plane. These covalently bonded 2D layers of molecules represent the primary ordering structure of 2D COFs.[43] In addition to the in-plane covalent bonding of the linker molecules, the resulting rigid 2D layers form layered structures through non-covalent interactions such as hydrogen bonding and π-π interactions. This alignment of 2D COF films along the z-direction creates open 1D channels and forms the high-order structure of 2D COFs.[43] Unlike other porous materials such as porous carbons or most noncrystalline CTFs, which have a distribution of pores of varying sizes and shapes that are usually only roughly controlled by the temperature applied during synthesis or templating methods,[44-45] COFs have pores of defined size and shape determined by the underlying network topology.[38] The network topology, in turn, is the result of the geometry of the building blocks that make up the COF.

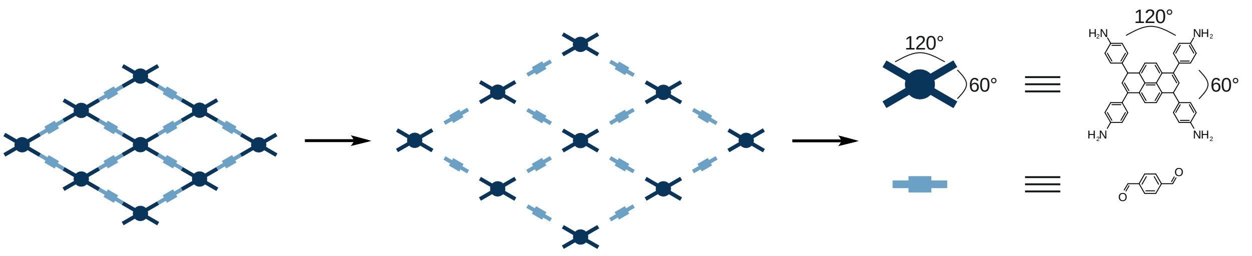

target topology
deconstruction of the topology
geometric units
molecular equivilents

**Figure 1-3.** Deconstruction of the topological framework into its geometric units, together with examples for molecular equivalents.

The targeted topological design of COFs is achieved by a stepwise retrosynthetic approach as described by Diercks *et al.*[38] In the first step, a desired mesh with a particular topology is selected (Figure 1-3). The selected mesh is then decomposed into smaller geometric units that serve as patterns for designing suitable building blocks. The building blocks must be designed to satisfy the geometric constraints imposed by the specified geometric units. Attention must be paid to connectivity, bond angles, and rigidity of the linker molecules. While connectivity and bond angles ensure the formation of the desired network topology, rigid building blocks are required to ensure a clear direction of each covalent bond and to protect the network from deformation and pore collapse. This is usually achieved by using organic monomers containing extended π-conjugated systems. The nodes in the network can be formed either by the linking reaction, as in in the case of triazine COFs by the trimerisation of nitriles (Figure 1-4), or by monomers bearing more than two reactive sites.[18, 46]

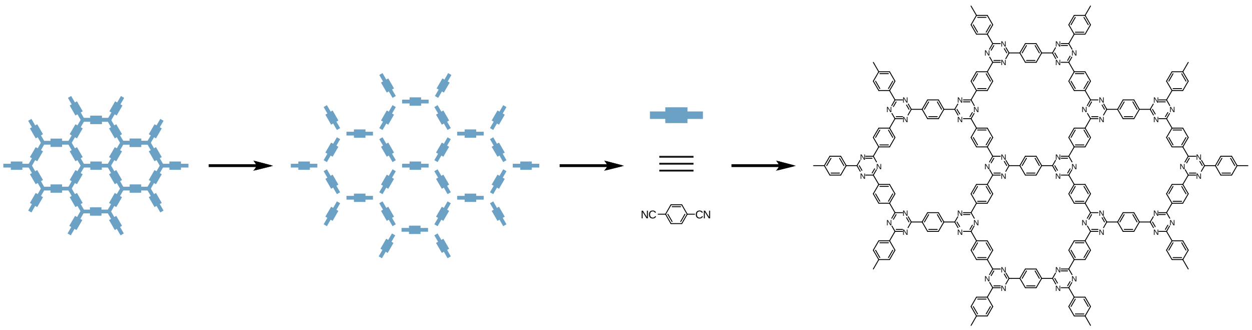

**Figure 1-4.** Construction of a COF in which the nodes are formed by the trimerization reaction of linear nitrile-functionalized building blocks.

This concept can be simplified by a modular design principle in which each building block is represented by a specific geometry that reflects the relative positions of the reactive sites in the molecule. The spatial orientation of the building blocks and the relative positions of the nearest linker molecules are determined by the covalent bonds. The repetition of this rule in every possible spatial direction limits the growth of the chain in a way that strictly follows the predesigned topology diagram. This topology diagram and the geometric alignment of the building blocks provide the chemical basis for the growth and control of the in-plane structure. [43]

By using this modular design principle, a variety of different network topologies can be realized by linking building blocks of different geometries. Most of the 2D COF structures reported so far are formed with highly symmetric building blocks (Figure 1-5). For example, the combination of a building block in which three reactive sites are distributed in a $C_3$ symmetric fashion with a building block with two reactive sites distributed in a $C_2$ symmetric fashion generates a hexagonal honeycomb network (*hcb*).[18, 36, 47] Note that the indicated symmetries ($C_2$, $C_3$, $C_4$, $C_6$) do not reflect the point groups of the molecules but are intended only to describe the relative positions of the reactive sites in a molecule with respect to each other. For simplicity, the connectivity of linker molecules (number of reactive sites) is given below as a superscript number before the (minimum) symmetry (relative position of reactive sites), e.g., a linker with four reactive sites distributed in a $C_2$ symmetric manner is shown as $^4C_2$.

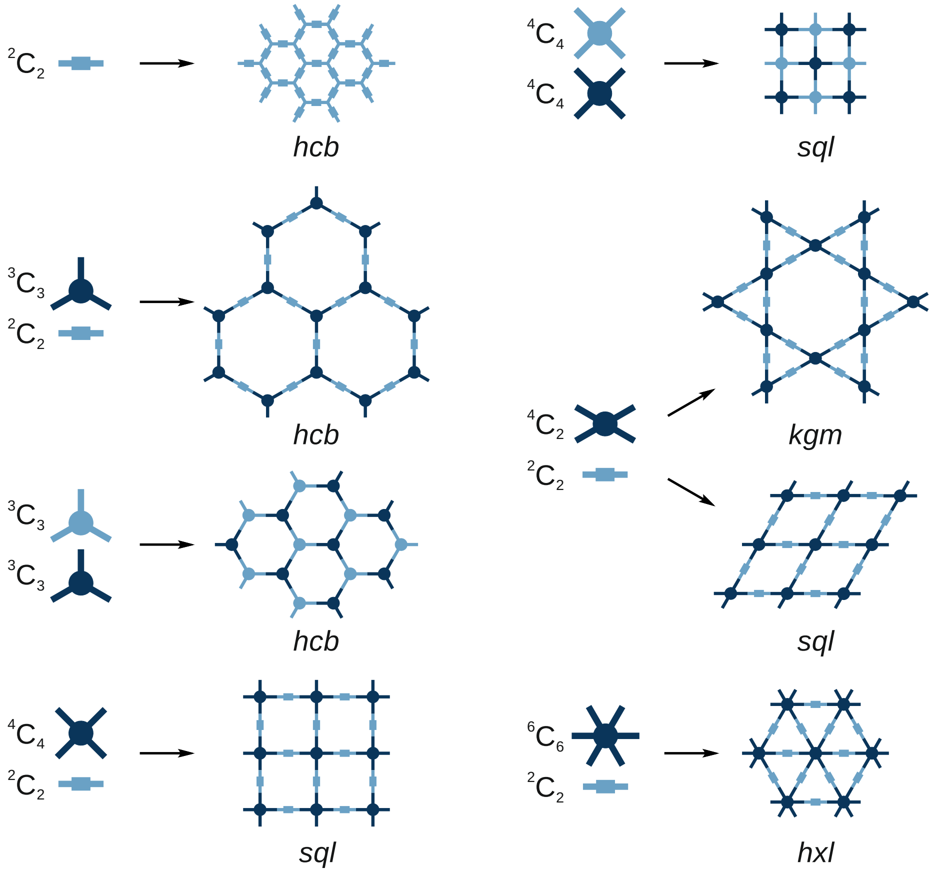

**Figure 1-5.** Schematic representation of different geometric units and resulting isotropic network topologies that have been realized in 2D COFs so far.

In addition to the combination [$^3C_3$+$^2C_2$], hexagonal *hcb* networks can also be synthesized by combining three linear building blocks [$^2C_2$+$^2C_2$+$^2C_2$] or two different trigonal building blocks [$^3C_3$+$^3C_3$].[18, 36] Tetragonal COFs with square (*sql*) lattice are synthesized using the building block combinations [$^4C_4$+$^2C_2$] and [$^4C_4$+$^4C_4$].[48-49] The reaction of a monomer with six reactive sites distributed in a $C_6$ symmetric fashion with a linear linker molecule [$^6C_6$+$^2C_2$] leads to the formation of a hexagonal (*hxl*) lattice with trigonal pores.[50-51] Another interesting combination of linker molecules is represented by the [$^4C_2$+$^2C_2$] combination, which forms either a rhombic *sql* lattice or a hexagonal kagome (*kgm*) lattice. The type of lattice formed depends on the linker molecules and is influenced by their bulkiness and the strength of interlayer interactions:[52-53] In general, $^4C_2$ building blocks with large π-systems that form strong π-π interactions tend to form the rhombic square lattice. Relatively flexible building blocks with weak interlayer interactions tend to form *kgm*-type structures and are stabilized by a docking effect of twisted linker parts.[54]

A special type of *kgm* lattice with a central hexagonal pore surrounded by six pentagonal pores is obtained by combining a building block carrying three reactive sites distributed $C_2$-symmetrically with a linear linker molecule [$^3C_2$+$^2C_2$] (Figure 1-6a).[55]

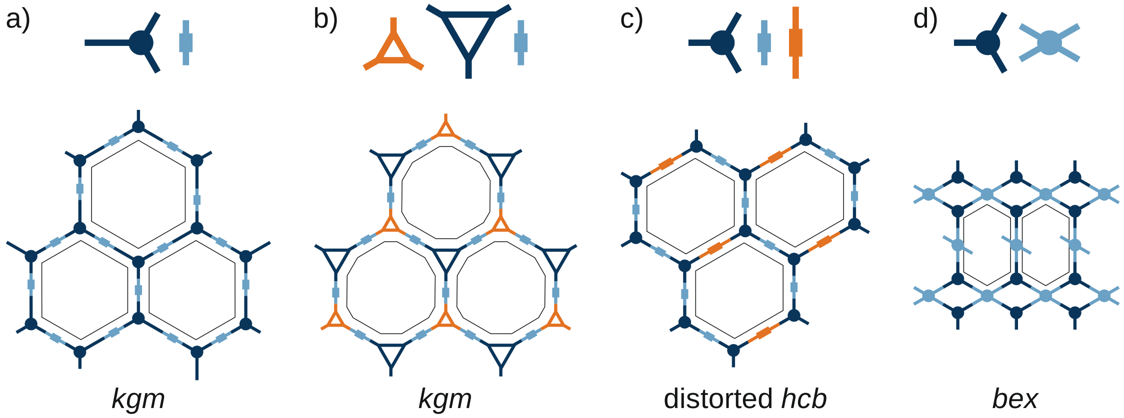

**Figure 1-6.** Schematic representation of selected geometric entities and resulting unique network topologies that have been realized in 2D COFs to date.

To increase compositional and structural complexity, COFs have been synthesized with complex molecules or macromolecules as nodes.[56-57] For example, using two different macrocycles as $^3C_3$ linkers, a [$^3C_3$+$^3C_3$+$^2C_2$] *kgm* network with three different pores was developed (Figure 1-6b).[58] In addition to regular nets, COFs can form distorted net topologies by combining linear linkers of different chain lengths with suitable nodal building blocks, resulting in distorted *sql*, *hcb*, and *kgm* lattices (Figure 1-6c).[59-60] An unusual network topology is the *bex* net (Figure 1-6d). This lattice can be formed either by a sub-stoichometric combination of [$^3C_3$+$^4C_4$] or by the stoichiometric combination of [$^2C_2$+$^3C_3$+$^4C_4$]. The first combination represents a special case, as the $^4C_4$ linker in such COFs acts simultaneously as a bidentate and a tetradentate linker in two different coordination environments, thus inherently leading to non-condensed functional groups in the framework.[61]

### *1.1.2 Reversible COF Forming Reactions*

The most commonly used strategy for the synthesis of COFs is through reversible reactions following the principles of DCC. In the past decades, since the seminal work of Yaghi and co-workers, a number of reversible reactions have been explored as COF linkages.[18]

Boron-based COFs, which researchers focused on in the early years of COF chemistry, are usually formed by a condensation reaction using precursor molecules functionalized with boronic acids. The weak boron-oxygen bonds formed in this way are highly reversible, allowing COFs with exceptional crystallinity to be prepared.[18] However, due to the weak linking bond, most boron-based COFs exhibit low stability as they tend to hydrolyze under ambient conditions, making them unsuitable for most applications.[62] Prominent examples of boron-based COFs formed *via* a boron-oxygen bond include bronic ester,[18] boronic acid anhydride,[18] and spiroborate COFs (Figure 1-7).[63] Moreover, boron-nitrogen bonds were constructed as in borazine,[64] while borosilicate-based COFs were prepared with boron-oxygen-silicon bonds.[65] These COF linkages represent a borderline case to MOFs and share with them a high crystallinity as well as a high sensitivity to hydrolysis.[66]

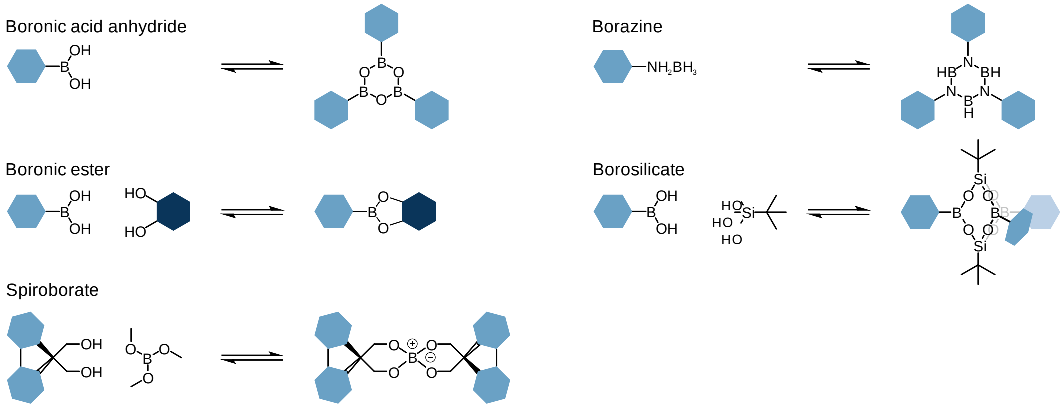

**Figure 1-7.** Collection of boron-based linkages explored for the synthesis of COFs.

Carbon-nitrogen and carbon-carbon based COFs represent an important development in COF synthesis. These systems are more stable and resistant to hydrolytic bond cleavage than their boron-containing counterparts, but harsher reaction conditions are required to obtain crystalline products. The most common linkage type among these COFs is the carbon-nitrogen double bond formed *via* a Schiff base reaction between amines and various carbonyl compounds.[34] Many variations of this archetypal imine bond have been explored with the aim of increasing stability against hydrolysis without sacrificing crystallinity (Figure 1-8).

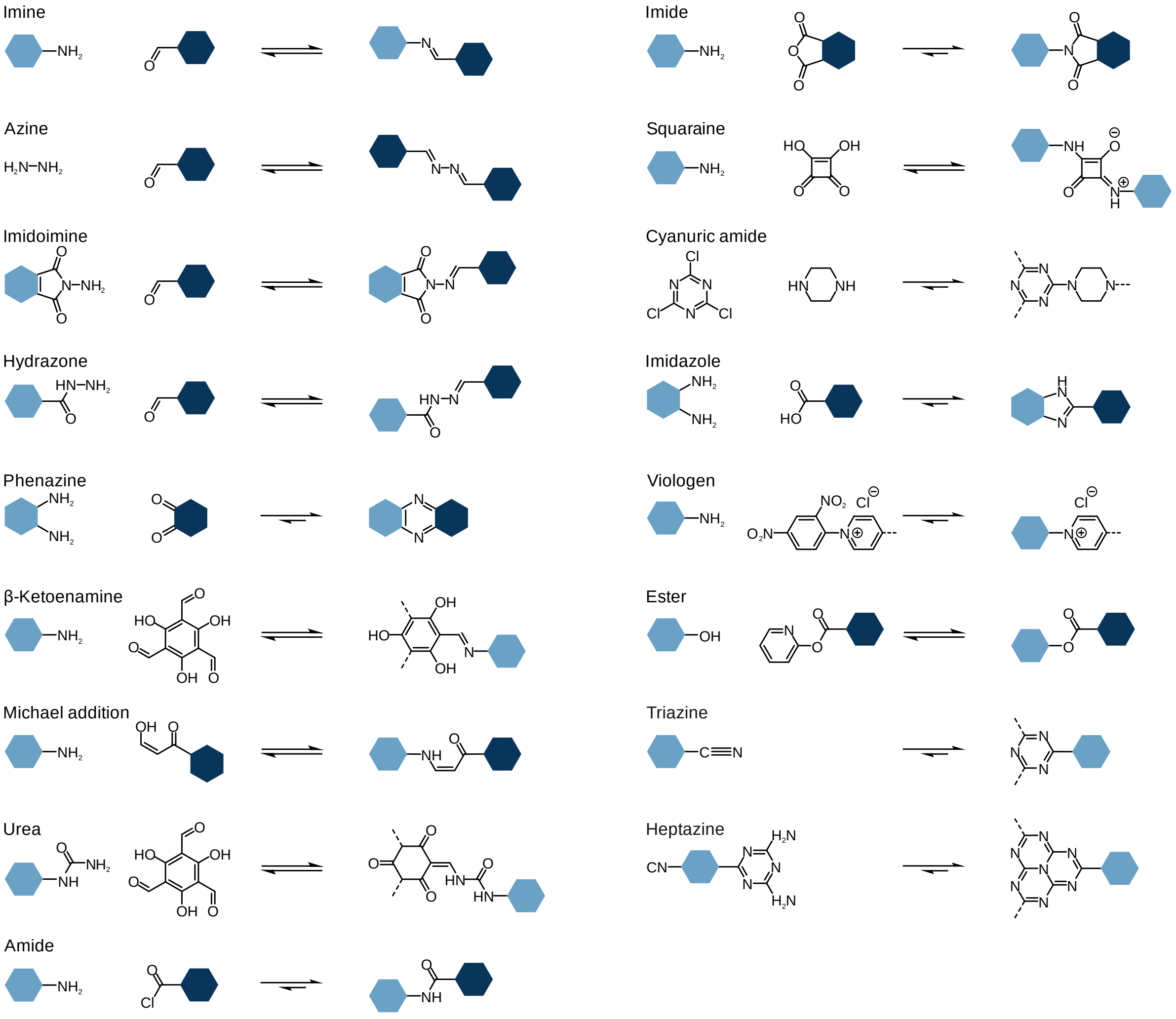

**Figure 1-8.** Collection of nitrogen- and oxygen-based linkages explored for the synthesis of COFs.

By using different types of nitrogen functions, linkages based on an $H_2N$-N motif have been developed, including azine,[67] imidoimine,[68] and hydrazone.[69-70] A special case of the imine linkage is the phenazine linkage,[71-72] since two imine bonds form an aromatic ring in a single COF linkage, which leads to significantly improved stability and hydrolysis resistance. However, the formation of the stable aromatic ring reduces the reversibility of the reaction and leads to poorly crystalline systems. Another strategy to protect the imine bond from hydrolysis is the insertion of adjacent functional groups that have a stabilizing effect. For example, it has been demonstrated that adjacent bulky hydrophobic sites sterically block the nucleophilic attack of water.[73-74] Moreover, the introduction of hydroxyl functional groups in *ortho*-position to the aldehyde functionality leads to keto-enol tautomerism and intramolecular hydrogen bonding, which stabilize the bond.[75-77] Keto-enol tautomerism can also be achieved by using a Michael-type system to synthesize an amine-type COF from amines and tritopic β-ketoenols.[78] Good chemical resistance to acids has been demonstrated for a urea-type COF synthesized by using a urea functionality instead of an amine.[79]

In addition to imine-type linkages (carbon-nitrogen double bonds), amide-type linkages (carbon-nitrogen single bonds) have also been used for the synthesis of COFs. Such linkages exhibit increased resistance to acids and bases.[80] However, the low reversibility of the amide bond must be compensated during synthesis by using reaction temperatures of >200 °C.[81] Other amide-type linkages include imides,[82] squaraines,[83] cyanuric amides,[84] and imidazoles.[85] Since imide-linked COFs are a central point in this thesis, a detailed summary of synthesis strategies, applications, and COFs formed *via* the imide condensation reaction is given in Chapter 2.

Furthermore, the Zincke reaction was used to introduce a quaternized pyridine (viologen) as a linkage leading to a charged COF backbone.[86] A carbon-oxygen bonded ester linkage was developed by reacting di(pyridin-2-yl)terephthalate with hydroxyls.[87]

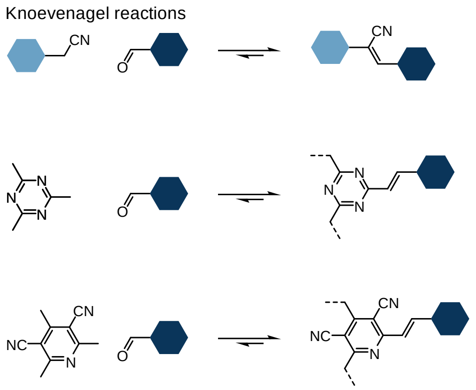

**Figure 1-9.** Various Knoevenagel reactions between different activated $CH_2$/$CH_3$ groups and aldehydes to form COFs.

The triazine linkage giving rise to covalent triazine frameworks (CTFs) is another interesting example of linkage based on carbon-nitrogen bonded aromatic heterocycles. CTFs are commonly synthesized by cyclotrimerization of nitriles using $ZnCl_2$ as a Lewis acidic catalyst at high temperatures up to 500 °C.[88] Alternative synthetic strategies for the synthesis of triazine units include the reaction of carboxylic acid amides with phosphorus pentoxide,[89] the use of trifluoromethanesulfonic acid as a superacidic catalyst,[90] or the reaction of multifunctionalized benzyl alcohols with amidines by slow *in situ* oxidation.[91] CTFs are very stable systems, however, the harsh reaction conditions often lead to partial carbonization of the frameworks and crystallinity is usually limited, so only a handful of the many reported CTF materials are crystalline. [46, 90, 92-94]

Linkages based on carbon-carbon bonds have recently attracted much attention because of the higher hydrolytic stability compared to their boron and nitrogen-based counterparts. The vinylic carbon-carbon bond can be formed by Knoevenagel reaction of aldehydes with activated methylene/methyl groups, such as cyanomethyl groups,[95] trimethyltriazine,[96] and trimethyldicyanopyridine as shown in Figure 1-9.[97]

### *1.1.3 Solving the COF Trilemma*

As discussed in Sections 1.1 and 1.1.2, COFs are synthesized predominantly following the principles of DCC, according to which the COF formation reaction must be reversible to allow thermodynamically controlled crystal defect correction.[18] Thus, for the synthesis of well-ordered COFs, bond formation reactions with high reversibility are desirable because they allow frequent bond breaking, which is as important as bond formation in order to achieve a high degree of defect correction during the crystallization process. Improving reversibility leads to an increased rearrangement rate of the linker molecules, which allows rapid convergence to the thermodynamic minimum structure. However, as a result of high reversibility, these COFs often suffer from reduced stability as the cleavage of the COF linkage corresponds to the backward reaction, a phenomenon frequently observed with boron-based COFs.[98] Conversely, COFs synthesized *via* reactions with only moderate reversibility, such as imide-linked COFs, are often poorly crystalline, and harsh reaction conditions must be applied to obtain crystalline products (see Chapter 2).[99-101] Thus, crystallinity and stability are inversely related.[42]

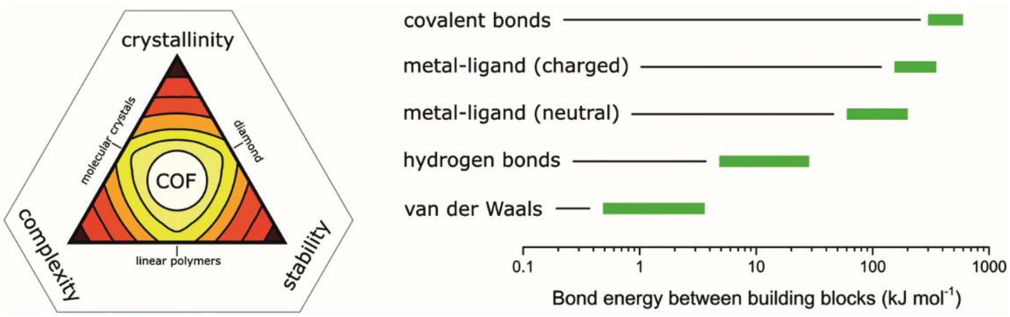

**Figure 1-10.** The trilemma of materials design for COF synthesis based on reversible reactions (left). Strengths of bonds that are used for the synthesis of molecularly defined materials (right). Reprinted from Ref. 42 with permission from the Royal Society of Chemistry.

In addition to crystallinity and stability, the third important feature of COFs to be considered is complexity, as it also competes with stability and crystallinity.[42] The complexity of COFs is usually achieved by using building blocks that carry one or more functional groups that are not involved in the COF formation reaction. As a result, the COF has accessible functional groups located on its rigid backbone, which may be desirable for certain applications.[102-103] However, with decreasing reversibility of the COF linkage, harsher reaction conditions are required to obtain a crystalline product.[46, 81] Therefore, the implementation of additional functional groups may be limited due to their thermal or chemical decomposition during synthesis.[104]

This trade-off between stability, crystallinity, and complexity has been called the "COF trilemma" (Figure 1-10).[42] One can escape this trilemma by adopting strategies that lead to ordered structures but do not depend entirely on reversible reactions, such as pre-orientation of reaction substrates or the single reaction pathway.[42] These alternative synthesis approaches can lead to improved crystallinity and stability of COFs without compromising functionality.

The underlying principle of the pre-orientation method, in contrast to synthesis *via* a reversible reaction, is the separation of simultaneous covalent bond formation and crystallization into two separate steps. In the first step, the building blocks are organized at the molecular level by weak interactions such as electrostatic or van der Waals forces in such a way that in a subsequent second step the pre-organized molecules can be linked by strong and often irreversible covalent bond formation under relatively mild conditions.[42] This methodology is closely related to the classical templating methods known from the synthesis of mesoporous silica[105-106] and two-dimensional polymers,[107-108] in which long-range order is created in otherwise disordered networks. Preorientation of the building blocks can be achieved *via* several approaches. One possibility is the preparation of molecular crystals from building blocks that can be crosslinked in a topotactic single-crystal-to-single-crystal transformation. This method has been demonstrated by cycloaddition between anthracenes and alkynes or by photochemical dimerization of anthracenes.[109-112] Another strategy is to use surfactants that allow electrostatic interactions and hydrogen bonding to direct the linker molecules. For example, an imide-linked COF was successfully synthesized by assembling and pre-organizing porphyrin linker molecules on a water surface using sodium oleyl sulfate as a surfactant.[113] In addition, a vinyl-pyridinium functionalized 3D COF was synthesized by utilizing directed host-guest molecule interactions using a two-step strategy.[114] A particular type of pre-organization strategy to realize otherwise inaccessible or difficult-to-obtain COFs is the COF-to-COF transformation.[115-118] In this strategy, reported COFs are used as ordered templates for subsequent linker exchange. For linker molecule exchange, the exchanging monomers must meet the requirements of matching functional groups and connectivity, and they must be approximately the same size to fit into the existing framework.

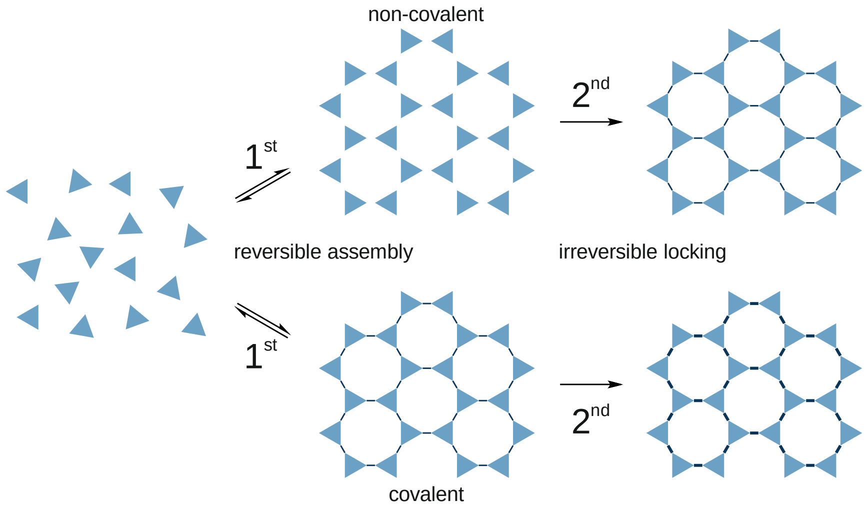

**Figure 1-11.** Schematic representation of the pre-orientation strategy used for COF synthesis. The upper path describes the assembly of the linker molecules through non-covalent interactions and the subsequent linking through irreversible

reactions. The path below shows the arrangement of the linker molecules through highly reversible covalent bonds and their subsequent locking through irreversible bond formation.

The strategies for pre-orienting COF precursors presented above were primarily intended to impart or enhance the crystallinity of a COF and did not focus on improving stability. One preorientation strategy for stabilizing otherwise labile COF linkages, such as the imine linkage, is the post-synthetic linkage modification approach, in which the COF itself serves as a pre-oriented platform.[119] In the first step, a desired COF is synthesized by reversible bond formation, which allows the synthesis of a highly crystalline and functional product under relatively mild conditions. Subsequently, the labile reversible bond is post-synthetically converted to a stabilized species, resulting in thermodynamic locking of the bond (Figure 1-11).[119] This synthetic method was demonstrated prior to COF chemistry in self-assembled organic cages, where thermodynamic locking of an imine-linked cage was achieved by an initial post-synthetic reduction of the imine bond to an amine bond, followed by a reaction with N,N'-carbonyldiimidazole to result in a carbamate cage.[120]

Post-synthetic transformations can be divided into two categories:[42] In the first category, the chemical nature of the COF linkage itself is changed during the transformation, e.g., by oxidation or reduction of an imine to an amide or amine, respectively.[80, 121-123] In the second category, additional bonds are created between linker molecules that parallel the existing COF bond, as in the oxidative cyclization of an imine to a benzothiazole with sulfur[119, 124] or to a benzoxazole with adjacent hydroxyl groups (Figure 1-12).[125] Quinolines,[126] tetrahydroquinolines[127] and chromenoquinolines could also be synthesized from reversibly formed imines *via* inter- and intramolecular irreversible Povarov reactions.[128]

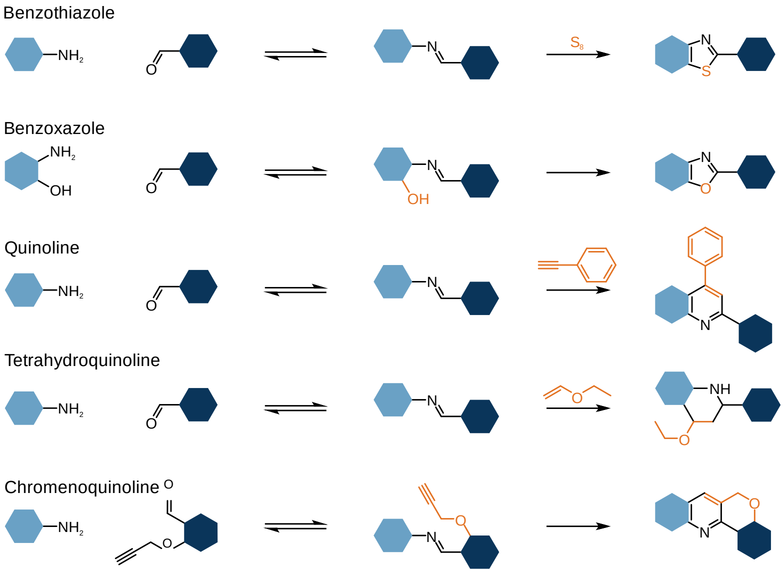

**Figure 1-12.** A collection of irreversible reactions used to lock linkages formed by reversible bond formation.

In addition to COF synthesis using reversible reactions or pre-oriented substrates, the single reaction route has been shown to be another possible strategy for the synthesis of COFs *via* irreversible bond formation:[129-130] While the method described above for the synthesis of COFs using irreversible bond formation uses a pre-orientation step to ensure the correct arrangement of linker molecules prior to polymerization, in the single reaction pathway the conformational degrees of freedom are restricted to limit the number of possible conjunctions during polymerization (Figure 1-13). The limitation of possible conjunctions is achieved by constructing highly rigid linker molecules that allow polymerization to propagate only at the correct reaction sites. However, once two building blocks are placed at adjacent positions on the crystallite, two possibilities arise for linking the available unsaturated functional groups: Adjacent building blocks can react with each other and form an internal linkage, leading to the growth of the crystallite, or a new building block can be attached to one of the free functional groups, leading to the formation of a defect site as can be seen in Figure 1-12 a).[42]

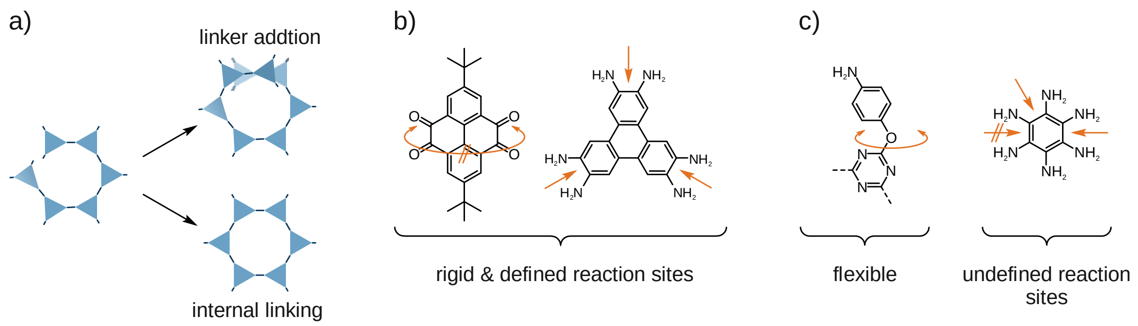

**Figure 1-13.** a) Schematic representation of the linker addition and internal linking opportunities during the single reaction pathway. b) Rigid linker molecules with defined reaction sites. c) Flexible linker molecules without defined reaction sites.

These defect sites cannot be repaired by error correction mechanisms if the linkage is formed by an irreversible reaction. However, the competition between building block addition and internal linking depends on the linker concentration and is therefore controllable: while the rate of linker addition increases with building block concentration, the rate of internal linking remains concentration independent.[42] Therefore, by reducing the rate of precursor addition to the reaction mixture, trapping of misaligned building blocks in the crystal can be minimized (Figure 1-14). In addition, reducing the building block concentration in the reaction mixture reduces the formation of dimers and oligomers, resulting in favored growth on the available particles and thus larger crystallites.[131] Loh and co-workers demonstrated the formation of crystalline COFs by an irreversible and uncatalyzed Ullman coupling reaction using the single reaction pathway with highly rigid aromatic bromine precursors.[132-133] A growing number of examples use the direct synthetic pathway to form crystalline COFs based on irreversible or kinetically controlled reactions such as carbon-carbon cross-coupling,[134] Glaser coupling,[135] and others.[130, 136-139]

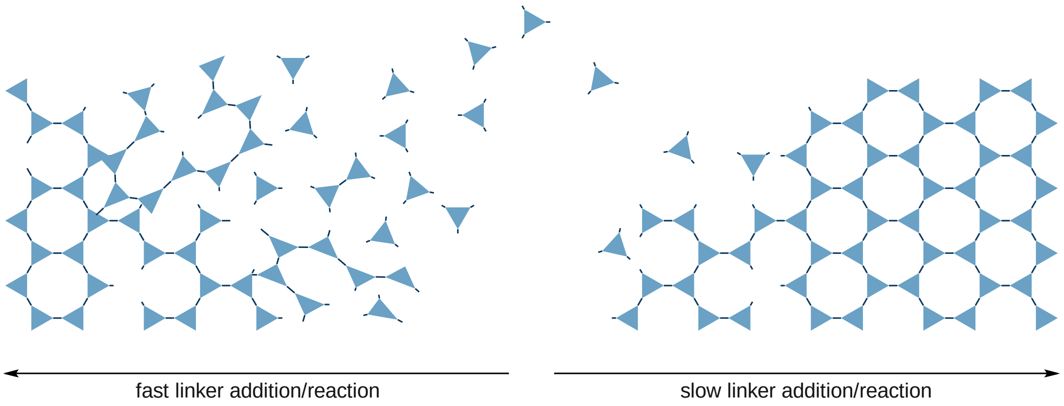

**Figure 1-14.** Schematic representation of the single reaction pathway showing its dependence on linker addition and reaction rate.

While a large number of building blocks of sufficient rigidity are available for designing COFs with a reduced number of conformers, COF linkages are limited in both number and modifiability.[42] Many COF linkages, such as the imine bond, introduce additional conformers to those of the building blocks into the structure, resulting in increased disorder in the crystal. For example, the imine linkage entails two diastereomers forming planar structures as shown in Figure 1-15. Considering the stacking of two COF sheets in three dimensions, the two diastereomers can lead to five conformers. The number of conformers multiplies with each additional COF sheet. As a consequence of this flexibility of the imine linkage, multiple structural conformers can in principle be formed with the same linker molecules.[34, 140-141] However, there are strategies to direct imine linkages so that the number of diastereomers is reduced. For example, the use of an *ortho*-hydroxyaldehyde linker molecule creates an intramolecular hydrogen bond, resulting in alignment of the imine group with the hydroxyl group, thereby locking the diastereomeric conformer.[75] The other diasteromeric conformer can be favoured with an *ortho*-methoxy-substituted aldehyde.[121] The bulky methoxy group creates steric repulsion, directing the imine bond away from it.

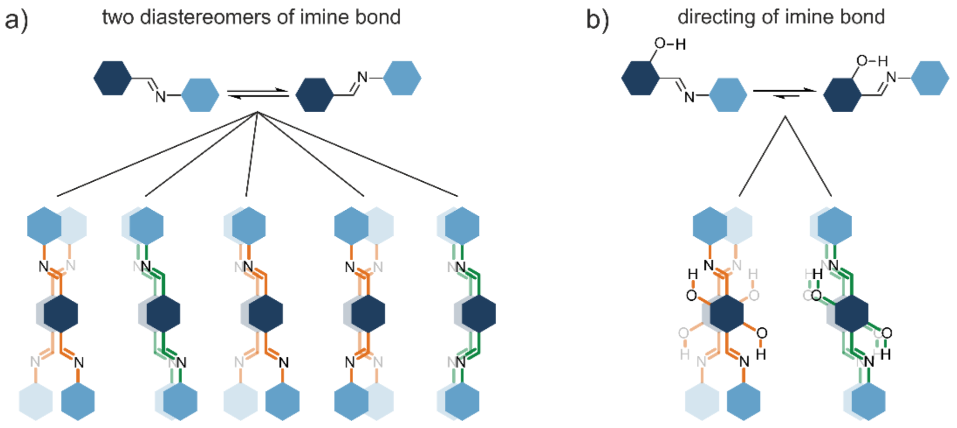

**Figure 1-15.** a) Diastereomers of the imine linkage and conformational isomers resulting from the stacking of COF layers. b) Locking of the imine linkage by favoring intramolecular hydrogen bonding leading to a reduction of conformational isomers.

## 1.2 Synthesis Strategies for Covalent Organic Frameworks

In addition to the choice of suitable building blocks and linkage types, an appropriate synthesis strategy is crucial to obtain COFs with high long-range order and intrinsic porosity. Several complementary strategies have been developed for synthesizing novel COF materials or to modify the properties of existing frameworks. A selection of the most important strategies is presented below.

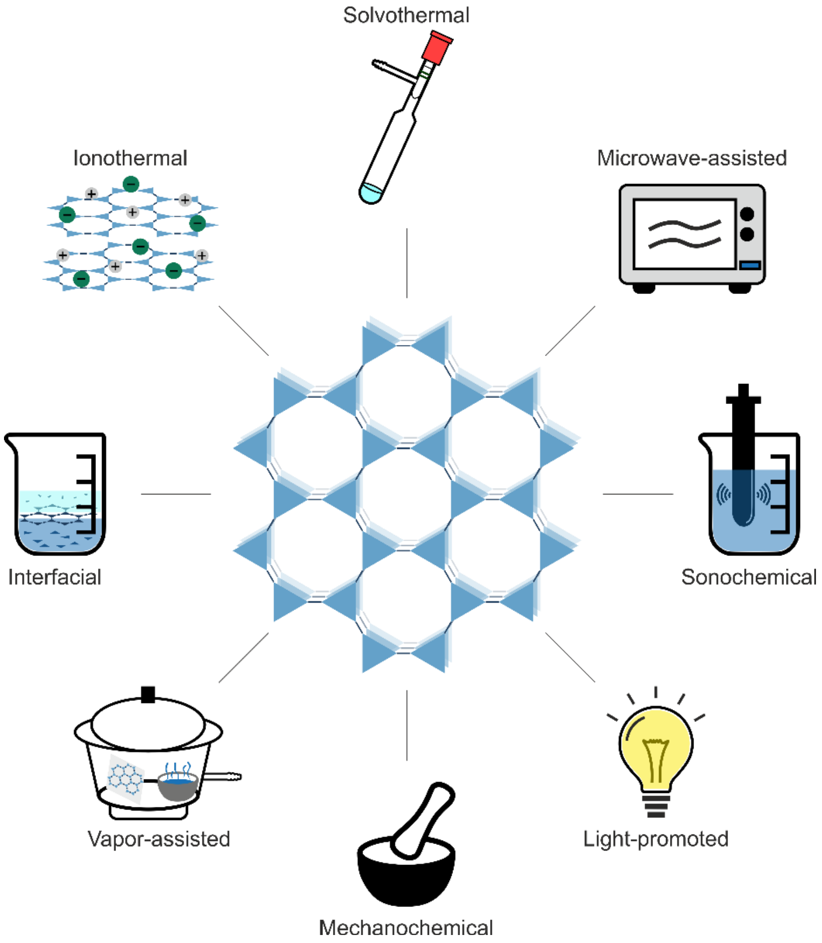

**Figure 1-16.** Schematic representation of the different strategies for the synthesis of COFs.

### 1.2.1 Solvothermal Synthesis

The most commonly used synthesis strategy for COFs is the solvothermal approach. In a typical solvothermal synthesis, the desired building blocks are suspended in a solvent mixture and heated in a closed vessel for 3-7 days. In this method, special attention must be paid to the solvent mixture and temperature. The target temperature of the reaction mixture depends on the type of linkage chosen. While boron-based COFs and imine COFs are usually formed at relatively mild temperatures of 80-120 °C,[18, 34] reaction temperatures >200 °C are often required for imide-linked COFs to ensure sufficient reversibility.[82, 142] In addition to temperature, the choice of a suitable solvent mixture is also crucial for the solvothermal synthesis of crystalline COFs. The type of solvent and the ratio in which the solvents are mixed must be precisely adjusted for each building block to allow its controlled diffusion into the solution. Controlling the availability of the building blocks during the reaction allows for controlled crystallite growth. Solvothermal reactions are usually carried out in closed vessels using sealed pyrex tubes or microwave flasks. This ensures a constant ratio of the solvents during the reaction by preventing their evaporation. When a COF is formed by a condensation reaction, the closed reaction environment serves another important function: the water formed during the condensation reaction is kept available to facilitate the back reaction by hydrolysis of the linkage.[143] This bond cleavage enables the error control mechanisms required for the formation of crystalline products. To further enhance the reversibility of the COF formation reaction, acidic or basic catalysts such as acetic acid or isoquinoline are often used. In addition to classical acids and bases, water-tolerant Lewis acids such as metal triflates have also been shown to be suitable catalysts for accelerating the formation of COFs at room temperature. For example, using $Sc(OTf)_3$ as a catalyst, TAPB-PDA-COF was synthesized in a mixture of 1,4-dioxane/mesitylene (4:1 v/v) at room temperature within 10 min.[144] In contrast, the solvothermal method requires more than 24 h and temperatures above 70 °C. Synthesis of COFs under such mild conditions may be an attractive strategy for fragile linker molecules, sensitive substrates, or simply to reduce the energy expenditure of COF synthesis. In yet another example of this type, by reacting 1,3,5-tris(3-dimethylamino-1-oxoprop-2-en-yl)benzene with various amines, β-ketoenamine-linked COFs could be synthesized by Michael addition-elimination reactions in aqueous media and under ambient conditions.[145]

### *1.2.2 Irradiation-Assisted Synthesis*

Another alternative strategy to the commonly used solvothermal method is microwave-assisted synthesis of COFs. This widely researched method allows precise and simultaneous control of temperature and pressure, as well as monitoring of phase behavior during the reaction.[146-147] As a result of the improved control of reaction parameters, the products obtained are often cleaner and reaction times are shorter. Cooper and co-workers demonstrated the synthesis of COF-5 using the microwave-assisted synthesis strategy.[148-149] The COF was synthesized at 100 °C within 20 min using 200 W microwave irradiation and exhibited a larger surface area than the same COF synthesized under solvothermal conditions. Another economical way to synthesize COFs is the sonochemical strategy.[150] In this method, ultrasound is used to create bubbles in the solvent that grow and collapse. This phenomenon, called cavitation, generates extremely high local pressures and temperatures and can thus be used to initiate and accelerate chemical reactions. Ahn *et al*. used this method to scale up the synthesis of COF-1 and COF-5 by a factor of 10 to the gram scale without compromising structural integrity or surface area.[151] In addition to microwave irradiation and ultrasound, simulated sunlight has been shown to facilitate the formation of a crystalline COF.[152] For example, hcc-COF was synthesized by suspending the precursor molecules hexaketocyclohexane octahydrate and 1,2,4,5-benzenetetramine tetrahydrochloride in a methanol/mesitylene solvent mixture. After addition of acetic acid and water as co-catalysts, the reaction mixture was irradiated with light at a wavelength of 200-2500 nm. An amorphous version of hcc-COF was obtained in the absence of light during the reaction, proving the effect of light on the reversibility of the reaction.

### *1.2.3 Mechanochemical Synthesis*

All of the strategies described above, including the widely used solvothermal and microwave-assisted methods, are carried out under rather complex conditions, as sealed Pyrex tubes, an inert atmosphere, suitable solvent mixtures, and appropriate temperatures are required to obtain crystalline products. In particular, the search for suitable solvent mixtures and reaction temperatures often requires thorough screening of reaction conditions and can be very time consuming. Therefore, the exploration of simple synthesis strategies is highly desirable. The mechanochemical approach offers a rapid, solvent-free, and environmentally friendly alternative to the previously mentioned solvent-based strategies. In the simplest mechanochemical synthesis of COFs, precursor molecules are placed in a mortar and ground under ambient conditions using a pestle. β-ketoenamine COFs have been successfully synthesized by Schiff base condensation using this primitive grinding method.[153] Optimization of the mechanochemical approach could be achieved by adding small amounts of solvent and catalyst to the precursor mixture during grinding.[154] This liquid-assisted grinding increases the reaction rate by promoting the homogeneity of the reactants, leading to improved crystallinity. Automation and better reproducibility of the mechanochemical method can be achieved by combining the liquid-assisted methods together with the use of ball mills instead of manual grinding.[155-157]

### *1.2.4 Ionothermal Synthesis*

The ionothermal synthetic route offers a synthetic strategy in which the reaction medium acts as both solvent and catalyst.[46] Thomas *et al*. demonstrated the synthesis of crystalline CTFs in molten $ZnCl_2$ by cyclic trimerization of nitriles at temperatures between 300 and 500 °C.[46, 94] In this reaction, $ZnCl_2$ acts as a solvent for the nitrile precursor molecules and as a Lewis acidic catalyst that promotes the cyclization reaction. Countless CTF materials have been synthesized using this ionothermal approach, but most of them do not exhibit the desired long-range order typical of COFs, which limits their application. Moreover, the harsh reaction conditions often lead to undesirable side reactions, partial decomposition, and carbonization of the building blocks, drastically limiting the selection of suitable linker molecules. To circumvent these problems by avoiding the high reaction temperatures, an ionothermal synthesis using ionic liquids as reaction media was developed by Qiu *et al.*[158] Using 1-butyl-3-methylimidazolium bis-((trifluoromethyl)sulfonyl)imide as the reaction medium for a Schiff base reaction, 3D-IL-COF could be synthesized within 12 hours at ambient temperatures and pressures. A novel ionothermal synthesis was developed as part of this work and is discussed in Chapter 4.

### *1.2.5 Synthesis of COF Thin Films*

All of the aforementioned synthesis protocols result in predominantly insoluble powders that are often unprocessable, thus limiting their potential range of applications. Interfacial synthesis provides a useful method for the preparation of COF thin films with controlled thickness.[159-161] In a typical reaction, the precursor molecules and a catalyst are dissolved in two separate immiscible solvents. By overlaying the two precursor solutions, a two-phase mixture is formed. At the interface of these two solutions, the previously separated precursor molecules combine and react in a controlled, layer-by-layer manner. Suitable solvent combinations include water/toluene or water/dichloromethane. With this method, imine COFs have been synthesized *via* a Schiff base reaction using acidic acid or $Sc(OTf)_3$ as catalyst,[159-160] and C-C bonded COFs were realized *via* Suzuki coupling.[134] Vapor-assisted synthesis provides a strategy for the efficient preparation of boroxin-COF thin films.[162] An acetone/ethanol precursor solution is dropped onto a substrate and placed in a closed desiccator along with a small vessel containing 1,4-dioxane/mesitylene (1:1 v/v). After a few days at room temperature, COF thin films are formed.

## *1.3 Properties and Applications of Covalent Organic Frameworks*

COFs have a high specific surface area, defined pores, and usually an aromatic backbone, which makes them suitable candidates for a variety of applications. One of the most researched applications is the adsorption and separation of guest molecules. The successful use of COFs for adsorption and separation applications strongly depends on their porous structure (pore size and shape), pore wall properties, and accessible specific surface area.[43] Research in this field has focused primarily on the adsorption of small gaseous molecules such as hydrogen,[163-165] methane,[166-167] or $CO_2$,[168-170] but also of other small molecules such as iodine,[171-173] and metal ions.[174-177] By incorporating functional groups onto the COF pores, chemisorption of toxic gases such as ammonia and $SO_2$ has been demonstrated,[178-179] although the reactivity of these toxic gases towards the host COF materials makes adsorption challenging. With further development in this field and the ability to synthesize COFs with larger pore diameters, more complex organic compounds such as rhodamine B,[82] methylene blue,[180] ibuprofen,[142] and others were demonstrated to be adsorbed or temporarily trapped. These adsorption properties make COFs prospective materials for potential applications in water treatment and drug delivery.[181-182] By designing pore diameter and pore wall properties that exhibit increased affinity for specific guest molecules, e.g., by tuning polarity, COFs are used for the selective separation of gas mixtures such as $CO_2/H_2$,[183] $CO_2/CH_4$,[184] $H_2/N_2$,[143] $H_2/CH_4$,[143] and $C_2H_2/C_2H_4$.[185-186]

The combination of accessible pores, which allow the uptake of guest molecules, and aromatic backbones, which allow the migration of charges, including (emissive) excitons, makes COFs suitable materials for selective and sensitive sensors. Detection of guest molecules is usually achieved by fluorescence quenching of the sensor COF by the guest molecule to be detected. The application of COFs in sensing ranges from selective detection of anions,[187] to toxic metal ions (e.g., $Cu^{II}$, $Hg^{II}$, $Fe^{III}$),[188-190] to hazardous chemicals,[191-192] and explosives.[67, 193] In recent years, COFs have gained interest for selective detection of biomolecules such as bovine serum albumin and double-stranded DNA.[194-195] By synthesizing chiral COFs, enantioselective detection of carbohydrates and amino acids could be realized.[196-197]

Most COFs contain rigid π-systems stacked on top of each other to form ordered columnar π-arrays interconnected by electronic coupling within the column. By appropriate design, it is thus possible to achieve electron,[198] hole,[199] or ambipolar charge transfer along these columns.[200] By integrating electron-donating building units into the COF backbone along with electron-accepting building blocks, donor-acceptor COFs can be developed that often have smaller band gaps, which can lead to improved conductivity.[201] These so-formed donor-acceptor heterojunctions can also be achieved by guest molecules.[202] For example, by integrating electron-accepting guest molecules into the pores of an electron-donating COF, photoexcited charge separation,[202] photoconductivity,[203] and ambipolar charge separation can be achieved.[204-205] Such donor-acceptor systems have been used for field-effect transistors,[204-205] photodetectors,[206] and thermoelectrics. [207] Recently, a fully $sp^2$-carbon conjugated COF was demonstrated to exhibit enhanced conductivity, high spin density, and paramagnetic properties upon oxidation with iodine.[208]

The ordered nature of COFs, with its aligned 1D pore channels that can accommodate guest molecules or ions, makes COFs suitable materials for mass transport applications such as proton conduction[209-212] and lithium ion conduction.[63, 213] In addition, COFs are of growing interest as organic electrode materials for battery devices because the redox-active frameworks promote energy storage and the open pore channels provide space for ion storage and transport.[214] COFs have thus found application in lithium-ion,[215-217] lithium-sulfur,[218-221] sodium-ion,[100, 222-224] and potassium-ion batteries.[225-227] More recently, COFs have also been used for multivalent ion systems such as zinc-ion,[228-231] magnesium-ion,[232] and aluminum-ion energy storage devices.[233]

The large surface area and modularity of COFs make them versatile platforms for various heterogeneous catalytic applications. For example, COFs have been shown to act as electrocatalysts for the reduction of oxygen and $CO_2$,[234-237] or for the oxygen evolution half-reaction.[238-239] However, in most cases, COFs are semiconductors with low conductivity and show limited electrocatalytic activity. To increase conductivity and thus catalytic activity, conductive additives such as carbon black or pyrolysis of the frameworks are required, often leading to a decrease in specific COF properties.[43] Due to their semiconducting properties and large accessible surface area, COFs are intensively studied as photosensitizers for photocatalytic hydrogen evolution,[240-241] $CO_2$ reduction,[242-243] and singlet oxygen generation.[83, 244] In addition, a variety of organic reactions, such as Suzuki cross-coupling,[245-246] Knoevenagel condensation,[247-248] or aerobic oxidation of amines to imines have been demonstrated using COFs as photocatalysts.[249] By introducing chiral sites into the COFs backbone, asymmetric organic catalysis has been realized.[250-251]

## *1.4 Bibliography*

[1] W. B. Jensen, *J. Chem. Educ.* **2008**, *85*, 624.

[2] H. Morawetz, Polymers: the origins and growth of a science, Courier Corporation, **2002**.

[3] P. C. Painter, M. M. Coleman, Fundamentals of Polymer Science: An Introductory Text (2nd ed.), Routledge, **1997**.

[4] Taylor, D.W. and Kennedy, J.F. (1994), An introduction to plastics, edited by H. G. Elias. VCH Verlagsgesellschaft, Weinheim, **1993**. pp. xviii + 349, price £32.00. ISBN 3-527-28578-4. Polym. Int., 34: 237-238.

[5] R. B. Seymour, *J. Chem. Educ.* **1988**, *65*, 327.

[6] H. Staudinger, *Ber. dtsch. Chem. Ges. A/B* **1920**, *53*, 1073-1085.

[7] H. Staudinger, *Ber. dtsch. Chem. Ges. A/B* **1926**, *59*, 3019-3043.

[8] W. H. Carothers, *Trans. Faraday Soc.* **1936**, *32*, 39-49.

[9] W. H. Carothers, U.S. Patent 2,071,250 to E. I. du Pont de Nemours & Company, **1931**.

[10] W. H. Carothers, U.S. Patent 2,130,948 to E. I. du Pont de Nemours & Company, **1937**.

[11] K. Ziegler, G. H.-G., Deutsches Patent: 961,537: Verfahren zur Herstellung von Aluminiumtrialkylen und Aluminiumalkylhydriden.

[12] K. Ziegler, H. Breil, E. Holzkamp, H. Martin, U.S. Patent 3,257,332: Catalysts for polymerizing olefins, especially ethylene., **1966**.

[13] G. Natta, I. Pasquon, A. Zambelli, *J. Am. Chem. Soc.* **1962**, *84*, 1488-1490.

[14] K. S. W. Sing, *Pure Appl. Chem.* **1985**, *57*, 603-619.

[15] N. Usahanunth, S. Tuprakay, *Case Stud. Constr. Mater.* **2017**, *6*, 120-133.

[16] H. Hayashi, A. P. Côté, H. Furukawa, M. O'Keeffe, O. M. Yaghi, *Nat. Mater.* **2007**, *6*, 501-506.

[17] H. Li, M. Eddaoudi, M. O'Keeffe, O. M. Yaghi, *Nature*, **1999**, *402*, 276-279.

[18] A. P. Cote, A. I. Benin, N. W. Ockwig, M. O'Keeffe, A. J. Matzger, O. M. Yaghi, *Science*, **2005**, *310*, 1166-1170.

[19] V. Komvokis, L. X. L. Tan, M. Clough, S. S. Pan, B. Yilmaz, in Zeolites in Sustainable Chemistry: Synthesis, Characterization and Catalytic Applications (Eds.: F.-S. Xiao, X. Meng), Springer Berlin Heidelberg, Berlin, Heidelberg, **2016**, pp. 271-297.

[20] A. Takahashi, R. T. Yang, C. L. Munson, D. Chinn, *Langmuir* **2001**, *17*, 8405-8413.

[21] M. S. Onyango, D. Kuchar, M. Kubota, H. Matsuda, *Ind. Eng. Chem. Res.* **2007**, *46*, 894-900.

[22] F. Su, C. Lu, S.-C. Kuo, W. Zeng, *Energy & Fuels*, **2010**, *24*, 1441-1448.

[23] D. Breck, W. Eversole, R. Milton, T. Reed, T. L. Thomas, *J. Am. Chem. Soc.* **1956**, *78*, 5963-5972.

[24] A. G. Wong-Foy, A. J. Matzger, O. M. Yaghi, *J. Am. Chem. Soc.* **2006**, *128*, 3494-3495.

[25] N. L. Rosi, J. Eckert, M. Eddaoudi, D. T. Vodak, J. Kim, M. O'Keeffe, O. M. Yaghi, *Science* **2003**, *300*, 1127-1129.

[26] M. P. Suh, H. J. Park, T. K. Prasad, D.-W. Lim, *Chem. Rev.* **2012**, *112*, 782-835.

[27] P. Kumar, A. Deep, K.-H. Kim, *Trends Anal. Chem.* **2015**, *73*, 39-53.

[28] C.-D. Wu, A. Hu, L. Zhang, W. Lin, *J. Am. Chem. Soc.* **2005**, *127*, 8940-8941.

[29] H. Liu, Y. Liu, Y. Li, Z. Tang, H. Jiang, *J. Phys. Chem. C* **2010**, *114*, 13362-13369.

[30] K. Leus, T. Bogaerts, J. De Decker, H. Depauw, K. Hendrickx, H. Vrielinck, V. Van Speybroeck, P. Van Der Voort, *Microporous Mesoporous Mater.* **2016**, *226*, 110-116.

[31] Y. Zhu, H. Long, W. Zhang, *Chem. Mater.* **2013**, *25*, 1630-1635.

[32] J. Ma, M. Wang, Z. Du, C. Chen, J. Gao, J. Xu, *Polym. Chem.* **2012**, *3*, 2346-2349.

[33] J. Liu, K.-K. Yee, K. K.-W. Lo, K. Y. Zhang, W.-P. To, C.-M. Che, Z. Xu, *J. Am. Chem. Soc.* **2014**, *136*, 2818-2824.

[34] F. J. Uribe-Romo, J. R. Hunt, H. Furukawa, C. Klock, M. O'Keeffe, O. M. Yaghi, *J. Am. Chem. Soc.* **2009**, *131*, 4570-4571.

[35] O. M. Yaghi, M. O'Keeffe, N. W. Ockwig, H. K. Chae, M. Eddaoudi, J. Kim, *Nature* **2003**, *423*, 705-714.

[36] A. P. Côté, H. M. El-Kaderi, H. Furukawa, J. R. Hunt, O. M. Yaghi, *J. Am. Chem. Soc.* **2007**, *129*, 12914-12915.

[37] S. J. Rowan, S. J. Cantrill, G. R. L. Cousins, J. K. M. Sanders, J. F. Stoddart, *Angew. Chem. Int. Ed.* **2002**, *41*, 898-952.

[38] C. S. Diercks, O. M. Yaghi, *Science* **2017**, *355*, eaal1585.

[39] H. M. El-Kaderi, J. R. Hunt, J. L. Mendoza-Cortes, A. P. Cote, R. E. Taylor, M. O'Keeffe, O. M. Yaghi, *Science* **2007**, *316*, 268-272.

[40] K.-D. Zhang, S. Matile, *Angew. Chem. Int. Ed.* **2015**, *54*, 8980-8983.

[41] A. Wilson, G. Gasparini, S. Matile, *Chem. Soc. Rev.* **2014**, *43*, 1948-1962.

[42] F. Haase, B. V. Lotsch, *Chem. Soc. Rev.* **2020**, *49*, 8469-8500.

[43] K. Geng, T. He, R. Liu, S. Dalapati, K. T. Tan, Z. Li, S. Tao, Y. Gong, Q. Jiang, D. Jiang, *Chem. Rev.* **2020**, *120*, 8814-8933.

[44] J. Lee, J. Kim, T. Hyeon, *Adv. Mater.* **2006**, *18*, 2073-2094.

[45] S. Hug, M. E. Tauchert, S. Li, U. E. Pachmayr, B. V. Lotsch, *J. Mater. Chem.* **2012**, *22*, 13956-13964.

[46] P. Kuhn, M. Antonietti, A. Thomas, *Angew. Chem. Int. Ed.* **2008**, *47*, 3450-3453.

[47] S. Wan, J. Guo, J. Kim, H. Ihee, D. Jiang, A Belt-Shaped, *Angew. Chem. Int. Ed.* **2008**, *47*, 8826-8830.

[48] E. L. Spitler, W. R. Dichtel, *Nat. Chem.* **2010**, *2*, 672-677.

[49] X. Feng, X. Ding, L. Chen, Y. Wu, L. Liu, M. Addicoat, S. Irle, Y. Dong, D. Jiang, *Sci. Rep.* **2016**, *6*, 32944.

[50] S. Dalapati, M. Addicoat, S. Jin, T. Sakurai, J. Gao, H. Xu, S. Irle, S. Seki, D. Jiang, *Nat. Commun.* **2015**, *6*, 7786.

[51] S.-Q. Xu, T.-G. Zhan, Q. Wen, Z.-F. Pang, X. Zhao, *ACS Macro Lett.* **2016**, *5*, 99-102.

[52] T. Y. Zhou, S. Q. Xu, Q. Wen, Z. F. Pang, X. Zhao, *J. Am. Chem. Soc.* **2014**, *136*, 15885-15888.

[53] X. Chen, N. Huang, J. Gao, H. Xu, F. Xu, D. Jiang, *Chem. Commun.* **2014**, *50*, 6161-6163.

[54] L. Ascherl, T. Sick, J. T. Margraf, S. H. Lapidus, M. Calik, C. Hettstedt, K. Karaghiosoff, M. Döblinger, T. Clark, K. W. Chapman, F. Auras, T. Bein, *Nat. Chem.* **2016**, *8*, 310-316.

[55] C. Qian, E.-C. Liu, Q.-Y. Qi, K. Xu, G.-F. Jiang, X. Zhao, *Polym. Chem.* **2018**, *9*, 279-283.

[56] L. A. Baldwin, J. W. Crowe, M. D. Shannon, C. P. Jaroniec, P. L. McGrier, *Chem. Mater.* **2015**, *27*, 6169-6172.

[57] H. Yang, Y. Du, S. Wan, G. D. Trahan, Y. Jin, W. Zhang, *Chem. Sci.* **2015**, *6*, 4049-4053.

[58] J. W. Crowe, L. A. Baldwin, P. L. McGrier, *J. Am. Chem. Soc.* **2016**, *138*, 10120-10123.

[59] N. Huang, L. Zhai, D. E. Coupry, M. A. Addicoat, K. Okushita, K. Nishimura, T. Heine, D. Jiang, *Nat. Commun.* **2016**, *7*, 12325.

[60] Z.-F. Pang, S.-Q. Xu, T.-Y. Zhou, R.-R. Liang, T.-G. Zhan, X. Zhao, *J. Am. Chem. Soc.* **2016**, *138*, 4710-4713.

[61] T. Banerjee, F. Haase, S. Trenker, B. P. Biswal, G. Savasci, V. Duppel, I. Moudrakovski, C. Ochsenfeld, B. V. Lotsch, *Nat. Commun.* **2019**, *10*, 2689.

[62] E. Vitaku, W. R. Dichtel, *J. Am. Chem. Soc.* **2017**, *139*, 12911-12914.

[63] Y. Du, H. Yang, J. M. Whiteley, S. Wan, Y. Jin, S. H. Lee, W. Zhang, *Angew. Chem. Int. Ed.* **2016**, *55*, 1737-1741.

[64] K. T. Jackson, T. E. Reich, H. M. El-Kaderi, *Chem. Commun.* **2012**, *48*, 8823-8825.

[65] J. R. Hunt, C. J. Doonan, J. D. LeVangie, A. P. Cote, O. M. Yaghi, *J. Am. Chem. Soc.* **2008**, *130*, 11872-11873.

[66] H. L. Nguyen, F. Gándara, H. Furukawa, T. L. H. Doan, K. E. Cordova, O. M. Yaghi, *J. Am. Chem. Soc.* **2016**, *138*, 4330-4333.

[67] S. Dalapati, S. Jin, J. Gao, Y. Xu, A. Nagai, D. Jiang, *J. Am. Chem. Soc.* **2013**, *135*, 17310-17313.

[68] G. Das, B. P. Biswal, S. Kandambeth, V. Venkatesh, G. Kaur, M. Addicoat, T. Heine, S. Verma, R. Banerjee, *Chem. Sci.* **2015**, *6*, 3931-3939.

[69] C. Liang, H. Lin, Q. Wang, E. Shi, S. Zhou, F. Zhang, F. Qu, G. Zhu, *J. Hazard. Mater.* **2020**, *381*, 120983.

[70] S. He, B. Yin, H. Niu, Y. Cai, *Appl. Catal.* **2018**, *239*, 147-153.

[71] J. Guo, Y. Xu, S. Jin, L. Chen, T. Kaji, Y. Honsho, M. A. Addicoat, J. Kim, A. Saeki, H. Ihee, S. Seki, S. Irle, M. Hiramoto, J. Gao, D. Jiang, *Nat. Commun.* **2013**, *4*, 2736.

[72] Y. Ma, X. Liu, X. Guan, H. Li, Y. Yusran, M. Xue, Q. Fang, Y. Yan, S. Qiu, V. Valtchev, *Dalton Trans.* **2019**, *48*, 7352-7357.

[73] L. M. Lanni, R. W. Tilford, M. Bharathy, J. J. Lavigne, *J. Am. Chem. Soc.* **2011**, *133*, 13975-13983.

[74] X. Wu, X. Han, Y. Liu, Y. Liu, Y. Cui, *J. Am. Chem. Soc.* **2018**, *140*, 16124-16133.

[75] S. Kandambeth, A. Mallick, B. Lukose, M. V. Mane, T. Heine, R. Banerjee, *J. Am. Chem. Soc.* **2012**, *134*, 19524-19527.

[76] S. Chandra, S. Kandambeth, B. P. Biswal, B. Lukose, S. M. Kunjir, M. Chaudhary, R. Babarao, T. Heine, R. Banerjee, *J. Am. Chem. Soc.* **2013**, *135*, 17853-17861.

[77] S. Kandambeth, D. B. Shinde, M. K. Panda, B. Lukose, T. Heine, R. Banerjee, *Angew. Chem. Int. Ed.* **2013**, *52*, 13052-13056.

[78] M. R. Rao, Y. Fang, S. De Feyter, D. F. Perepichka, *J. Am. Chem. Soc.* **2017**, *139*, 2421-2427.

[79] C. Zhao, C. S. Diercks, C. Zhu, N. Hanikel, X. Pei, O. M. Yaghi, *J. Am. Chem. Soc.* **2018**, *140*, 16438-16441.

[80] P. J. Waller, S. J. Lyle, T. M. Osborn Popp, C. S. Diercks, J. A. Reimer, O. M. Yaghi, *J. Am. Chem. Soc.* **2016**, *138*, 15519-15522.

[81] D. Stewart, D. Antypov, M. S. Dyer, M. J. Pitcher, A. P. Katsoulidis, P. A. Chater, F. Blanc, M. J. Rosseinsky, *Nat. Commun.* **2017**, *8*, 1102.

[82] Q. Fang, Z. Zhuang, S. Gu, R. B. Kaspar, J. Zheng, J. Wang, S. Qiu, Y. Yan, *Nat. Commun.* **2014**, *5*, 4503.

[83] A. Nagai, X. Chen, X. Feng, X. Ding, Z. Guo, D. Jiang, *Angew. Chem. Int. Ed.* **2013**, *52*, 3770-3774.

[84] H. Zhao, Z. Jin, H. Su, X. Jing, F. Sun, G. Zhu, *Chem. Commun.* **2011**, *47*, 6389-6391.

[85] K. C. Ranjeesh, R. Illathvalappil, S. D. Veer, J. Peter, V. C. Wakchaure, Goudappagouda, K. V. Raj, S. Kurungot, S. S. Babu, *J. Am. Chem. Soc.* **2019**, *141*, 14950-14954.

[86] G. Das, T. Skorjanc, S. K. Sharma, F. Gándara, M. Lusi, D. S. Shankar Rao, S. Vimala, S. Krishna Prasad, J. Raya, D. S. Han, R. Jagannathan, J.-C. Olsen, A. Trabolsi, *J. Am. Chem. Soc.* **2017**, *139*, 9558-9565.

[87] C. Zhao, H. Lyu, Z. Ji, C. Zhu, O. M. Yaghi, *J. Am. Chem. Soc.* **2020**, *142*, 14450-14454.

[88] K. Schwinghammer, S. Hug, M. B. Mesch, J. Senker, B. V. Lotsch, *Energy Environ. Sci.* **2015**, *8*, 3345-3353.

[89] S.-Y. Yu, J. Mahmood, H.-J. Noh, J.-M. Seo, S.-M. Jung, S.-H. Shin, Y.-K. Im, I.-Y. Jeon, J.-B. Baek, *Angew. Chem. Int. Ed.* **2018**, *57*, 8438-8442.

[90] S. Ren, M. J. Bojdys, R. Dawson, A. Laybourn, Y. Z. Khimyak, D. J. Adams, A. I. Cooper, *Adv. Mater.* **2012**, *24*, 2357-2361.

[91] M. Liu, Q. Huang, S. Wang, Z. Li, B. Li, S. Jin, B. Tan, *Angew. Chem. Int. Ed.* **2018**, *57*, 11968-11972.

[92] M. Liu, X. Wang, J. Liu, K. Wang, S. Jin, B. Tan, *ACS Appl. Mater. Interfaces* **2020**, *12*, 12774-12782.

[93] P. Katekomol, J. Roeser, M. Bojdys, J. Weber, A. Thomas, *Chem. Mater.* **2013**, *25*, 1542-1548.

[94] M. J. Bojdys, J. Jeromenok, A. Thomas, M. Antonietti, *Adv. Mater.* **2010**, *22*, 2202-2205.

[95] X. Zhuang, W. Zhao, F. Zhang, Y. Cao, F. Liu, S. Bi, X. Feng, *Polym. Chem.* **2016**, *7*, 4176-4181.

[96] A. Acharjya, P. Pachfule, J. Roeser, F.-J. Schmitt, A. Thomas, *Angew. Chem. Int. Ed.* **2019**, *58*, 14865-14870.

[97] S. Bi, C. Yang, W. Zhang, J. Xu, L. Liu, D. Wu, X. Wang, Y. Han, Q. Liang, F. Zhang, *Nat. Commun.* **2019**, *10*, 2467.

[98] C. R. DeBlase, W. R. Dichtel, *Macromolecules* **2016**, *49*, 5297-5305.

[99] T. Wang, R. Xue, H. Chen, P. Shi, X. Lei, Y. Wei, H. Guo, W. Yang, *New J. Chem.* **2017**, *41*, 14272-14278.

[100] R. van der Jagt, A. Vasileiadis, H. Veldhuizen, P. Shao, X. Feng, S. Ganapathy, N. C. Habisreutinger, M. A. van der Veen, C. Wang, M. Wagemaker, S. van der Zwaag, A. Nagai, *Chem. Mater.* **2021**, *33*, 818-833.

[101] V. A. Kuehl, M. J. Wenzel, B. A. Parkinson, L. d. Sousa Oliveira, J. O. Hoberg, *J. Mater. Chem. A* **2021**, *9*, 15301-15309.

[102] M. S. Lohse, T. Stassin, G. Naudin, S. Wuttke, R. Ameloot, D. De Vos, D. D. Medina, T. Bein, *Chem. Mater.* **2016**, *28*, 626-631.

[103] Y. Liang, L. Feng, X. Liu, Y. Zhao, Q. Chen, Z. Sui, N. Wang, *Chem. Eng. J.* **2021**, *404*, 127095.

[104] A. M. Evans, M. R. Ryder, W. Ji, M. J. Strauss, A. R. Corcos, E. Vitaku, N. C. Flanders, R. P. Bisbey, W. R. Dichtel, *Faraday Discuss.* **2021**, *225*, 226-240.

[105] C. T. Kresge, M. E. Leonowicz, W. J. Roth, J. C. Vartuli, J. S. Beck, *Nature* **1992**, *359*, 710-712.

[106] D. Zhao, J. Feng, Q. Huo, N. Melosh, G. H. Fredrickson, B. F. Chmelka, G. D. Stucky, *Science* **1998**, *279*, 548-552.

[107] S. I. Stupp, S. Son, H. C. Lin, L. S. Li, *Science* **1993**, *259*, 59-63.

[108] T. Takami, H. Ozaki, M. Kasuga, T. Tsuchiya, A. Ogawa, Y. Mazaki, D. Fukushi, M. Uda, M. Aono, *Angew. Chem. Int. Ed. Engl.* **1997**, *36*, 2755-2757.

[109] P. Kissel, R. Erni, W. B. Schweizer, M. D. Rossell, B. T. King, T. Bauer, S. Götzinger, A. D. Schlüter, J. Sakamoto, *Nat. Chem.* **2012**, *4*, 287-291.

[110] M. J. Kory, M. Wörle, T. Weber, P. Payamyar, S. W. van de Poll, J. Dshemuchadse, N. Trapp, A. D. Schlüter, *Nat. Chem.* **2014**, *6*, 779-784.

[111] P. Kissel, D. J. Murray, W. J. Wulftange, V. J. Catalano, B. T. King, *Nat. Chem.* **2014**, *6*, 774-778.

[112] R. Z. Lange, G. Hofer, T. Weber, A. D. Schlüter, *J. Am. Chem. Soc.* **2017**, *139*, 2053-2059.

[113] K. Liu, H. Qi, R. Dong, R. Shivhare, M. Addicoat, T. Zhang, H. Sahabudeen, T. Heine, S. Mannsfeld, U. Kaiser, Z. Zheng, X. Feng, *Nat. Chem.* **2019**, *11*, 994-1000.

[114] Z.-Z. Gao, Z.-K. Wang, L. Wei, G. Yin, J. Tian, C.-Z. Liu, H. Wang, D.-W. Zhang, Y.-B. Zhang, X. Li, Y. Liu, Z.-T. Li, *ACS Appl. Mater. Interfaces*, **2020**, *12*, 1404-1411.

[115] Y. Zhai, G. Liu, F. Jin, Y. Zhang, X. Gong, Z. Miao, J. Li, M. Zhang, Y. Cui, L. Zhang, Y. Liu, H. Zhang, Y. Zhao, Y. Zeng, *Angew. Chem. Int. Ed.* **2019**, *58*, 17679-17683.

[116] C. Qian, Q. Y. Qi, G. F. Jiang, F. Z. Cui, Y. Tian, X. Zhao, *J. Am. Chem. Soc.* **2017**, *139*, 6736-6743.

[117] H.-L. Qian, Y. Li, X.-P. Yan, *J. Mater. Chem. A*, **2018**, *6*, 17307-17311.

[118] Z. Li, X. Ding, Y. Feng, W. Feng, B.-H. Han, *Macromolecules* **2019**, *52*, 1257-1265.

[119] F. Haase, E. Troschke, G. Savasci, T. Banerjee, V. Duppel, S. Dorfler, M. M. J. Grundei, A. M. Burow, C. Ochsenfeld, S. Kaskel, B. V. Lotsch, *Nat. Commun.* **2018**, *9*, 2600.

[120] X.-Y. Hu, W.-S. Zhang, F. Rominger, I. Wacker, R. R. Schröder, M. Mastalerz, *Chem. Commun.* **2017**, *53*, 8616-8619.

[121] S. J. Lyle, T. M. Osborn Popp, P. J. Waller, X. Pei, J. A. Reimer, O. M. Yaghi, *J. Am. Chem. Soc.* **2019**, *141*, 11253-11258.

[122] H. Liu, J. Chu, Z. Yin, X. Cai, L. Zhuang, H. Deng, *Chem* **2018**, *4*, 1696-1709.

[123] L. Grunenberg, G. Savasci, M. W. Terban, V. Duppel, I. Moudrakovski, M. Etter, R. E. Dinnebier, C. Ochsenfeld, B. V. Lotsch, *J. Am. Chem. Soc.* **2021**, *143*, 3430-3438.

[124] K. Wang, Z. Jia, Y. Bai, X. Wang, S. E. Hodgkiss, L. Chen, S. Y. Chong, X. Wang, H. Yang, Y. Xu, F. Feng, J. W. Ward, A. I. Cooper, *J. Am. Chem. Soc.* **2020**, *142*, 11131-11138.

[125] P.-F. Wei, M.-Z. Qi, Z.-P. Wang, S.-Y. Ding, W. Yu, Q. Liu, L.-K. Wang, H.-Z. Wang, W.-K. An, W. Wang, *J. Am. Chem. Soc.* **2018**, *140*, 4623-4631.

[126] X. Li, C. Zhang, S. Cai, X. Lei, V. Altoe, F. Hong, J. J. Urban, J. Ciston, E. M. Chan, Y. Liu, *Nat. Commun.* **2018**, *9*, 2998.

[127] C. Li, Y. Ma, H. Liu, L. Tao, Y. Ren, X. Chen, H. Li, Q. Yang, *Chin. J. Catal.* **2020**, *41*, 1288-1297.

[128] X.-R. Ren, B. Bai, Q. Zhang, Q. Hao, Y. Guo, L.-J. Wan, D. Wang, *J. Am. Chem. Soc.* **2022**, *144*, 2488-2494.

[129] K. Baek, G. Yun, Y. Kim, D. Kim, R. Hota, I. Hwang, D. Xu, Y. H. Ko, G. H. Gu, J. H. Suh, C. G. Park, B. J. Sung, K. Kim, *J. Am. Chem. Soc.* **2013**, *135*, 6523-6528.

[130] K. Baek, I. Hwang, I. Roy, D. Shetty, K. Kim, *Acc. Chem. Res.* **2015**, *48*, 2221-2229.

[131] A. M. Evans, L. R. Parent, N. C. Flanders, R. P. Bisbey, E. Vitaku, M. S. Kirschner, R. D. Schaller, L. X. Chen, N. C. Gianneschi, W. R. Dichtel, *Science* **2018**, *361*, 52-57.

[132] W. Liu, X. Luo, Y. Bao, Y. P. Liu, G.-H. Ning, I. Abdelwahab, L. Li, C. T. Nai, Z. G. Hu, D. Zhao, B. Liu, S. Y. Quek, K. P. Loh, *Nat. Chem.* **2017**, *9*, 563-570.

[133] W. Liu, M. Ulaganathan, I. Abdelwahab, X. Luo, Z. Chen, S. J. Rong Tan, X. Wang, Y. Liu, D. Geng, Y. Bao, J. Chen, K. P. Loh, *ACS Nano* **2018**, *12*, 852-860.

[134] D. Zhou, X. Tan, H. Wu, L. Tian, M. Li, *Angew. Chem. Int. Ed.* **2019**, *58*, 1376-1381.

[135] D. Schwarz, A. Acharjya, A. Ichangi, Y. S. Kochergin, P. Lyu, M. V. Opanasenko, J. Tarábek, J. Vacek Chocholoušová, J. Vacek, J. Schmidt, J. Čejka, P. Nachtigall, A. Thomas, M. J. Bojdys, *ChemSusChem* **2019**, *12*, 194-199.

[136] S. Jhulki, J. Kim, I.-C. Hwang, G. Haider, J. Park, J. Y. Park, Y. Lee, W. Hwang, A. A. Dar, B. Dhara, S. H. Lee, J. Kim, J. Y. Koo, M. H. Jo, C.-C. Hwang, Y. H. Jung, Y. Park, M. Kataria, Y.-F. Chen, S.-H. Jhi, M.-H. Baik, K. Baek, K. Kim, *Chem*, **2020**, *6*, 2035-2045.

[137] S. Thomas, H. Li, R. R. Dasari, A. M. Evans, I. Castano, T. G. Allen, O. G. Reid, G. Rumbles, W. R. Dichtel, N. C. Gianneschi, S. R. Marder, V. Coropceanu, J.-L. Brédas, *Mater. Horiz.* **2019**, *6*, 1868-1876.

[138] R. Matsuoka, R. Sakamoto, K. Hoshiko, S. Sasaki, H. Masunaga, K. Nagashio, H. Nishihara, *J. Am. Chem. Soc.* **2017**, *139*, 3145-3152.

[139] E. Tavakoli, A. Kakekhani, S. Kaviani, P. Tan, M. M. Ghaleni, M. A. Zaeem, A. M. Rappe, S. Nejati, *J. Am. Chem. Soc.* **2019**, *141*, 19560-19564.

[140] T. Ma, E. A. Kapustin, S. X. Yin, L. Liang, Z. Zhou, J. Niu, L.-H. Li, Y. Wang, J. Su, J. Li, X. Wang, W. D. Wang, W. Wang, J. Sun, O. M. Yaghi, *Science* **2018**, *361*, 48-52.

[141] Y.-X. Ma, Z.-J. Li, L. Wei, S.-Y. Ding, Y.-B. Zhang, W. Wang, *J. Am. Chem. Soc.* **2017**, *139*, 4995-4998.

[142] Q. Fang, J. Wang, S. Gu, R. B. Kaspar, Z. Zhuang, J. Zheng, H. Guo, S. Qiu, Y. Yan, *J. Am. Chem. Soc.* **2015**, *137*, 8352-8355.

[143] H. Lu, C. Wang, J. Chen, R. Ge, W. Leng, B. Dong, J. Huang, Y. Gao, *Chem. Commun.* **2015**, *51*, 15562-15565.

[144] M. Matsumoto, R. R. Dasari, W. Ji, C. H. Feriante, T. C. Parker, S. R. Marder, W. R. Dichtel, *J. Am. Chem. Soc.* **2017**, *139*, 4999-5002.

[145] Y. Liu, Y. Wang, H. Li, X. Guan, L. Zhu, M. Xue, Y. Yan, V. Valtchev, S. Qiu, Q. Fang, *Chem. Sci* **2019**, *10*, 10815-10820.

[146] M. B. Gawande, S. N. Shelke, R. Zboril, R. S. Varma, *Acc. Chem. Res.* **2014**, *47*, 1338-1348.

[147] M. Nüchter, B. Ondruschka, W. Bonrath, A. Gum, *Green Chem.* **2004**, *6*, 128-141.

[148] L. K. Ritchie, A. Trewin, A. Reguera-Galan, T. Hasell, A. I. Cooper, *Microporous Mesoporous Mater.* **2010**, *132*, 132-136.

[149] N. L. Campbell, R. Clowes, L. K. Ritchie, A. I. Cooper, *Chem. Mater.* **2009**, *21*, 204-206.

[150] J. H. Bang, K. S. Suslick, *Adv. Mater.* **2010**, *22*, 1039-1059.

[151] S.-T. Yang, J. Kim, H.-Y. Cho, S. Kim, W.-S. Ahn, *RSC Adv.* **2012**, *2*, 10179-10181.

[152] S. Kim, H. C. Choi, *Commun. Chem.* **2019**, *2*, 60.

[153] B. P. Biswal, S. Chandra, S. Kandambeth, B. Lukose, T. Heine, R. Banerjee, *J. Am. Chem. Soc.* **2013**, *135*, 5328-5331.

[154] G. Das, D. Balaji Shinde, S. Kandambeth, B. P. Biswal, R. Banerjee, *Chem. Commun.* **2014**, *50*, 12615-12618.

[155] D. B. Shinde, H. B. Aiyappa, M. Bhadra, B. P. Biswal, P. Wadge, S. Kandambeth, B. Garai, T. Kundu, S. Kurungot, R. Banerjee, *J. Mater. Chem. A* **2016**, *4*, 2682-2690.

[156] Y. Peng, G. Xu, Z. Hu, Y. Cheng, C. Chi, D. Yuan, H. Cheng, D. Zhao, *ACS Appl. Mater. Interfaces* **2016**, *8*, 18505-18512.

[157] S. T. Emmerling, L. S. Germann, P. A. Julien, I. Moudrakovski, M. Etter, T. Friščić, R. E. Dinnebier, B. V. Lotsch, *Chem* **2021**, *7*, 1639-1652.

[158] X. Guan, Y. Ma, H. Li, Y. Yusran, M. Xue, Q. Fang, Y. Yan, V. Valtchev, S. Qiu, Fast, *J. Am. Chem. Soc.* **2018**, *140*, 4494-4498.

[159] K. Dey, M. Pal, K. C. Rout, S. Kunjattu H, A. Das, R. Mukherjee, U. K. Kharul, R. Banerjee, *J. Am. Chem. Soc.* **2017**, *139*, 13083-13091.

[160] M. Matsumoto, L. Valentino, G. M. Stiehl, H. B. Balch, A. R. Corcos, F. Wang, D. C. Ralph, B. J. Mariñas, W. R. Dichtel, *Chem* **2018**, *4*, 308-317.

[161] Q. Hao, C. Zhao, B. Sun, C. Lu, J. Liu, M. Liu, L.-J. Wan, D. Wang, *J. Am. Chem. Soc.* **2018**, *140*, 12152-12158.

[162] D. D. Medina, J. M. Rotter, Y. Hu, M. Dogru, V. Werner, F. Auras, J. T. Markiewicz, P. Knochel, T. Bein, *J. Am. Chem. Soc.* **2015**, *137*, 1016-1019.
[163] S. S. Han, H. Furukawa, O. M. Yaghi, W. A. Goddard, *J. Am. Chem. Soc.* **2008**, *130*, 11580-11581.
[164] S. S. Han, J. L. Mendoza-Cortés, W. A. Goddard Iii, *Chem. Soc. Rev.* **2009**, *38*, 1460-1476.
[165] J. L. Mendoza-Cortes, W. A. Goddard, H. Furukawa, O. M. Yaghi, *J. Phys. Chem. Lett.* **2012**, *3*, 2671-2675.
[166] J. L. Mendoza-Cortes, S. S. Han, H. Furukawa, O. M. Yaghi, W. A. Goddard, *J. Phys. Chem. A* **2010**, *114*, 10824-10833.
[167] J. L. Mendoza-Cortes, T. A. Pascal, W. A. Goddard, *J. Phys. Chem. A* **2011**, *115*, 13852-13857.
[168] H. Furukawa, O. M. Yaghi, *J. Am. Chem. Soc.* **2009**, *131*, 8875-8883.
[169] Y. J. Choi, J. H. Choi, K. M. Choi, J. K. Kang, *J. Mater. Chem.* **2011**, *21*, 1073-1078.
[170] R. Babarao, J. Jiang, *Energy & Environmental Science*, **2008**, *1*, 139-143.
[171] P. Wang, Q. Xu, Z. Li, W. Jiang, Q. Jiang, D. Jiang, *Adv. Mater.* **2018**, *30*, 1801991.
[172] Z.-J. Yin, S.-Q. Xu, T.-G. Zhan, Q.-Y. Qi, Z.-Q. Wu, X. Zhao, *Chem. Commun.* **2017**, *53*, 7266-7269.
[173] Z. Yan, Y. Yuan, Y. Tian, D. Zhang, G. Zhu, *Angew. Chem. Int. Ed.* **2015**, *54*, 12733-12737.
[174] N. Huang, L. Zhai, H. Xu, D. Jiang, *J. Am. Chem. Soc.* **2017**, *139*, 2428-2434.
[175] Q. Sun, B. Aguila, J. Perman, L. D. Earl, C. W. Abney, Y. Cheng, H. Wei, N. Nguyen, L. Wojtas, S. Ma, *J. Am. Chem. Soc.* **2017**, *139*, 2786-2793.
[176] M. Dinari, M. Hatami, *J. Environ. Chem. Eng.* **2019**, *7*, 102907.
[177] Q. Lu, Y. Ma, H. Li, X. Guan, Y. Yusran, M. Xue, Q. Fang, Y. Yan, S. Qiu, V. Valtchev, *Angew. Chem. Int. Ed.* **2018**, *57*, 6042-6048.
[178] C. J. Doonan, D. J. Tranchemontagne, T. G. Glover, J. R. Hunt, O. M. Yaghi, *Nat. Chem.* **2010**, *2*, 235-238.
[179] G.-Y. Lee, J. Lee, H. T. Vo, S. Kim, H. Lee, T. Park, *Sci. Rep.* **2017**, *7*, 557.
[180] X. Zhu, S. An, Y. Liu, J. Hu, H. Liu, C. Tian, S. Dai, X. Yang, H. Wang, C. W. Abney, S. Dai, *AIChE J.* **2017**, *63*, 3470-3478.
[181] E. Haque, J. W. Jun, S. H. Jhung, *J. Hazar. Mater.* **2011**, *185*, 507-511.
[182] W. Zhang, L. Zhang, H. Zhao, B. Li, H. Ma, *J. Mater. Chem. A* **2018**, *6*, 13331-13339.
[183] Z. Kang, Y. Peng, Y. Qian, D. Yuan, M. A. Addicoat, T. Heine, Z. Hu, L. Tee, Z. Guo, D. Zhao, *Chem. Mater.* **2016**, *28*, 1277-1285.
[184] M. Shan, B. Seoane, E. Rozhko, A. Dikhtiarenko, G. Clet, F. Kapteijn, J. Gascon, *Chem. Eur. J.* **2016**, *22*, 14467-14470.
[185] L. Jiang, Y. Tian, T. Sun, Y. Zhu, H. Ren, X. Zou, Y. Ma, K. R. Meihaus, J. R. Long, G. Zhu, *J. Am. Chem. Soc.* **2018**, *140*, 15724-15730.
[186] L. Jiang, P. Wang, M. Li, P. Zhang, J. Li, J. Liu, Y. Ma, H. Ren, G. Zhu, *Chem. Eur. J.* **2019**, *25*, 9045-9051.
[187] Y. Zhou, J. F. Zhang, J. Yoon, *Chem. Rev.* **2014**, *114*, 5511-5571.
[188] Z. Li, Y. Zhang, H. Xia, Y. Mu, X. Liu, *Chem. Commun.* **2016**, *52*, 6613-6616.

[189] S. Y. Ding, M. Dong, Y. W. Wang, Y. T. Chen, H. Z. Wang, C. Y. Su, W. Wang, *J. Am. Chem. Soc.* **2016**, *138*, 3031-3037.

[190] G. Chen, H.-H. Lan, S.-L. Cai, B. Sun, X.-L. Li, Z.-H. He, S.-R. Zheng, J. Fan, Y. Liu, W.-G. Zhang, *ACS Appl. Mater. Interfaces* **2019**, *11*, 12830-12837.

[191] Y.-F. Xie, S.-Y. Ding, J.-M. Liu, W. Wang, Q.-Y. Zheng, *J. Mater. Chem. C* **2015**, *3*, 10066-10069.

[192] F.-Z. Cui, J.-J. Xie, S.-Y. Jiang, S.-X. Gan, D.-L. Ma, R.-R. Liang, G.-F. Jiang, X. Zhao, *Chem. Commun.* **2019**, *55*, 4550-4553.

[193] C. Zhang, S. Zhang, Y. Yan, F. Xia, A. Huang, Y. Xian, *ACS Appl. Mater. Interfaces* **2017**, *9*, 13415-13421.

[194] P. Wang, M. Kang, S. Sun, Q. Liu, Z. Zhang, S. Fang, *Chin. J. Chem.* **2014**, *32*, 838-843.

[195] A. Mal, R. K. Mishra, V. K. Praveen, M. A. Khayum, R. Banerjee, A. Ajayaghosh, *Angew. Chem. Int. Ed.* **2018**, *57*, 8443-8447.

[196] X. Han, J. Zhang, J. Huang, X. Wu, D. Yuan, Y. Liu, Y. Cui, *Nat. Commun.* **2018**, *9*, 1294.

[197] J. Dong, X. Li, S. B. Peh, Y. D. Yuan, Y. Wang, D. Ji, S. Peng, G. Liu, S. Ying, D. Yuan, J. Jiang, S. Ramakrishna, D. Zhao, *Chem. Mater.* **2019**, *31*, 146-160.

[198] X. Ding, L. Chen, Y. Honsho, X. Feng, O. Saengsawang, J. Guo, A. Saeki, S. Seki, S. Irle, S. Nagase, V. Parasuk, D. Jiang, *J. Am. Chem. Soc.* **2011**, *133*, 14510-14513.

[199] X. Ding, J. Guo, X. Feng, Y. Honsho, J. Guo, S. Seki, P. Maitarad, A. Saeki, S. Nagase, D. Jiang, *Angew. Chem. Int. Ed.* **2011**, *50*, 1289-1293.

[200] X. Feng, L. Liu, Y. Honsho, A. Saeki, S. Seki, S. Irle, Y. Dong, A. Nagai, D. Jiang, *Angew. Chem. Int. Ed.* **2012**, *51*, 2618-2622.

[201] X. Feng, L. Chen, Y. Honsho, O. Saengsawang, L. Liu, L. Wang, A. Saeki, S. Irle, S. Seki, Y. Dong, D. Jiang, *Adv. Mater.* **2012**, *24*, 3026-3031.

[202] M. Dogru, M. Handloser, F. Auras, T. Kunz, D. Medina, A. Hartschuh, P. Knochel, T. Bein, *Angew. Chem. Int. Ed.* **2013**, *52*, 2920-2924.

[203] Y. Chen, H. Cui, J. Zhang, K. Zhao, D. Ding, J. Guo, L. Li, Z. Tian, Z. Tang, *RSC Adv.* **2015**, *5*, 92573-92576.

[204] J. I. Feldblyum, C. H. McCreery, S. C. Andrews, T. Kurosawa, E. J. G. Santos, V. Duong, L. Fang, A. L. Ayzner, Z. Bao, *Chem. Commun.* **2015**, *51*, 13894-13897.

[205] B. Sun, C.-H. Zhu, Y. Liu, C. Wang, L.-J. Wan, D. Wang, *Chem. Mater.* **2017**, *29*, 4367-4374.

[206] D. Bessinger, L. Ascherl, F. Auras, T. Bein, *J. Am. Chem. Soc.* **2017**, *139*, 12035-12042.

[207] L. Wang, B. Dong, R. Ge, F. Jiang, J. Xu, *ACS Appl. Mater. Interfaces* **2017**, *9*, 7108-7114.

[208] E. Jin, M. Asada, Q. Xu, S. Dalapati, M. A. Addicoat, M. A. Brady, H. Xu, T. Nakamura, T. Heine, Q. Chen, D. Jiang, *Science* **2017**, *357*, 673-676.

[209] S. Chandra, T. Kundu, K. Dey, M. Addicoat, T. Heine, R. Banerjee, *Chem. Mater.* **2016**, *28*, 1489-1494.

[210] S. Chandra, T. Kundu, S. Kandambeth, R. BabaRao, Y. Marathe, S. M. Kunjir, R. Banerjee, *J. Am. Chem. Soc.* **2014**, *136*, 6570-6573.

[211] H. Xu, S. Tao, D. Jiang, *Nat. Mater.* **2016**, *15*, 722-726.

[212] H. Ma, B. Liu, B. Li, L. Zhang, Y.-G. Li, H.-Q. Tan, H.-Y. Zang, G. Zhu, *J. Am. Chem. Soc.* **2016**, *138*, 5897-5903.

[213] H. Chen, H. Tu, C. Hu, Y. Liu, D. Dong, Y. Sun, Y. Dai, S. Wang, H. Qian, Z. Lin, L. Chen, *J. Am. Chem. Soc.* **2018**, *140*, 896-899.

[214] C. R. DeBlase, K. Hernández-Burgos, K. E. Silberstein, G. G. Rodríguez-Calero, R. P. Bisbey, H. D. Abruña, W. R. Dichtel, *ACS Nano*, **2015**, *9*, 3178-3183.

[215] F. Xu, S. Jin, H. Zhong, D. Wu, X. Yang, X. Chen, H. Wei, R. Fu, D. Jiang, *Sci. Rep.* **2015**, *5*, 8225.

[216] D. Chen, S. Huang, L. Zhong, S. Wang, M. Xiao, D. Han, Y. Meng, *Adv. Funct. Mater.* **2020**, *30*, 1907717.

[217] Z. Zhao, W. Chen, S. Impeng, M. Li, R. Wang, Y. Liu, L. Zhang, L. Dong, J. Unruangsri, C. Peng, C. Wang, S. Namuangruk, S.-Y. Lee, Y. Wang, H. Lu, J. Guo, *J. Mater. Chem. A* **2020**, *8*, 3459-3467.

[218] B. Guo, T. Ben, Z. Bi, G. M. Veith, X.-G. Sun, S. Qiu, S. Dai, *Chem. Commun.* **2013**, *49*, 4905-4907.

[219] H. Liao, H. Ding, B. Li, X. Ai, C. Wang, *J. Mater. Chem. A* **2014**, *2*, 8854-8858.

[220] Z. A. Ghazi, L. Zhu, H. Wang, A. Naeem, A. M. Khattak, B. Liang, N. A. Khan, Z. Wei, L. Li, Z. Tang, *Adv. Energy Mater.* **2016**, *6*, 1601250.

[221] Z. Yang, C. Peng, R. Meng, L. Zu, Y. Feng, B. Chen, Y. Mi, C. Zhang, J. Yang, *ACS Cent. Sci.* **2019**, *5*, 1876-1883.

[222] B. C. Patra, S. K. Das, A. Ghosh, A. Raj K, P. Moitra, M. Addicoat, S. Mitra, A. Bhaumik, S. Bhattacharya, A. Pradhan, *J. Mater. Chem. A* **2018**, *6*, 16655-16663.

[223] M.-S. Kim, W.-J. Lee, S.-M. Paek, J. K. Park, *ACS Appl. Mater. Interfaces* **2018**, *10*, 32102-32111.

[224] S. Gu, S. Wu, L. Cao, M. Li, N. Qin, J. Zhu, Z. Wang, Y. Li, Z. Li, J. Chen, Z. Lu, *J. Am. Chem. Soc.* **2019**, *141*, 9623-9628.

[225] X. Chen, H. Zhang, C. Ci, W. Sun, Y. Wang, *ACS Nano* **2019**, *13*, 3600-3607.

[226] E. R. Wolfson, L. Schkeryantz, E. M. Moscarello, J. P. Fernandez, J. Paszek, Y. Wu, C. M. Hadad, P. L. McGrier, *ACS Appl. Mater. Interfaces* **2021**, *13*, 41628-41636.

[227] X.-X. Luo, W.-H. Li, H.-J. Liang, H.-X. Zhang, K.-D. Du, X.-T. Wang, X.-F. Liu, J.-P. Zhang, X.-L. Wu, *Angew. Chem. Int. Ed.* **2022**, *61*, e202117661.

[228] A. Khayum M, M. Ghosh, V. Vijayakumar, A. Halder, M. Nurhuda, S. Kumar, M. Addicoat, S. Kurungot, R. Banerjee, *Chem. Sci.* **2019**, *10*, 8889-8894.

[229] W. Wang, V. S. Kale, Z. Cao, Y. Lei, S. Kandambeth, G. Zou, Y. Zhu, E. Abouhamad, O. Shekhah, L. Cavallo, M. Eddaoudi, H. N. Alshareef, *Adv. Mater.* **2021**, *33*, 2103617.

[230] M. Yu, N. Chandrasekhar, R. K. M. Raghupathy, K. H. Ly, H. Zhang, E. Dmitrieva, C. Liang, X. Lu, T. D. Kühne, H. Mirhosseini, I. M. Weidinger, X. Feng, *J. Am. Chem. Soc.* **2020**, *142*, 19570-19578.

[231] W. Wang, V. S. Kale, Z. Cao, S. Kandambeth, W. Zhang, J. Ming, P. T. Parvatkar, E. Abou-Hamad, O. Shekhah, L. Cavallo, M. Eddaoudi, H. N. Alshareef, *ACS Energy Lett.* **2020**, *5*, 2256-2264.

[232] R. Sun, S. Hou, C. Luo, X. Ji, L. Wang, L. Mai, C. Wang, *Nano Lett.* **2020**, *20*, 3880-3888.

[233] H. Lu, F. Ning, R. Jin, C. Teng, Y. Wang, K. Xi, D. Zhou, G. Xue, *ChemSusChem* **2020**, *13*, 3447-3454.

[234] S. Lin, C. S. Diercks, Y.-B. Zhang, N. Kornienko, E. M. Nichols, Y. Zhao, A. R. Paris, D. Kim, P. Yang, O. M. Yaghi, C. J. Chang, *Science* **2015**, *349*, 1208-1213.

[235] C. S. Diercks, S. Lin, N. Kornienko, E. A. Kapustin, E. M. Nichols, C. Zhu, Y. Zhao, C. J. Chang, O. M. Yaghi, *J. Am. Chem. Soc.* **2018**, *140*, 1116-1122.

[236] W. Ma, P. Yu, T. Ohsaka, L. Mao, *Electrochem. Commun.* **2015**, *52*, 53-57.

[237] J. Wu, H. Yang, *Acc. Chem. Res.* **2013**, *46*, 1848-1857.

[238] H. B. Aiyappa, J. Thote, D. B. Shinde, R. Banerjee, S. Kurungot, *Chem. Mater.* **2016**, *28*, 4375-4379.

[239] D. Mullangi, V. Dhavale, S. Shalini, S. Nandi, S. Collins, T. Woo, S. Kurungot, R. Vaidhyanathan, *Adv. Energy Mater.* **2016**, *6*, 1600110.

[240] L. Stegbauer, K. Schwinghammer, B. V. Lotsch, *Chem. Sci.* **2014**, *5*, 2789-2793.

[241] V. S. Vyas, F. Haase, L. Stegbauer, G. Savasci, F. Podjaski, C. Ochsenfeld, B. V. Lotsch, *Nat. Commun.* **2015**, *6*, 8508.

[242] S. Yang, W. Hu, X. Zhang, P. He, B. Pattengale, C. Liu, M. Cendejas, I. Hermans, X. Zhang, J. Zhang, J. Huang, *J. Am. Chem. Soc.* **2018**, *140*, 14614-14618.

[243] W. Zhong, R. Sa, L. Li, Y. He, L. Li, J. Bi, Z. Zhuang, Y. Yu, Z. Zou, *J. Am. Chem. Soc.* **2019**, *141*, 7615-7621.

[244] X. Chen, M. Addicoat, E. Jin, L. Zhai, H. Xu, N. Huang, Z. Guo, L. Liu, S. Irle, D. Jiang, *J. Am. Chem. Soc.* **2015**, *137*, 3241-3247.

[245] S. Y. Ding, J. Gao, Q. Wang, Y. Zhang, W. G. Song, C. Y. Su, W. Wang, *J. Am. Chem. Soc.* **2011**, *133*, 19816-19822.

[246] R. S. B. Gonçalves, A. B. V. de Oliveira, H. C. Sindra, B. S. Archanjo, M. E. Mendoza, L. S. A. Carneiro, C. D. Buarque, P. M. Esteves, *ChemCatChem* **2016**, *8*, 743-750.

[247] Q. Fang, S. Gu, J. Zheng, Z. Zhuang, S. Qiu, Y. Yan, *Angew. Chem. Int. Ed.* **2014**, *53*, 2878-2882.

[248] Q. Sun, B. Aguila, S. Ma, *Mater. Chem. Front.* **2017**, *1*, 1310-1316.

[249] R. Chen, J.-L. Shi, Y. Ma, G. Lin, X. Lang, C. Wang, *Angew. Chem. Int. Ed.* **2019**, *58*, 6430-6434.

[250] H. Xu, J. Gao, D. Jiang, *Nat. Chem.* **2015**, *7*, 905-912.

[251] X. Wang, X. Han, J. Zhang, X. Wu, Y. Liu, Y. Cui, *J. Am. Chem. Soc.* **2016**, *138*, 12332-12335.

# 2 Imide-Linked Covalent Organic Frameworks

In the rapidly developing field of covalent organic frameworks, imide-linked COFs have attracted increasing attention for numerous applications since their discovery in 2014.[1-2] In particular, due to the high thermal and chemical stability of the imide linkage, PI-COFs have great advantages over most other COF linkages which often suffer from low long-term stability. However, the synthesis of two- or three-dimensional polyimide frameworks in a crystalline fashion by reversible bond formation is still a challenge. In this context, a brief overview of the development of synthetic methods for 1D polyimides (PIs), leading to the synthesis of porous aromatic PIs and eventually to the development of crystalline two- and three-dimensional PI-COFs, is presented in Section 2.1. Insights into the synthetic strategies optimized for PI-COFs and the challenges posed by the need to use harsh reaction conditions to achieve reversible bond formation are provided in Sections 2.2 and 2.3 along with an overview of all PI-COFs known to date. Finally, the application areas for PI-COFs, including adsorption and separation, drug delivery, photocatalysis and electrocatalysis, energy storage, and sensing, are presented in detail in Section 2.4.

## 2.1 Historical Overview of the Synthesis of Polyimides

Polyimides (PIs) are a class of high-performance polymers (HPPs) with cyclic imide groups in the molecular chain, which differ from other "softer" polymers in their excellent thermal and chemical stability, radiation resistance, and outstanding mechanical properties.[2] In particular, fully aromatic PIs have rigid chains and strong inter-chain interactions, resulting in poor solubility and high melting point of the PIs. The highly symmetric and highly polar imide groups lead to the formation of charge transfer complexes and induce electronic polarization.[3] These charge transfer complexes are a result of the strong electron acceptor properties of imides and electron donor properties of amine segments, which makes PIs interesting materials for electrochemical applications.

HPPs such as polyimides are the lightweight materials of choice in working conditions where "soft" polymers fail.[4] Conditions that place high demands on polymeric materials, often required for applications in today's high-tech industry, include high temperatures and mechanical strain, e.g. in electronic devices,[5] or corrosive environments at elevated temperatures such as those found in fuel cells.[6] Other applications for HPPs include photoresists,[7-8] liquid crystal alignment materials,[9-11] gas separation membranes,[12-14] polyelectrolytes,[15-17] electroluminescent devices,[18-20] and electrochromic films.[3, 21-22]

The first polyimide was discovered in 1908 by Bogart and Renshaw by heating 4-aminophthalic anhydride (Figure 2-1).[23] It was observed that the molecule did not melt when heated, but formed a PI of high molecular weight by self-polymerization through water elimination. However, it took nearly 50 years to develop the first PI of significant commercial importance – Kapton. The pioneering work of Endrey in 1962,[24-29] in which he described a two-step synthetic route for PIs, initiated a rapid development in this field. The first step of the synthetic process involves rapid, exothermic polymerization at relatively low temperatures to form a poly(amic acid). Poly(amic acid) is prepared by the reaction of alternating electron acceptor (dianhydrides) and electron donor (diamines) units at relatively low temperatures in polar, aprotic solvents such as NMP, DMAc, or DMF. Subsequently, it is converted to the corresponding PI by intramolecular cyclization, in which water is released as the byproduct. Two main methods are used for this second "imidization" step: thermal and chemical conversion.[30]

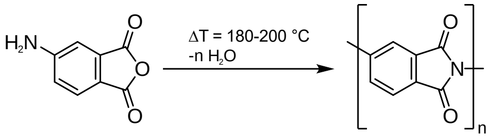

**Figure 2-1.** The temperature induced polycondensation of 4-aminophthalic anhydride discovered by Bogart and Renshaw.[23]

The thermal conversion process involves initial partial drying of a solvated poly(amic acid) film to a solid content of about 65-75 %.[31-33] The film is then gradually heated to 300 °C and maintained at this temperature for several hours to ensure high conversion rates (Figure 2-2). A variation of the preparation of aromatic polyimides using the thermal conversion method was demonstrated by Dinehart and Wright, who reacted pyromellitic dianhydride with various aromatic diamines in tetrahydrofuran.[34] The result was the simultaneous formation and precipitation of free poly(amic acid) and amine salt analogs. These could then be thermally converted to the corresponding PI.

An alternative strategy to convert the poly(amic acid) intermediate to the corresponding PI, commonly known as the chemical conversion method, has been described by Endrey.[24-29] In this strategy, dehydrating agents such as acetic anhydride are used in combination with a basic catalyst such as pyridine to initiate the imide condensation reaction (Figure 2-2). In a typical PI film preparation process, the poly(amic acid) is immersed as a film in a benzene solution of acetic anhydride and pyridine. After several hours, the PI is removed and dried. In addition to acetic anhydride, propionic anhydride, n-butyric anhydride, benzoic anhydride, etc. have been described by Endrey as suitable dehydrating agents for the chemical conversion to PIs. Alternatives to the basic catalyst pyridine include trimethylamine and isoquinoline. A variant of the chemical conversion method allows the direct addition of a dehydrating agent and a basic catalyst to the cold poly(amic acid) solution.[35] Both chemical conversion methods require final heating to temperatures >300 °C to ensure complete PI conversion.[30]

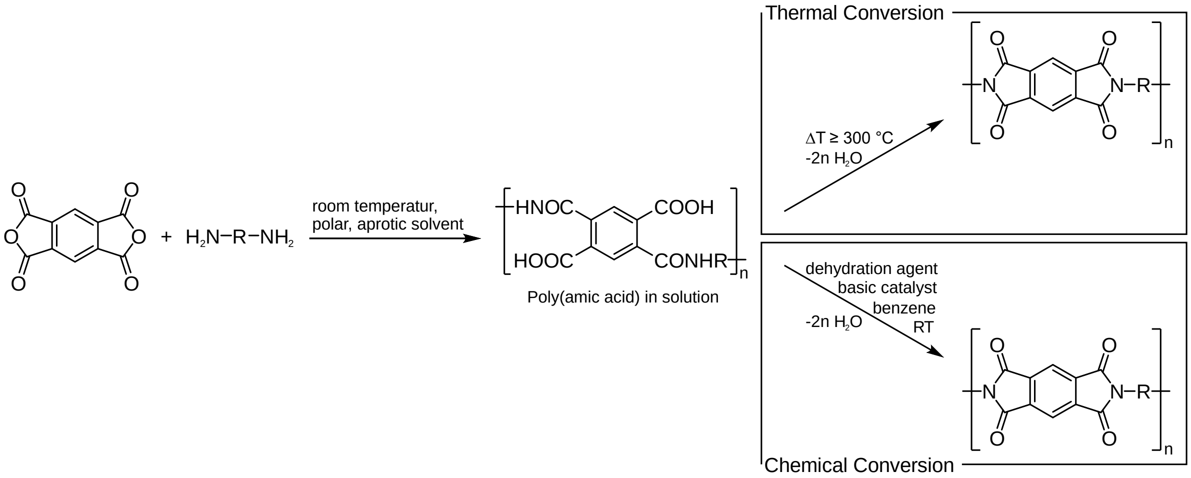

**Figure 2-2.** Comparison of the predominantly used thermal and chemical conversion methods for the imide cyclization reaction.

In addition to the originally invented two-step synthetic protocols, Vinogradova *et al.* reported a one-step synthesis of PIs in phenolic solvents such as phenol, p-chlorophenol, or *m*-cresol at elevated temperatures and in the presence of basic catalysts such as tertiary amines.[36] Extensions of this early work showed that the one-step method works not only for PIs commonly synthesized by the two-step method, but also for monomers that are difficult to polymerize by the two-step polymerization. Thus, monomers bearing sterically demanding groups or having unsuitable acid-base relationships, which render them inactive in the two-step process, can be successfully polymerized using the one-step reaction.[37-41]

For the preparation of PI coatings, a process for vapor deposition of the monomers has been developed:[42-44] By passing separate vapor streams of the monomers diamine and dianhydride into a mixing chamber at 200 °C, the mixed monomer vapor can be impinged on a film target and subsequently be polymerized.

Although PIs already have numerous applications, crystallinity is a desirable feature for such HPPs: It improves properties such as mechanical and thermal strength[45] and directional properties such as electrical conductivity.[46] However, polymers with high molecular weight are usually more difficult to crystallize than small molecules, and in most cases they are obtained as amorphous products.[47] While polymers with sufficient molecular flexibility can still be recrystallized from solution or melt, this is rarely possible for HPPs because they are generally insoluble and infusible.[47] In particular, aromatic PIs are difficult to obtain in crystalline form due to their low solubility in any solvent and the poor reversibility of the imide bond formation. In addition, as described above, harsh reaction conditions are required to obtain high molecular weight PIs, including high-boiling solvents, toxic catalysts, corrosive and flammable drying agents, and reaction temperatures of several hundred degrees Celsius.[30]

Recent advances in PI polymerization chemistry were made by Unterlass and coworkers, who gained access to crystalline PIs through an environmentally friendly one-pot synthesis strategy. By mimicking the hydrothermal conditions found in hydrothermal veins in the Earth's crust,[48-49] highly crystalline 1D polyimides could be synthesized in the laboratory in nothing but water.[47, 50] At first glance, a chemical reaction with water as a by-product carried out in water seems to contradict Le Chatelier's principle,[51] and the irony of this approach is underscored by the fact that PIs could be obtained by classical polymerization methods only with the complete exclusion of water.[52-53] However, in hydrothermal polymerization (HTP), the amine and anhydride comonomers form an intermediate salt that can be described as an ammonium carboxylate carboxylic acid (Figure 2-3).[47, 54-55] In this process, the dianhydride is first hydrolyzed to a tetracarboxylic acid and undergoes an acid-base reaction with the diamine to form a diaminium dicarboxylic acid salt. This monomer salt dissolves and polymerizes to form the PI. It is postulated that this intermediate salt provides a pre-oriented platform due to electrostatic interactions, which leads to an improvement in the crystallinity of the resulting 1D PI. At higher temperatures and pressures (200 °C, 20 bar), the pre-oriented intermediate salt is polycondensed and the PI forms in a crystalline manner.

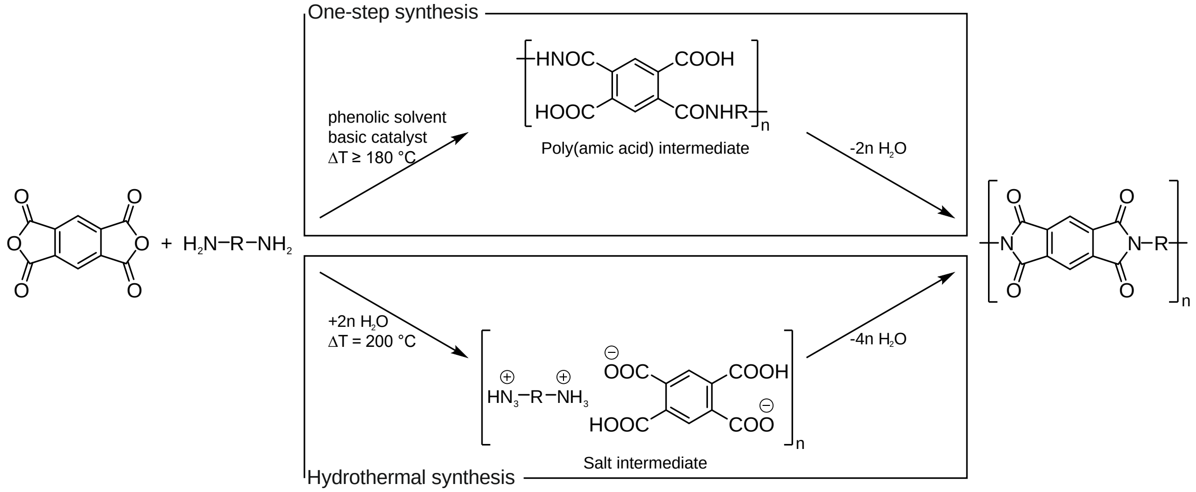

**Figure 2-3.** Comparison of the classically used one-step procedure with the recently developed hydrothermal method for the synthesis of 1D PIs.

In addition to the classical and hydrothermal reaction pathways from dianhydrides and diamines, PIs can also be prepared by lesser known synthetic protocols using diisocyanates and dianhydrides,[56-58] or diamines and dithioanhydrides,[59-61] or from silylated diamines and dianhydrides (Figure 2-4a-c).[62-63] It was further demonstrated that Michael addition can be used to convert bis(maleimide) and diamines to a PI. In this case, unlike other methods, the imide ring is not formed during polymerization, but originates from the bis(maleimide) monomer (Figure 2-4d).[64] Chi *et al.* prepared polyimides at 80 °C in the presence of NaI in DMSO by the *in situ* Diels-Alder polymerization of 1,4-bis[4-(methyloxy)phenyloxy]-2,3,6,7-tetrakis-(bromomethyl)benzene with four different arylene bis-maleimides (Figure 2-4e).[65] Finally, the reaction of di(hydroxyalkyl) compounds and diimides under Mitsunobu conditions leads to the direct formation of PIs in a single step (Figure 4-2f).[66-67]

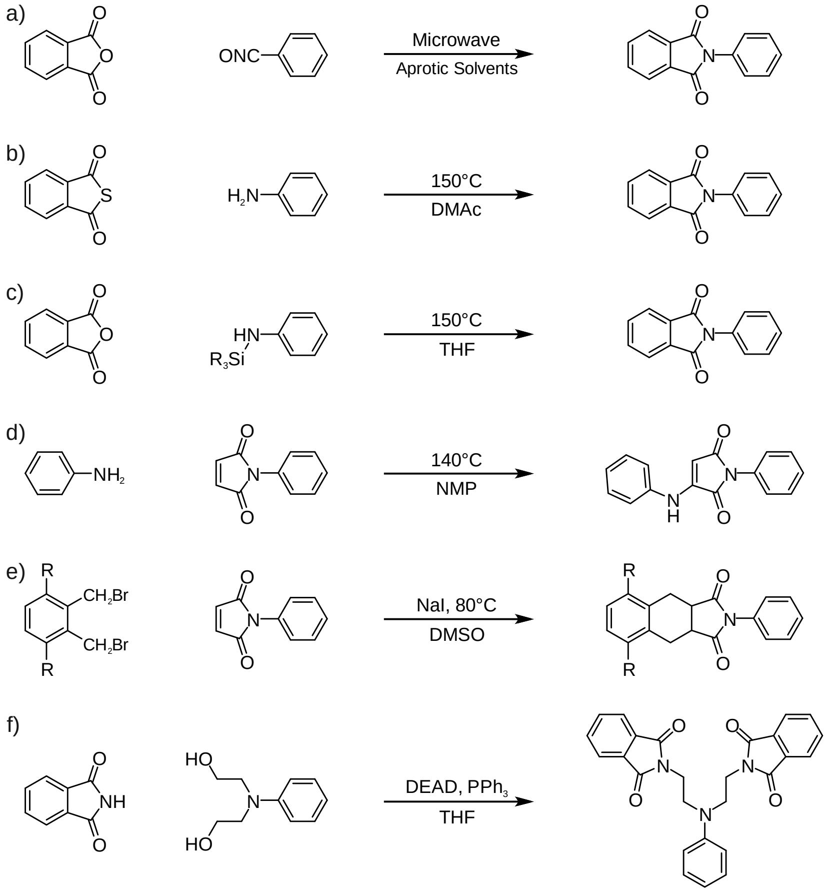

**Figure 2-4.** Schematic representation of lesser known synthetic protocols for the synthesis of PI-COFs.

While 1D polymers have been extensively developed and studied over the past century, research interest has shifted to 2D and 3D polymers in recent decades. Combining the functional diversity of common 1D polymers with the porosity and structural integrity of two- or three-dimensional frameworks remains a growing area of research today. In this context, microporous aromatic PIs were synthesized in 2007 using spirobifluorene units as structure guiding motifs. [68-70] The resulting porous PIs were amorphous due to random stacking but exhibited rigid and twisted macromolecular chains, leading to good thermal stability typical of PIs. However, due to their low specific surface area and nonspecific pore size, their applications were limited. As a natural step in the development of PIs, Fang *et al*. demonstrated the first synthesis of crystalline 2D polyimide-based covalent organic frameworks (PI-COFs) in 2014 and even extended the dimensionality to three dimensions in 2015. [1, 71] Further development in the field of PI-COFs by using new monomers and novel polymerization methods are discussed in detail in Section 2.2.

## *2.2 Synthesis of Imide-Linked Covalent Organic Frameworks*

As an emerging class of functional porous materials, COFs have attracted considerable attention and have experienced rapid growth over the past decade since the seminal work of Yaghi and coworkers.[72] Developments in this regard include PI-COFs synthesized by the reaction of symmetric, rigid primary amine moieties with carboxylic anhydride units to form a pyrrolidine-2,5-dione backbone. In contrast to the classical synthesis of amorphous 1D-PIs, in which imide formation is essentially irreversible (Figure 2-2), and the hydrothermal method for the synthesis of crystalline 1D-PIs, where the need for reversible bond formation is circumvented by pre-orientation of the monomers using an intermediate salt (Figure 2-3),[47] the imide cyclization in PI-COF synthesis must be reversible and carried out following the principles of dynamic covalent chemistry.[72-73] In recent years, a variety of synthetic approaches for the synthesis of PI-COFs have been demonstrated and are discussed below.

### *2.2.1 Solvothermal Synthesis of PI-COFs*

The protocol predominantly used for the synthesis of PI-COFs is the solvothermal bottom-up synthesis method.[2] To carry out the imidization reaction in an ordered fashion, it is important to use a mixture of two solvents and adjust the ratio of the two solvents to control the solubility of the monomers.[1] A suitable catalyst, such as isoquinoline, is needed to adjust the rate of the reactions that occur, and in addition, an appropriate temperature and pressure is required to promote the ring closure reaction. These conditions are fundamentally different from those used in the one-step synthesis of amorphous 1D PIs, in which kinetic products are formed by complete solubilization of the monomers, which thus react rapidly and irreversibly to form amorphous materials.[74]

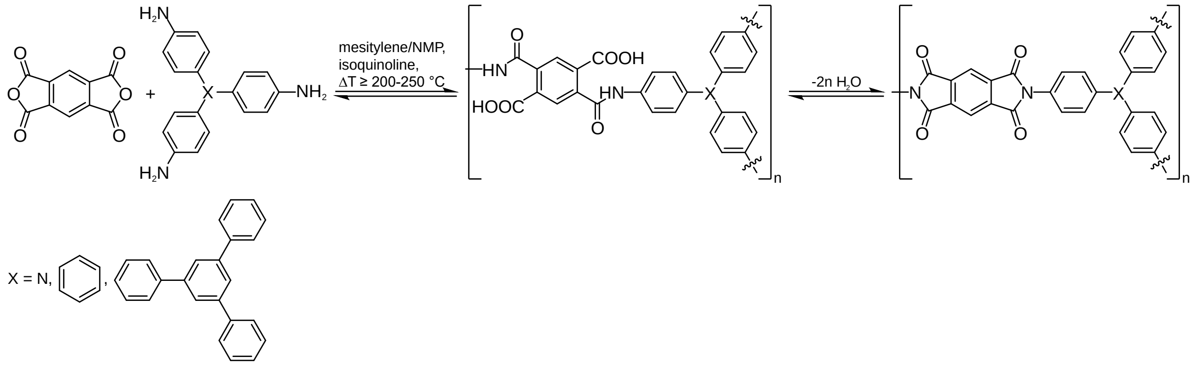

**Figure 2-5.** Synthesis of the first PI-COFs following the principles of DCC.

In 2014, Yan's research group synthesized three 2D PI-COFs of high porosity and long-range order for the first time (Figure 2-5).[1] Using pyromellitic dianhydride as linear linker molecule and three different trisamines, namely tris(4-aminophenyl)amine (TAPA), tris(4-aminophenyl)benzene

(TAPB), and tris[4-amino(1,1-biphenyl-4-yl)]benzene (TABPB) as nodal building blocks, TAPA-PMDA-. TAPB-PMDA and TABPB-PMDA-COF were synthesized in a solvent mixture of mesitylene and NMP together with isoquinoline as the basic and nucleophilic catalyst. Similar to amorphous porous PIs, these PI-COFs showed high thermal stability up to 535 °C as determined by thermogravimetric analysis. Following this pioneering work, a variety of 2D and 3D PI-COFs were synthesized using this general protocol. A summary of the PI-COFs synthesized using the solvothermal method and the respective reaction conditions are shown in Table 2-1. In a typical solvothermal synthesis of PI-COFs, a heat-resistant glass tube is filled with the desired monomers, a mixture of two solvents, and a basic catalyst. The glass tube is sealed under vacuum and then heated to 150-250 °C for 3-7 days.[1, 71, 75-77] Although in most cases a catalyst is required, there are exceptions. Lv *et al*. demonstrated that the synthesis of TAPA-NDA-COF in dry DMF at reaction temperatures of 180 °C is possible without the use of a catalyst.[77] The resulting COF showed good crystallinity and a large surface area of 1276 $m^2/g$. Another PI-COF synthesized without the use of a catalyst is MA-PMDA-COF.[78-79]

**Table 2-1.** Summary of the PI-COFs synthesized using the solvothermal method together with the respective reaction conditions used.

| COF | Solvent mixture | Catalyst | Temperature | Reaction time |
|---|---|---|---|---|
| TAPA-PMDA[1, 80] | Mesitylene/NMP | Isoquinoline | 200 °C | 5 days |
| | *m*-Cresol/NMP | Isoquinoline | 200 °C | 3 days |
| TAPB-PMDA[1, 80-81] | Mesitylene/NMP | Isoquinoline | 200 °C | 5 days |
| | *m*-Cresol/NMP | Isoquinoline | 200 °C | 3 days |
| | Mesitylene/NMP | Acetic acid | 120 °C | 3 days |
| TABPB-PMDA[1] | Mesitylene/NMP | Isoquinoline | 250 °C | 7 days |
| TT-PMDA[76] | Mesitylene/NMP | Isoquinoline | 160 °C | 5 days |
| TAPP-PTCDA[75] | Mesitylene/NMP | Isoquinoline | 180 °C | 4 days |
| TAPA-NDA[80, 82-83] | Mesitylene/NMP | Isoquinoline | 160 °C | 5 days |
| | DCB/NMP | Isoquinoline | 200 °C | 3 days |
| | Mesitylene/DMI | Isoquinoline | 200 °C | 5 days |
| | DMF | / | 180 °C | 3 days |
| TAPB-NDA[80, 84] | Mesitylene/NMP | Isoquinoline | 150 °C | 5 days |
| | *m*-Cresol/NMP | Isoquinoline | 200 °C | 3 days |
| TAPA-MTA[85] | *m*-Cresol/NMP | Isoquinoline | 150 °C | 3 days |
| TAPB-MTA[85] | *m*-Cresol/NMP | Isoquinoline | 150 °C | 3 days |
| MA-PMDA[79] | Ethylene glucol/DMF | / | 180 °C | 3 days |
| TAA-PMDA[71] | Mesitylene/NMP | Isoquinoline | 160 °C | 5 days |
| TAPM-PMDA-COF[71] | Mesitylene/NMP | Isoquinoline | 160 °C | 5 days |
| TAPA(3D)-M(TAPc)[86] | *n*-butanol/NMP | Isoquinoline | 180 °C | 5 days |

In addition to the predominantly used solvothermal method, other more unique alternative strategies for the synthesis of crystalline PI-COFs such as high-temperature solid-state synthesis,[87] interfacial synthesis,[88] hydrothermal synthesis,[89] and the synthesis in ionic liquids[90] have been demonstrated. Figure 2-7 shows a timeline of the evolution of all PI-COFs and a collection of the linker molecules used to prepare them. The color code indicates the synthetic procedure used for the initial production of the respective COF.

### *2.2.2 High-Temperature Solid-State Approach*

In the high-temperature solid-state approach, reminiscent of the first discovery of polyimides by Bogart and Renshaw,[23] the trigonal amine linker molecule melamine (MA) is heated together with the linear anhydride linker molecules PMDA and NDA, respectively, under an inert atmosphere at reaction temperatures of 325-345 °C.[87] The XRPD patterns of the resulting MA-PMDA- and MA-NDA-COFs show COF-related reflections, but the specific BET surface areas of the COFs were measured to be only 4 to 9 $m^2/g$. The low surface area, as well as additional non-COF-related reflections in the XRPD pattern, indicate enormous pore clogging by nanocrystals.[87]

### *2.2.3 Surfactant Supported Synthesis of a PI-COF Thin Film*

Liu *et al*. demonstrated the synthesis of a crystalline few-layer 2D-PI-COF on a water surface in 2019 (Figure 2-6).[88] In the synthesis of TAPP-PTCDA-COF, a monolayer of the surfactant sodium (9Z)-octadec-9-en-1-yl sulfate (sodium oleyl sulfate, SOS) was first prepared on a water surface. Then, the first monomer TAPP was slowly added to the water phase, which was adsorbed and pre-organized by electrostatic interactions and hydrogen bonding under the surfactant monolayer. Subsequently, PTCDA was injected into the water phase which then diffused to the pre-organized TAPP, where 2D polymerization was initiated at the water surface. The polycondensation reaction was carried out under particularly mild conditions at 20 °C for 7 days.

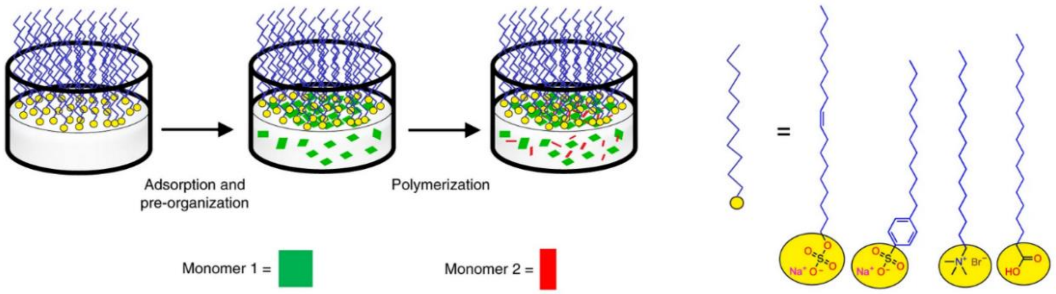

**Figure 2-6.** A schematic representation of the synthetic procedure of TAPP-PTCDA-COF on a water surface assisted by a surfactant monolayer. Reprinted and adapted with permission from reference [88].

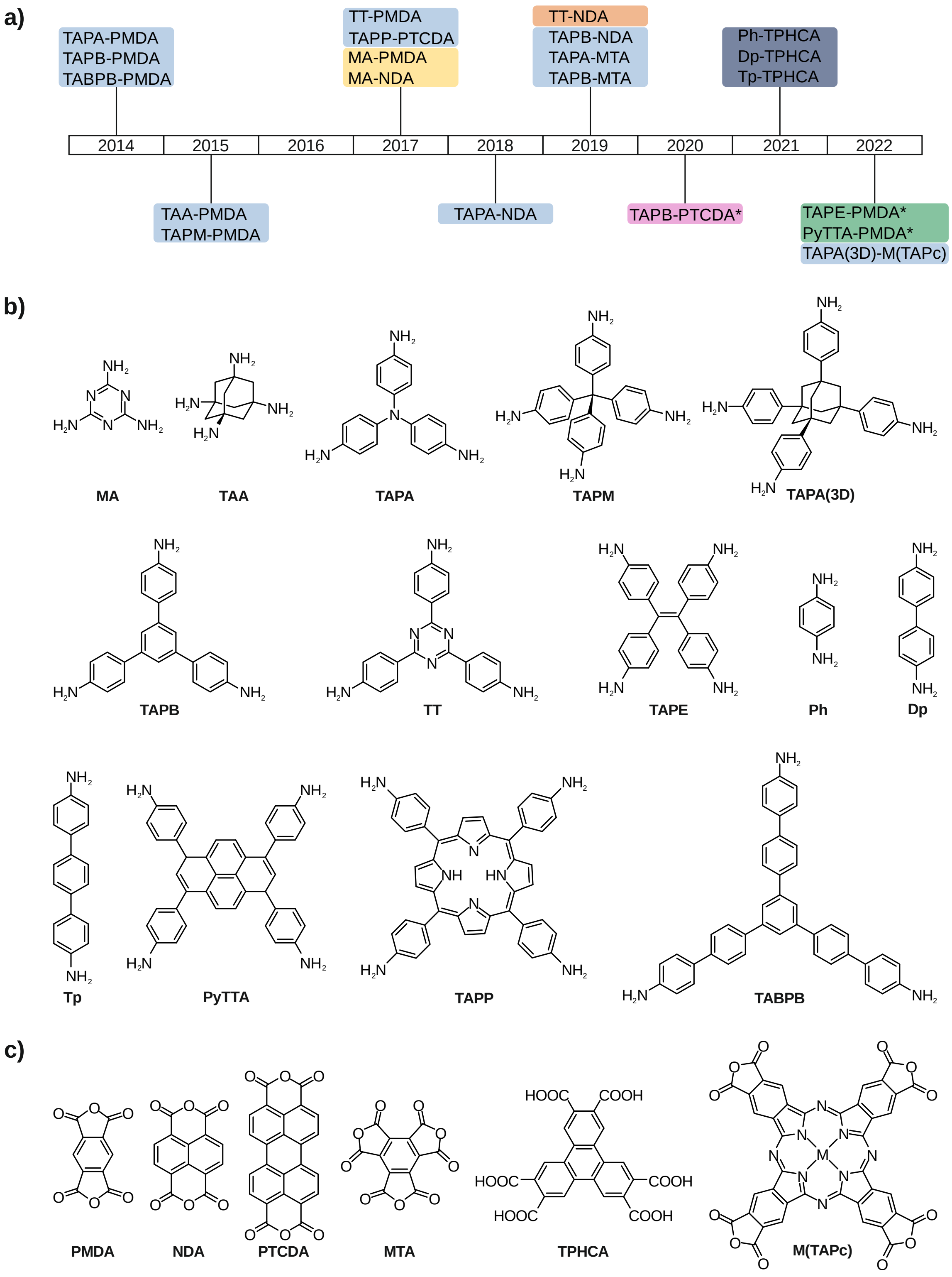

**Figure 2-7.** a) Timeline of the development of PI-COFs. The color code indicates which synthesis method was first used to produce the COFs. Blue: solvothermal, yellow: high-temperature solid-state, orange: linker-exchange, red: ionothermal, grey: hydrothermal, green: alcohol-assisted hydrothermal. COFs marked with an asterisk have been developed within the scope of this thesis. b) Amine linker molecules and c) anhydride and carboxylic acid linker molecules used to prepare crystalline PI-COFs.

### *2.2.4 Synthesis in Ionic Liquids*

In 2020, Zhao *et al*. showed that ionic liquids can be suitable candidates for the low-temperature synthesis of PI-COFs.[90] Using the ionic liquid [BMIm][$HSO_4$] as a solvent for the synthesis of TAPA-PMDA- and TAPB-PMDA COF, remarkably low reaction temperatures of 130 °C could be realized. While TAPA-PMDA-COF exhibits a specific BET surface area of 903 $m^2/g$, which is comparable to the surfaces achieved by the solvothermal method, TAPB-PMDA-COF has a specific BET surface area of only 35 $m^2/g$ – orders of magnitude lower than when using other synthesis methods.[1] Furthermore, the general applicability of this method has yet to be proven.

### *2.2.5 Linker-Exchange Strategy*

As an alternative strategy to bottom-up synthesis, Zhai *et al*. recently exploited the relatively low reversibility and high stability of imide linkages compared to imine linkages by converting amorphous covalent organic imine polymers (COPs) into crystalline PI-COFs *via* linker exchange under standard solvothermal conditions in a mixture of mesitylene, NMP, and isoquinoline.[91] First, amorphous imine polymers were synthesized and then reacted with PMDA or NDA and the original linker terephthalic aldehyde is replaced by the anhydride linker to form TT-PMDA- and TT-NDA-COF. A reduced reaction rate as well as a possible modulating effect due to the released aldehyde linker during the reaction could support the formation of crystalline products during exchange.

### *2.2.6 Hydrothermal Synthesis*

During the preparation of this dissertation, a novel hydrothermal synthesis for PI-COFs was developed.[89] Inspired by the work of the Unterlass group on the hydrothermal synthesis of crystalline 1D PIs,[47, 50, 54-55] Kim *et al*. demonstrated the hydrothermal synthesis of 2D PI-COFs for the first time in 2021. By reacting the trigonal linker molecule triphenylene-2,3,6,7,10,11-hexacarboxylic acid (TPHCA) with the linear linker molecules p-phenylenediamine (Ph), 4,4'-diaminobiphenyl (Dp), and 4,4'-diamino-p-terphenyl (Tp), respectively, TPHCA-Ph-, TPHCA-Dp-, and TPHCA-Tp-COFs were obtained. Although this work represented a milestone in the green synthesis of PI-COFs, this synthesis protocol has a major drawback due to the use of water as the only solvent. To obtain crystalline products, all linker molecules must be appropriately soluble in water under hydrothermal reaction conditions. The quality of the PI-COFs obtained by Kim *et al*. thus decreases significantly with the decrease in aqueous solubility of amine linker molecules from TPHCA-Ph-COF ($S_{BET}$ = 669 $m^2/g$) to TPHCA-Tp-COF ($S_{BET}$ = 54 $m^2/g$).[89]

Circumventing the solubility issue of the hydrothermal approach, we have developed an alcohol-assisted hydrothermal polymerization (aaHTP) method for the synthesis of PI-COFs, which is described in detail in Chapter 5.[92] In addition, our group has developed a novel ionothermal synthesis protocol, which is described in detail in Chapter 4.[93]

## *2.3 Challenges in the Synthesis of Imide-Linked COFs*

As mentioned earlier, PI-COFs exhibit exceptional chemical and thermal stability similar to that of their 1D PI counterparts and offer diverse framework topologies and pore sizes (Figure 2-8).[1-2] However, in PI-COF synthesis, the high stability of the imide ring has become an obstacle that hinders the rapid and functionally diverse growth of this field.

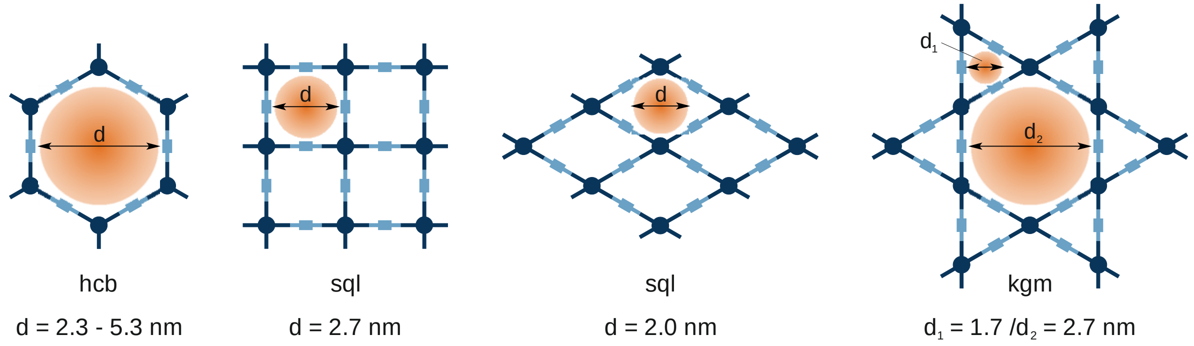

**Figure 2-8.** Schematic representation of different topologies and pore sizes realized with PI-COFs.

As discussed in Section 1.1, COFs are synthesized following the principles of dynamic covalent chemistry,[72-73] according to which the COF formation reaction must be reversible to allow correction of crystal defects under thermodynamic control. Thus, bond breaking is as important as bond formation. As stated in Section 1.1.3, Haase *et al*. described the “COF trilemma” in reversible COF synthesis, pointing out that the three characteristics of crystallinity, stability, and functionality compete with each other (Figure 1-10).[94] Crystallinity and stability are inversely related, as the stability of the COF linkage negatively affects reversibility. Furthermore, synthesis of stable COFs using reactions that are reversible only at very high temperatures or under harsh conditions[95-96] limits the types of functional groups and functionalities that can be incorporated into the COFs framework because they can be chemically and thermally decomposed during synthesis.[94, 97] In polyimide condensation reactions, the formation of the cyclic imide is essentially irreversible under standard solvothermal conditions, which complicates the formation of the thermodynamic and crystalline product.[47] As described in Section 2.2, to avoid the formation of disordered, amorphous, kinetic products, harsh reaction conditions such as high-boiling and toxic solvents, toxic catalysts, and high processing temperatures up to several hundred degrees Celsius are usually required. Despite these harsh conditions, the reversibility of the imide formation reaction is still low and often results in COFs with only moderate crystallinity and specific surface area, which shows the importance of searching for additional complementary synthetic methods.[85, 87, 89] This becomes even more important when considering the functionality problem that PI-COFs suffer from. Till date, there are no PI-COFs bearing additional functional groups besides the imide bond, which hinders the tunability of electronic properties or the applicability of PI-COFs for specific applications such as scaffolds for molecular catalysts. Therefore, the development of new synthetic methods for the preparation of both crystalline and functional PI-COFs is crucial for the further development of this field. Notwithstanding, PI-COFs have attracted attention in many application areas already, as discussed in detail in Section 2.4.

## *2.4 Properties and Applications of Imide-Linked Covalent Organic Frameworks*

PI-COFs exhibit good stability, defined pores, and high specific surface areas, making them promising candidates for the storage and separation of guest molecules,[80, 82, 84-85, 98-99] drug delivery,[71] or adsorption of organic dye molecules.[1, 76] The ability of PI-COFs to form intramolecular redox-active charge transfer complexes through the transfer of electrons from the electron-donating amine linker to the electron-accepting imide segments led to their application in sensing,[1, 75, 81] energy storage,[77-78, 80, 83, 89, 100-101] and electro- and photocatalysis.[79, 86, 102-103]

### *2.4.1 Adsorption and Drug Delivery*

The applicability of PI-COFs and COFs in general, e.g. for adsorption and separation applications, strongly depends on their porous structure (pore size and shape), pore wall properties, and accessible specific surface area. In their pioneering work on PI-COFs, Yan's research group demonstrated the adsorption of dye molecules using TABPB-PMDA-COF.[1] TABPB-PMDA-COF has large pores of 51 Å pore diameter and a very high specific surface area of 2346 $m^2/g$, making it a suitable material for adsorption of large dye molecules such as rhodamine B (16x10 $Å^2$). When TABPB-PMDA-COF was loaded with the macromolecular dye, the emission spectrum was observed to be temperature dependent, suggesting that dye-doped PI-COFs could be used for temperature sensors.[1] Another example of adsorption of organic dye molecules with PI-COFs was shown by Zhu *et al*. who used TT-PMDA-COF to adsorb methylene blue from aqueous solution.[76] TT-PMDA-COF with a pore size of 33 Å and a specific surface area of 1484 $m^2/g$ showed superior uptake capacity and extracted nearly 169 wt. % of the dye methylene blue, making it the most effective porous adsorbent reported for this application at that time.[76] Fang *et al*. successfully used the 3D-PI-COFs TAA-PMDA- and TAPM-PMDA-COF for drug delivery with high loading and good release control (Figure 2-9).[71] The COFs were loaded with a variety of drugs, including ibuprofen, captopril, and caffeine, which were subsequently released in simulated body fluid (pH = 7.4, standard buffer solution, 37 °C).

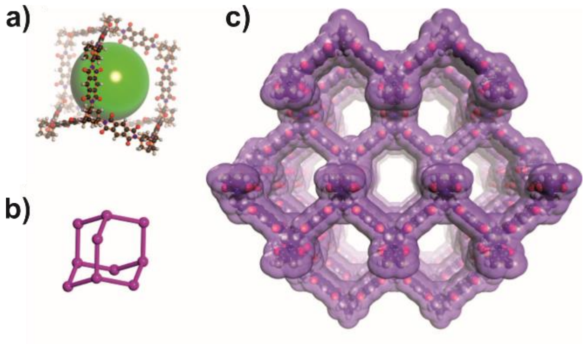

**Figure 2-9.** Structural representations of the extended structure of TAA-PMDA-COF: a) single diamond network; b) diamond topology; c) 3D porous structure with 15 Å pores. Reprinted and adapted with permission from reference [71].

In addition to the adsorption and release of organic dye molecules from solutions, the adsorption and separation of various gases is also an important area of application. In particular, the extraction and separation of $CO_2$ and other toxic gases from air continues to be a growing field. For $CO_2$ adsorption, microporous materials with polar pore walls have been shown to have the highest storage capacities and are therefore the most suitable candidates for this application.[104] In this context, a number of PI-COFs were investigated for their applicability as $CO_2$ adsorption scaffolds. An overview of PI-COFs with their respective specific surface areas, pore diameters and $CO_2$ uptake capacities is shown in Table 2-2.

**Table 2-2.** Summary of PI-COFs used as $CO_2$ adsorption scaffolds with their respective specific BET surface areas, pore diameters, and $CO_2$ uptake capacities.

| COF | $S_{BET}$ | Pore diameter | $CO_2$ uptake capacity |
|---|---|---|---|
| TAPA-PMDA[80] | 759 $m^2/g$ | 26.3 Å | 64 $cm^3/g$ |
| TAPB-PMDA[80] | 582 $m^2/g$ | 31.9 Å | 51 $cm^3/g$ |
| TAPA-NDA[80] | 1430 $m^2/g$ | 25.7 Å | 66 $cm^3/g$ |
| TAPB-NDA[80] | 990 $m^2/g$ | 31.0 Å | 56 $cm^3/g$ |
| TAPA-MTA[85] | 397 $m^2/g$ | 12.4 Å | 46 $cm^3/g$ |
| TAPB-MTA[85] | 339 $m^2/g$ | 14.1 Å | 39 $cm^3/g$ |

Taking advantage of the high chemical stability of PI-COFs, Lee *et al*. demonstrated the first $SO_2$ sorption with COFs.[98] The basis for their experiments was TAPA-PMDA-COF, into which 4-[(dimethylamino)methyl]aniline was incorporated as a modulator in different ratios to increase possible binding sites for reversible $SO_2$ adsorption (Figure 2-10). While modulator-free synthesis yielded TAPA-PMDA-COFs with a surface area of 1003 $m^2/g$, the specific surface areas decreased with increasing modulator content from 831 $m^2/g$ at 10% to 93 $m^2/g$ at 60% modulator. However, these PI-COFs utilizing $SO_2$ and tertiary amine interactions showed high $SO_2$ uptake up to 6.3 mmol/g (10% modulator) and could be recovered in a recycling process.[98]

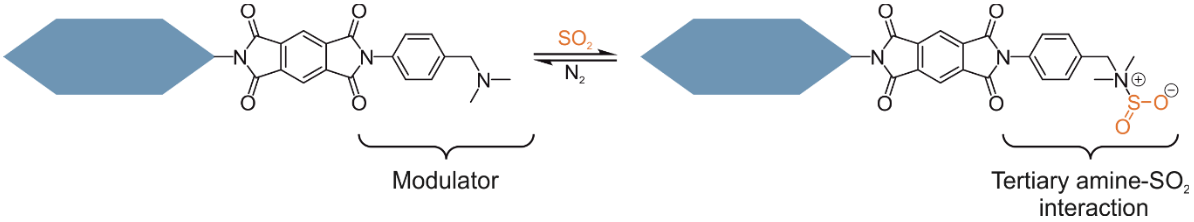

**Figure 2-10.** Schematic representation of functionalized PI-COF and its interaction with $SO_2$.

The first example of a COF capable of selectively separating acetylene from ethylene was TAPA-NDA-COF demonstrated by Jiang *et al.*[82] At ambient conditions, the acetylene sorption capacity of TAPA-NDA-COF was calculated to be 2.23 mmol/g, and ethylene reached 1.29 mmol/g. Moreover, under the same conditions, the framework exhibits a moderate acetylene/ethylene selectivity of 3.9. Calculations suggest that these properties are due in part to a stronger electrostatic interaction between TAPA-NDA-COF and acetylene, mediated by a tight hydrogen bonding between the carbonyl oxygen atoms of the framework and the hydrogen atoms of acetylene (Figure 2-11).[82] The study was repeated by the same group using TAPB-NDA-COF instead of TAPA-NDA-COF.[84] TAPB-PMDA-COF showed increased uptake capacity for acetylene (3.50 mmol/g) and ethylene (1.89 mmol/g), as well as a slightly increased selectivity of 4.1 compared to the previously published TAPA-NDA-COF. [82, 84]

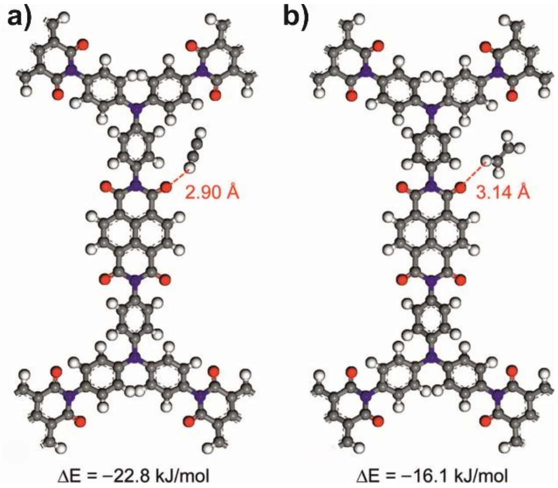

**Figure 2-11.** Optimized binding sites and binding energies for a) acetylene and b) ethylene within TAPA-NDA-COF. Reprinted with permission from reference [82].

### 2.4.2 *Sensing*

In addition to simple adsorption and release of guest molecules, some PI-COFs exhibiting luminescence properties can interact with specific adsorbed species, making this class of materials a suitable candidate for sensing applications. Zhang *et al*. designed highly efficient fluorescent PI-COF nanosheets (PI-CONs) as sensors for 2,4,6-trinitrophenol (TNP, Figure 2-12).[75] The research group fabricated few-layer nanosheets of TAPP-PTCDA-COF by ultrasound-assisted exfoliation. The obtained CONs showed much higher fluorescence intensity than the bulk material. The fluorescence is caused by the p-n heterojunctions between the TAPP and PTCDA units. During the adsorption of TNP into the TAPP-PTCDA-COF nanosheets, a PI-COF-picrate complex is formed by electron transfer between the PI-COF and the electron-deficient TNP. Density functional theory calculations showed that the ground state electrons can be transferred from TNP$^-$ to PI-COF, resulting in fluorescence quenching. In addition, PI-COFs have been used as fluorescent sensors for the detection of Fe$^{3+}$ and for the electrochemical detection of Pb$^{2+}$.[81]

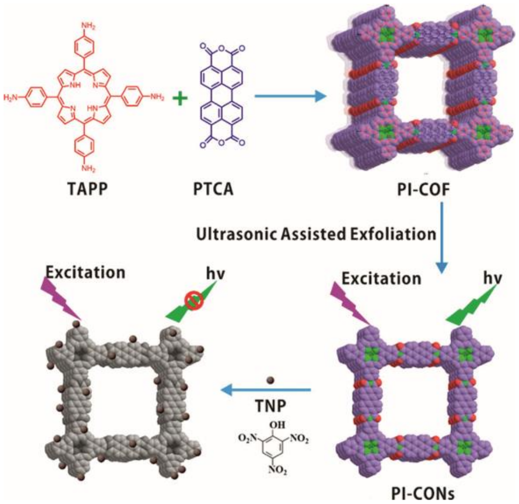

**Figure 2-12.** Schematic representation for the preparation of the fluorescent PI-CONs and their application in the detection of TNP. Reprinted with permission from reference [75].

### 2.4.3 *Energy Storage*

Taking advantage of the strong intramolecular interactions, charge transfer complexes, and electronic polarizations in PI-COFs, Lv *et al.* demonstrated the applicability of TAPA-NDA-COF as a cathode material for a photosensitive Li-ion battery (LIB).[77] Photo- and electrochemical measurements revealed an "ultrahigh efficiency" intramolecular charge transfer from the TAPA to the NDA building unit and a highly reversible electrochemical reaction in TAPA-NDA-COF. In TAPA-NDA-COF, a synergistic effect is observed between the reversible electrochemical reaction in the battery and the intramolecular charge transfer with improved solar energy efficiency. According to the authors, TAPA-NDA-COF as a cathode can couple the photo-induced charge transfer and the reversible electrochemical processes of de/lithiation, enabling direct conversion and storage of solar energy into electrochemical energy (Figure 2-13).

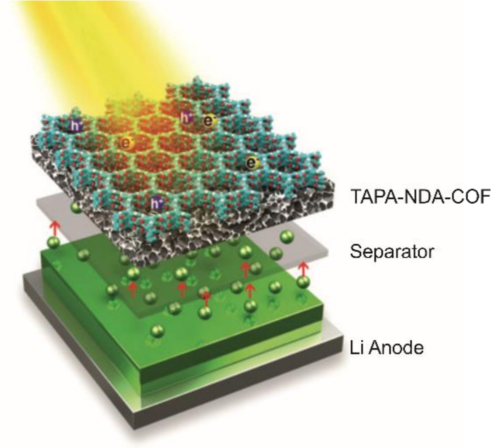

**Figure 2-13.** Schematic representation of a photo-responsive Li-ion battery. Reprinted and adapted with permission from reference [77].

Since the seminal work of Lv *et al*., a variety of PI-COFs have been used as cathode or anode materials in different types of energy storage devices. Wang *et al*. and Zhao *et al*. fabricated cathode materials for LIBs from few-layer TAPA-PMDA-COF, TAPB-PMDA-COF, and TT-PMDA-COF composites with reduced graphene oxide (rGO) to enhance charge transfer.[100] [101] Experiments showed that the use of exfoliated PI-COFs improve accessibility to the redox-active sites compared to bulk PI-COFs, which can therefore be used more efficiently. Duan *et al*. investigated exfoliated MA-PMDA-COF as a potential sulfur host material for application as a cathode in lithium-sulfur batteries (LSBs).[78] As a result of the synergy of the robust conjugated porous framework and the strong oxygen-lithium interactions, the fabricated LSB delivered capacities of 1205 mAh/g at 0.1 C, rates of 503 mAh/g at 4 C, and cycling stability of 96 % capacity retention at 0.2 C after 100 cycles.[78]

Yu *et al*. demonstrated that PI-COFs can be used not only as cathode materials but also as anode materials for aqueous Zn-ion energy storage devices.[83] The well-organized pore channels of TAPA-NDA-COF enabled good accessibility of the incorporated redox-active carbonyl groups and efficient ion diffusion with a low energy barrier. *In situ* Raman studies and first-principle calculations revealed a two-step $Zn^{2+}$ storage mechanism in which imide carbonyl groups reversibly form negatively charged enolates. Van der Jagt *et al*. showed in a proof-of-concept study that TAPA-NDA-COF could be a suitable candidate as an anode material for Na-ion batteries.[80] Finally, TPHCA-Ph-COF was recently used as an active anode for LIBs.[89]

### *2.4.4 Catalysis*

In addition to the use of PI-COFs in energy storage devices, PI-COFs were also discovered to be suitable candidates for electrocatalytic and photocatalytic energy conversion applications due to their highly redox-active backbone. Royuela *et al*. discovered that the naphthalimide units in TAPB-NDA-COF can be used as an efficient metal-free electrocatalyst for oxygen reduction in alkaline media.[102] By comparing the electrochemical response of bare glassy carbon (GC) electrodes, amorphous TAPB-NDA polymer/GC and TAPB-NDA-COF nanosheet/GC disk electrodes, the authors found that the electrocatalytic performance of the amorphous polymer was poor, which was probably due to the disordered structure and low porosity that hindered the diffusion of $O_2$. This work demonstrates the importance of high crystallinity and porosity in COFs and highlights the need for new and complementary synthesis methods. Han *et al*. used carbon-doped 3D-TAPA(3D)-Co(TAPc)-COF to fabricate an electrocatalytic cathode for the reduction of $CO_2$ in aqueous $KHCO_3$ solution.[86] The PI-COF showed a Faradaic efficiency of 88-96 % for the conversion of $CO_2$ to CO in a voltage range of -0.60 to -1.00 V compared to a reversible hydrogen electrode. An efficient electrocatalyst for the hydrogen evolution reaction was developed by Pan *et al*. by dispersing ruthenium nanoclusters with small particle sizes (less than 2 nm) on MA-PMDA-COF.[79] It was found that MA-PMDA-COF-Ru required an overpotential of only 35.1 mV in alkaline media to achieve a current density of 10 mA/cm$^2$, which outperformed the benchmark catalyst with 20 % Pt/C (37.3 mV). It is proposed that the good performance of MA-PMDA-COF-Ru is probably due to the uniform and ultrasmall Ru nanoclusters with satisfactory dispersion, which provide multiple active sites for the hydrogen evolution reaction.[79]

In addition to electrocatalysis, photocatalysis is an extensive research area in COF chemistry. In this regard, Chen *et al*. prepared a series of hexagonal PI-COFs using TAPA, TAPB, and TT as amine linker molecules and PMDA as an anhydride building block.[103] Single Ni sites were integrated into the hexagonal pores of the COFs and serve as active sites for the selective photoreduction of $CO_2$ to CO (Figure 2-14). The photogenerated electron-hole pairs in the PI-COFs could be efficiently separated by intra- and intermolecular charge transfer mechanisms to drive the reduction of $CO_2$. It is proposed that the PI-COFs not only act as a photosensitizer to generate charge carriers, but also exert a promoting effect on selectivity.

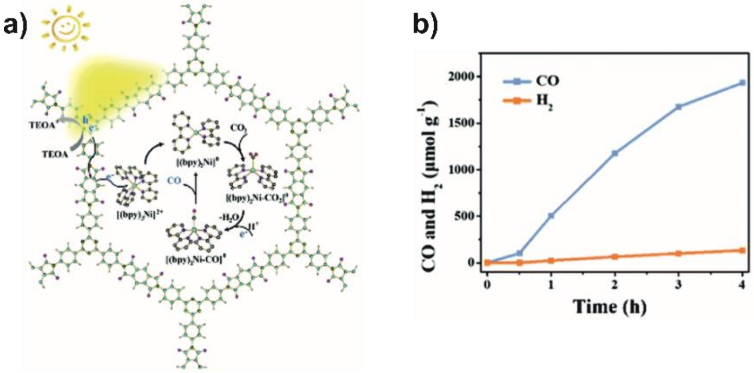

**Figure 2-14.** a) Proposed reaction mechanism for the photoreduction of $CO_2$; b) Kinetic profile of photocatalytic CO and $H_2$ production by TT-PMDA-COF. Reproduced and adapted from reference [103] with permission from the Royal Society of Chemistry.

## 2.5 Bibliography

[1] Q. Fang, Z. Zhuang, S. Gu, R. B. Kaspar, J. Zheng, J. Wang, S. Qiu, Y. Yan, *Nat. Commun.* **2014**, *5*, 4503.

[2] Y. Zhang, Z. Huang, B. Ruan, X. Zhang, T. Jiang, N. Ma, F. C. Tsai, *Macromol. Rapid. Commun.* **2020**, *41*, e2000402.

[3] D.-J. Liaw, K.-L. Wang, Y.-C. Huang, K.-R. Lee, J.-Y. Lai, C.-S. Ha, *Prog. Polym. Sci.* **2012**, *37*, 907-974.

[4] P. M. Hergenrother, *High Perform. Polym.* **2016**, *15*, 3-45.

[5] J. J. Licari, Coating materials for electronic applications: polymers, processing, reliability, testing, **2003**.

[6] H. Zhang, P. K. Shen, *Chem. Rev.* **2012**, *112*, 2780-2832.

[7] D. Yu, A. Gharavi, L. J. M. Yu, *Macromolecules* **1995**, *28*, 784-786.

[8] W. N. Leng, Y. M. Zhou, Q. H. Xu, J. Z. Liu, *Polymer* **2001**, *42*, 7749-7754.

[9] T. N. Oo, T. Iwata, M. Kimura, T. Akahane, *Science and Technology of Adv. Mater.* **2016**, *6*, 149-157.

[10] C. Xu, T. Shiono, T. Ikeda, Y. Wang, Y. Takeuchi, *J. Mater. Chem.* **2003**, *13*, 669-671.

[11] H.-T. Kim, J.-W. Lee, S.-J. Sung, J.-K. Park, *Liquid Crystals* **2000**, *27*, 1343-1356.

[12] S. A. Stern, Y. Mi, H. Yamamoto, A. K. S. Clair, *J. Polym. Sci. B Polym. Phys.* **1989**, *27*, 1887-1909.

[13] T. H. Kim, W. J. Koros, G. R. Husk, K. C. O'Brien, *J. Membr. Sci.* **1988**, *37*, 45-62.

[14] Y.-C. Wang, S.-H. Huang, C.-C. Hu, C.-L. Li, K.-R. Lee, D.-J. Liaw, J.-Y. Lai, *J. Membr. Sci.* **2005**, *248*, 15-25.

[15] J. Fang, X. Guo, S. Harada, T. Watari, K. Tanaka, H. Kita, K.-i. Okamoto, *Macromolecules* **2002**, *35*, 9022-9028.

[16] X. Guo, J. Fang, T. Watari, K. Tanaka, H. Kita, K.-i. Okamoto, *Macromolecules* **2002**, *35*, 6707-6713.

[17] Y. Yin, J. Fang, T. Watari, K. Tanaka, H. Kita, K.-i. Okamoto, *J. Mater. Chem.* **2004**, *14*, 1062-1070.

[18] A. Wu, T. Akagi, M. Jikei, M.-a. Kakimoto, Y. Imai, S. Ukishima, Y. Takahashi, *Thin Solid Films* **1996**, *273*, 214-217.

[19] E. I. Mal'tsev, M. A. Brusentseva, V. A. Kolesnikov, V. I. Berendyaev, B. V. Kotov, A. V. Vannikov, *Appl. Phys. Lett.* **1997**, *71*, 3480-3482.

[20] E. I. Mal'tsev, V. I. Berendyaev, M. A. Brusentseva, A. R. Tameev, V. A. Kolesnikov, A. A. Kozlov, B. V. Kotov, A. V. Vannikov, *Polym. Int.* **1997**, *42*, 404-408.

[21] Y. Kim, J.-G. Lee, K. Han, H.-K. Hwang, D.-K. Choi, Y.-Y. Jung, J.-H. Keum, S. Kim, S.-S. Park, W.-B. Im, *Thin Solid Films* **2000**, *363*, 263-267.

[22] S.-H. Hsiao, W. Guo, W.-F. Lee, Y.-C. Kung, Y.-J. Lee, *Mater. Chem. Phys.* **2011**, *130*, 1086-1093.

[23] M. T. Bogert, R. R. Renshaw, *J. Am. Chem. Soc.* **2002**, *30*, 1135-1144.

[24] A. L. Endrey, Canada Patent 645,073 to E. I. du Pont de Nemours, Inc., **1962**.

[25] A. L. Endrey, Canada Patent 659,328 to E. I. du Pont de Nemours, Inc., **1963**.

[26] A. L. Endrey, U.S. Patent 3,179,630 to E. I. du Pont de Nemours, Inc, **1965**.

[27] A. L. Endrey, U.S. Patent 3,179,631 to E. I. du Pont de Nemours, Inc., **1965**.

[28] A. L. Endrey, U.S. Patent 3,179,633 to E. I. du Pont de Nemours, Inc., **1965**.

[29] A. L. Endrey, U.S. Patent 3,179,635 to E. I. du Pont de Nemours, Inc., **1965**.

[30] C. E. Sroog, *Prog. Polym. Sci.* **1991**, *16*, 561-694.

[31] J. J. Jones, F. W. Ochynski, F. A. Rackley, *Chem. Ind.* **1962**, 1686.

[32] G. M. Bower, L. W. Frost, *J. Polym. Sci., Part A: Gen. Pap.* **1963**, *1*, 3135-3150.

[33] C. E. Sroog, A. L. Endrey, S. V. Abramo, C. E. Berr, W. M. Edwards, K. L. Olivier, *J. Polym. Sci., Part A: Gen. Pap.* **1965**, *3*, 1373-1390.

[34] R. A. Dine-Hart, W. W. Wright, *J. Appl. Polym. Sci.* **1967**, *11*, 609-627.

[35] A. L. Endrey, U.S. Patent 3,242,136 to E. I. du Pont de Nemours, Inc, **1966**.

[36] S. V. Vinogradova, Y. S. Vygodskii, V. V. Korshak, *Polym. Sci. (USSR) (Engl. Transl.)* **1970**, *12*, 2254-2262.

[37] Y. Sasaki, U.S. Patent 4,290,936 to Ube Industries, **1981**.

[38] Y. Sasaki, U.S. Patent 4,247,442 to Ube Industries, **1981**.

[39] Y. Sasaki, U.S. Patent 4,473,523 to Ube Industries, **1984**.

[40] T. Kaneda, T. Katsura, K. Nakagawa, H. Makino, M. Horio, *J. Appl. Polym. Sci.* **1986**, *32*, 3151-3176.

[41] H. Itatani, U.S. Patent 4,568,715 to Ube Industries, **1986**.

[42] R. J. Angelo, U.S. Patent 4,104,438 to E. I. du Pont de Nemours, Inc., **1978**.

[43] R. J. Angelo, U.S. Patent 4,180,614 to E. I. du Pont de Nemours, Inc., **1979**.

[44] S. Numata, U.S. Patent 4,759,958 to Hitachi, **1988**.

[45] R. J. Young, D. Lu, R. J. Day, W. F. Knoff, H. A. Davis, *J. Mater. Sci.* **1992**, *27*, 5431-5440.

[46] D. Bloor, D. J. Ando, F. H. Preston, G. C. Stevens, *Chem. Phys. Lett.* **1974**, *24*, 407-411.

[47] B. Baumgartner, M. J. Bojdys, M. M. Unterlass, *Polym. Chem.* **2014**, *5*, 3771-3776.

[48] K. Byrappa and M. Yoshimura, Handbook of Hydrothermal Technology, William Andrew Publishing, Norwich, NY, **2001**.

[49] J. Bohm, R. A. LAUDISE. The Growth of Single Crystals. 352 Seiten, zahlreiche Figuren, Tabellen und Literaturhinweise im Text, Autoren- und Sachverzeichnis. £ 7.25 Englewood Cliffs, New Jersey 1970, Prentice-Hall International, *Kristall und Technik*, **1972**, *7*, K17-K18.

[50] M. M. Unterlass, D. Kopetzki, M. Antonietti, J. Weber, *Polym. Chem.* **2011**, *2*, 1744-1753.

[51] J. H. Hodgkin and T. C. Morton, *Polym. Prepr.*, **2000**, *41*, 208.

[52] J. K. Fink, in High Performance Polymers (Ed.: J. K. Fink), William Andrew Publishing, Norwich, NY, **2008**, pp. 475-519.

[53] A. A. Kuznetsov, *High Perform. Polym.* **2000**, *12*, 445-460.

[54] B. Baumgartner, M. J. Bojdys, P. Skrinjar, M. M. Unterlass, *Macromol. Chem. Phys.* **2016**, *217*, 485-500.

[55] B. Baumgartner, M. Puchberger, M. M. Unterlass, *Polym. Chem.* **2015**, *6*, 5773-5781.

[56] H. Yeganeh, B. Tamami, I. Ghazi, *Eur. Polym. J.* **2004**, *40*, 2059-2064.

[57] J. R. Ebdon, Synthetic polymers. Technology, properties, applications, D. Feldman and A. Barbalata. Chapman & Hall, London, 1996. pp. xv+370, price £49.00. ISBN 0-412-71040-4, *Polymer International*, **1997**, *42*, 127-127.

[58] J.-Q. Pan, W. W. Y. Lau, Z. F. Zhang, X. Z. Hu, *J. Appl. Polym. Sci.* **1996**, *61*, 1405-1412.

[59] G.-S. Liou, S.-H. Hsiao, M. Ishida, M. Kakimoto, Y. Imai, *J. Polym. Sci. A Polym. Chem.* **2002**, *40*, 3815-3822.

[60] Y. Imai, K. Kojima, *Polym. Sci. A Polym. Chem.* **1972**, *10*, 2091-2096.

[61] Y. Oishi, M. Ishida, M.-A. Kakimoto, Y. Imai, T. Kurosaki, *Polym. Sci. A Polym. Chem.* **1992**, *30*, 1027-1035.

[62] T. Kaneda, S. Ishikawa, H. Daimon, T. Katsura, M. Ueda, K. Oda, M. Horio, *Makromol. Chem.* **1982**, *183*, 417-432.

[63] E. M. Boldebuck, J. F. Klebe, U.S. Patent 3,303,157 to General Electric Co **1967**.

[64] S. Di Bella, G. Consiglio, N. Leonardi, S. Failla, P. Finocchiaro, I. Fragalà, *Eur. J. Inorg. Chem.* **2004**, *2004*, 2701-2705.

[65] J. H. Chi, G. J. Shin, Y. S. Kim, J. C. Jung, *J. Appl. Polym. Sci.* **2007**, *106*, 3823-3832.

[66] E. Gubbelmans, T. Verbiest, M. Van Beylen, A. Persoons, C. Samyn, *Polymer* **2002**, *43*, 1581-1585.

[67] C. B. Yoon, H. K. Shim, *J. Mater. Chem.* **1999**, *9*, 2339-2344.

[68] J. Weber, Q. Su, M. Antonietti, A. Thomas, *Macromol. Rapid Commun.* **2007**, *28*, 1871-1876.

[69] O. K. Farha, A. M. Spokoyny, B. G. Hauser, Y.-S. Bae, S. E. Brown, R. Q. Snurr, C. A. Mirkin, J. T. Hupp, *Chem. Mater.* **2009**, *21*, 3033-3035.

[70] B. S. Ghanem, N. B. McKeown, P. M. Budd, J. D. Selbie, D. Fritsch, *Adv. Mater.* **2008**, *20*, 2766-2771.

[71] Q. Fang, J. Wang, S. Gu, R. B. Kaspar, Z. Zhuang, J. Zheng, H. Guo, S. Qiu, Y. Yan, *J. Am. Chem. Soc.* **2015**, *137*, 8352-8355.

[72] A. P. Cote, A. I. Benin, N. W. Ockwig, M. O'Keeffe, A. J. Matzger, O. M. Yaghi, *Science* **2005**, *310*, 1166-1170.

[73] H. M. El-Kaderi, J. R. Hunt, J. L. Mendoza-Cortes, A. P. Cote, R. E. Taylor, M. O'Keeffe, O. M. Yaghi, *Science* **2007**, *316*, 268-272.

[74] R. Dawson, A. I. Cooper, D. J. Adams, *Prog. Polym. Sci.* **2012**, *37*, 530-563.

[75] C. Zhang, S. Zhang, Y. Yan, F. Xia, A. Huang, Y. Xian, *ACS Appl. Mater. Interfaces* **2017**, *9*, 13415-13421.

[76] X. Zhu, S. An, Y. Liu, J. Hu, H. Liu, C. Tian, S. Dai, X. Yang, H. Wang, C. W. Abney, S. Dai, *AIChE J.* **2017**, *63*, 3470-3478.

[77] J. Lv, Y. X. Tan, J. Xie, R. Yang, M. Yu, S. Sun, M. D. Li, D. Yuan, Y. Wang, *Angew. Chem. Int. Ed. Engl.* **2018**, *57*, 12716-12720.

[78] H. Duan, K. Li, M. Xie, J. M. Chen, H. G. Zhou, X. Wu, G. H. Ning, A. I. Cooper, D. Li, *J. Am. Chem. Soc.* **2021**, *143*, 19446-19453.

[79] R. Pan, J. Wu, W. Wang, C. Cheng, X. Liu, *Colloids Surf. A: Physicochem. Eng. Asp.* **2021**, *621*, 126511.

[80] R. van der Jagt, A. Vasileiadis, H. Veldhuizen, P. Shao, X. Feng, S. Ganapathy, N. C. Habisreutinger, M. A. van der Veen, C. Wang, M. Wagemaker, S. van der Zwaag, A. Nagai, *Chem. Mater.* **2021**, *33*, 818-833.

[81] X. Liang, Z. Ni, L. Zhao, B. Ge, H. Zhao, W. Li, *Microchem. J.* **2021**, *170*, 106663.

[82] L. Jiang, Y. Tian, T. Sun, Y. Zhu, H. Ren, X. Zou, Y. Ma, K. R. Meihaus, J. R. Long, G. Zhu, *J. Am. Chem. Soc.* **2018**, *140*, 15724-15730.

[83] M. Yu, N. Chandrasekhar, R. K. M. Raghupathy, K. H. Ly, H. Zhang, E. Dmitrieva, C. Liang, X. Lu, T. D. Kuhne, H. Mirhosseini, I. M. Weidinger, X. Feng, *J. Am. Chem. Soc.* **2020**, *142*, 19570-19578.

[84] L. Jiang, P. Wang, M. Li, P. Zhang, J. Li, J. Liu, Y. Ma, H. Ren, G. Zhu, *Chem. Eur. J.* **2019**, *25*, 9045-9051.

[85] H. Veldhuizen, A. Vasileiadis, M. Wagemaker, T. Mahon, D. P. Mainali, L. Zong, S. Zwaag, A. Nagai, *J. Polym. Sci. Part A: Polym. Chem.* **2019**, *57*, 2373-2377.

[86] B. Han, Y. Jin, B. Chen, W. Zhou, B. Yu, C. Wei, H. Wang, K. Wang, Y. Chen, B. Chen, J. Jiang, *Angew. Chem. Int. Ed. Engl.* **2022**, *61*, e202114244.

[87] T. Wang, R. Xue, H. Chen, P. Shi, X. Lei, Y. Wei, H. Guo, W. Yang, *New J. Chem.* **2017**, *41*, 14272-14278.

[88] K. Liu, H. Qi, R. Dong, R. Shivhare, M. Addicoat, T. Zhang, H. Sahabudeen, T. Heine, S. Mannsfeld, U. Kaiser, Z. Zheng, X. Feng, *Nat. Chem.* **2019**, *11*, 994-1000.

[89] T. Kim, S. H. Joo, J. Gong, S. Choi, J. H. Min, Y. Kim, G. Lee, E. Lee, S. Park, S. K. Kwak, H. S. Lee, B. S. Kim, *Angew. Chem. Int. Ed. Engl.* **2022**, *61*, e202113780.

[90] L. Zhao, H. Liu, Y. Du, X. Liang, W. Wang, H. Zhao, W. Li, *New J. Chem.* **2020**, *44*, 15410-15414.

[91] Y. Zhai, G. Liu, F. Jin, Y. Zhang, X. Gong, Z. Miao, J. Li, M. Zhang, Y. Cui, L. Zhang, Y. Liu, H. Zhang, Y. Zhao, Y. Zeng, *Angew. Chem. Int. Ed. Engl.* **2019**, *58*, 17679-17683.

[92] J. Maschita, T. Banerjee, B. V. Lotsch, *Chem. Mater.* **2022**, *34*, 2249-2258.

[93] J. Maschita, T. Banerjee, G. Savasci, F. Haase, C. Ochsenfeld, B. V. Lotsch, *Angew. Chem. Int. Ed. Engl.* **2020**, *59*, 15750-15758.

[94] F. Haase, B. V. Lotsch, *Chem. Soc. Rev.* **2020**, *49*, 8469-8500.

[95] D. Stewart, D. Antypov, M. S. Dyer, M. J. Pitcher, A. P. Katsoulidis, P. A. Chater, F. Blanc, M. J. Rosseinsky, *Nat. Commun.* **2017**, *8*, 1102.

[96] P. Kuhn, M. Antonietti, A. Thomas, *Angew. Chem. Int. Ed. Engl.* **2008**, *47*, 3450-3453.

[97] A. M. Evans, M. R. Ryder, W. Ji, M. J. Strauss, A. R. Corcos, E. Vitaku, N. C. Flanders, R. P. Bisbey, W. R. Dichtel, *Faraday Discuss.* **2021**, *225*, 226-240.

[98] G. Y. Lee, J. Lee, H. T. Vo, S. Kim, H. Lee, T. Park, *Sci. Rep.* **2017**, *7*, 557.

[99] M. Kato, R. Ota, T. Endo, T. Yanase, T. Nagahama, T. Shimada, *ACS Appl. Nano Mater.* **2022**, *5*, 2367-2374.

[100] Z. Wang, Y. Li, P. Liu, Q. Qi, F. Zhang, G. Lu, X. Zhao, X. Huang, *Nanoscale* **2019**, *11*, 5330-5335.

[101] G. Zhao, H. Li, Z. Gao, L. Xu, Z. Mei, S. Cai, T. Liu, X. Yang, H. Guo, X. Sun, *Adv. Funct. Mater* **2021**, *31*, 2101019.

[102] S. Royuela, E. Martinez-Perinan, M. P. Arrieta, J. I. Martinez, M. M. Ramos, F. Zamora, E. Lorenzo, J. L. Segura, *Chem. Commun.* **2020**, *56*, 1267-1270.

[103] X. Chen, Q. Dang, R. Sa, L. Li, L. Li, J. Bi, Z. Zhang, J. Long, Y. Yu, Z. Zou, *Chem. Sci.* **2020**, *11*, 6915-6922.

[104] Y. Zeng, R. Zou, Y. Zhao, *Adv. Mater.* **2016**, *28*, 2855-2873.

# 3 *Research Objective*

COFs have experienced tremendous research interest over the past two decades, leading to the development of materials with many different linkage types. One of these developments was the harnessing of the imide condensation reaction for the synthesis of crystalline COFs. Imide-linked COFs are characterized by many advantageous properties, such as high thermal and chemical stability and redox-active backbones, making them promising candidates for a variety of applications, including gas storage/separation, catalysis, and energy storage. However, the stability and low reversibility of the imide linkage makes the synthesis of PI-COFs exceptionally challenging, and synthesis strategies to obtain well oriented and high surface area COFs are scarce. The lack of synthesis strategies hinders the rapid and functionally diverse growth of the research field and is reflected in the small number of published PI-COFs (Figure 2-7). In fact, only one synthesis strategy for the preparation of PI-COFs is considered to be "universally applicable" – the solvothermal method, which requires the use of high reaction temperatures, expensive toxic solvents, and hazardous catalysts. The high energy consumption and the high cost and toxicity of the required reaction media are the main disadvantages of this method and may hinder the economic production of imide-linked COFs on a large scale. With the tightening of government regulations and the increasing environmental and health awareness of the public, the need for less harmful synthetic methods is also increasing. Therefore, the development of additional, complementary, and environmentally friendly synthetic methods for the production of crystalline PI-COFs is crucial for further growth in this field.

The aim of this dissertation is to develop alternative, environmentally friendly synthesis strategies for the preparation of well-defined PI-COFs with large surface areas. By expanding the synthetic toolbox for the preparation of COFs with an ionothermal and an alcohol-assisted hydrothermal approach, universally applicable synthesis protocols for the preparation of PI-COFs will be introduced, enabling the synthesis of novel COFs that could not be prepared in known ways. At the same time, the use of toxic substances is reduced and the reaction time is shortened, thus taking the environment into account.

As demonstrated in numerous publications, COFs provide a suitable platform for adsorption, separation and release of small guest molecules such as $H_2$, $CO_2$ or $CH_4$. Despite the extensive research in this field, adsorption of reactive and hazardous substances such as ammonia or $SO_2$ is rarely reported, possibly due to remaining concerns regarding their stability. Therefore, an exploration of the applicability of COFs for adsorption, separation and release of highly reactive gases such as NO is largely lacking, although they are potential materials for effective exhaust gas cleaning or drug delivery.

Taking advantage of the high chemical stability of some COF linkages such as imide or thiazole, this work further investigates the adsorption behavior of highly reactive NO gas on COFs with different linkages including imide, imine, amine and thiazole. The suitability of these different COF linkages for NO-related applications is evaluated by investigating the integrity of the frameworks, gas adsorption capacities and IAST selectivities of NO adsorption. Furthermore, the results will be combined with a $^{15}$N CP MAS ssNMR in-depth study to decipher the various physical and chemical interactions of NO with the materials.

# 4 *Ionothermal Synthesis of Imide-Linked Covalent Organic Frameworks*

The work in this chapter was published, reproduced and adapted from:

*Ionothermal Synthesis of Imide-Linked Covalent Organic Frameworks*

Johannes Maschita, Tanmay Banerjee, Gökcen Savasci, Frederik Haase, Christian Ochsenfeld, and Bettina V. Lotsch

*Angew. Chem. Int. Ed. Engl.* **2020**, *59*, 15750-15758. DOI: 10.1002/anie.202007372

Johannes Maschita, Tanmay Banerjee and Frederik Haase conceived the project. Johannes Maschita, Tanmay Banerjee and Bettina V. Lotsch wrote the manuscript with input from all other authors. Johannes Maschita synthesized the materials and performed the structural analysis and evaluated the data. Tanmay Banerjee performed the photoluminescence measurements. Gökcen Savasci performed the quantum-chemical calculations with supervision of Christian Ochsenfeld. All authors assisted the analysis of their respective experiments and the overall discussion. Bettina V. Lotsch supervised the work.

Supporting information can be found in Section 8.2.

## *Abstract*

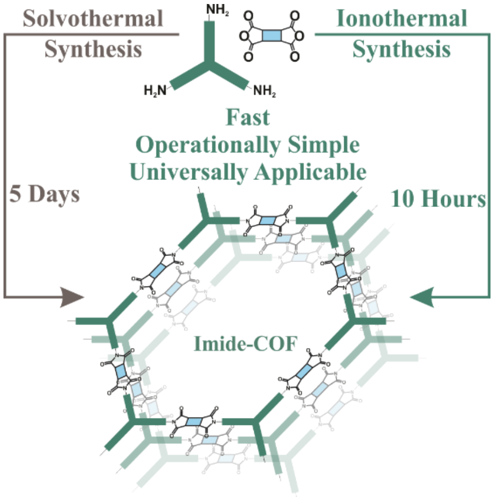

**Figure 4-1.** Table of contents figure for ionothermal synthesis of imide-linked covalent organic frameworks.

Covalent organic frameworks (COFs) are an extensively studied class of porous materials, which distinguish themselves from other porous polymers in their crystallinity and high degree of modularity, enabling a wide range of applications. COFs are most commonly synthesized solvothermally, which is often a time consuming process and restricted to well soluble precursor molecules. Synthesis of polyimide-linked COFs (PI-COFs) is further complicated by the poor reversibility of the ring closing reaction under solvothermal conditions. Herein, we report the ionothermal synthesis of crystalline and porous PI-COFs in zinc chloride and eutectic salt mixtures. This synthesis does not require soluble precursors and the reaction time is significantly reduced as compared to standard solvothermal synthesis methods. In addition to applying the synthesis to previously reported imide COFs, a new perylene based COF was also synthesized, which could not be obtained

by using the classical solvothermal route. *In situ* high temperature XRPD analysis hints to the formation of precursor-salt adducts as crystalline intermediates, which then react with each other to form the COF.

## 4.1 Introduction

Covalent organic frameworks (COFs) are crystalline, porous organic materials composed of light, earth-abundant elements that are constructed from molecular building blocks. 2D-COFs form extended planar networks via in-plane covalent bonding and are further stacked in the third dimension by virtue of out-of-plane $\pi$-$\pi$ interactions and van-der-Waals forces.[1] Owing to their modularity and tunability, over the past years, COFs have found applications in various fields including gas separation and storage,[2-3] catalysis,[4-5] and optoelectronics.[6-7] COFs are synthesized following the principles of dynamic covalent chemistry, according to which the COF formation reaction has to be reversible to enable crystal defect correction under thermodynamic control.[1, 8] Bond breaking is thus as crucial as bond formation: Stability is achieved at the expense of crystallinity, which frequently leads to poorly crystalline products, rendering COF synthesis of stable and crystalline COFs challenging. COFs are synthesized in a variety of ways, including solvothermal synthesis,[1] microwave-assisted synthesis,[9] mechanochemical synthesis,[10] vapor-assisted conversion[11] *etc*. Nevertheless, solvothermal synthesis is the most prominent and frequently used method in COF synthetic chemistry. Although countless COFs have been synthesized using this approach, this method typically requires long reaction times ranging from 3-7 days and also requires precursor molecules with an appreciable solubility. In particular, the complexity of the crystallization and aggregation processes strongly affects the crystallinity and porosity of COF systems.[12] In order to obtain satisfactory products, unique synthesis conditions are often required, resulting in re-optimization of reaction conditions with each new COF. This leads to time-consuming and empirical rather than rational solvent screening. The challenge associated with the synthesis of highly crystalline, porous materials has partially motivated the quest for new COF linkages such as ester borosilicate,[13] imine,[14] hydrazone,[15] or borazine.[16] However, in order to improve the stability and crystallinity of the products, further optimization of the thermodynamics and kinetics of the condensation processes by exploring new synthesis routes and linkage chemistry is quintessential. In this regard the imide-linkage introduced by Yan and co-workers is of particular interest.[17] The imide formation reaction is used to produce commercially relevant one-dimensional imide polymers – especially aromatic polyimides – which are high-performance polymers known for their good chemical resistance, high thermal stability, and extraordinary mechanical properties.[18] Adorned with many of these properties, polyimide-linked COFs (PI-COFs) have been used for sensing,[19] decontamination,[20] and energy storage applications.[21-22] In polyimide condensation reactions, however, the formation of the cyclic imide is essentially irreversible under solvothermal conditions, which makes the formation of the thermodynamic and crystalline product challenging.[23] To overcome this obstacle, the classical synthesis of polyimides involves harsh conditions, namely, usage of high-boiling and toxic solvents, toxic catalysts, high processing temperatures, and long reactions times of up to seven days.[17, 19-21, 24]

Research on carbon nitrides has demonstrated the pertinence of ionothermal synthesis approaches using salt melts both as high-temperature solvent and structure directing agent. While the 1D polymer melon is obtained by classical solid state reactions, eutectic mixtures of alkali metal chlorides furnish the 2D polymers poly(triazine imide), PTI, or poly(heptazine imide), PHI.[25-28] Likewise, covalent triazine frameworks (CTFs) have been synthesized from $ZnCl_2$ salt melts, which act as reactive high temperature solvent and catalyst.[2] Following these observations, we present an ionothermal synthesis of porous, crystalline imide-linked COFs using an inorganic salt, namely $ZnCl_2$, as reaction medium. This new method allows us to avoid the usage of environmentally harmful solvents and catalysts in large quantities and to reduce the reaction time significantly compared to the conventional solvothermal methods. As compared to CTFs, the low temperature ionothermal synthesis further prevents the formation of carbonaceous products, while still leading to complete COF formation. We then optimized our reaction protocol to further increase the substrate scope and report the synthesis of porous, crystalline imide-linked COFs in eutectic salt mixtures for the first time.

## *4.2 Results and Discussion*

In the first step of this study, two PI-COFs, namely TAPB-PMDA- and TAPB-PTCDA-COF, were synthesized using the trigonal linker molecule 2,4,6-tris(4-aminophenyl)-benzene (TAPB) and the two linear linker molecules pyromellitic dianhydride (PMDA) and perylene-3,4,9,10-tetracarboxylic dianhydride (PTCDA), respectively (Figure 4-2). While TAPB-PMDA-COF has been reported before,[17] this is the first report of the synthesis of the TAPB-PTCDA-COF, which is not accessible using previously reported reaction conditions.

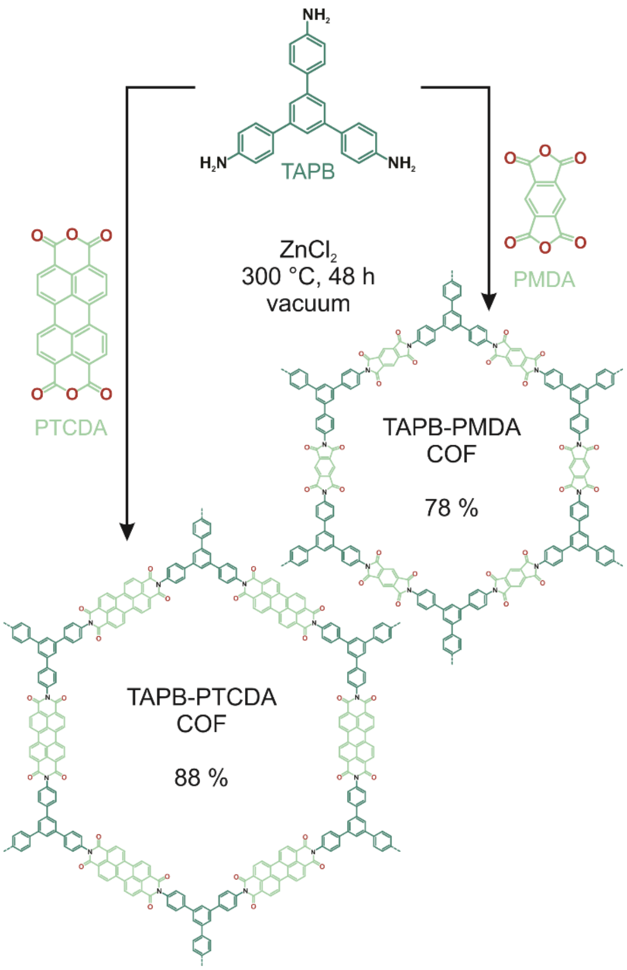

**Figure 4-2.** Synthesis of TAPB-PTCDA- and TAPB-PMDA-COF in $ZnCl_2$ under ionothermal conditions.

In a typical reaction procedure, the precursor molecules - the linear dianhydride and the trigonal amine - were mixed together with anhydrous $ZnCl_2$ and heated to 300 °C in a flame sealed glass tube under vacuum for 48 h to give crystalline solids at yields of 88 % for TAPB-PTCDA-COF, and 78 % for TAPB-PMDA-COF (Figure 4-2). The imide formation reaction was confirmed by Fourier transform infrared spectroscopy (FT-IR) as depicted in Figure 4-3a and c. The spectra show signals at 1696 and 1662 $cm^{-1}$ for TAPB-PTCDA-COF, and at 1776 and 1721 $cm^{-1}$ for TAPB-PMDA-COF, corresponding to the asymmetric and symmetric C=O stretching vibrations of the six- and five- membered imide rings, respectively. Additional signals at 1344 and 1371 $cm^{-1}$ are observed, corresponding to the C-N-C stretching vibration of the imide rings. Together with the absence of anhydride C=O stretching and amine N-H stretching vibrations corresponding to the respective starting materials (see Figures S8-1 and S8-2), this proves the successful and complete reaction between TAPB and PTCDA/PMDA to form the respective COFs. The formation of the imide ring was further confirmed by solid-state $^{13}C$ cross-polarization magic-angle-spinning nuclear magnetic resonance (CP-MAS ssNMR) spectroscopy with the spectra showing the carbonyl carbon of the imide ring at 162.5 ppm for TAPB-PTCDA-COF, and at 163.3 ppm for TAPB-PMDA-COF (Figure 4-3b, d).[17] Quantum-chemical calculations of the expected NMR shifts (Figure 4-3b, d and S8-3 to S8-8) further support this assignment. X-ray powder diffraction (XRPD) shows that both TAPB-PTCDA-COF and TAPB-PMDA-COF are crystalline. The XRPD pattern of TAPB-PTCDA-COF (Figure 4-3e and S8-9) shows reflections at 2.14, 4.44, 5.92, and 8.09 ° $2\theta$ corresponding to the 100, 200, 210, and 220/310 Bragg peaks of a trigonal lattice with $P\bar{3}1m$ symmetry. Structure simulation and geometry optimization was carried out by applying the universal force field method with the Materials Studio software package.[29] Using this simulated model, the experimental powder pattern was then Rietveld refined yielding the unit cell parameters of $a = b = 43.6(2)$ Å and $c = 3.71$ Å with α = β = 90 ° and γ = 120 ° ($R_{wp} = 3.92$).

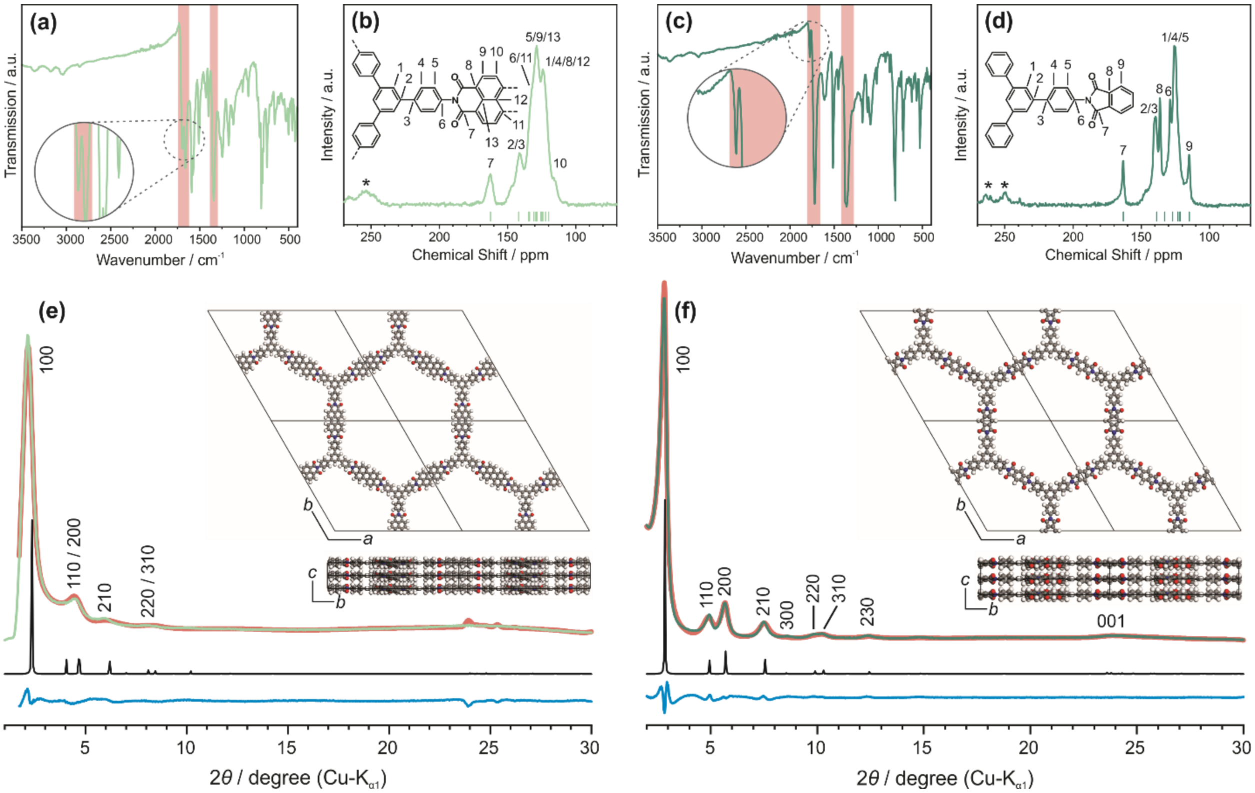

**Figure 4-3.** Characterization of TAPB-PTCDA-COF (light green) and TAPB-PMDA-COF (dark green): (a) and (c) IR-spectra showing the imide vibrational bands indicating quantitative imide formation. (b) and (d) $^{13}C$ ssNMR showing the chemical shifts of the imide ring carbons between 162 and 164 ppm. Spinning side bands are marked with asterisks. NMR chemical shifts for the TAPB-PTCDA and TAPB-PMDA-COF were calculated on B97-2/pcsSeg-2 level of theory[30-33] using the FermiONs++[32-33] software package and are shown as green dashes. (e) and (f) Experimental XRPD pattern of the respective COF (green) together with the Rietveld fit (red), simulated patterns based on space group $P\bar{3}1m$ (black) and difference curve (blue). Inset: Simulated structures of the respective COF along the *a* and *c* axis.

The XRPD pattern of TAPB-PMDA-COF shows reflections at 2.77, 4.90, 5.64, 7.48, 8.55, 9.88, 10.20, 12.35, and 23.92 ° $2\theta$ corresponding to the 100, 110, 200, 210, 300, 220, 310, 230, and 001 Bragg peaks, again indexed in a trigonal lattice with $P\bar{3}1m$ symmetry (Figure 4-3f and S8-10). Rietveld refinement yielded the unit cell parameters $a = b = 35.7(4)$ Å and $c = 3.76(5)$ Å with α = β = 90 ° and γ = 120 ° ($R_{wp} = 4.98$). We also calculated models with AB stacked $P\bar{3}1c$ symmetry, but we found that the eclipsed model fits the experimental data for both COFs best (Figure S8-9 and S8-10). Following a previous report[17] we also took a model with *Cmcm* symmetry into account, which matches the experimental data as well. However, DFT calculations indicate a non-planar geometry of the COF layers with the benzene units and the anhydride building blocks twisted against each other, leading to a structure with the higher $P\bar{3}1m$ symmetry (Figures S8-3 to S8-8). In the DFT calculations atom positions and lattices of all periodic structures were optimized on the RI-PBE-D3/def2-TZVP[34-37] level of theory using an acceleration scheme based on the resolution of the identity (RI) technique and the continuous fast multipole method (CFMM[38-40]) implemented[41-42] in Turbomole[43] version V7.3.

Argon sorption measurements at 87 K (Figures S8-12) were performed to determine the porosity of the samples. Both TAPB-PTCDA-COF and TAPB-PMDA-COF show type-IV behavior and sharp gas uptakes below 0.4 $p/p_0$. Pore size distributions (PSD) were calculated using the quenched solid-state functional theory (QSDFT) method, which reveals pores of 31 Å width for TAPB-PTCDA-COF, and 29 Å for TAPB-PMDA-COF. For TAPB-PMDA-COF these results are in good agreement with the pore size extracted from transmission electron microscopy (TEM) (30 Å) (Figure S8-13) and with the calculated pore size of 31 Å. For TAPB-PTCDA-COF, the pore size obtained by PSD calculations does not match the pore sizes extracted from TEM (36 Å) (Figure S8-14) and theoretical calculations (37 Å) equally well. The Brunauer-Emmett-Teller (BET) model revealed surface areas of 460 $m^2g^{-1}$ for TAPB-PTCDA-COF and 1250 $m^2g^{-1}$ for TAPB-PMDA-COF. The relatively small surface area of TAPB-PTCDA-COF together with the unexpectedly small pore size obtained from sorption measurements is an indication of possible pore blocking through insoluble precursor molecules (e.g. PTCDA) or oligomers; it may also indicate random AA' slip stacking contributions which effectively decrease the measured pore size. For TAPB-PMDA-COF, the BET surface area is similar the previously reported surface area of 1297 $m^2g^{-1}$ that employs the classical solvothermal synthesis.[17] To understand the parameters of the ionothermal synthesis protocol that influence the crystallinity, the relative amount of $ZnCl_2$, the reaction time and temperature on the PI-COF synthesis method were investigated by testing different reaction conditions using TAPB-PMDA-COF. This COF was chosen for our studies because of its higher crystallinity and porosity compared to TAPB-PTCDA-COF. The quality of the products obtained were compared based on XRPD and FT-IR spectroscopy. While varying the equivalents of $ZnCl_2$, the reaction temperature was kept constant at 300 °C and the reaction was carried out for 48 h. With progressive increase in the equivalents of $ZnCl_2$ with respect to PMDA, the crystallinity of the final product was observed to increase up to 12.5 equivalent amounts. Using more $ZnCl_2$ did not increase the crystallinity further (Figure 4-4a). As $ZnCl_2$ starts to melt slightly above 300 °C (Figure S8-15), at the reaction temperature of 300 °C, we did not observe the formation of a melt (Figures S8-15 and S8-16). Thus, the increase in crystallinity is likely a blend of several factors, including thorough mixing of the reactants and increased exposure of the precursors to reactive zinc and chloride ions, which become increasingly mobile close to the melting point. This complete exposure is possibly reached at 12.5 equiv. $ZnCl_2$ and further increase shows no effect. However, the fact that no melting is observed in our case stands in contrast to CTF syntheses where the nitrile precursor molecules get dissolved in the $ZnCl_2$ melt, forming a clear solution.[2] Also, ionothermal synthesis enables highly crystalline COF formation from reactants sparingly soluble in typical organic solvents, such as PTCDA.

It is also interesting to note that even when no $ZnCl_2$ is used, the IR spectrum of the final product shows the typical imide vibrations (asymmetric and symmetric C=O stretching vibration at 1776 and 1721 cm$^{-1}$, and C-N-C stretching vibration at 1371 cm$^{-1}$) (Figure 4-4d). However, no crystalline product is formed in the absence of the salt. The fact that the imide condensation reaction takes place even when no $ZnCl_2$ is used highlights the important role of $ZnCl_2$ in imparting reversibility to the imide formation reaction, and thereby crystallinity to the final product.

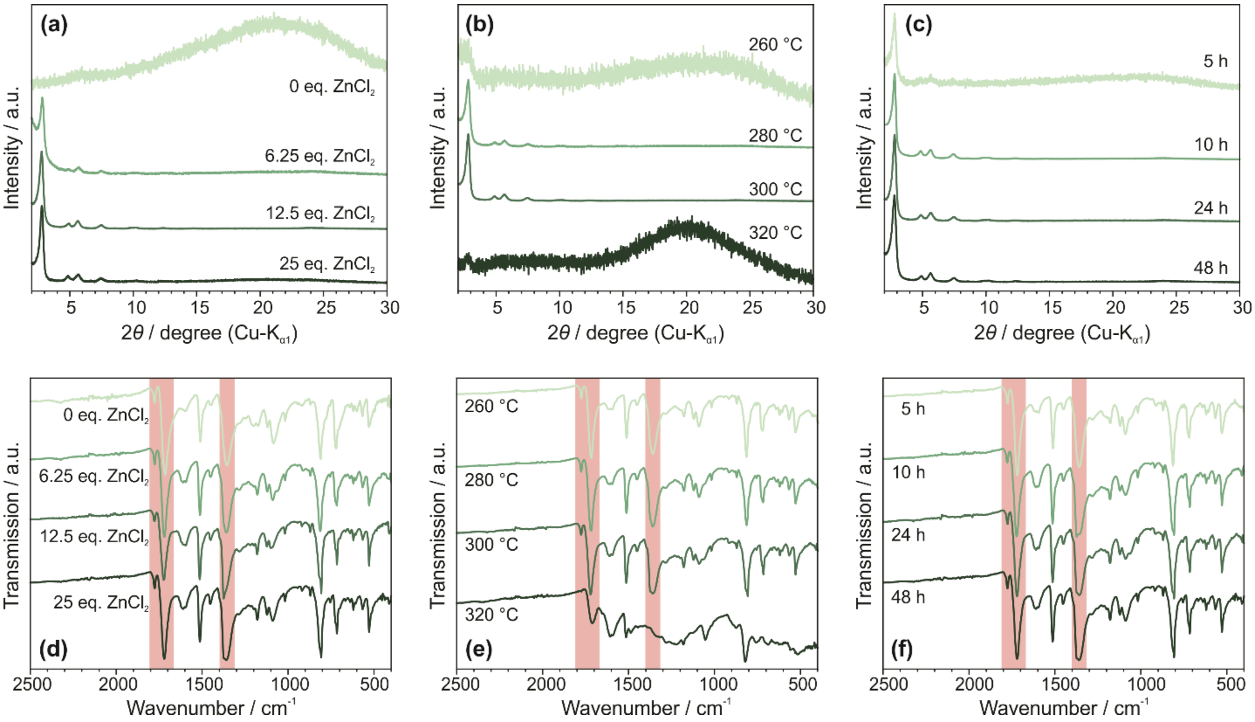

**Figure 4-4.** XRPD patterns (a-c) and IR spectra (d-f) of *ex-situ* reaction condition optimization experiments with TAPB-PMDA-COF. (a) and (d) show the XRPD patterns and IR spectra of experiments in which the $ZnCl_2$ ratio was varied between 0 and 25 equivalents with respect to PMDA. The reaction time and temperature were kept constant at 48 h and 300 °C, respectively. (b) and (e) show the XRPD patterns and IR spectra of experiments in which the reaction temperature was varied between 260 and 320 °C, with constant $ZnCl_2$ to precursor ratio (12.5 equiv.) and reaction time (48 h). (c) and (f) show the XRPD pattern and the IR spectra of experiments in which the reaction time was varied between 5 and 48 h with constant $ZnCl_2$ concentration (12.5 equiv.) and reaction temperature (300 °C).

As mentioned previously, the commonly used method for synthesizing PI-COFs is solvothermal synthesis using high boiling solvents such as mesitylene, N-methyl-2-pyrrolidone (NMP), or dimethylformamide (DMF) at temperatures between 160 and 250 °C for three to seven days. To impart reversibility to the formation of the very stable imide ring, a base (usually isoquinoline) is added as a catalyst.[17, 20-21, 24, 44] On the other hand, with our newly developed synthesis route, only $ZnCl_2$ is needed for the PI-COF synthesis, completely circumventing the need for any additional solvent or catalysts.

The reaction temperature was then varied (48 h, 12.5 equiv. $ZnCl_2$) and crystalline product was found to form only between 280 and 300 °C (Figure 4-4b). The fact that no crystalline product formed below 280 °C shows that not only the presence of $ZnCl_2$ is necessary but an increased ion mobility of the zinc and chloride ions induced by the elevated temperature is required. At temperatures above 300 °C, the system begins to lose its short- and long-range ordering, possibly owing to the harsh (*i.e.* high temperature and Lewis acidic) conditions induced by the complete melting of $ZnCl_2$. This decomposition of the polymer is indicated by the analysis of the IR spectrum wherein a significant broadening of the vibrational bands is observed when the reaction is carried out at 320 °C, *vs*. the reaction carried out at 300 °C (Figure 4-4e). Nevertheless, the possibility of achieving higher reaction temperatures compared to solvothermal synthesis is beneficial in terms of overcoming the activation energy of the imide ring closing/opening reaction, resulting in a significantly decreased reaction time. It is also important to note that, in contrast to the ionothermal synthesis of CTFs where a high reaction temperature (≈400 °C) leads to partial carbonization[45-46] and a lower reaction temperature leads predominantly to oligomers[47], the lower reaction temperatures in the ionothermal synthesis of imide-linked COFs reported herein leads to porous and highly crystalline PI-COFs.

Keeping the [$ZnCl_2$] to [precursor] ratio fixed at 12.5 and the reaction temperature constant at 300 °C, the reaction time was varied. Crystalline product was detected already after five hours of reaction and beyond ten hours, the crystallinity remained nearly unchanged (Figure 4-4c, f). This shows a significant advantage of this new method over previously reported solvothermal methods, where three to seven days are usually required to form crystalline products.[17, 19-21, 24] The faster ionothermal reaction can be rationalized on the basis of a two-fold effect of $ZnCl_2$: First, due to the Lewis acidic properties, $ZnCl_2$ activates the carbonyl functions of the anhydride and the imide, rendering them more reactive. Second, access to higher reaction temperature facilitates the overcoming of the activation barrier for the condensation reaction in both directions, leading to higher reversibility.

To get further insights into the COF formation process and to clarify the role of $ZnCl_2$ in this method, *in situ* high temperature XRPD (HT-XRPD) measurements of TAPB-PMDA-COF were carried out in a quartz capillary. In this HT-XRPD measurement, the temperature was raised from room temperature to 300 °C and cooled down again with a dwelling period of 10 h at 300 °C (Figure 4-5a, see Figure S8-17 for full data). Significant changes in the XRPD pattern of the reaction mixture were observed with increasing temperature. The reflections corresponding to the resulting COF are not visible, likely due to its lower scattering contrast and poorer crystallinity as compared to the other (inorganic) species present, and due to significant pore blocking during the reaction, further reducing the scattering

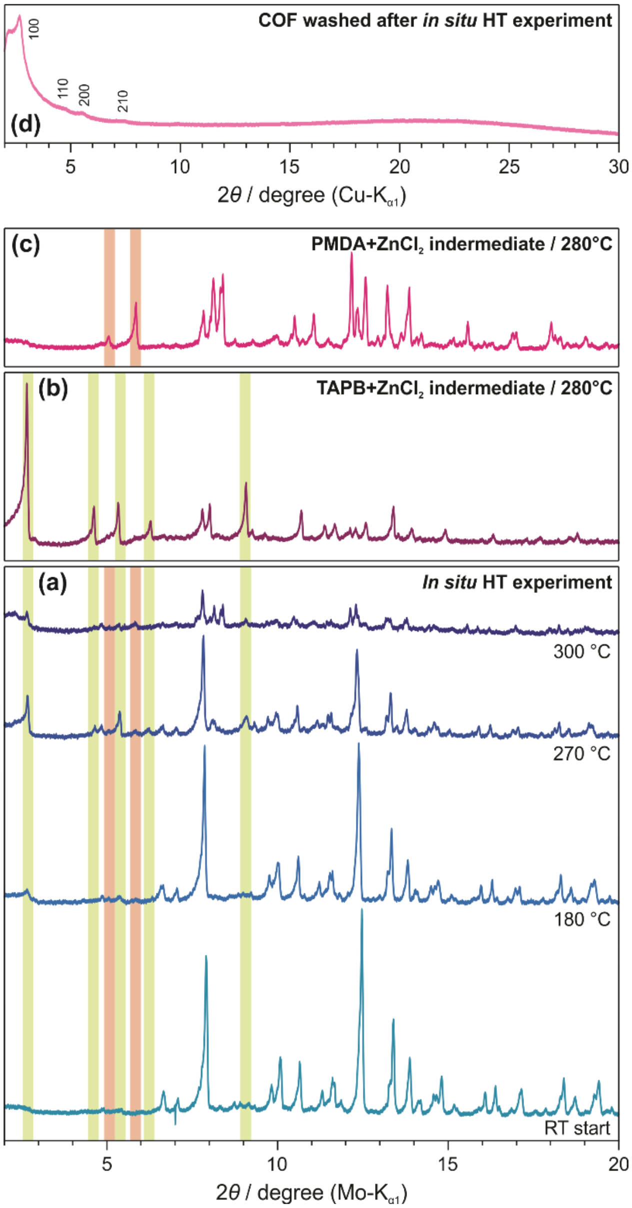

**Figure 4-5.** *In situ* HT-XRPD (Mo-K$_{\alpha1}$) experiments (a) of the TAPB-PMDA-COF reaction mixture, (b) of a mixture of TAPB and ZnCl$_2$ and (c) of a mixture of PMDA and ZnCl$_2$. (d) The XRPD pattern (Cu-K$_{\alpha1}$) of the resulting TAPB-PMDA-COF from (a). Reflections corresponding to the TAPB-ZnCl$_2$ adduct are marked green while the ones corresponding to the PMDA-ZnCl$_2$ adduct are marked orange.

contrast. However, after isolating and washing the COF, the corresponding reflections can be observed (Figure 4-5d). To be able to identify the appearing side phases, all precursor molecules (TAPB, PMDA and ZnCl$_2$) and all possible combinations of the precursors were also investigated via HT-XRPD (Figures S8-18 to S8-23). In the HT-XRPD experiment of the COF formation, the reflections corresponding to ZnCl$_2$ dominate the pattern at room temperature and the low intensity reflections of the precursor molecules are not visible. With increasing temperature, a phase transition of ZnCl$_2$ is observed - above 240 °C, the monoclinic γ-form undergoes phase transition to the orthorhombic δ-form. Additional reflections at 2.67, 4.63, 5.05, 5.38, 5.86, 6.34, and 9.13 ° $2\theta$ were observed in the HT-XRPD patterns at 180 °C and higher (see pattern at 270 °C). The intensities of these appearing reflections decrease significantly at the final reaction temperature of 300 °C (Figure 4-5a), indicating that these transient reflections correspond to reaction intermediates, which then react to form the COF. Crystallite sizes and the relative proportions of the crystalline phases calculated using Scherrer analysis support the formation of reaction intermediates (Figure S8-24). A successive increase of the crystallite size and relative amounts of the intermediate phases with a maximum at the optimized reaction temperature between 280 and 300 °C can be observed. This was further confirmed by recording the HT-XRPD pattern of individual mixtures of PMDA and TAPB with $ZnCl_2$. For the mixture of PMDA and $ZnCl_2$ at 280 °C, the formation of a new species was evident with reflections at 5.05 and 5.86 ° $2\theta$, observed neither in the diffraction pattern of pure PMDA nor in the pattern of pure $ZnCl_2$ (Figures 4-5c and S8-22). These reflections however correspond exactly to two of the additional reflections from the HT-XRPD pattern of the COF reaction mixture at 180 °C and higher, suggesting the species to be a reaction intermediate (Figure 4-5a, c – marked orange) in the imide-linked COF formation reaction. FT-IR spectroscopy of the intermediate revealed significant changes of the C-O related vibrational bands when compared to the precursor molecule, hinting towards the possible formation of a PMDA-$ZnCl_2$-adduct (Figure S8-25). Again, for the mixture of TAPB and $ZnCl_2$ at 280 °C, the formation of a highly crystalline species is evident with reflections at 2.67, 4.63, 5.38, 6.34, and 9.13 ° $2\theta$ (Figures 4-5b and S8-23). These reflections correspond to the reflections from the HT-XRPD pattern at 270 °C of the COF reaction mixture as well, again suggesting this species to be a reaction intermediate (Figure 4-5a, b – marked green) in the COF formation reaction. FT-IR spectroscopy of this intermediate shows a significant shift of all amine group related vibrational bands when compared to the precursor molecule, also hinting towards the formation of an adduct consisting of TAPB and $ZnCl_2$ (Figure S8-26). It is important to note that the formation of these reaction intermediates occurs at temperatures lower than the melting points of the individual precursor molecules and $ZnCl_2$ (Figures S8-18 to S8-20). In order to confirm whether the aforementioned adducts generated from mixtures of TAPB/$ZnCl_2$ and PMDA/$ZnCl_2$ are true intermediates of the COF formation reaction or correspond to side-reactions, we synthesized the COF in two steps. In the first step, the two air sensitive intermediate species from TAPB and PMDA were synthesized separately with a slight excess of $ZnCl_2$ to ensure their complete formation. In the second step, these intermediates were combined and heated at 290 °C for 20 h, *i.e.* under standard imide-COF synthesis conditions, resulting in the formation of the crystalline TAPB-PMDA-COF (Figure S8-27). As crystalline COFs form already at 280 °C (Figure 4-4b, e) and as the intermediates are stable in this temperature regime (Figure 4-5b, c), it is thus evident that the formed adducts from reactions of the individual precursors with $ZnCl_2$ are indeed true intermediates of the ionothermal COF reaction. It must also be noted that reaction of a single precursor-$ZnCl_2$ adduct with the other precursor also leads to COF formation. While this might suggest that one intermediate is dominant for COF formation, it must also be kept in mind that *in situ* formation of the $ZnCl_2$ adduct of the other precursor is possible via partial $ZnCl_2$ exchange. Quantum-chemical calculations were carried out in order to gain insights into the underlying possible mechanism (Figures S8-28 to S8-31). Calculations on phthalic anhydride and aniline as model compounds indicate that adduct formation of the precursors with $ZnCl_2$ is exothermic in each case (Reaction 1, 2, Figure S8-28). The subsequent imide formation is again exothermic irrespective of whether the precursors react as $ZnCl_2$ adducts or not (Reaction 3-6, Figure S8-28), indicating that all investigated reaction pathways are possibly operative. The comparison of calculated partial charges[48] (Figure S8-32) between the anhydride and the anhydride adduct visualizes the polarization by $ZnCl_2$. This activation of the carbonyl group then likely reduces the activation barrier during imide formation, also affecting the back reaction, hence increasing reversibility.

Apart from providing a reactive flux, the exact role of $ZnCl_2$ is not clear at this point. By lowering the structural degrees of freedom with the formation of adducts, it can possibly aid formation of not only ordered intermediates, but also the formation of pre-organized COF pores for further nucleation and thereby facilitate formation of larger crystalline domains when compared to solvothermal synthesis (Figure S8-33, Tables S8-5 to S8-8). In that regard, it is important to note that formation of a $ZnCl_2$ adduct of the product imide is thermodynamically favored as well (Reaction 7, 8, Figure S8-28). Thus, COF formation by heating the amorphous product, obtained by reacting the precursors only (Figure S8-34), in $ZnCl_2$ is possibly hindered only by a lack of accessibility of $ZnCl_2$ in the polymeric structure. Further investigations into understanding the structure of the adducts, the exact role of $ZnCl_2$ in forming these ordered structures, and the mechanism of imide-linked COF formation from these adducts is currently underway.

While the elevated reaction temperature of 300 °C is beneficial in terms of imparting reversibility to the reaction, it could be a hindrance towards fragile linkers, which are not stable enough to withstand the strong Lewis acidic conditions at such high reaction temperatures. For example, the previously reported 2,4,6-tris(4-aminophenyl)-triazine (TT) containing TT-PMDA-COF[20] could not be synthesized using this method due to the decomposition of the triazine core at around 300 °C,[2] which results in an ill-defined non-crystalline PI-polymer/oligomer mixture instead of a well-defined crystalline COF (Figures S8-35 to S8-37). In order to avoid decomposition of fragile linker molecules such as TT and 2,4,6-tris(4-aminophenyl)-amine (TAPA) (Figure S8-38) and to make the ionothermal synthesis universally applicable, we tested other salts with melting points below 280 °C, e.g. zinc sulfate heptahydrate (mp: ~100 °C), aluminum chloride (~190 °C), gallium chloride (~78 °C) and an eutectic mixture containing $NaNO_3/NaNO_2/KNO_3$ (142 °C). No COF formation was observed in any of these reaction media, hinting possibly at the importance of $ZnCl_2$ and $ZnCl_2$ –precursor adducts observed previously in the COF formation reaction. In order to test this hypothesis, we used a $ZnCl_2$ containing three-salt eutectic mixture, namely $NaCl/KCl/ZnCl_2$,[49] with a theoretical melting point of 240 °C. In a typical reaction, the three salts (see SI for exact composition) were ground thoroughly and mixed together with the respective starting materials PMDA and TT/TAPA, followed by heating to 250 °C under vacuum (Figure 4-6). Indeed, compared to the experiments with pure $ZnCl_2$, this reduction in the reaction temperature not only prevented decomposition of TT and TAPA, but also TT-PMDA-COF and TAPA-PMDA-COF could be obtained in yields of 64 % and 85 %, respectively.

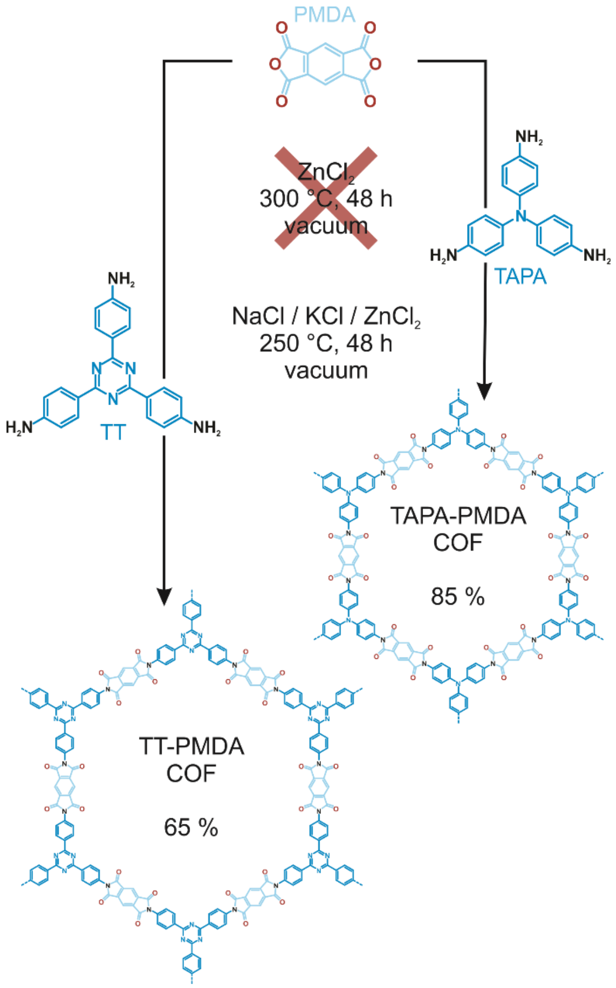

**Figure 4-6.** Synthesis of TT-PMDA- and TAPA-PMDA-COF in an eutectic salt mixture under ionothermal conditions.

The imide formation was again confirmed by FT-IR spectroscopy as shown in Figure 4-7a and c with C=O stretching vibrations of the imide rings at 1778 and 1723 $cm^{-1}$ for both TT-PMDA–COF and TAPA-PMDA-COF, together with C-N-C stretching vibrations of the imide rings at 1357 and 1373 $cm^{-1}$, respectively. The anhydride C=O stretching and amine N-H stretching vibrations corresponding to the respective starting materials are again absent, which proves a complete reaction between the starting materials to form the respective COFs in the eutectic salt mixture (Figures S8-39 and S8-40). $^{13}C$ ssNMR spectra show the carbonyl carbons of the imide ring at 164.6 ppm for TT-PMDA-COF (Figure 4-7d), and 165.0 ppm for TAPA-PMDA-COF (Figure 4-7b), which is consistent with the quantum-chemical calculations (Figures 4-7b, d and S8-41 to S8-46).

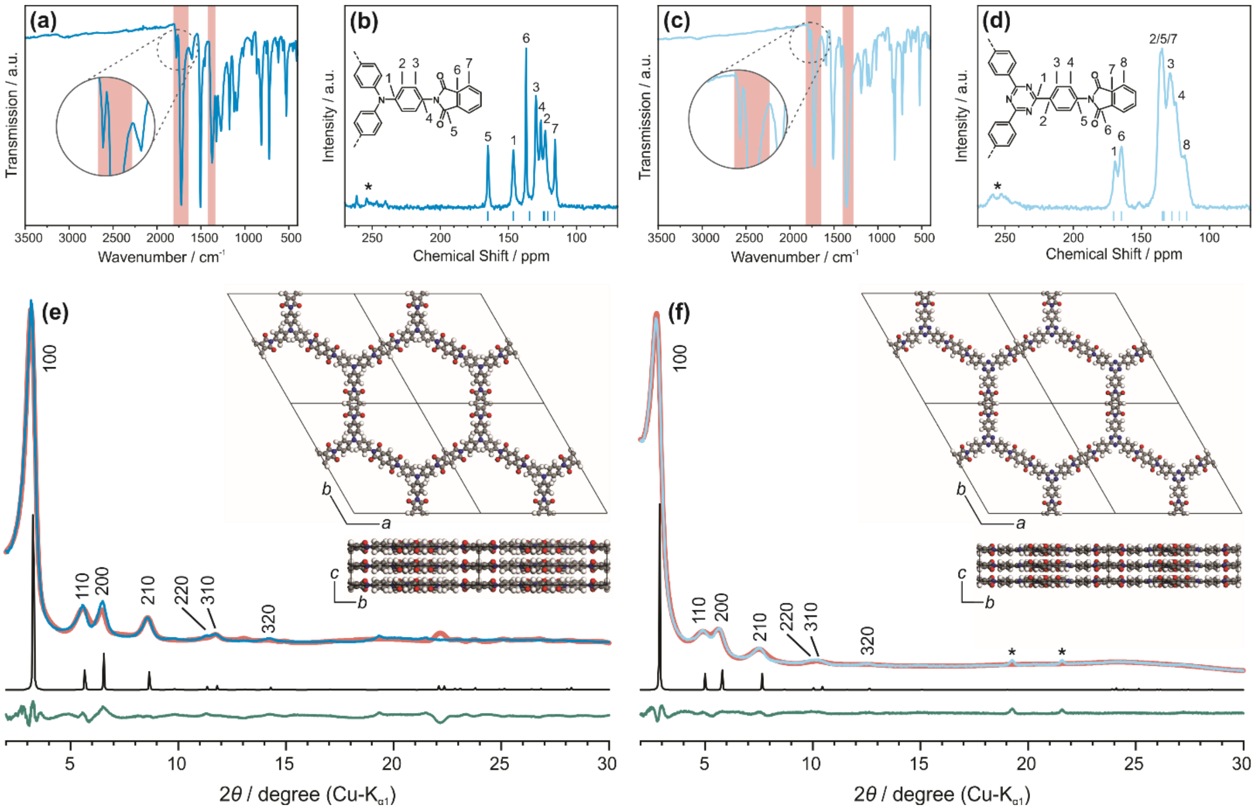

**Figure 4-7.** Characterization of TAPA-PMDA-COF (dark blue) and TT-PMDA-COF (light blue): (a) and (c) IR-spectra showing the imide vibrational bonds indicating full imide formation. (b) and (d) $^{13}$C ssNMR showing the chemical shifts of the carbonyl carbons of the imide ring around 164 ppm together with triazine carbons of the TT linker at 169 ppm and the carbons connected to the central nitrogen of the TAPA linker at 146 ppm. Spinning side bands are marked with asterisks. NMR chemical shifts for the TAPA-PMDA and TT-PMDA-COF were calculated on B97-2/pcsSeg-2 level of theory[30-33] using the FermiONs++[32-33] software package and are shown as blue dashes. (e) and (f) Experimental XRPD pattern of the respective COF (blue) together with the Rietveld fit (red), simulated patterns based on $P\bar{3}1m$ structure type (black), and difference curve (green). Insets: Simulated structures of the respective COF along the *a* and *c* axis. Reflections marked with an asterisk show impurities, which could not be eliminated.

Retention of the molecular structure of the building blocks in the framework is evident from the signal of the triazine carbon at 169.3 ppm for TT-PMDA–COF corresponding to the TT linker, as well as that for the carbons connected to the central nitrogen of the TAPA linker at 146.4 ppm for TAPA-PMDA-COF.[17, 20] The XRPD pattern of TAPA-PMDA-COF shows reflections at 3.16, 5.56, 6.48, 9.82, 11.34, 11.71, and 14.22 ° 2θ (Figure 4-7e and S8-47) which can be assigned to the 100, 210, 200, 210, 220, 310, and 320 Bragg peaks of a trigonal lattice with $P\bar{3}1m$ symmetry. Using the $P\bar{3}1m$ simulated model, which is in agreement with DFT calculations (Figures S8-41), the experimental powder pattern was Rietveld refined yielding the unit cell parameters $a = b = 31.1(6)$ Å and $c = 4.02$ Å with $\alpha = \beta = 90$ ° and $\gamma = 120$ ° ($R_{wp} = 9.03$) with a theoretical pore size of 27 Å. The theoretical value is in good agreement with the experimentally observed pore sizes extracted from TEM (26 Å; Figure S8-48) and argon sorption measurements (27 Å; Figure S8-49). Applying the BET model revealed a surface area of 1592 $m^2g^{-1}$ for our ionothermally synthesized TAPA-PMDA-COF, which is significantly higher when compared to that prepared solvothermally (1027 $m^2g^{-1}$).[17] For TT-PMDA-COF XRPD reflections at 2.73, 4.89, 5.65, 7.50, 9.97, 10.26, and 12.50 ° $2\theta$ are observed, which can be assigned to the 100, 110, 200, 210, 220, 310, and 320 Bragg peaks of a trigonal lattice with $P\bar{3}1m$ symmetry (Figures 4-7f and S8-50) and the unit cell parameters $a = b$ = 35.2(5) Å and $c$ = 3.7(2) Å with $\alpha = \beta = 90$ ° and $\gamma = 120$ ° ($R_{wp}$ = 3.65). This is in agreement with the previously reported AA-type stacking for this COF prepared solvothermally.[20] PSD analysis (Figure S8-49) revealed pores with 30 Å diameter, which is again in good agreement with the pore channels observed in TEM (30 Å) (Figure S8-52) and the theoretical value of 30.6 Å. The BET surface area extracted from argon sorption measurements was calculated to be 706 $m^2g^{-1}$. AB stacked structure types were found unfeasible for both of the COFs as evident by comparison with the simulated patterns (Figures S8-47 and S50). It is noteworthy that all four COFs synthesized via the new ionothermal method show a comparable or even higher degree of crystallinity as compared to the solvothermally synthesized ones[17, 20]. It is further important to note that energy-dispersive X-ray (EDX) spectroscopy revealed either none or only traces (<0.1 %) of zinc or chloride in all of the final COFs (Figures S8-53 to S8-60). This is most likely due to the highly ordered framework structure of the COFs, which not only increases the reaction efficiency by increasing accessibility to the mobilized zinc and chloride ions but also renders removal of $ZnCl_2$ easier after the COF formation as compared to amorphous CTF systems where $ZnCl_2$ residues are extremely difficult to eliminate.[2, 50] Ionothermal synthesis thus appears as a promising approach to access crystalline imide COFs, but also other types of COFs built from highly stable linkages with limited reversibility.

## *4.3 Conclusion*

We have established a new ionothermal synthesis route for imide-linked COFs, with which we were able to synthesize two crystalline and porous COFs (TAPB-PTCDA- and TAPB-PMDA-COF) in pure $ZnCl_2$. The COF formation is straightforward and does not require the use of toxic solvents and additional base catalysts and is also potentially scalable. It is rapid and happens within 10 h under these conditions as opposed to 3-7 days in classical solvothermal synthesis. Furthermore, by lowering the reaction temperature using a three salt eutectic mixture instead of pure $ZnCl_2$, we were able to apply this ionothermal synthesis protocol to less stable linker molecules such as TAPA and TT. We could also show, using the example of TAPB-PMDA-COF, that crystalline adducts consisting of the respective precursors and $ZnCl_2$ act as intermediates in the ionothermal synthesis of the COF. Formation of these intermediates possibly activates the anhydride and imide rings, thus lowering the overall activation barrier leading to a higher degree of reversibility in COF formation. We expect this new method of COF synthesis to greatly broaden the scope of imide-linked COFs in particular and COFs based on inert linkages in general, which are inaccessible by traditional methods, but indispensable for future applications.

## *4.4 Bibliography*

[1] A. P. Cote, A. I. Benin, N. W. Ockwig, M. O'Keeffe, A. J. Matzger, O. M. Yaghi, *Science* **2005**, *310*, 1166-1170.

[2] P. Kuhn, M. Antonietti, A. Thomas, *Angew. Chem. Int. Ed.* **2008**, *47*, 3450-3453.

[3] H. Furukawa, O. M. Yaghi, *J. Am. Chem. Soc.* **2009**, *131*, 8875-8883.

[4] S. Y. Ding, J. Gao, Q. Wang, Y. Zhang, W. G. Song, C. Y. Su, W. Wang, *J. Am. Chem. Soc.* **2011**, *133*, 19816-19822.

[5] T. Banerjee, F. Haase, G. Savasci, K. Gottschling, C. Ochsenfeld, B. V. Lotsch, *J. Am. Chem. Soc.* **2017**, *139*, 16228-16234.

[6] M. Dogru, M. Handloser, F. Auras, T. Kunz, D. Medina, A. Hartschuh, P. Knochel, T. Bein, *Angew. Chem. Int. Ed.* **2013**, *52*, 2920-2924.

[7] X. Ding, L. Chen, Y. Honsho, X. Feng, O. Saengsawang, J. Guo, A. Saeki, S. Seki, S. Irle, S. Nagase, V. Parasuk, D. Jiang, *J. Am. Chem. Soc.* **2011**, *133*, 14510-14513.

[8] H. M. El-Kaderi, J. R. Hunt, J. L. Mendoza-Cortes, A. P. Cote, R. E. Taylor, M. O'Keeffe, O. M. Yaghi, *Science* **2007**, *316*, 268-272.

[9] N. L. Campbell, R. Clowes, L. K. Ritchie, A. I. Cooper, *Chem. Mater.* **2009**, *21*, 204-206.

[10] B. P. Biswal, S. Chandra, S. Kandambeth, B. Lukose, T. Heine, R. Banerjee, *J. Am. Chem. Soc.* **2013**, *135*, 5328-5331.

[11] D. D. Medina, J. M. Rotter, Y. Hu, M. Dogru, V. Werner, F. Auras, J. T. Markiewicz, P. Knochel, T. Bein, *J. Am. Chem. Soc.* **2015**, *137*, 1016-1019.

[12] F. D. Wang, V. N. Richards, S. P. Shields, W. E. Buhro, *Chem. Mater.* **2014**, *26*, 5-21.

[13] J. R. Hunt, C. J. Doonan, J. D. LeVangie, A. P. Cote, O. M. Yaghi, *J. Am. Chem. Soc.* **2008**, *130*, 11872-11873.

[14] F. J. Uribe-Romo, J. R. Hunt, H. Furukawa, C. Klock, M. O'Keeffe, O. M. Yaghi, *J. Am. Chem. Soc.* **2009**, *131*, 4570-4571.

[15] F. J. Uribe-Romo, C. J. Doonan, H. Furukawa, K. Oisaki, O. M. Yaghi, *J. Am. Chem. Soc.* **2011**, *133*, 11478-11481.

[16] K. T. Jackson, T. E. Reich, H. M. El-Kaderi, *Chem. Commun.* **2012**, *48*, 8823-8825.

[17] Q. Fang, Z. Zhuang, S. Gu, R. B. Kaspar, J. Zheng, J. Wang, S. Qiu, Y. Yan, *Nat. Commun.* **2014**, *5*, 4503.

[18] B. Baumgartner, M. Puchberger, M. M. Unterlass, *Polym. Chem.* **2015**, *6*, 5773-5781.

[19] C. Zhang, S. Zhang, Y. Yan, F. Xia, A. Huang, Y. Xian, *ACS Appl. Mater. Interfaces* **2017**, *9*, 13415-13421.

[20] X. Zhu, S. H. An, Y. Liu, J. Hu, H. L. Liu, C. C. Tian, S. Dai, X. J. Yang, H. L. Wang, C. W. Abney, S. Dai, *AIChE J.* **2017**, *63*, 3470-3478.

[21] J. Lv, Y. X. Tan, J. Xie, R. Yang, M. Yu, S. Sun, M. D. Li, D. Yuan, Y. Wang, *Angew. Chem. Int. Ed.* **2018**, *57*, 12716-12720.

[22] Z. Wang, Y. Li, P. Liu, Q. Qi, F. Zhang, G. Lu, X. Zhao, X. Huang, *Nanoscale* **2019**, *11*, 5330-5335.

[23] B. Baumgartner, M. J. Bojdys, M. M. Unterlass, *Polym. Chem.* **2014**, *5*, 3771-3776.

[24] Q. Fang, J. Wang, S. Gu, R. B. Kaspar, Z. Zhuang, J. Zheng, H. Guo, S. Qiu, Y. Yan, *J. Am. Chem. Soc.* **2015**, *137*, 8352-8355.

[25] Y. Ham, K. Maeda, D. Cha, K. Takanabe, K. Domen, *Chem. Asian J.* **2013**, *8*, 218-224.

[26] M. B. Mesch, K. Barwinkel, Y. Krysiak, C. Martineau, F. Taulelle, R. B. Neder, U. Kolb, J. Senker, *Chem. Eur. J.* **2016**, *22*, 16878-16890.

[27] E. Wirnhier, M. Doblinger, D. Gunzelmann, J. Senker, B. V. Lotsch, W. Schnick, *Chem. Eur. J.* **2011**, *17*, 3213-3221.

[28] H. Schlomberg, J. Kroger, G. Savasci, M. W. Terban, S. Bette, I. Moudrakovski, V. Duppel, F. Podjaski, R. Siegel, J. Senker, R. E. Dinnebier, C. Ochsenfeld, B. V. Lotsch, *Chem. Mater.* **2019**, *31*, 7478-7486.

[29] D. S. BIOVIA, *Materials Studio software*, Dassault Systèmes BIOVIA, Materials Studio software, **2017**.

[30] P. J. Wilson, T. J. Bradley, D. J. Tozer, *J. Chem. Phys.* **2001**, *115*, 9233-9242.

[31] F. Jensen, *J. Chem. Theory Comput.* **2015**, *11*, 132-138.

[32] J. Kussmann, C. Ochsenfeld, *J. Chem. Phys.* **2013**, *138*, 134114.

[33] J. Kussmann, C. Ochsenfeld, *J. Chem. Theory Comput.* **2015**, *11*, 918-922.

[34] A. Schafer, C. Huber, R. Ahlrichs, *J. Chem. Phys.* **1994**, *100*, 5829-5835.

[35] J. P. Perdew, K. Burke, M. Ernzerhof, *Phys. Rev. Lett.* **1996**, *77*, 3865-3868.

[36] K. Eichkorn, F. Weigend, O. Treutler, R. Ahlrichs, *Theor. Chem. Acc.* **1997**, *97*, 119-124.

[37] S. Grimme, J. Antony, S. Ehrlich, H. Krieg, *J. Chem. Phys.* **2010**, *132*, 154104.

[38] A. M. Burow, M. Sierka, F. Mohamed, *J. Chem. Phys.* **2009**, *131*, 214101.

[39] L. Grajciar, *J. Comput. Chem.* **2015**, *36*, 1521-1535.

[40] A. M. Burow, M. Sierka, *J. Chem. Theory Comput.* **2011**, *7*, 3097-3104.

[41] R. Lazarski, A. M. Burow, L. Grajciar, M. Sierka, *J. Comput. Chem.* **2016**, *37*, 2518-2526.

[42] R. Lazarski, A. M. Burow, M. Sierka, *J. Chem. Theory Comput.* **2015**, *11*, 3029-3041.

[43] L. Zhang, Y. Cao, N. S. Colella, Y. Liang, J. L. Bredas, K. N. Houk, A. L. Briseno, *Acc. Chem. Res.* **2015**, *48*, 500-509.

[44] L. Liu, Y. J. Xia, J. Zhang, *RSC Adv.* **2014**, *4*, 59102-59105.

[45] P. Kuhn, A. Forget, D. Su, A. Thomas, M. Antonietti, *J. Am. Chem. Soc.* **2008**, *130*, 13333-13337.

[46] I. B. Johns, J. O. Smith, E. A. Mcelhill, *Ind. Eng. Chem. Prod. Res. Dev.* **1962**, *1*, 2-&.

[47] K. Schwinghammer, S. Hug, M. B. Mesch, J. Senker, B. V. Lotsch, *Energy Environ. Sci.* **2015**, *8*, 3345-3353.

[48] A. E. Reed, R. B. Weinstock, F. Weinhold, *J. Chem. Phys.* **1985**, *83*, 735-746.

[49] C. Robelin, P. Chartrand, *J. Chem. Thermodyn.* **2011**, *43*, 377-391.

[50] M. J. Bojdys, J. Jeromenok, A. Thomas, M. Antonietti, *Adv. Mater.* **2010**, *22*, 2202-2205.

# 5 Direct and Linker-Exchange Alcohol-Assisted Hydrothermal Synthesis of Imide-Linked Covalent Organic Frameworks

The work in this chapter was published, reproduced and adapted from:

*Direct and Linker-Exchange Alcohol-Assisted Hydrothermal Synthesis of Imide-Linked Covalent Organic Frameworks*

Johannes Maschita, Tanmay Banerjee and Bettina V. Lotsch

*Chem. Mater.* **2022**, *34*, 5, 2249–2258. DOI: 10.1021/acs.chemmater.1c04051

Johannes Maschita and Bettina V. Lotsch conceived the project. Johannes Maschita, Tanmay Banerjee and Bettina V. Lotsch wrote the manuscript. Johannes Maschita synthesized the materials and performed the structural analysis and evaluated the data. All authors assisted the interpretation of the experiments and the overall discussion. Tanmay Banerjee and Bettina V. Lotsch supervised the work.

Supporting information can be found in chapter 8.3.

## *Abstract*

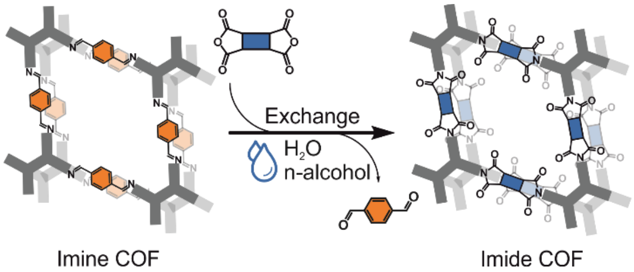

**Figure 5-1.** Table of contents figure for direct and linker-exchange alcohol-assisted hydrothermal synthesis of imide-linked covalent organic frameworks.

Covalent organic frameworks (COFs) are an extensively studied class of porous materials, which distinguish themselves from other porous polymers in their crystallinity and high degree of modularity, enabling a wide range of applications. However, the established synthetic protocols for the synthesis of stable and crystalline COFs, such as imide-linked COFs, often requires the use of high boiling solvents and toxic catalysts, making their synthesis expensive and environmentally harmful. Herein, we report a new environmentally friendly strategy – an alcohol-assisted hydrothermal polymerization approach (aaHTP) for the synthesis of a wide range of crystalline and porous imide-linked COFs. This method allows us to gain access to new COFs and to avoid toxic solvents by up to 90 % through substituting commonly used organic solvent mixtures with water and small amounts of n-alcohols without being restricted to water-soluble linker molecules. Additionally, we use the aaHTP to demonstrate an eco-friendly COF-to-COF transformation of an imine-linked COF into a novel imide-linked COF via linkage replacement, inaccessible using published reaction conditions.

## 5.1 Introduction

Two-dimensional (2D) covalent organic frameworks (COFs) are built of organic building blocks that form extended planar networks via in-plane covalent bonding and are further stacked in the third dimension by out-of-plane π–π interactions and van-der-Waals forces.[1]

As with many high-performance polymers, for COFs, enhanced crystallinity is a desired feature: not only does it improve mechanical and thermal strength[2-3] but it can impart directionality to functional properties like electron transport and thus enhance, e.g., electrical conductivity.[4-5] However, unlike (zero-dimensional) molecules, and one-dimensional (1D) polymers of sufficient molecular flexibility, which may still be recrystallized from solution or a salt-melt, postsynthesis recrystallization of 2D COFs is an outstanding challenge due to the insoluble and infusible nature of COFs, once formed. Therefore, COF synthesis is typically conducted according to the principles of dynamic covalent chemistry: the COF formation reaction has to be reversible to enable crystal defect correction during the polymerization process, carried out under precise thermodynamic and kinetic control.[1, 6] However – bond breaking being as crucial as bond formation in dynamic covalent synthesis – stability is achieved at the expense of crystallinity, frequently leading to poorly crystalline products, rendering synthesis of stable and crystalline COFs challenging.[7] To achieve sufficient reversibility of the COF formation reaction, toxic and high boiling solvents like mesitylene, 1,2-dioxane, *o*-dichlorobenzene, or *N*-Methyl-2-pyrrolidone (NMP) and high temperatures between 120 and 250 °C are usually required.[8]

There is however an increasing need for less harmful synthetic procedures,[9] and therefore, the development of simple, low cost, and green synthetic protocols for the synthesis of COFs has attracted increasing interest in the past few years, leading to the hydrothermal synthesis of keto-enamine-linked, azine-linked, and imine-linked COFs.[10-12] The high reversibility of these linkages and the fact that they are commonly produced by adding aqueous acetic acid as catalyst, aided the development of hydrothermal synthetic protocols for these types of COFs. In contrast, for the synthesis of imide-linked COFs, which are adorned with many beneficial and desired properties, such as high chemical resistance, high thermal stability, and outstanding mechanical properties,[9, 13-14] harsh reaction conditions are required to form these polymers in a crystalline fashion.[13, 15] In fact, there are only two established procedures for the synthesis of bulk imide-linked COFs with reasonable framework crystallinity: (i) the solvothermal approach introduced by Yan *et al*. in which the precursors are reacted in a mixture of the high boiling solvents mesitylene/NMP in varying ratios together with a catalytic base, namely, isoquinoline at temperatures between 200 and 250 °C for several days;[13-14, 16-19] (ii) the ionothermal approach, recently introduced by our group, where the linker molecules are mixed with $ZnCl_2$, or with a $ZnCl_2$ containing eutectic salt mixture.[15] In the latter approach, while the reaction time could be reduced from days to only a few hours and the amount of environmentally harmful chemicals could be minimized, the use of temperatures as high as 250-300 °C could not be avoided.[15]

Unterlass and co-workers demonstrated that polycondensation under hydrothermal conditions can lead to crystalline 1D polyimides (PI).[20-22] Although this method works well for 1D PIs, the adaptation of this hydrothermal synthetic strategy for 2D COFs is rather challenging. Following the work of Unterlass and co-workers, Kim and co-workers recently reported the synthesis of PIC-Ph COF under hydrothermal conditions.[23] However, its applicability in synthesizing crystalline, high surface area COFs is restricted to the *p*-phenylenediamine linker, a water-soluble linker molecule. Using less water-soluble linker molecules such as 4,4'-diaminobiphenyl or 4,4'-diamino-*p*-terphenyl results in a limited long-range growth of the 2D structure and therefore in COFs with very low surface areas.[23]

We now report a general environmentally friendly approach for the synthesis of imide-linked COFs by alcohol-assisted hydrothermal polyimide condensation (aaHTP). We investigate the factors affecting the COF formation under aaHTP conditions thoroughly and optimize the synthetic protocol with respect to sustainability. Three COFs were synthesized with high long-range order and porosity of which one, the TAPE-PMDA-COF, crystallizes in a *kagome*-type lattice and could only be synthesized with sufficient crystallinity using the aaHTP protocol.

Another strategy to realize otherwise inaccessible COFs is to employ reported COFs as templates and modify them by postsynthetic modification or linker exchange. For instance, Yaghi *et al.*[24-25] and others[7, 26-27] used the chemical conversion method to modify the linkage of COFs postsynthetically. Dichtel *et al.*[28] and others,[17, 29-31] on the other hand, performed COF-to-COF or COP-to-COF transformations via monomer exchange reactions.

In this manuscript, we demonstrate that an imine-linked COF can be transformed into an imide-linked COF via linkage replacement using a sustainable hydrothermal polyimide condensation strategy, thus enabling a unique access to imide-linked COFs inaccessible using solvothermal, ionothermal, and direct hydrothermal routes.

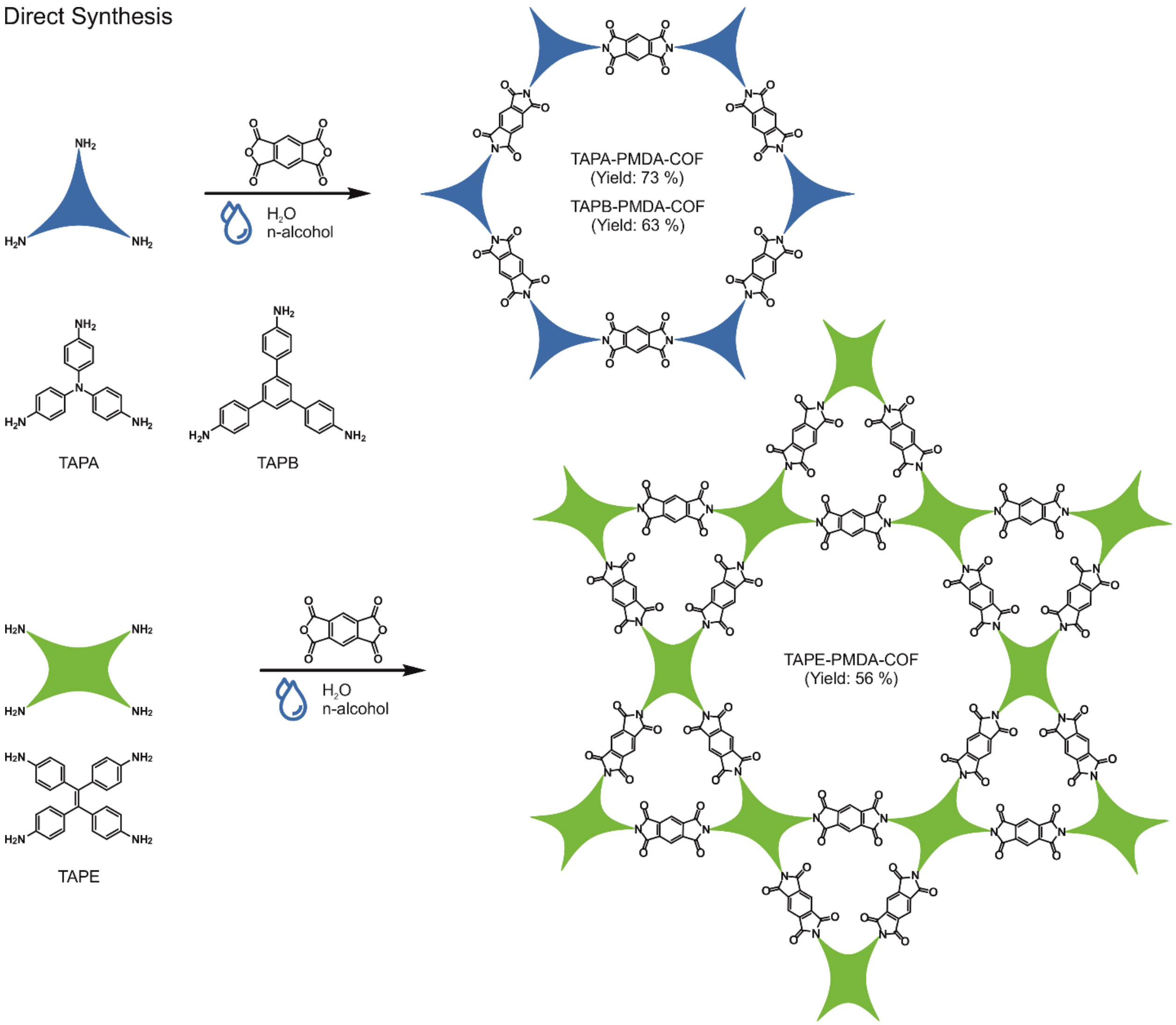

**Figure 5-2.** Direct synthesis of imide-linked COFs from the respective amine precursor molecules TAPA, TAPB and TAPE and the anhydride precursor molecule PMDA via direct aaHTP.

## *5.2 Results and Discussion*

We started our research with the literature-known TAPA-PMDA-COF and TAPB-PMDA-COF, which are synthesized from the precursor molecules tris(4-aminophenyl)amine (TAPA), 1,3,5-tris(4-aminophenyl)benzene (TAPB), and pyromellitic dianhydride (PMDA) (Figure 5-2).[13]

First attempts to synthesize these imide-linked COFs in water only were unsuccessful and yielded amorphous PIs (Figure S8-62). Interestingly, the imide polymerization itself seemed to occur in the presence of water as evident from the typical imide vibrational bands in the fourier transform infrared (FT-IR) spectra of the precipitate (Figure S8-62). We thus reasoned that crystallization may either be prevented by a lack of solubility of the amine precursor molecules and imide oligomers in water,[23] hindering the growth of well oriented COF sheets, or the lack of polarity differences in the reaction mixture. Indeed, most COFs have been reported to form crystalline structures in two-solvent mixtures of varying polarity, e.g., mesitylene ($\varepsilon = 2.4$)[32] and NMP ($\varepsilon = 32$)[33] for imide-linked COFs.[34] One possible reason could be the dielectric stabilization of oligomers or agglomerates in solution, keeping them accessible during the reaction. Further, the reversibility of the imide condensation reaction in water alone might not be sufficient enough for the defect healing processes needed to form well oriented 2D COF sheets in accordance with the principles of dynamic covalent chemistry.[1]

With this in mind, and with an aim to keep the reaction conditions as environmentally friendly as possible, we added n-alcohols of different chain lengths to the reaction mixture of the TAPA-PMDA-COF, together with catalytic amounts of pyridine (40 µl), and analyzed the received products. n-Alcohols were chosen because of the less toxic nature of this solvent class as compared to other organic solvents.[35] Pyridine was added as a basic and nucleophilic catalyst and substitutes isoquinoline that is commonly used in solvothermal approaches.[13] While no precipitation occurred in the reaction mixture with methanol and only an amorphous polymer could be isolated using ethanol, the reaction mixture with n-propanol yielded crystalline TAPA-PMDA-COF (Figure S8-63) (The complete characterization of TAPA-PMDA-COF, synthesized under optimized conditions, is presented later).

Motivated by the results and to get further insights into the factors affecting the aaHTP for imide-linked COFs, we tested a series of different n-alcohols in various concentrations and pyridine in the reaction mixture using TAPA-PMDA-COF as the model system. Additionally, to further reduce the energy expenditure of the aaHTP, we tested if a reduction of the reaction temperature and time is possible. The results of these investigations are depicted in Figure 5-3. Figure 5-3a shows the X-ray powder diffraction (XRPD) patterns of TAPA-PMDA-COF synthesized using different n-alcohols, ranging from n-propanol to n-hexanol, with varying concentrations. It can be seen that, while with all of the tested n-alcohols crystalline products form, the concentration of alcohol needed to produce crystalline products follows a trend: With increasing length of the alkane chain of the n-alcohol, and thereby increasing polarity difference in the solvent mixture (Figure S8-64), the amount of alcohol needed to get crystalline products is reduced. For example, while with n-propanol the alcohol content of the reaction mixture can only be reduced to 30 % in order to obtain a crystalline product, with n-butanol a reduction to 20 % is possible. Further, with n-hexanol, a reduction of the alcohol content to 10 % could be achieved for the synthesis of TAPA-PMDA-COF. Ar sorption experiments of the most promising samples revealed that the BET surface area follows roughly the same trend as crystallinity (Figure S8-65): The higher the polarity difference of the solvent system, the higher the measured BET surface area. However, there are “sweet spots” for the water/n-alcohol ratios for each of the tested n-alcohols. While COFs synthesized in 20 % n-hexanol or 20 % n-butanol have calculated BET surface areas of 1062 m²/g and 244 m²/g, respectively, by varying the alcohol content by only 10 % the surface areas increase to 1619 m²/g (10 % n-hexanol) and 1327 m²/g (30 % n-butanol).

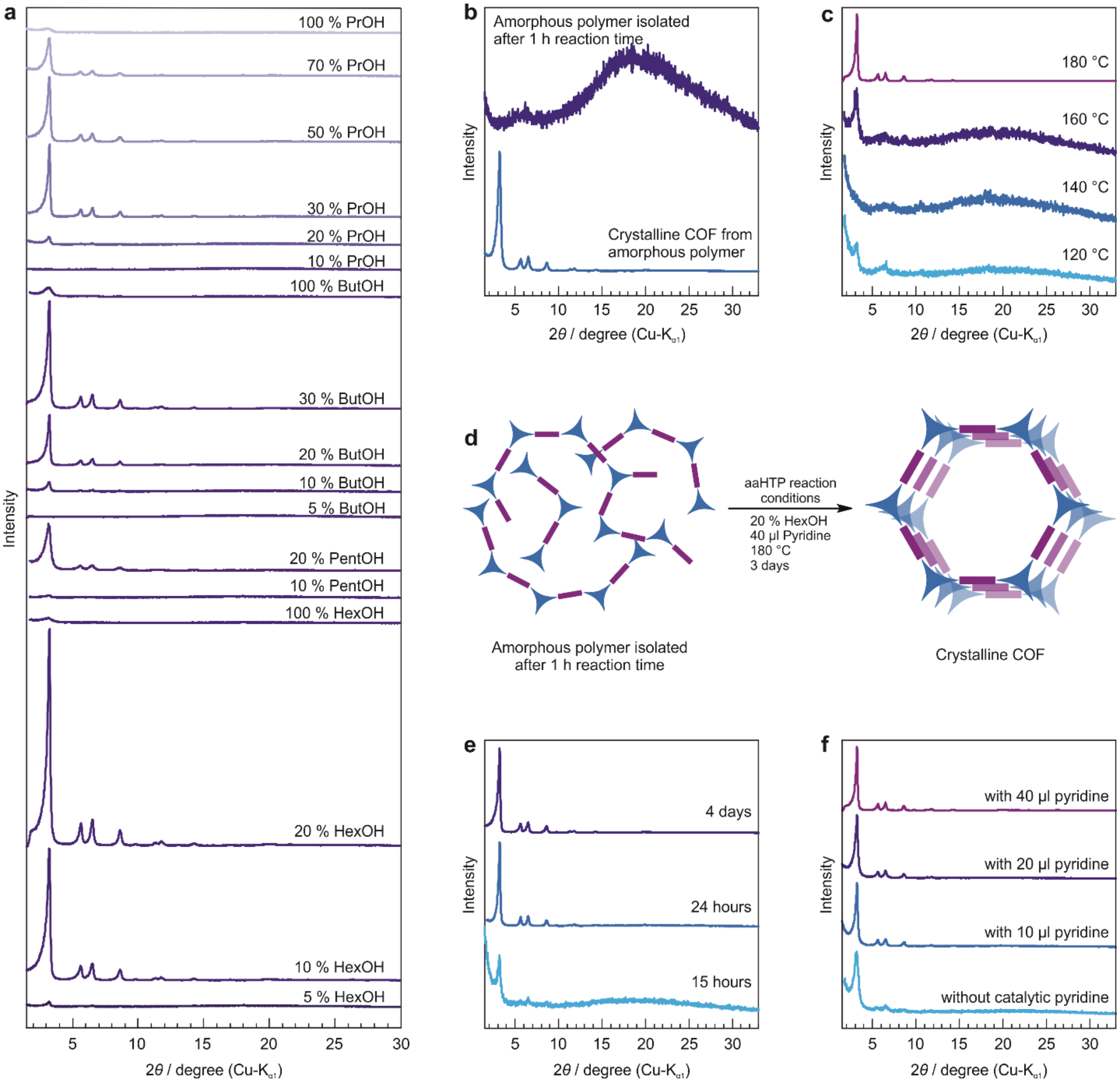

**Figure 5-3.** Optimization of the aaHTP protocol with TAPA-PMDA-COF as model system. XRPD patterns of TAPA-PMDA-COF synthesized using differing conditions showing a) the effect of the type and the amount of the n-alcohol on aaHTP, b), d) the recrystallization of the amorphous PI into the crystalline COF under aaHTP conditions, c) the effect of different reaction temperatures, e) the effect of different reaction times and f) the COF synthesized using varying amounts of catalytic pyridine.

It should also be noted that the synthesis of TAPA-PMDA-COF in 100 % alcohol did not lead to crystalline products in any case, indicating that the interplay between the respective alcohol and water is crucial for the hydrothermal imide-COF formation.

To further elucidate the role of the alcohol in the aaHTP, two COF reactions were performed in which one reaction was carried out in water and pyridine and the other one in water, 30 % butanol and pyridine. Both experiments were done simultaneously and multiple images were taken during the process of heating to 200 °C (Figure S8-66). After 1 h at 200 °C, the reaction mixtures were allowed to cool down to approximately 100 °C in order to reduce the inside pressure, and the supernatant was filtered off hot and analyzed via FT-IR and $^1$H nuclear magnetic resonance (NMR) spectroscopy. Additionally, the precipitate was analyzed via FT-IR spectroscopy and XRPD. During this experiment, two observations were made: (i) In both cases, the precipitation of the amorphous TAPA-PMDA-PI occurred rapidly and already during the heating process (Figure S8-67). This indicates recrystallization of the amorphous PI after precipitation to form the final COF. This could indeed be confirmed by heating the isolated amorphous polymer a second time under aaHTP conditions for 3 days without adding additional precursor molecules, which resulted in the crystalline TAPA-PMDA-COF (Figure 5-3b, d). (ii) While in the supernatant of the alcohol containing reaction mixture imide and amic acid species could be detected, the supernatant of the water reaction mixture contained predominantly deprotonated pyromellitic acid and protonated amine linker molecules (Figure S8-68 to S8-71). This indicates the formation of a monomer-salt intermediate in the COF formation reaction prior to polymerization, by protonation of the amine linker by the hydrolyzed PMDA as described previously.[20, 23] We observed that this monomer-salt intermediate (Figure S8-72) dissolves in water and also in the water/n-alcohol mixtures during the heating process, and amorphous PI begins to precipitate thereafter. Thus, while water could serve as a good solvent for PMDA and the intermediate salt, enabling the primary diffuse polymerization, and enhances the reversibility of the equilibrium reaction (Le Chatelier's principle), the alcohol could contribute to enhancing the solubility of the amine precursor, enabling exchange of the amine linker molecule from the precipitated amorphous network during the defect healing processes. Indeed, solubility experiments with TAPA in pure water and in a series of n-alcohols (Figure S8-73) revealed that it is barely soluble in pure water, even at 180 °C, whereas it dissolves completely in all alcohols tested.

In addition, the less polar imide dimers and oligomers, detected in the supernatant of the alcohol-containing reaction, are possibly kept longer in solution due to a surfactant-like behavior of the longer chain n-alcohols which can interact with the less polar benzylic groups of the oligomers in a manner similar to that observed in surfactant-based MOF formation.[36] This could explain the requirement of progressively smaller alcohol concentrations as one moves from n-propanol to n-hexanol and provides a great advantage over the pure hydrothermal synthesis approach, circumventing the need for water-soluble linker molecules and oligomers to achieve high quality COFs.[23]

Figure 5-3c shows the XRPD pattern of TAPA-PMDA-COF synthesized at different reaction temperatures ranging from 120 to 180 °C in 10 % n-hexanol/pyridine for 4 days. It can be seen that a reduction of the reaction temperature to <180 °C results in a significant loss of crystallinity. This shows that a certain reaction temperature and therefore also a certain autogenous pressure (approximately 12 bar) of the reaction mixture is required to ensure sufficient reversibility of the imide condensation reaction. It is hence not possible to reduce the energy expenditure of the aaHTP by lowering the reaction temperature. Nevertheless, as shown in Figure 5-3e, we were able to reduce the reaction time for the synthesis of TAPA-PMDA-COF to 24 h. A further reduction of the reaction time led to a significant loss of crystallinity. However, the calculated BET surface area of 603 $m^2/g$ after 24 h indicates that further time is required for the COF crystallization to be completed (Figure S8-74).

Since the most toxic substance used in the aaHTP is pyridine, we tried to reduce its usage and tested additionally if the reaction yields crystalline products when using lower amounts of this catalyst or in the absence of pyridine. As depicted in Figure 5-3f, the samples synthesized with reduced amounts of pyridine (20 % n-hexanol, 180 °C, 4 days) are crystalline. However, with decreasing pyridine content, we observed a progressive broadening of the reflections and a reduction of the BET surface areas (Figure S8-75). The sample synthesized without pyridine shows broad reflections as well, and the poor signal intensities point toward the formation of only a few small crystalline domains due to the reduced reversibility. Argon sorption measurements of this sample revealed a BET surface area of only 320 $m^2/g$ (Figure S8-75), corroborating this argument.

Nevertheless, with TAPA-PMDA-COF, it could be demonstrated that the aaHTP at 180 °C, in a reaction mixture consisting of 90 % water, leads to crystalline imide-linked COFs, thus making this method substantially more sustainable than the commonly used solvothermal or ionothermal approach for imide-linked COFs.[13, 15] Additionally, the water treatment after the reaction is simplified with this method because the organic phase consisting of either n-butanol or n-hexanol and pyridine can easily be separated from the aqueous phase after the COF synthesis due to phase separation at room temperature. The separated organic phase can be recycled and used for further synthesis of the same COF (Figure S8-76).

With the knowledge gained from optimizing the synthesis of TAPA-PMDA-COF, we were able to adapt the aaHTP to synthesize two additional imide-linked COFs directly from their respective linker molecules. TAPB-PMDA-COF and TAPE-PMDA-COF have been synthesized from the precursor molecules TAPB, 1,1,2,2-tetrakis(4aminophenyl)ethylene (TAPE), and PMDA (Figure 5-2). While TAPB-PMDA-COF has previously been known,[13] TAPE-PMDA-COF has not been reported so far. Attempts to synthesize TAPE-PMDA-COF using known literature methods failed (Figure S8-77) showing the importance of the development of new synthetic protocols and hence of the aaHTP.[13,15] The optimized reaction conditions have been found to be 90 % $H_2O$/10 % n-hexanol/pyridine for TAPA-PMDA-COF, 80 % $H_2O$/20 % n-hexanol/pyridine for TAPB-PMDA-COF, 67 % $H_2O$/33 % n-butanol/pyridine for TAPE-PMDA-COF.

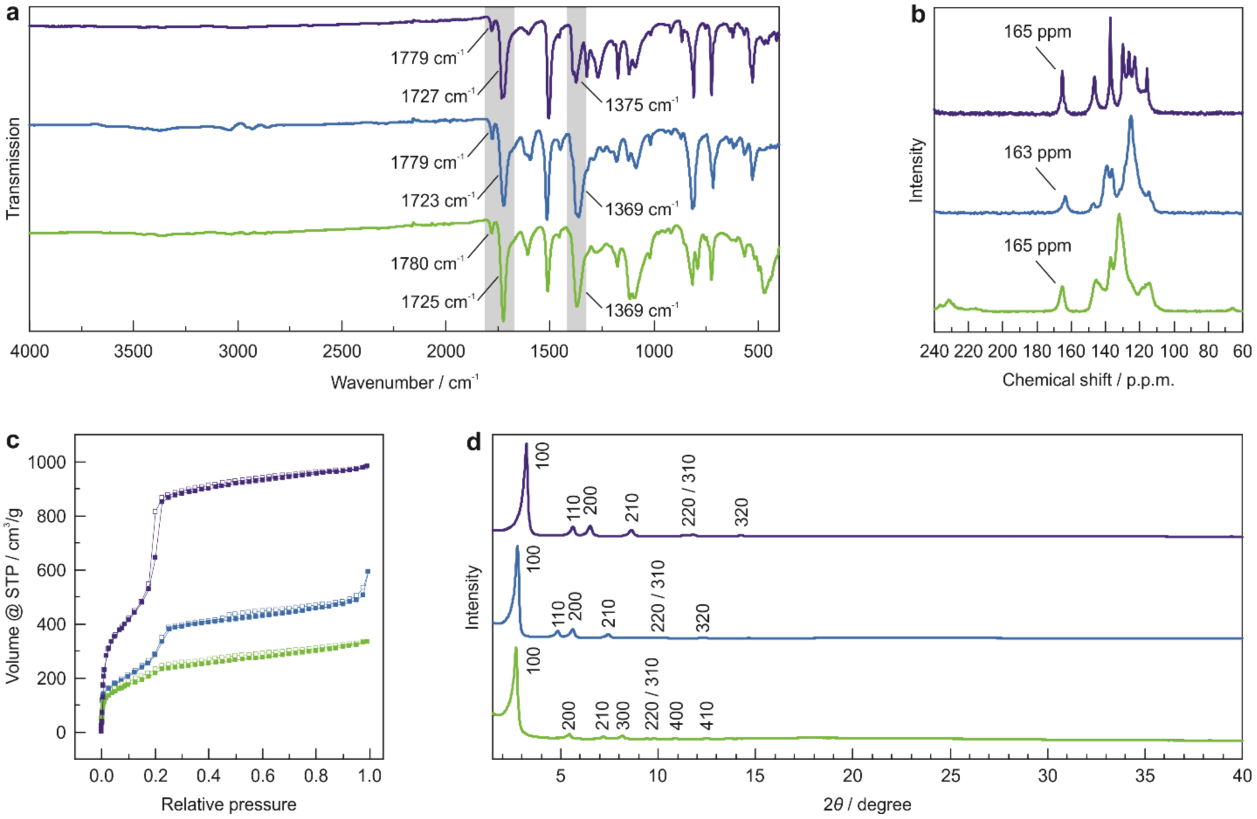

**Figure 5-4.** Characterization of TAPA-PMDA-COF (violet), TAPB-PMDA-COF (blue) and TAPE-PMDA-COF (green). a) Normalized FT-IR spectra showing the characteristic C=O and C-N-C vibrations of the imide-ring. b) $^{13}C$ ssNMR spectra showing the chemical shifts of the imide ring carbon at 165 ppm. c) Ar adsorption (filled symbols)/desorption (hollow symbols) isotherms. d) Experimental XRPD patterns normalized to the highest intensity 100 Bragg peak.

FT-IR, $^{13}C$ CP-MAS solid-state NMR (ssNMR), XRPD, and argon sorption measurements of the resulting solids corroborated the formation of the COFs (Figure 5-4). FT-IR spectra of the COFs show the presence of imide vibrational bands with the appearance of the characteristic antisymmetric and symmetric C=O stretching vibrations at around 1779 and 1725 cm$^{-1}$ and the C-N-C stretching vibration at around 1369 cm$^{-1}$ (Figure 5-4a). Moreover, the absence of the characteristic vibrational bands of the anhydride (1700 cm$^{-1}$) and amine (3367 cm$^{-1}$) functional groups in the FT-IR spectra point to the completeness of the reaction (Figure S8-78). $^{13}C$ ssNMR further confirmed the formation of the imide linkage with the characteristic carbonyl carbon of the imide ring appearing at around 165 ppm (Figure 5-4b). All three COFs are crystalline, as evident from their respective XRPD patterns (Figure 5-4d) and TEM images (Figure S8-79). Rietveld[37] refinement of the experimental powder diffraction patterns (Figures S8-80, S8-81) yielded the unit cell parameters $a$ = 31.06 Å and $c$ = 3.91 Å for TAPA-PMDA COF ($P622$ symmetry) and $a$ = 36.04 Å and $c$ = 3.75 Å for TAPB-PMDA-COF ($P\bar{3}1m$ symmetry). TAPE-PMDA-COF was simulated with $P622$ symmetry and *kagome*-type structure. Rietveld refinement yielded the unit cell parameters $a$ = 37.46 Å and $c$ = 5.00 Å (Figures S8-80, S8-81). The porosity of the hydrothermally synthesized COFs was confirmed by argon sorption measurements at 87.15 K from which BET surface areas of 1619 $m^2/g$ (TAPA-PMDA-COF), 939 $m^2/g$ (TAPB-PMDA-COF) and 689 $m^2/g$ (TAPE-PMDA-COF) were calculated (Figure 5-4c, S8-82). The calculated pore size distribution (PSD) of TAPE-PMDA-COF shows a dual pore system with pore sizes of 1.67 and 2.66 nm, further confirming the *kagome*-type structure with a dual pore system. Note, that the BET surface area of TAPA-PMDA-COF is the highest reported so far for this system and that the value for TAPB-PMDA-COF compares to previously reported values for this COF synthesized either under standard solvothermal conditions using high boiling organic solvents or under ionothermal conditions at high temperatures.[13, 15, 38-40]

As an alternative strategy to the direct aaHTP for the synthesis of imide-linked COFs, we explored if the aaHTP protocol can be adapted in a possible linker exchange strategy for the synthesis of otherwise inaccessible imide-linked COFs from imine-linked COFs. As shown for other COF systems, the exchange of linker molecules in a COF relies on the requirement that the replaced linkage is more reversible and less stable under the chosen reaction conditions, while the substituting linkage has to be less reversible and more stable.[17, 28-30, 41] In addition, the preorientation through – or template function of – the starting COF, and a reduced reaction speed when compared to the direct synthesis from the respective precursor molecules, assist the formation of crystalline products after exchange.

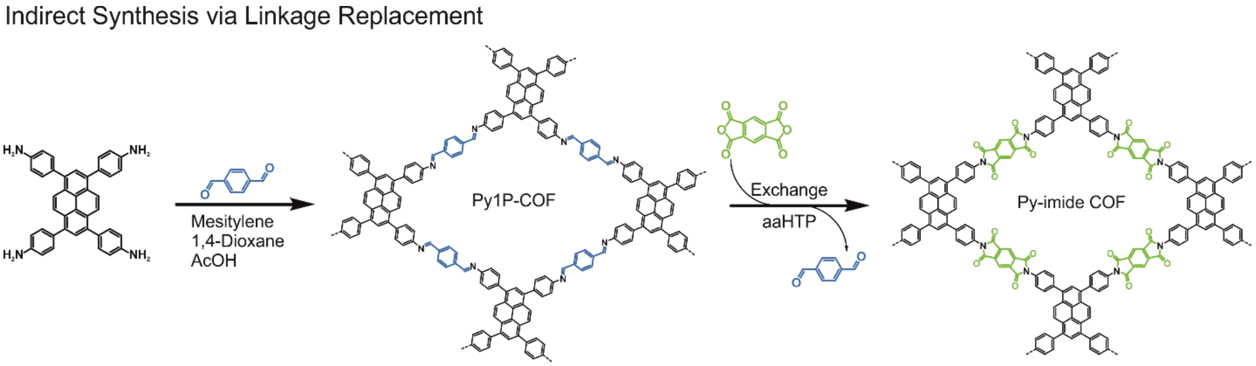

**Figure 5-5.** Synthesis of the imine-linked precursor Py1P-COF and its transformation into the imide-linked Py-imide COF via linkage replacement using aaHTP conditions.

As the model precursor COF system for the imine-linked to imide-linked COF transformation using the aaHTP method, we chose imine-linked Py1P-COF for its transformation to Py-imide COF, previously unreported and inaccessible using all known synthetic methods including direct aaHTP (Figure S8-83). The lack of crystallinity when using direct aaHTP could be explained due to a reduced solubility of the large amine linker in the n-alcohol/$H_2O$ mixture compared to the smaller linker molecules used successfully in direct aaHTP (Figure S8-84, S8-85). Using the linkage exchange strategy, we take advantage of the preorientation of the imine COF and additionally have a potential modulating effect through the released aldehyde linker during the reaction. The model system was chosen because the exchanging linker molecules terephthaldehyde and PMDA are nearly equally sized (Figure S8-86).

Py1P-COF, synthesized following a reported procedure from the precursor molecules 4,4',4'',4'''-(pyrene-1,3,6,8-tetrayl)tetraaniline (PyTTA) and terephthalaldehyde in a mixture of mesitylene/1,4-dioxane/6M AcOH (Figure 5-5),[42] was reacted with PMDA in a mixture of 67 % $H_2O$/33 % n-butanol/0.04 ml pyridine for 4 days. FT-IR spectroscopy of the resulting brown-orange powder reveals vibrational bands at 1778, 1728 and 1364 $cm^{-1}$, which can be assigned to the characteristic antisymmetric and symmetric C=O stretching vibrations and the C-N-C stretching vibration of the imide ring of Py-imide COF (Figure 5-6a). The characteristic N=CH vibrational band at 1623 $cm^{-1}$ of the imine-linked Py1P-COF vanishes, indicating the successful transformation into the Py-imide COF. $^{13}C$ and $^{15}N$ CP-MAS ssNMR spectroscopy further confirm the conversion of Py1P-COF to Py-imide COF as evident by the disappearance of the signals for carbon **1** and **2** at 156.3 and 149.6 ppm (Figure 5-6b) and the appearance of the signal for carbon **3** at 164.5 ppm, as well as the disappearance of the imine nitrogen at -49 ppm (red dot) and the appearance of the imide nitrogen at -208 ppm (Figure 5-6c, d). Two additional signals at -254 and -318 ppm appear in the $^{15}N$ spectrum of the Py-imide COF. These signals can be assigned to unreacted or dangling amine functional groups and to the amic acid intermediate described previously for the imide-COF condensation reaction (Figure 5-6c, d).[43] Note that the ssNMR spectra are measured using N–H cross-polarization methods and are therefore not quantitative.

The signals of nitrogen atoms connected to hydrogen atoms appear more intense than those without hydrogen atoms. Since there is no indication for greater amounts of amic acid or imine residuals in the $^{13}C$ ssNMR spectrum (peak missing at 173 ppm), we assume an almost complete condensation. However, a peak at 146 ppm appears in the $^{13}C$ spectrum which corresponds to carbon **4**, revealing an increased amount of free amine groups. Further, argon sorption measurements indicate that the porosity of the structure is largely retained after transformation and reveals only a small change of the BET surface area from 1531 $m^2/g$ to 1334 $m^2/g$ (Figure 5-6f, S8-87). Pore size distribution analysis of the Py-imide COF using the QSDFT method reveals pores of 2 nm for Py-imide COF, in accordance with the theoretical pore size of 2 nm for the refined crystal lattice (*vide infra*).

The experimental XRPD patterns (Figure 5-6e) and TEM images (Figure S8-88) of the precursor Py1P-COF and the product Py-imide COF show high crystallinity and reveal that the framework remains intact upon transformation. The diffraction patterns of the two COFs look very similar, which is expected since the geometry and the size of the unit cell before and after conversion should not differ significantly due to the nearly equally sized linker molecules terephthaldehyde and PMDA. Py1P-COF shows reflections at 3.71, 5.36, 7.47, 8.47, 11.24 and 23.44 ° $2\theta$, and Py-imide COF shows reflections at 3.75, 5.43, 7.54, 8.59, 11.34 and 23.1 ° $2\theta$.

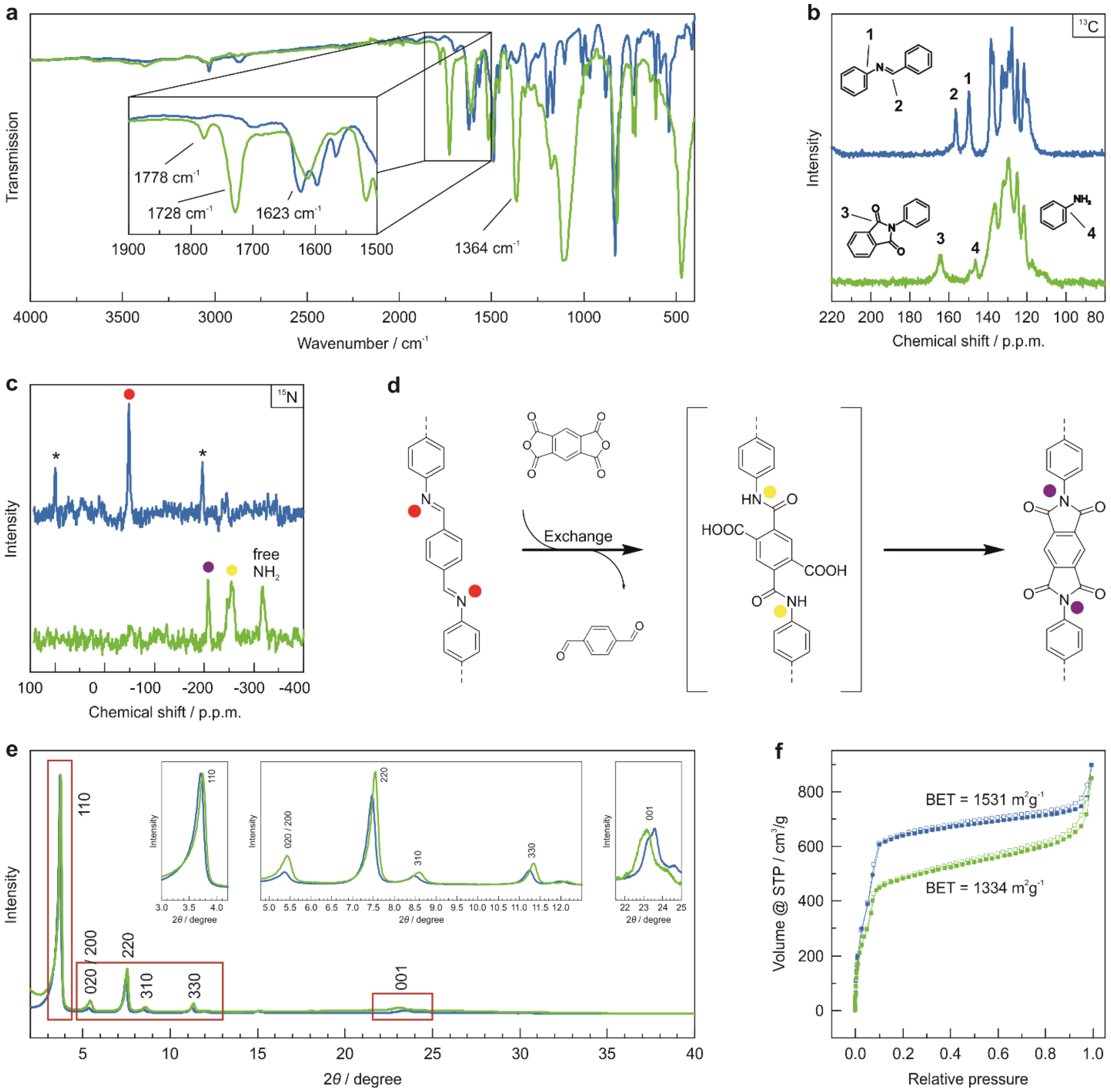

**Figure 5-6.** Characterization of Py1P-COF (blue) and Py-Imide COF (green). a) FT-IR spectra showing the appearance of the characteristic imide vibrational bands and the disappearance of the imine C=N vibration. b) $^{13}C$ ssNMR spectra demonstrating the conversion of the imine linkage to the imide linkage. c) $^{15}N$ ssNMR spectra showing the successful conversion into the Py-imide COF and revealing intermediate amic acid residuals. d) Scheme of the conversion of the imine linkage to the imide linkage together with the assignments of the $^{15}N$ ssNMR spectra. e) Overlay of the COFs' experimental XRPD pattern normalized to the highest intensity 110 reflection together with enlargements of the COFs' XRPD patterns to visualize the differences in relative intensity and reflection position upon transformation. f) Ar adsorption (filled symbols)/desorption (hollow symbols) confirming the retention of porosity.

It can be observed that all reflections shift slightly towards higher scattering angles, except the 001 stacking reflection at around 23 ° 2$\theta$, which shifts towards lower angles. This indicates a slight decrease of the unit cell parameters in the *a*-*b* plane and a simultaneous increase of the stacking distance in the [001] direction. Further, it can be observed that the intensity of the reflections between 5 and 12 ° $2\theta$ increases upon transformation, which is most likely an effect of an increasing layer offset after linker exchange as can be seen by the differing $\beta$ values.[44]

The experimental XRPD patterns are in good agreement with simulated reflection patterns using $C2/m$ symmetry for both COFs, suggesting a topotactic transformation (Figure S8-89, S8-90). Rietveld refinement of the XRPD patterns yield unit cell parameters of $a$ = 38.06 Å, $b$ = 32.47 Å, $c$ = 3.82 Å, $\alpha = \gamma$ = 90 °, and $\beta$ = 63.3 ° for Py1P-COF and $a$ = 33.87 Å, $b$ = 32.16 Å, $c$ = 3.9 Å, $\alpha = \gamma$ = 90 °, and $\beta$ = 86.7 ° for Py-imide COF.

Stability tests were then performed (Figure S8-91) to ensure a successful exchange of the PMDA linker molecule into the COFs framework. While both COFs show high stability under strongly acidic conditions (conc. HCl, 60 °C, 24 h), there is a distinct difference between the two COFs under reductive conditions (50 % HCOOH, 60 °C, 24 h). Py1P-COF partially dissolves, and the remaining solid turns amorphous. On the other hand, Py-imide COF shows high stability under these conditions with full retention of its crystalline structure. The stability of Py-imide COF over Py1P-COF under reductive conditions further substantiates a successful transformation of the latter to the former under aaHTP reaction conditions.

## *5.3 Conclusion*

We report an environmentally friendly alcohol-assisted hydrothermal polymerization approach (aaHTP) for the synthesis of imide-linked COFs. Using this method, we were able to synthesize TAPA-PMDA-, TAPB-PMDA-, and the previously unreported TAPE-PMDA-COF directly from their respective linker molecules. TAPE-PMDA-COF, which crystallizes in a *kagome*-type structure, could only be synthesized using the aaHTP protocol, showing the importance of such complementary procedures for the synthesis of COFs. The aaHTP is special in that a wide range of imide-linked COFs can now be synthesized in reaction mixtures consisting of up to 90 % water, irrespective of the water solubility of their linker molecules, making this an eco-friendly and general alternative method to all previously reported synthetic procedures. Additionally, using the example of the newly synthesized imide-linked Py-imide COF, we demonstrate the applicability of aaHTP in COF-to-COF transformations via linkage replacement from imine-linked COFs in an environmentally friendly fashion enabling access to imide-linked COFs that were inaccessible before. This work thus provides a simple and low-cost synthesis strategy for imide-linked COFs and presents a substantial contribution to the field of green chemistry in general and to the field of sustainable COF synthesis in particular.

## 5.4 *Bibliography*

[1] Cote, A. P.; Benin, A. I.; Ockwig, N. W.; O'Keeffe, M.; Matzger, A. J.; Yaghi, O. M., *Science* **2005**, *310* (5751), 1166-70.

[2] Young, R. J.; Lu, D.; Day, R. J.; Knoff, W. F.; Davis, H. A., *J. Mater. Sci.* **1992**, *27* (20), 5431-5440.

[3] Li, H. Y.; Bredas, J. L., *Chem. Mater.* **2021**, *33* (12), 4529-4540.

[4] Bloor, D.; Ando, D. J.; Preston, F. H.; Stevens, G. C., *Chem. Phys. Lett.* **1974**, *24* (3), 407-411.

[5] Rotter, J. M.; Guntermann, R.; Auth, M.; Mahringer, A.; Sperlich, A.; Dyakonov, V.; Medina, D. D.; Bein, T., *Chem Sci* **2020**, *11* (47), 12843-12853.

[6] El-Kaderi, H. M.; Hunt, J. R.; Mendoza-Cortes, J. L.; Cote, A. P.; Taylor, R. E.; O'Keeffe, M.; Yaghi, O. M., *Science* **2007**, *316* (5822), 268-72.

[7] Haase, F.; Troschke, E.; Savasci, G.; Banerjee, T.; Duppel, V.; Dorfler, S.; Grundei, M. M. J.; Burow, A. M.; Ochsenfeld, C.; Kaskel, S.; Lotsch, B. V., *Nat. Commun.* **2018**, *9* (1), 2600.

[8] Lohse, M. S.; Bein, T., *Adv. Funct. Mater.* **2018**, *28* (33), 1705553.

[9] Baumgartner, B.; Bojdys, M. J.; Skrinjar, P.; *Macromol. Chem. Phys.* **2016**, *217* (3), 485-500.

[10] Lu, J.; Lin, F.; Wen, Q.; Qi, Q. Y.; Xu, J. Q.; Zhao, X., *New J. Chem.* **2019**, *43* (16), 6116-6120.

[11] Martin-Illan, J. A.; Rodriguez-San-Miguel, D.; Franco, C.; Imaz, I.; Maspoch, D.; Puigmarti-Luis, J.; Zamora, F., *Chem Commun* **2020**, *56* (49), 6704-6707.

[12] Thote, J.; Barike Aiyappa, H.; Rahul Kumar, R.; Kandambeth, S.; Biswal, B. P.; Balaji Shinde, D.; Chaki Roy, N.; Banerjee, R., *IUCrJ* **2016**, *3* (Pt 6), 402-407.

[13] Fang, Q.; Zhuang, Z.; Gu, S.; Kaspar, R. B.; Zheng, J.; Wang, J.; Qiu, S.; Yan, Y., *Nat. Commun.* **2014**, *5*, 4503.

[14] Veldhuizen, H.; Vasileiadis, A.; Wagemaker, M.; Mahon, T.; Mainali, D. P.; Zong, L.; Zwaag, S.; Nagai, A., *J. Polym. Sci. A Polym. Chem.* **2019**, *57* (24), 2373-2377.

[15] Maschita, J.; Banerjee, T.; Savasci, G.; Haase, F.; Ochsenfeld, C.; Lotsch, B. V., *Angew. Chem. Int. Ed. Engl.* **2020**, *59* (36), 15750-15758.

[16] Zhu, X.; An, S. H.; Liu, Y.; Hu, J.; Liu, H. L.; Tian, C. C.; Dai, S.; Yang, X. J.; Wang, H. L.; Abney, C. W.; Dai, S., *Aiche J.* **2017**, *63* (8), 3470-3478.

[17] Zhai, Y.; Liu, G.; Jin, F.; Zhang, Y.; Gong, X.; Miao, Z.; Li, J.; Zhang, M.; Cui, Y.; Zhang, L.; Liu, Y.; Zhang, H.; Zhao, Y.; Zeng, Y., *Angew. Chem. Int. Ed. Engl.* **2019**, *58* (49), 17679-17683.

[18] Lv, J.; Tan, Y. X.; Xie, J.; Yang, R.; Yu, M.; Sun, S.; Li, M. D.; Yuan, D.; Wang, Y., *Angew. Chem. Int. Ed. Engl.* **2018**, *57* (39), 12716-12720.

[19] Jiang, L.; Wang, P.; Li, M.; Zhang, P.; Li, J.; Liu, J.; Ma, Y.; Ren, H.; Zhu, G., *Chem. Eur. J.* **2019**, *25* (38), 9045-9051.

[20] Baumgartner, B.; Bojdys, M. J.; Unterlass, M. M., *Polym. Chem.* **2014**, *5* (12), 3771-3776.

[21] Baumgartner, B.; Puchberger, M.; Unterlass, M. M., *Polym. Chem.* **2015**, *6* (31), 5773-5781.

[22] Unterlass, M. M.; Kopetzki, D.; Antonietti, M.; Weber, J., *Polym. Chem.* **2011**, *2* (8), 1744-1753.

[23] Kim, T.; Joo, S. H.; Gong, J.; Choi, S.; Min, J. H.; Kim, Y.; Lee, G.; Lee, E.; Park, S.; Kwak, S. K.; Lee, H. S.; Kim, B. S., *Angew. Chem. Int. Ed. Engl.* **2022**, *61*, *e202113780*.

[24] Waller, P. J.; Lyle, S. J.; Osborn Popp, T. M.; Diercks, C. S.; Reimer, J. A.; Yaghi, O. M., *J. Am. Chem. Soc.* **2016**, *138* (48), 15519-15522.

[25] Waller, P. J.; AlFaraj, Y. S.; Diercks, C. S.; Jarenwattananon, N. N.; Yaghi, O. M., *J. Am. Chem. Soc.* **2018**, *140* (29), 9099-9103.

[26] Li, X.; Zhang, C.; Cai, S.; Lei, X.; Altoe, V.; Hong, F.; Urban, J. J.; Ciston, J.; Chan, E. M.; Liu, Y., *Nat. Commun.* **2018**, *9* (1), 2998.

[27] Grunenberg, L.; Savasci, G.; Terban, M. W.; Duppel, V.; Moudrakovski, I.; Etter, M.; Dinnebier, R. E.; Ochsenfeld, C.; Lotsch, B. V., *J. Am. Chem. Soc.* **2021**, *143* (9), 3430-3438.

[28] Daugherty, M. C.; Vitaku, E.; Li, R. L.; Evans, A. M.; Chavez, A. D.; Dichtel, W. R., *Chem. Commun.* **2019**, *55* (18), 2680-2683.

[29] Qian, C.; Qi, Q.-Y.; Jiang, G.-F.; Cui, F.-Z.; Tian, Y.; Zhao, X., *J. Am. Chem. Soc.* **2017**, *139* (19), 6736-6743.

[30] Qian, H.-L.; Li, Y.; Yan, X.-P., *J. Mater. Chem. A* **2018**, *6* (36), 17307-17311.

[31] Li, Z.; Ding, X.; Feng, Y.; Feng, W.; Han, B.-H., *Macromolecules* **2019**, *52* (3), 1257-1265.

[32] Workman, J., 26 - Dielectric Constants of Materials (In Alphabetical Order), in *The Handbook of Organic Compounds*, Workman, J., Ed. Academic Press: Burlington, 2001; pp 275-292.

[33] Evlampieva, N. P., Polushin, S. G., Lavrenko, P. N., Korneeva, E. V., Zgonnik, V. N., Ryumtsev, E. I., *Russ. J. Phys. Chem. A* **2000**, *74* (7), 1183-1187.

[34] Zhang, Y.; Huang, Z.; Ruan, B.; Zhang, X.; Jiang, T.; Ma, N.; Tsai, F. C., *Macromol. Rapid Commun.* **2020**, *41* (22), e2000402.

[35] Byrne, F. P.; Jin, S.; Paggiola, G.; Petchey, T. H. M.; Clark, J. H.; Farmer, T. J.; Hunt, A. J.; Robert McElroy, C.; Sherwood, J., *Sustain. Chem. Process.* **2016**, *4* (1), 7.

[36] Seoane, B.; Dikhtiarenko, A.; Mayoral, A.; Tellez, C.; Coronas, J.; Kapteijn, F.; Gascon, J., *CrystEngComm* **2015**, *17* (7), 1693-1700.

[37] Rietveld, H. M., *J. Appl. Crystallogr.* **1969**, *2* (2), 65-&.

[38] van der Jagt, R.; Vasileiadis, A.; Veldhuizen, H.; Shao, P.; Feng, X.; Ganapathy, S.; Habisreutinger, N. C.; van der Veen, M. A.; Wang, C.; Wagemaker, M.; van der Zwaag, S.; Nagai, A., *Chem. Mater.* **2021**, *33* (3), 818-833.

[39] Chen, X.; Dang, Q.; Sa, R.; Li, L.; Li, L.; Bi, J.; Zhang, Z.; Long, J.; Yu, Y.; Zou, Z., *Chem. Sci.* **2020**, *11* (26), 6915-6922.

[40] Wang, Z.; Li, Y.; Liu, P.; Qi, Q.; Zhang, F.; Lu, G.; Zhao, X.; Huang, X., *Nanoscale* **2019**, *11* (12), 5330-5335.

[41] Li, Z.; Ding, X. S.; Feng, Y. Y.; Feng, W.; Han, B. H., *Macromolecules* **2019**, *52* (3), 1257-1265.

[42] Auras, F.; Ascherl, L.; Hakimioun, A. H.; Margraf, J. T.; Hanusch, F. C.; Reuter, S.; Bessinger, D.; Doblinger, M.; Hettstedt, C.; Karaghiosoff, K.; Herbert, S.; Knochel, P.; Clark, T.; Bein, T., *J. Am. Chem. Soc.* **2016**, *138* (51), 16703-16710.

[43] Kuehl, V. A.; Wenzel, M. J.; Parkinson, B. A.; Oliveira, L. D.; Hoberg, J. O., *J. Mater. Chem. A* **2021**, *9* (27), 15301-15309.

[44] Emmerling, S. T.; Schuldt, R.; Bette, S.; Yao, L.; Dinnebier, R. E.; Kastner, J.; Lotsch, B. V., *J. Am. Chem. Soc.* **2021**, *143* (38), 15711-15722.

# 6 NO as a Reagent for Topochemical Framework Transformation and Controlled Nitric Oxide Release in Covalent Organic Frameworks

The work in this chapter was published, reproduced and adapted from:

*NO as a Reagent for Topochemical Framework Transformation and Controlled Nitric Oxide Release in Covalent Organic Frameworks*

Sebastian T. Emmerling,[⊥] Johannes Maschita,[⊥] and Bettina V. Lotsch

*ChemRxiv*. Cambridge: Cambridge Open Engage; **2022**; This content is a preprint and has not been peer-reviewed. DOI: 10.26434/chemrxiv-2022-czptr

Sebastian T. Emmerling[⊥] and Johannes Maschita[⊥] initiated the project and carried out all experiments, analysis and data interpretation. Bettina V. Lotsch supervised the project. The manuscript was discussed and written through contributions of all authors.

[⊥] S.E. and J.M. contributed equally to this work.

Supporting information can be found in chapter 8.4.

## *Abstract*

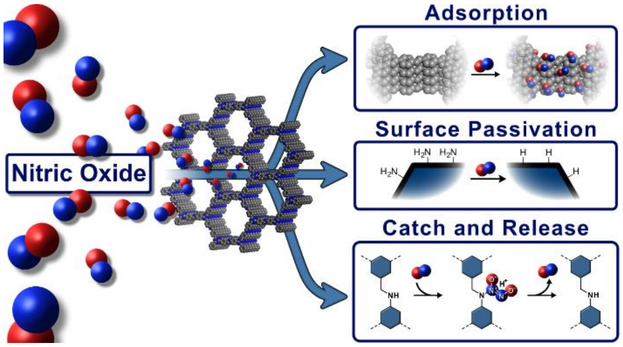

**Figure 6-1.** Table of contents figure for NO as a Reagent for Topochemical Framework Transformation and Controlled Nitric Oxide Release in Covalent Organic Frameworks

Covalent organic frameworks (COFs) have emerged as versatile platforms for the separation and storage of hazardous gases. Simultaneously, the synthetic toolbox to tackle the "COF trilemma" has been diversified to include topochemical linkage transformations and post-synthetic stabilization strategies. Herein, we converge these themes and reveal the unique potential of NO as a new reagent for the scalable gas-phase transformation of COFs. Using physisorption and solid-state nuclear magnetic resonance spectroscopy on $^{15}$N-enriched COFs, we study the gas uptake capacity and selectivity of NO adsorption and unravel the interactions of NO with COFs. Our study reveals the clean deamination of terminal amine groups on the particle surfaces by NO, exemplifying a unique surface passivation strategy for COFs. We further describe the formation of a NONOate-linkage by the reaction of NO with an amine-linked COF, which shows controlled release of NO under physiological

conditions. NONOate-COFs thus show promise as tunable NO delivery platforms for bioregulatory NO release in biomedical applications.

## 6.1 Introduction

Beginning in the late 1980s, nitric oxide (NO) gained increasing interest in biological research after its key role as signal molecule in various physiological processes in the human body was discovered.[1] While NO plays a significant role for human health by regulating blood pressure, wound healing, and neurotransmission,[2-5] it is more widely known as a (problematic) component of $NO_x$ found in exhaust gases of combustion engines.[6] With increasing road traffic, agriculture productivity, or electricity generation, artificial NO pollution became almost omnipresent in the environment around us.[7-9] However, in contrast to the essential NO needed for physiological processes, in which NO rarely exceeds an internal concentration of 5 nM, the artificial presence of NO in our external environment can have adverse effects on human health.[10-12] The combustion-based $NO_x$ emissions count as major air pollutants and as gaseous precursor of fine particulate matter ($PM_{2.5}$), which is considered a leading environmental health risk factor, associated with 3 to 4 million premature deaths each year and a significantly reduced life expectancy.[13] Environmental and healthcare organizations like the World Health Organization (WHO) repeatedly appeal for a reduction of air pollution and readjust their guidelines for $PM_{2.5}$ to lower levels.[14] Current strategies to reduce NO emissions are based on rare earth metal three-way catalysts, as found in automobiles, which reduce NO to nitrogen while simultaneously oxidizing noxious CO and hydrocarbons to $CO_2$.[15] Other strategies focus on capture and release systems, "washing" the exhaust gas by binding NO onto functional groups by forming nitrosamines, N-diazeniumdiolates (NONOates), and nitroso-metal-complexes.[16,17] The reversible formation of these species allows the subsequent controlled release and recycling of NO and can also be the basis of various pharmaceuticals.[18,19]

Recent advances in heterogeneous systems for NO release were made including surface-crafted polymers and silica particles with exposed NO-binding functional groups.[20-22] Lately, highly porous materials were discovered as candidates for NO removal *via* adsorption and chemisorption or as catalyst/catalyst support materials for NO decomposition.[23] Metal organic frameworks (MOF) have been developed as NO release materials utilizing either unsaturated and open metal sites or implemented amino functionalities to adsorb NO in their pores.[1,24,25]

Covalent organic frameworks (COFs) are recent additions to the class of highly porous framework materials.[26] Due to their high specific surface area, defined structure, high modularity and low density COFs could be promising candidates for NO adsorption/separation applications or as heterogeneous catalyst/catalyst support materials for NO decomposition.[27-29] Conductive COFs have already been successfully used in chemiresistive sensor devices to detect NO and other harmful gases in the ppb range.[30,31] Despite the possible applicability of COFs as functional materials for such applications, there remain concerns regarding their stability. Assembled into frameworks by reversible covalent bond formation, their stability against the reactive NO gas might be limited at these crucial points of connection. Especially early introduced and well-established linkages like boronic esters or imine bonds suffer from instability against harsher chemical conditions.[32] However, in recent years numerous novel linkages, post-synthetic-modifications and other stabilization strategies for COFs have been developed, broadening our tool-box to design materials that can be suitable for NO adsorption.[33-37]

In this work we determine the stability of four different COF linkages – imine, amine, thiazole, and imide – against NO exposure and examine their suitability for NO separation applications by calculating their specific selectivity against $N_2$ and $CO_2$. By targeted $^{15}N$ enrichment at the crucial COF-linkages, we investigate and identify chemical modifications in the COFs' frameworks induced by NO. These chemical modifications, including a novel type of linkage, are evaluated for their potential applications in COF chemistry and biomedical research.

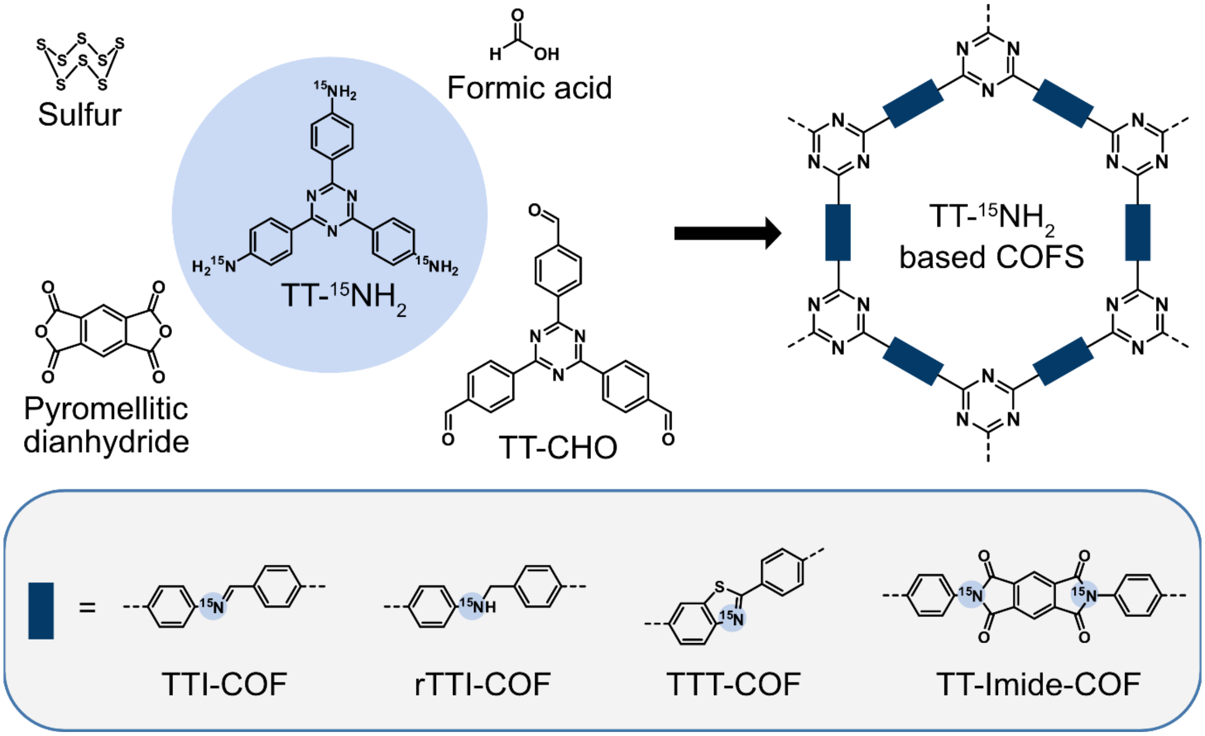

**Figure 6-2.** Synthesis of the four $^{15}N$-enriched COFs TTI-COF, rTTI-COF, TTT-COF and TT-Imide-COF bearing imine, amine, thiazole, and imide linkages, respectively. All COFs are based on an enriched 4,4',4''-(1,3,5-triazine-2,4,6-triyl)trianiline-$^{15}N$ linker, TT-$^{15}NH_2$, which was synthesized starting from 4-cyanobenzoyl chloride and $^{15}NH_4Cl$ (Scheme S8-1) in a three-step procedure with a good overall yield of 12.6 %.

## *6.2 Results and Discussion*

To study the effect of NO on COFs, we synthesized four $^{15}$N-enriched frameworks, namely TTI-COF, rTTI-COF, TTT-COF, and TT-Imide-COF (Figure 6-2),[33,37-39] which are all based on an enriched 4,4',4''-(1,3,5-triazine-2,4,6-triyl)trianiline-$^{15}$N linker (TT-$^{15}NH_2$, Figure 6-2). The isotope enrichment of the COFs enhances the sensitivity in $^{15}$N CP-MAS solid-state nuclear magnetic resonance (ssNMR) spectroscopy and thus allows a detailed analysis of the respective linkages. This is essential since we expect these nitrogen sites to be the most reactive groups towards NO and therefore to constitute the most interesting moieties in the COFs during this study.

### *NO Uptake*

NO sorption measurements on $^{15}$N-enriched COFs were performed starting at 298 K. In all cases, an initial high but only partially reversible adsorption capacity was found within the first adsorption cycle. In this first measurement COF-dependent uptakes between 1.5 and 6 mmol $g^{-1}$ NO were observed. In addition, a steep adsorption slope below 2 kPa for TT-Imide-COF and TTI-COF (Figure 6-3a and Figure S8-119), around 30 kPa for TTT-COF (Figure S8-123) and around 90 kPa for rTTI-COF was found (Figure S8-121). The steep uptake within the first cycle at different pressure points for each COF indicates differing mechanisms for the irreversible chemisorption of NO. Thus, in each case the hysteresis does not close to the initial point during the first measurement. Multiple adsorption and desorption cycles at 298 K show a strong decrease in NO uptake after the first cycle towards a fraction of the initial uptake. This trend of an initial high and irreversible NO uptake and its strong decline in further cycles indicates a chemisorption process of NO on the frameworks, consistent with a progressive quenching of the reactive sites.

For all frameworks, the decline in irreversible uptake of NO towards the second cycle is most prominent, while the following sorption cycles show only a small decrease which stabilizes after approximately three cycles (Figures S8-120, S8-122, S8-124, S8-125). To ensure reproducible NO physisorption data at different temperatures, all COFs were cycled seven times to ensure stabilization of the systems before measurements at 273 K, 288 K, and 298 K were performed (Figures 6-3b, c and Figure S8-126). In contrast to the initial NO sorption cycles, subsequent measurements show fully reversible isotherms for all four COFs indicating a saturation of the systems. Further, they reveal an unusual hysteresis due to delayed NO desorption visible for all temperatures and COFs.

The measured NO physisorption capacities at 298 K - ranging between 0.2 mmol $g^{-1}$ and 0.4 mmol $g^{-1}$ as compared to 1.5-6 mmol $g^{-1}$ during initial uptake - are in good agreement with the values found for simulated NO adsorption isotherms for boronate ester-based COF-105 and COF-108 by Wang *et al.*[40] Note that experimental values on NO sorption in COFs have not yet been reported.

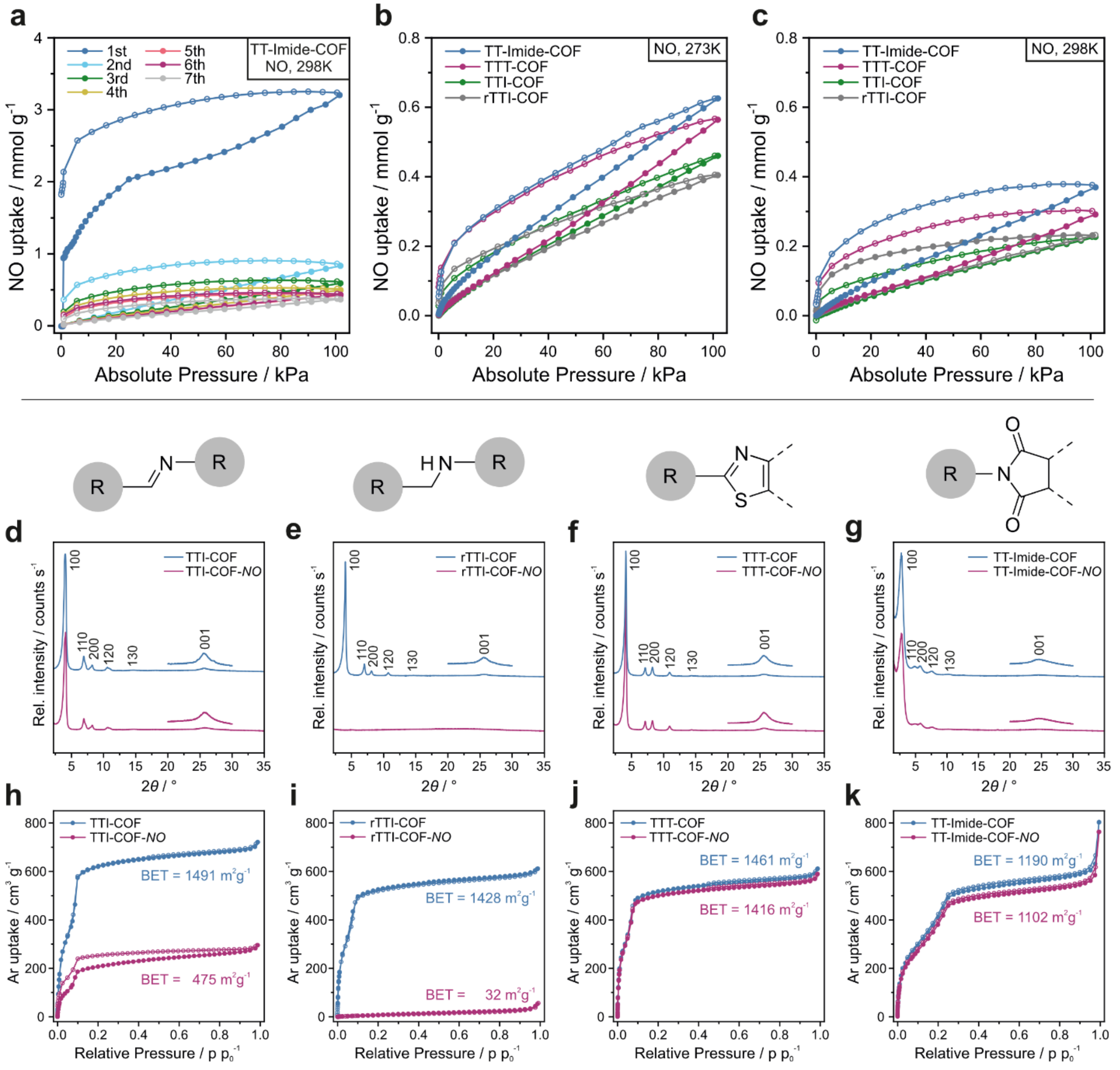

**Figure 6-3.** (a) NO-adsorption cycles of TT-Imide-COF. Comparison of stabilized NO-adsorption of TTI-COF, rTTI-COF, TTT-COF, and TT-Imide-COF at (b) 273 K and (c) 298 K after completing the 7th run. PXRD and argon sorption measurement at 87 K of TTI-COF (d,h), rTTI-COF (e,i), TTT-COF (f,j), and TT-Imide-COF (g,k) before (blue) and after (red) NO exposure. Filled circles represent the adsorption, empty circles the desorption.

The measured NO physisorption capacities at 298 K - ranging between 0.2 mmol $g^{-1}$ and 0.4 mmol $g^{-1}$ as compared to 1.5-6 mmol $g^{-1}$ during initial uptake - are in good agreement with the values found for simulated NO adsorption isotherms for boronate ester-based COF-105 and COF-108 by Wang *et al.*[40] Note that experimental values on NO sorption in COFs have not yet been reported.

Since the NO sorption measurements suggest a reaction of NO with the frameworks, we investigated the reactions occurring during contact with the highly reactive gas. At first, the stability of the COFs towards NO was evaluated by examining the materials after exposure. These will be labeled with *-NO* further on.

Powder X-ray diffraction (PXRD) analysis of the samples reveals that TTI-COF-*NO* becomes slightly less crystalline after NO exposure and rTTI-COF-*NO* turns amorphous (Figures 6-3d, e). The Brunauer–Emmett–Teller specific surface area ($S_{BET}$) and specific pore volume ($V_P$) decreases for the imine-COF (Figure 6-3h) from $S_{BET} = 1491\ m^2\ g^{-1}$ ($V_P = 0.917$) to less than a third for the post-NO imine-COF with $S_{BET} = 475\ m^2\ g^{-1}$ ($V_P = 0.376$). The amine-COF rTTI-COF (Figure 6-3i) with initially $S_{BET} = 1428\ m^2\ g^{-1}$ ($V_P = 0.778$) becomes non-porous after NO exposure with $S_{BET} = 32\ m^2\ g^{-1}$ ($V_P = 0.071\ cm^3\ g^{-1}$). For TTT-COF and TT-Imide-COF (Figures 6-3j, k) no changes in crystallinity after exposure are noticeable and the $S_{BET}$ and pore volume of the samples decrease just by small amounts from $1461\ m^2\ g^{-1}$ ($V_P = 0.778\ cm^3\ g^{-1}$) to $1416\ m^2\ g^{-1}$ ($V_P = 0.750\ cm^3\ g^{-1}$) and from $1190\ m^2\ g^{-1}$ ($V_P = 0.802\ cm^3\ g^{-1}$) to $1102\ m^2\ g^{-1}$ ($V_P = 0.744\ cm^3\ g^{-1}$), respectively. For the latter, the Fourier-transform infrared (FT-IR) spectra before and after NO exposure show no difference (Figures S8-99, S8-100). However, TTI-COF-*NO* displays a new band at 1699 $cm^{-1}$, a typical range for an aldehyde HC=O vibration, while otherwise remaining unchanged (Figure S8-97). The spectrum of rTTI-COF-*NO* shows significant changes compared to pristine rTTI-COF; most prominent is the appearance of three distinct bands at 1700 $cm^{-1}$, 1084 $cm^{-1}$, and 916 $cm^{-1}$ (Figure S8-98). We also observed a color change of the sample after NO exposure. UV-Vis measurements reveal slightly altered absorption spectra for the post-NO COFs (Figures S8-110 to S8-113). The most obvious color changes were perceived for TTI-COF and rTTI-COF– both changing from yellow to brownish color. This analysis reveals that the thiazole and imide linkages are largely inert against NO exposure since the structural integrity and porosity of the respective COFs remains unaffected. In contrast, the imine and amine linkages seem to react to a varying degree with the gas, indicated by changes in the FT-IR spectra, resulting in a loss of structural integrity and porosity.

Narrowing down suitable COF linkages for NO adsorption and separation applications to thiazole and imide functionalities, we further investigated the physisorption performance and calculated the selectivity for NO compared to carbon dioxide by applying the ideal adsorption solution theory (IAST). Using the post-NO $CO_2$ adsorption isotherms as a reference, we calculated the initial heats of adsorption, $Q_{st}$, adsorption capacities, and IAST selectivities over nitrogen for $CO_2$ and NO (Table S8-14). For the selectivity calculations we chose a 15/85 gas mixture for $CO_2/N_2$ as commonly found in the literature,[41] and a 3/97 gas mixture for $NO/N_2$, due to the low abundance of NO in exhaust gas mixtures.[42] We calculated the IAST selectivity of $CO_2$ over nitrogen for TT-Imide-COF-*NO* and TTT-COF-*NO* as 9.22 and 6.44, respectively. The IAST selectivities of NO over nitrogen were calculated to be 5.55 for the TT-Imide-COF-*NO* and 3.95 for TTT-COF-*NO*. Furthermore, the pressure dependent selectivties of a binary $CO_2$/NO (50/50) gas mixture were calculated (Figure S8-127c). Overall, our results show that imide- and thiazole-linked COFs exhibit remarkable resistance to NO gas and are promising platforms for NO gas capture or separation. Moreover, these systems show significant IAST selectivity of NO uptake over $N_2$.

### *Solid-State NMR Analysis*

Next, we turn our attention to the imine and amine linkages which are more susceptible to NO exposure. To deconvolute the irreversible chemisorption phenomenon during the first NO adsorption cycles and to gain insights into possible reactions involved, we performed $^{13}C$ and $^{15}N$ CP-MAS ssNMR experiments. Utilizing the high sensitivity of our $^{15}N$-enriched COFs we were able to capture even less-sensitive species like the thiazole nitrogen and minor framework defects as will be discussed in the following.

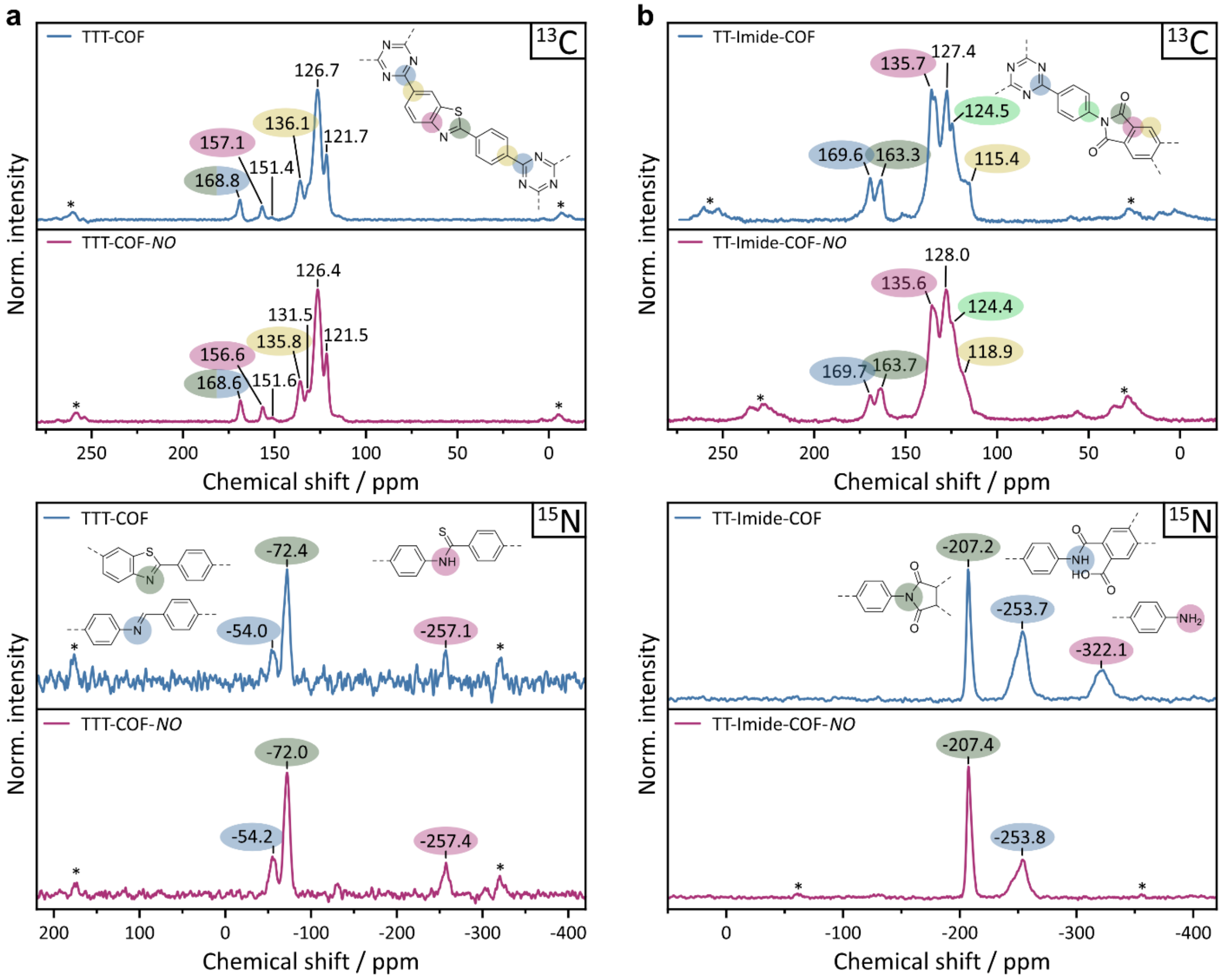

**Figure 6-4.** $^{13}C$ CP-MAS (top row) and $^{15}N$ CP-MAS ssNMR (bottom row) of (a) TTT-COF (blue) and TTT-COF-NO (red) and (b) TT-Imide-COF (blue) and TT-Imide-COF-NO (red).

As one of the NO resistant frameworks, TTT-COF-*NO* shows no visible changes in its $^{13}$C and $^{15}$N spectra compared to the pristine TTT-COF (Figure 6-4a). Interestingly, the high sensitivity of our $^{15}$N measurements reveals small amounts of imine residuals at -54 ppm (Figure 6-4a, bottom) that were not transformed into thiazole during the topochemical conversion. Another unexpected peak was found at -257 ppm, which we assign to a thioamide, the proposed intermediate of the topochemical conversion.[33] It should be noted that the intensities of both moieties are more pronounced in the CP-MAS experiments compared to thiazole due to polarization transfer from neighboring protons. The related signal for the imine bond in $^{13}$C CP-MAS ssNMR, expected at 151 ppm,[33] is barely visible. No obvious signs of the increased initial NO uptake are visible. Considering the relatively minor irreversible NO uptake of 1.5 mmol g$^{-1}$ compared to the other COFs (3-6 mmol g$^{-1}$), reactions of NO with remaining oligomer impurities, sulfur and/or remaining imine bonds, as observed for TTI-COF (infra vide), are plausible.

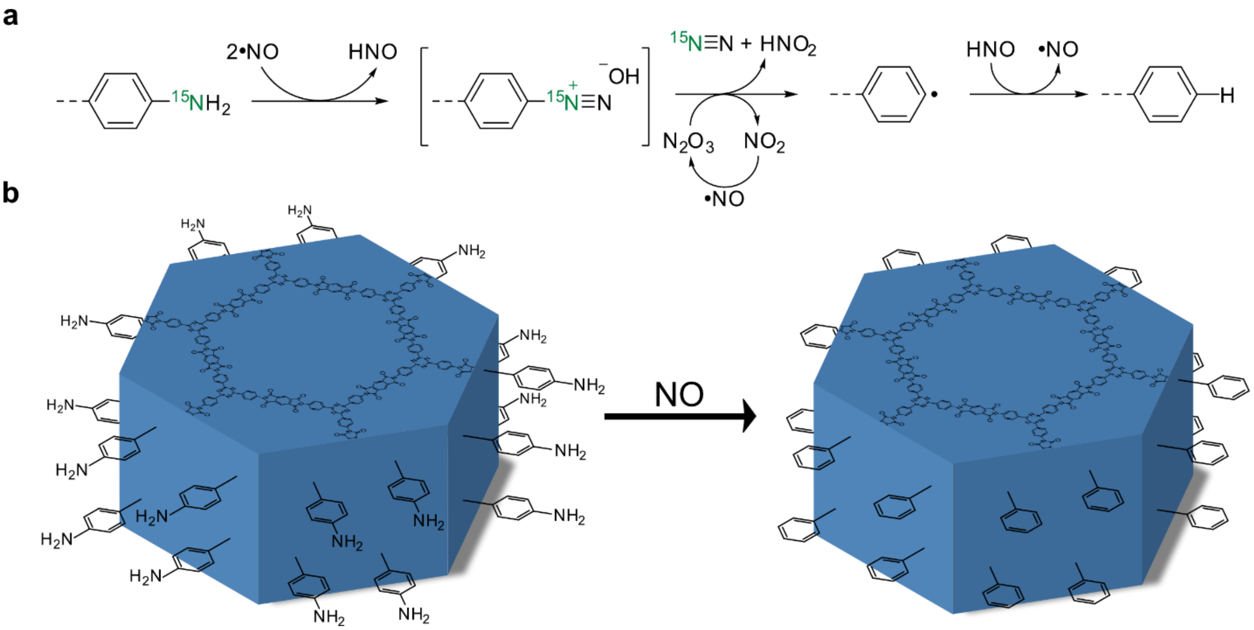

**Figure 6-5.** (a) Proposed mechanism for deamination of arylamines upon NO exposure. First, a diazonium salt is formed in the reaction of the free amine with NO. This salt further reacts with catalytic amounts of $N_2O_3$ impurities in the NO gas, cleaving the diazonium moiety as dinitrogen and nitrous acid. The resulting phenyl radical is subsequently quenched by exposure to the nitroxyl released in the first step or any other proton-bearing volatile compound, like $H_2O$.[43] (b) Schematic representation of crystal surface passivation of terminal amines by NO-induced deamination.

The $^{13}$C spectrum of TT-Imide-COF-*NO* resembles the spectrum of the pristine COF (Figure 6-4b, top). A minor peak broadening is observed which might be a result of slightly increased structural disorder of the framework. The $^{15}$N-CP-MAS spectrum of TT-Imide-COF reveals three signals at -207 ppm, -254 ppm, and -322 ppm, assigned to the imide, the intermediate amic acid, and the remaining terminal amine nitrogen at the crystallite edges, respectively (Figure 6-4b, bottom). However, only the imide signal is observed in a (quantitative) direct excitation experiment, suggesting that the proton-bearing species constitute a minor side phase and are overemphasized due to their sensitivity in CP-MAS experiments (Figure S8-102). Upon exposure to NO, the signal at -322 ppm, assigned to terminal amine groups, vanished completely, giving the first direct indication for a chemical reaction of the framework with the adsorbate. Furthermore, the relative intensity of the amide at -254 ppm is lowered compared to the imide at 207 ppm after NO treatment. Lacking any new signals, we suspect a clean conversion of the amines by NO, passivating the crystallite surface edges, according to a proposed denitrogenation radical reaction mechanism depicted in Figure 6-5 based on findings of Itoh *et al*. on the deamination of aniline.[43]

First, a diazonium salt is formed in the reaction of the free amine with NO. This salt further reacts with catalytic amounts of $N_2O_3$ impurities in the NO gas, cleaving the diazonium moiety as dinitrogen and nitrous acid. The resulting phenyl radical is subsequently quenched by exposure to the nitroxyl released in the first step or any other proton-bearing volatile compound, like $H_2O$. Due to the deamination of the enriched $^{15}N$ the amine peak disappears and no new signal is visible. We envision that this interaction between the free amine groups and the NO gas could be used as a rational surface passivation strategy to purposefully remove the remaining and potentially reactive amine sites. Clearing the COF's surface from terminal amines could be of particular interest when their chemical reactivity or electronic properties hinder or alter the targeted properties of the framework (e.g., in catalysis), especially when exposed at the crystal surface.

A reaction with the remaining amic acid intermediates remains uncertain. While a slight decline in the relative intensity compared to the imide signal is observed, only a single case of a reaction of NO with primary amides (under strongly basic conditions) has been reported in the literature, making at least a quantitative reaction unlikely in this case.[44]

Judging from the diffraction and sorption results, we expect more significant changes in the ssNMR spectra of TTI-COF and rTTI-COF. Indeed, TTI-COF shows a slight broadening of the peaks in the $^{13}C$ CP-MAS NMR after NO exposure and a new signal at 191 ppm appears (Figure 6-6a, top). This peak corresponds to the proposed aldehyde, visible in the FT-IR spectra as a new band at 1699 $cm^{-1}$. In parallel, a reduction of the imine signal intensity at 151 ppm compared to the remaining signals is observed, which is especially visible when comparing to the neighboring signal at 157 ppm. These findings indicate a partial cleavage of imine bonds, resulting in exposed aldehyde groups. The $^{15}N$ CP-MAS NMR of TTI-COF-*NO* exhibits the same removal of terminal amine groups (Figure 6-6a, bottom), visible at 316 ppm, by deamination after contact with NO as found for TT-Imide-COF (Figure 6-5). The imine signal at 58 ppm remains with minor peak broadening, as do the $^{13}C$ signals.

We rationalize these observations with an incipient decomposition according to a reaction mechanism upon NO contact shown in Scheme S8-4: By a [2+2] cycloaddition of NO to the imine bond, as described by Hrabie *et al.* for Schiff-bases,[45] the adduct is cleaved into the free aldehyde as observed by the $^{13}C$ signal at 191 ppm, and a diazo radical. Subsequently, an aryl radical is formed by elemination of nitrogen, which is ultimately quenched.

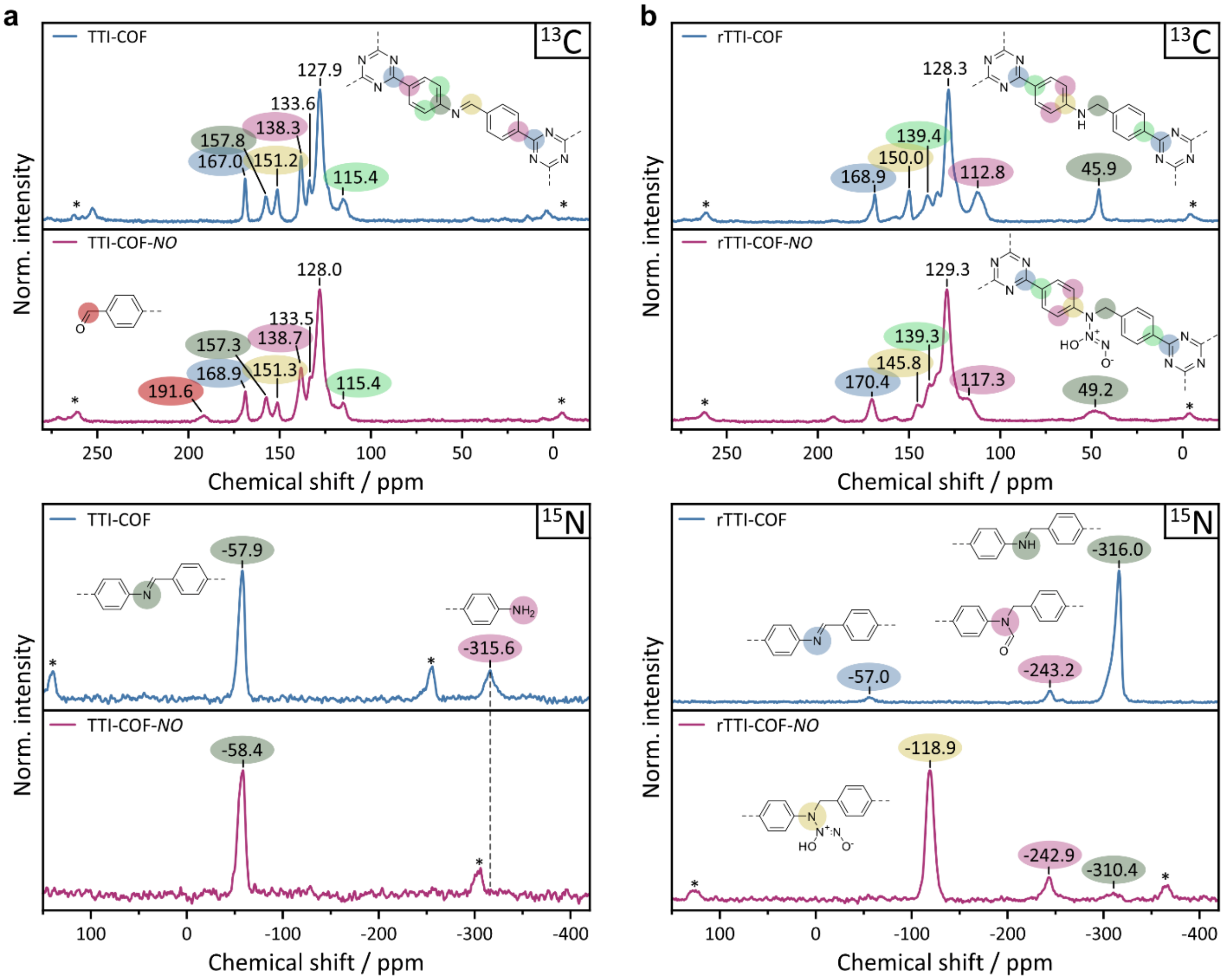

**Figure 6-6.** $^{13}C$ (top row) and $^{15}N$ CP-MAS (bottom row) ssNMR of (a) TTI-COF (blue) and TTI-COF-NO (red) and (b) rTTI-COF (blue) and rTTI-COF-NO (red).

rTTI-COF-*NO* shows a strong broadening of all signals in the $^{13}C$ spectrum (Figure 6-6b, top). Especially the benzylic quaternary carbon at 49 ppm broadens and almost disappears into the background. This observation reflects the disorder introduced into the framework and is in good agreement with the amorphization and loss of long-distance order seen in the PXRD pattern (Figure 6-3e). The $^{15}N$ spectrum reveals a significant shift of the $^{15}N$ signal of the linkage (Figure 6-6b, bottom). The secondary amine-related peak of rTTI-COF at 316 ppm shifts to 119 ppm for rTTI-COF-*NO*, indicating a complete transformation of the bond. This novel linkage is identified as *N*-diazeniumdiolate (NONOate), a species that is also observed during NO adsorption in amine functionalized MOFs and is formed by the addition of two equivalents of NO to the amine linkage of rTTI-COF at 95 kPa NO pressure (Figures 6-7a, b).[1,24] The post-synthetic linkage modification is mirrored in the FT-IR spectrum by the appearance of three new, distinct bands at 1700 cm$^{-1}$, 1084 cm$^{-1}$, and 916 cm$^{-1}$ as mentioned above (Figure S8-98). The complete disappearance of the $^{15}$N-amine indicates full conversion of the amine into the NONOate linkage. Introducing such polar, bulky NONOate groups adds both steric and electrostatic repulsion between the layers, thus forcing the layers to distort and shift, resulting in the observed loss of long-range order, layer integrity and porosity. Besides this drawback, the described simple gas phase modification of amine-linked COFs by NO introducing NONOate groups displays exciting new possibilities for the design of polymers and COFs bearing novel linkages and functionalities.

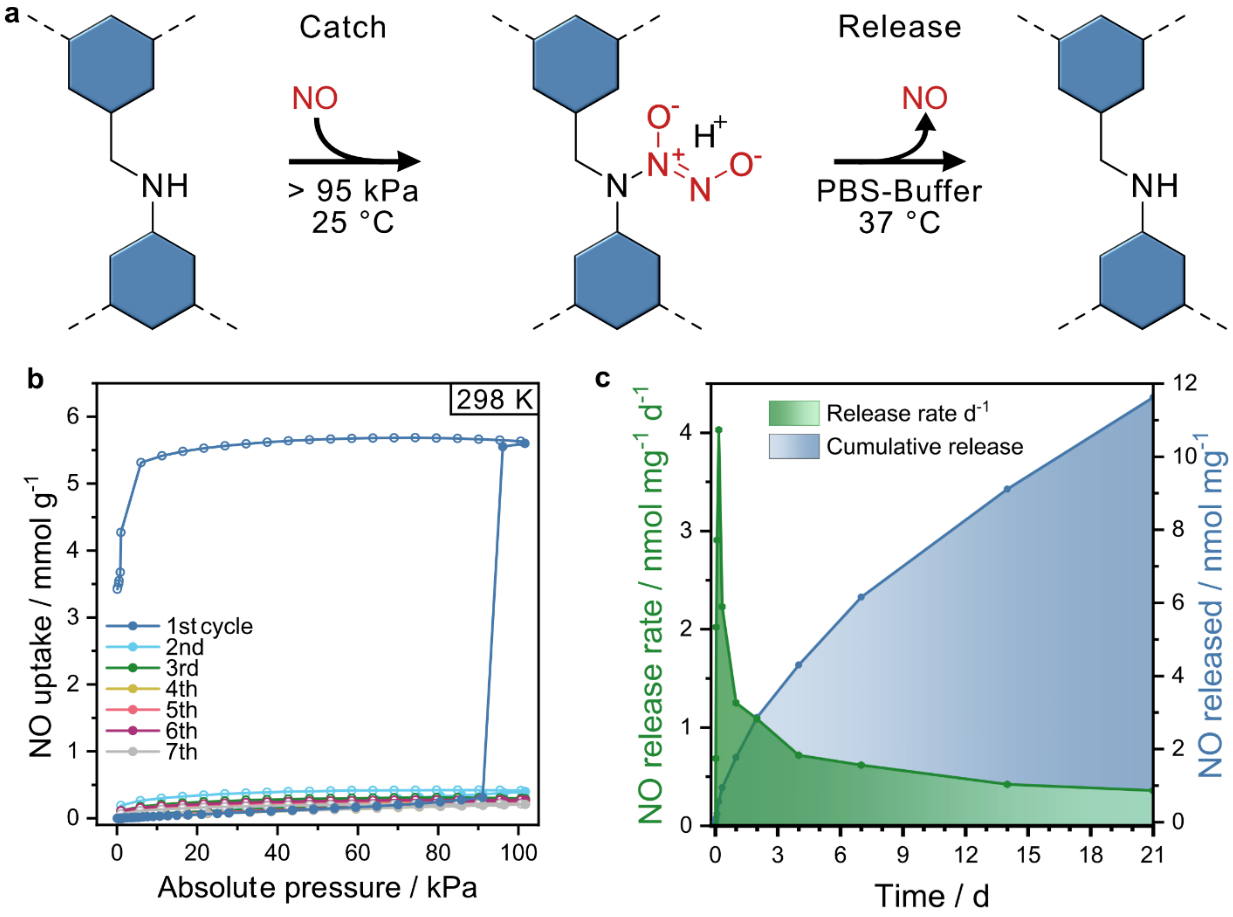

**Figure 6-7.** (a) Catch and release steps of the secondary amine-COF-linkage. (b) NO adsorption cycles of rTTI-COF. (c) NO release and estimated release rate of rTTI-COF-NO in a pH 7.4 PBS-buffer solution monitored by the Griess assay.

### *NO Release*

Along these lines, implementing NONOate functional groups holds great promise towards COFs as nitric oxide releasing delivery platforms for bioregulatory NO release in therapeutic or medicinal chemistry applications (Figure 6-7a).[5,46,47] Nitric oxide release under physiological conditions was tested by suspending rTTI-COF-*NO* in a pH 7.4 PBS-buffer solution at 37 °C and monitoring the NO release using a Griess assay.[48] The NO release profile of rTTI-COF-*NO* shows an exponential release behavior with an overall very slow but steady release of the chemisorbed NO over several days (Figure 6-7c). An initial faster release over the first 24 h of around 1.8 nmol NO is observed, followed by a long period of 3 weeks in which another 9.9 nmol NO is released. After NO release, crystallinity and specific surface area are partially recovered (Figures S8-96, S8-130), evidencing the successful rearrangement of the regenerated amine-linked domains into an ordered structure. While the total amount of NO delivered by the COF is significantly lower than the NO physiosorbed in recently published MOFs or polymers,[23,46,49] they are well in the concentration range of physiological processes.[10,50] In addition, the controlled release of NO over such long periods (i.e. multiple days to weeks) sets rTTI-COF-*NO* apart from the typical rapid release over seconds to hours observed for other NONOate derivatives and suggests that NONOate-COFs could be promising candidates for wound healing or related applications where a slow NO release is key.[18,50] Unlike MOFs, COFs also do not contain heavy metals that can prevent their use in pharmaceuticals. Further, we presume that the origin of this moderate but gradual release is due to the limited diffusion of water into and NO out of the disordered and non-porous, but flexible framework. The diffusion of water into the framework is crucial to protonate the NONOate functional groups and trigger the NO release. Hence, control over the crystallinity during linkage transformation may be used to control the rate and amount of NO released by NONOate-COFs. Crystallinity and therefore enhanced accessibility of the NONOate functional groups in the COF pores could be achieved by implementing readily available strategies to direct and lock the layer stacking, or by using 3D COFs.[51-54]

Taken together, our NMR analysis explains the different linkage stabilities and transformations, and rationalizes the observed initial irreversible adsorption behavior, which is largely due to the chemical reaction of NO with terminal amine groups or linkages of the frameworks.

## *6.3 Conclusion*

We have identified NO as a synthetically flexible reagent for the rational topochemical framework modification in COFs. We have developed a straightforward synthesis of a $^{15}$N enriched version of the commonly used TT-amine linker, which was successfully used to prepare multiple COFs with varying linkage chemistries – imine, amine, thiazole, and imide. The $^{15}$N-enriched linkage-archetypes were then used as chemical probes to verify the existence of previously postulated terminal groups and reaction intermediates during linkage formation and modification. We demonstrated that all frameworks with unreacted terminal amine sites can be quantitatively passivated with NO by a denitrogenation reaction, leading to a clean surface defunctionalization of the frameworks. In addition, we could show that the reactivity of the different linkages towards NO is distinctly different:

While imide and thiazole-linked COFs were found to be largely unreactive towards NO, imine and amine-linked COFs undergo local (imine) and global (amine) linkage conversions leading to significant changes in the surface area and framework crystallinity. We have further demonstrated a topochemical modification of amine-linked COFs by NO, forming the novel NONOate COF linkage by a solid-gas phase reaction at room temperature. Controlled and extended NO release by this NONOate linkage was observed under physiological conditions, which opens the door to the use of amine-linked COFs as potential platforms for "NO catch and release" scenarios in biomedical applications. We have thus demonstrated that besides being toxic and highly reactive, NO is a versatile reagent for crystal surface and linkage modification, thus greatly expanding the synthetic toolbox of COF chemistry.

## 6.4 Bibliography

[1] K. Peikert, L. J. McCormick, D. Cattaneo, M. J. Duncan, F. Hoffmann, A. H. Khan, M. Bertmer, R. E. Morris, M. Fröba, *Microporous Mesoporous Mater.* **2015**, *216*, 118–126.

[2] M. Shabani, S. K. Pulfer, J. P. Bulgrin, D. J. Smith, *Wound Repair Regen.* **1996**, *4*, 353–362.

[3] M. T. Gladwin, J. H. Crawford, R. P. Patel, *Free Radic. Biol. Med.* **2004**, *36*, 707–717.

[4] A. W. Carpenter, M. H. Schoenfisch, *Chem. Soc. Rev.* **2012**, *41*, 3742–3752.

[5] S. Paul, S. Pan, A. Mukherjee, P. De, *Mol. Pharm.* **2021**, *18*, 3181–3205.

[6] E. Sher, *Handbook of Air Pollution From Internal Combustion Engines*. Elsevier, **1998**.

[7] F. Klingstedt, K. Arve, K. Eränen, D. Y. Murzin, *Acc. Chem. Res.* **2006**, *39*, 273–282.

[8] S. Roy, A. Baiker, *Chem. Rev.* **2009**, *109*, 4054–4091.

[9] W. Song, X. Y. Liu, C. C. Hu, G. Y. Chen, X. J. Liu, W. W. Walters, G. Michalski, C. Q. Liu, *Nat. Commun.* **2021**, *12*, 243.

[10] C. N. Hall, J. Garthwaite, *Nitric Oxide - Biol. Chem.* **2009**, *21*, 92–103.

[11] G. B. Hamra, F. Laden, A. J. Cohen, O. Raaschou-Nielsen, M. Brauer, D. Loomis, *Environ. Health Perspect.* **2015**, *123*, 1107–1112.

[12] O. K. Kurt, J. Zhang, K. E. Pinkerton, *Curr. Opin. Pulm. Med.* **2016**, *22*, 138.

[13] V. A. Southerland, M. Brauer, A. Mohegh, M. S. Hammer, A. van Donkelaar, R. V Martin, J. S. Apte, S. C. Anenberg, *Lancet Planet. Heal.* **2022**, *6*, e139–e146.

[14] World Health Organization. Regional Office for Europe & Joint WHO/Convention Task Force on the Health Aspects of Air Pollution: Health risks of particulate matter from long-range transboundary air pollution, **2006**, Copenhagen: WHO Regional Office for Europe.

[15] P. Granger, V. I. Parvulescu, *Chem. Rev.* **2011**, *111*, 3155–3207.

[16] J. F. Quinn, M. R. Whittaker, T. P. Davis, *J. Control. Release* **2015**, *205*, 190–205.

[17] J. Cheng, K. He, Z. Shen, G. Zhang, Y. Yu, J. Hu, *Front. Chem.* **2019**, *7*, 530.

[18] M. R. Miller, I. L. Megson, *Br. J. Pharmacol.* **2007**, *151*, 305–321.

[19] S. P. Nichols, W. L. Storm, A. Koh, M. H. Schoenfisch, *Adv. Drug Deliv. Rev.* **2012**, *64*, 1177–1188.

[20] M. M. Reynolds, J. A. Hrabie, B. K. Oh, J. K. Politis, M. L. Citro, L. K. Keefer, M. E. Meyerhoff, *Biomacromolecules* **2006**, *7*, 987–994.

[21] J. H. Shin, S. K. Metzger, M. H. Schoenfisch, *J. Am. Chem. Soc.* **2007**, *129*, 4612–4619.

[22] J. Kim, Y. Lee, K. Singha, H. W. Kim, J. H. Shin, S. Jo, D. K. Han, W. J. Kim, *Bioconjug. Chem.* **2011**, *22*, 1031–1038.

[23] A. C. McKinlay, B. Xiao, D. S. Wragg, P. S. Wheatley, I. L. Megson, R. E. Morris, *J. Am. Chem. Soc.* **2008**, *130*, 10440–10444.

[24] A. H. Khan, K. Peikert, F. Hoffmann, M. Fröba, M. Bertmer, *J. Phys. Chem. C* **2019**, *123*, 4299–4307.

[25] A. M. Wright, C. Sun, M. Dincă, *J. Am. Chem. Soc.* **2021**, *143*, 681–686.

[26] C. Diercks, M. Kalmutzki, O. Yaghi, *Molecules* **2017**, *22*, 1575.

[27] Y. Ge, H. Zhou, Y. Ji, L. Ding, Y. Cheng, R. Wang, S. Yang, Y. Liu, X. Wu, Y. Li, *J. Phys. Chem. C* **2018**, *122*, 27495–27506.

[28] X. Cao, Z. Wang, Z. Qiao, S. Zhao, J. Wang, *ACS Appl. Mater. Interfaces* **2019**, *11*, 5306–5315.

[29] Y. Huang, X. Hao, S. Ma, R. Wang, Y. Wang, *Chemosphere* **2022**, *291*, 132795.

[30] Z. Meng, R. M. Stolz, K. A. Mirica, *J. Am. Chem. Soc.* **2019**, *141*, 11929–11937.

[31] M. Yar, K. Ayub, *Microporous Mesoporous Mater.* **2020**, *300*, 110146.

[32] S. Kandambeth, A. Mallick, B. Lukose, M. V. Mane, T. Heine, R. Banerjee, *J. Am. Chem. Soc.* **2012**, *134*, 19524–19527.

[33] F. Haase, E. Troschke, G. Savasci, T. Banerjee, V. Duppel, S. Dörfler, M. M. J. Grundei, A. M. Burow, C. Ochsenfeld, S. Kaskel, B. V. Lotsch, *Nat. Commun.* **2018**, *9*, 1–10.

[34] A. Halder, M. Ghosh, A. Khayum M, S. Bera, M. Addicoat, H. S. Sasmal, S. Karak, S. Kurungot, R. Banerjee, *J. Am. Chem. Soc.* **2018**, *140*, 10941–10945.

[35] C. Zhao, C. S. Diercks, C. Zhu, N. Hanikel, X. Pei, O. M. Yaghi, *J. Am. Chem. Soc.* **2018**, *140*, 16438–16441.

[36] H. Lyu, C. S. Diercks, C. Zhu, O. M. Yaghi, *J. Am. Chem. Soc.* **2019**, *141*, 6848–6852.

[37] L. Grunenberg, G. Savasci, M. W. Terban, V. Duppel, I. Moudrakovski, M. Etter, R. E. Dinnebier, C. Ochsenfeld, B. V. Lotsch, *J. Am. Chem. Soc.* **2021**, *143*, 3430–3438.

[38] F. Haase, K. Gottschling, L. Stegbauer, L. S. Germann, R. Gutzler, V. Duppel, V. S. Vyas, K. Kern, R. E. Dinnebier, B. V. Lotsch, *Mater. Chem. Front.* **2017**, *1*, 1354–1361.

[39] X. Zhu, S. An, Y. Liu, J. Hu, H. Liu, C. Tian, S. Dai, X. Yang, H. Wang, C. W. Abney, S. Dai, *AIChE J.* **2017**, *63*, 3470–3478.

[40] L. Wang, L. Wang, J. Zhao, T. Yan, *J. Appl. Phys.* **2012**, *111*, 112628.

[41] S. Bin Baek, D. Moon, R. Graf, W. J. Cho, S. W. Park, T. U. Yoon, S. J. Cho, I. C. Hwang, Y. S. Bae, H. W. Spiess, H. C. Lee, K. S. Kim, *Proc. Natl. Acad. Sci. U. S. A.* **2015**, *112*, 14156–14161.

[42] S. Eckert, S. Rakowski, *Grundlagen Verbrennungsmotoren*, Springer Fachmedien Wiesbaden, Wiesbaden, **2014**.

[43] T. Itoh, K. Nagata, Y. Matsuya, M. Miyazaki, A. Ohsawa, *J. Org. Chem.* **1997**, *62*, 3582–3585.

[44] R. J. Holland, J. R. Klose, J. R. Deschamps, Z. Cao, L. K. Keefer, J. E. Saavedra, *J. Org. Chem.* **2014**, *79*, 9389–9393.

[45] J. A. Hrabie, A. Srinivasan, C. George, L. K. Keefer, *Tetrahedron Lett.* **1998**, *39*, 5933–5936.

[46] N. A. Stasko, M. H. Schoenfisch, *J. Am. Chem. Soc.* **2006**, *128*, 8265–8271.

[47] Y. L. Zhao, S. L. Garrison, C. Gonzalez, W. D. Thweatt, M. Marquez, *J. Phys. Chem. A* **2007**, *111*, 2200–2205.

[48] J. Sun, X. Zhang, M. Broderick, H. Fein, *Sensors* **2003**, *3*, 276–284.

[49] H. T. T. Duong, K. Jung, S. K. Kutty, S. Agustina, N. N. M. Adnan, J. S. Basuki, N. Kumar, T. P. Davis, N. Barraud, C. Boyer, *Biomacromolecules* **2014**, *15*, 2583–2589.

[50] Y. Kang, J. Kim, Y. M. Lee, S. Im, H. Park, W. J. Kim, *J. Control. Release* **2015**, *220*, 624–630.

[51] Y. B. Zhang, J. Su, H. Furukawa, Y. Yun, F. Gándara, A. Duong, X. Zou, O. M. Yaghi, *J. Am. Chem. Soc.* **2013**, *135*, 16336–16339.

[52] Y. Liu, Y. Ma, J. Yang, C. S. Diercks, N. Tamura, F. Jin, O. M. Yaghi, *J. Am. Chem. Soc.* **2018**, *140*, 16015–16019.

[53] S. B. Alahakoon, K. Tan, H. Pandey, S. D. Diwakara, G. T. McCandless, D. I. Grinffiel, A. Durand-Silva, T. Thonhauser, R. A. Smaldone, *J. Am. Chem. Soc.* **2020**, *142*, 12987–12994.

[54] S. T. Emmerling, R. Schuldt, S. Bette, L. Yao, R. E. Dinnebier, J. Kästner, B. V. Lotsch, *J. Am. Chem. Soc.* **2021**, *143*, 15711–15722.

# 7 *Conclusion*

In contrast to the classical synthesis of amorphous 1D-PIs, where imide formation is essentially irreversible and leads to kinetic products (Figure 2-2), and the hydrothermal method for the synthesis of crystalline 1D-PIs, where the need for reversible bond formation is circumvented by pre-orienting the monomers using an intermediate salt (Figure 2-3),[1] imide cyclization in PI-COF synthesis is carried out reversibly following the principles of dynamic covalent chemistry.[2] However, as discussed in Section 1.1.3, the three properties of crystallinity, stability, and functionality compete with each other in reversible COF synthesis.[3] The exceptional stability and consequent low reversibility of the imide linkage make the synthesis of PI-COFs particularly challenging. To overcome these challenges and to advance research in this field, two additional synthesis protocols for the bulk preparation of PI-COFs were developed in this work – the ionothermal method and the hydrothermal method.[4-5]

In the ionothermal synthesis protocol, the anhydride and amine functionalized precursor molecules are mixed with anhydrous zinc chloride and heated to reaction temperatures ranging from 280 °C to 300 °C. Using this method, the synthesis of PI-COFs from robust linker molecules such as TAPB, PMDA, and PTCDA was demonstrated. COF formation using the ionothermal approach does not require toxic solvents and additional base catalysts. In contrast to the classical solvothermal synthesis, this method does not require soluble precursors, and the reaction time could be significantly reduced to a few hours as opposed to 3-7 days. However, the high reaction temperature required for ionothermal synthesis using pure $ZnCl_2$ as the reaction medium limits the selection of suitable linker molecules, as they may decompose under these harsh reaction conditions. To increase the generality of the developed synthesis protocol, we used a eutectic salt mixture of $ZnCl_2$/NaCl/KCl, which resulted in a decrease of the reaction temperature to 250 °C. The achieved temperature reduction allowed the preparation of PI-COFs from less stable linker molecules such as TAPA and TT. Mechanistic studies on the example of TAPB-PMDA-COF using *in situ* high-temperature XRPD revealed that crystalline adducts are formed from the respective precursors and $ZnCl_2$ and act as intermediates in the ionothermal synthesis of the COF. Quantum chemical calculations indicate that these intermediates activate the anhydride and imide rings, lowering the overall activation barrier, leading to a higher degree of reversibility in COF formation, ultimately resulting in well-crystalline high surface area materials.

Inspired by the hydrothermal synthesis approach for crystalline 1D PIs presented by Unterlass and co-workers,[1] we developed an environmentally friendly alcohol-assisted hydrothermal polymerization (aaHTP) approach for the synthesis of imide-linked COFs. Initial attempts to synthesize PI-COFs in pure water did not lead to crystalline products, which was due to the reduced solubility of the precursor molecules and formed oligomers under hydrothermal conditions that hindered the exchange of the amine linker molecule from the precipitated amorphous network during the defect healing processes. However, the addition of small amounts of different n-alcohols improves the solubility of the precursor molecules and the less polar imide dimers and oligomers are retained in solution for longer periods of time, as the longer chain n-alcohols exhibit surfactant-like behavior and can interact with the less polar benzyl groups of the oligomers in a manner similar to that observed during the formation of surfactant-based MOFs.[6] The aaHTP enables the synthesis of a wide range of imide-linked COFs, including a new PI-COF crystallizing in a *kagome*-type structure, in reaction mixtures consisting of up to 90 % water, thus providing an environmentally friendly and general alternative to the previously known solvothermal and ionothermal synthesis methods. In addition to the direct synthesis of PI-COFs from their respective linker molecules, we demonstrated the applicability of aaHTP in COF-to-COF transformations by linkage exchange of imine-linked COFs in an environmentally friendly manner. Using the linkage exchange strategy, we were able to synthesize the imide-linked PyTTA-PMDA-COF, a COF that was previously inaccessible.

Thus, in this work, we were able to overcome the stability-crystallinity dilemma in the synthesis of PI-COFs and identify universal and environmentally friendly synthesis alternatives. However, the synthesis of crystalline PI-COFs still requires harsh reaction conditions such as high reaction temperatures of >180 °C, Lewis acidic environments, or high pressures. As a consequence of the harsh reaction conditions, the COF trilemma for PI-COFs in terms of functionality could not be fully solved, since functional groups generally do not survive these harsh conditions and therefore functional PI-COFs cannot be prepared by these methods. However, the importance of this work is underscored by the many other synthetic approaches to the preparation of imide-linked COFs developed by other groups during the preparation of this work, including high-temperature solid-state synthesis,[7] interfacial synthesis,[8] hydrothermal synthesis,[9] and ionic liquid synthesis.[10] However, most of these strategies have only been demonstrated for single specific systems and are not generally applicable. Nevertheless, the development of additional complementary synthetic approaches is essential for the synthesis of novel PI-COFs, as demonstrated by the synthesis of TAPB-PTCDA-COF, TAPE-PMDA-COF, or PyTTA-PMDA-COF, which could be synthesized exclusively by the ionothermal and aaHTP methods, respectively, newly developed in this work. Furthermore, based on the obtained knowledge, new methods could be developed in the future that can cope with milder reaction conditions and thus allow the synthesis of functionalized PI-COFs.

To investigate COFs as potential platforms for specific physisorption of highly reactive nitric oxide gas, four different COFs were synthesized, differing only in their respective linkages, including the imine-linked TTI-COF, the amine-linked rTTI-COF, the thiazole-based TTT-COF, and the imide-linked TT-PMDA-COF. All four COFs are based on the TT-$^{15}NH_2$ linker enriched with $^{15}N$ allowing detailed analysis of the linkage nitrogen before and after NO contact. Prior to the NO sorption experiments, the improved sensitivity of $^{15}N$ CP-MAS ss-NMR spectroscopy allowed us to prove the existence of previously postulated terminal groups and reaction intermediates during bond formation and modification. By analyzing the materials after NO contact, we were able to show that the reactivity of the different linkages towards NO is significantly different: while imide- and thiazole-linked COFs were found to be largely unreactive towards NO and thus represent suitable platforms for NO physisorption applications, imine- and amine-linked COFs undergo local (imine) and global (amine) linkage transformations leading to significant changes in surface area and framework crystallinity. While the imine bond is successively cleaved by NO, leading to slow decomposition of the material, the amine bond is topochemically transformed by NO to form the novel NONOate-COF linkage at room temperature. This NONOate linkage exhibits controlled and prolonged NO release under physiological conditions, enabling the use of amine-linked COFs as potential platforms for "NO catch-and-release" or drug delivery scenarios in biomedical applications. In addition to the reaction of NO with the various linkages, we demonstrated that all frameworks with unreacted terminal amine sites can be quantitatively passivated with NO by a reductive denitrogenation reaction, leading to a clean surface defunctionalization of the frameworks. Thus, we have demonstrated that NO is not only toxic and highly reactive, but also a versatile reagent for altering crystal surfaces and linkages, thus greatly expanding the synthetic toolbox of COF chemistry.

Having provided proof of concept for NO as a reagent for topochemical framework transformations and the suitability of COFs for NO gas storage and separation applications, further studies are needed to unlock the full potential of our findings. In this regard, a wider range of COFs with different linkages and/or binding sites for NO should be tested to investigate and improve NO uptake capacity and selectivity. Moreover, the effect of the surface passivation strategy in actual catalytic reactions where free amine groups could affect the conversion rate of the reaction should be investigated in detail. Furthermore, the transformation to NONOate-linked COFs should be optimized to develop a universally applicable strategy for the synthesis of crystalline NONOate-linked COFs. One way to obtain crystalline systems could be to use linker molecules that have stronger π-π interactions or interpenetrating structures that could stabilize the framework and prevent its amorphization upon insertion of the bulky and ionic NONOate groups. Another strategy could be to change the reaction conditions so that vacuum is no longer required, which could prevent pore collapse. This could be achieved, for example, by simply passing NO gas over the COF to be converted and then purging with dry inert gas. Finally, more sophisticated NO catch and release experiments should be performed with optimized and crystalline COFs to significantly improve performance and make them competitive with state of the art molecular or polymeric systems.

## *7.1 Bibliography*

[1] B. Baumgartner, M. J. Bojdys, M. M. Unterlass, *Polym. Chem.* **2014**, *5*, 3771-3776.

[2] Q. Fang, Z. Zhuang, S. Gu, R. B. Kaspar, J. Zheng, J. Wang, S. Qiu, Y. Yan, *Nat. Commun.* **2014**, *5*, 4503.

[3] F. Haase, B. V. Lotsch, *Chem. Soc. Rev.* **2020**, *49*, 8469-8500.

[4] J. Maschita, T. Banerjee, G. Savasci, F. Haase, C. Ochsenfeld, B. V. Lotsch, *Angew. Chem. Int. Ed. Engl.* **2020**, *59*, 15750-15758.

[5] J. Maschita, T. Banerjee, B. V. Lotsch, *Chem. Mater.* **2022**, *34*, 2249-2258.

[6] B. Seoane, A. Dikhtiarenko, A. Mayoral, C. Tellez, J. Coronas, F. Kapteijn, J. Gascon, *CrystEngComm* **2015**, *17*, 1693-1700.

[7] T. Wang, R. Xue, H. Chen, P. Shi, X. Lei, Y. Wei, H. Guo, W. Yang, *New J. Chem.* **2017**, *41*, 14272-14278.

[8] K. Liu, H. Qi, R. Dong, R. Shivhare, M. Addicoat, T. Zhang, H. Sahabudeen, T. Heine, S. Mannsfeld, U. Kaiser, Z. Zheng, X. Feng, *Nat. Chem.* **2019**, *11*, 994-1000.

[9] T. Kim, S. H. Joo, J. Gong, S. Choi, J. H. Min, Y. Kim, G. Lee, E. Lee, S. Park, S. K. Kwak, H. S. Lee, B. S. Kim, *Angew. Chem. Int. Ed. Engl.* **2022**, *61*, e202113780.

[10] L. Zhao, H. Liu, Y. Du, X. Liang, W. Wang, H. Zhao, W. Li, *New J. Chem.* **2020**, *44*, 15410-15414.

# 8 Appendix

## 8.1 Abbreviations

| | |
|---|---|
| 1D | one-dimensional |
| 2D | two-dimensional |
| 3D | three-dimensional |
| aaHTP | alcohol-assisted hydrothermal polymerization |
| CFMM | continuous fast multipole method |
| COF | covalent organic framework |
| CON | covalent organic nanosheet |
| COP | covalent organic polymer |
| CP-MAS | cross-polarization magic angle-spinning |
| CTF | covalent triazine framework |
| DCC | dynamic covalent chemistry |
| DMAc | dimethylacetamide |
| DMF | *N,N*-Dimethylformamide |
| Dp | 4,4'-diaminobiphenyl |
| EDX | energy-dispersive X-ray |
| FT-IR | fourier transform infrared spectroscopy |
| GC | glassy carbon |
| HPP | high-performance polymer |
| HTTP | hydrothermal polymersization |
| HT-XRPD | in situ high temperature X-Ray powder diffraction |
| IAST | ideal adsorption solution theory |
| LIB | Li-ion battery |
| LSB | lithium-sulfur batteries |

| | |
|---|---|
| M(TAPc) | 2,3,9,10,16,17,23,24-octacarboxyphthalocyanine tetraanhydride |
| MA | melamine |
| MOF | metal-organic framework |
| MTA | mellitic trianhydride |
| NDA | naphthalene-1,4,5,8-tetracarboxylic acid anhydride |
| NMP | *N*-methyl-2-pyrrolidone |
| NMR | nuclear magnetic resonance spectroscopy |
| NO | nitric oxide |
| NONOate | *N*-diazeniumdiolate |
| PE | polyethylene |
| PF | poly-phenol-formaldehyde |
| Ph | *p*-phenylenediamine |
| PI | polyimide |
| PM | particulate matter |
| PMDA | pyromellitic dianhydride |
| POP | porous organic polymer |
| PP | polypropylene |
| PPF | porous polymer framework |
| PSD | pore size distribution |
| PTCDA | perylene-3,4,9,10-tetracarboxylic acid dianhydride |
| PyTTA | 4,4',4'',4''' (pyrene-1,3,6,8-tetrayl)tetraaniline |
| QSDFT | quenched solid-state functional theory |
| rGO | reduced graphene oxide |
| rTTI-COF | reduced triazine triphenyl imine COF |
| SBET | Brunauer-Emmett-Teller surface area |
| ssNMR | solid-state nuclear magnetic resonance spectroscopy |

| | |
|---|---|
| TAA | 1,3,5,7-tetraaminoadamantane |
| TABPB | tris[4-amino(1,1-biphenyl-4-yl)]benzene |
| TAPA | tris(4-aminophenyl)amine |
| TAPA(3D) | 1,3,5,7-tetra(4-aminophenyl)adamantine |
| TAPB | tris(4-aminophenyl)benzene |
| TAPE | 1,1,2,2-tetrakis(4aminophenyl)ethylene |
| TAPM | tetra(4-aminophenyl)methane |
| TAPP | tetra(4-aminophenyl)porphyrin |
| TEM | transmission electron microscopy |
| TGA | thermogravimetric analysis |
| TNP | 2,4,6-trinitrophenol |
| Tp | 4,4'-diamino-p-terphenyl |
| TPHCA | triphenylene-2,3,6,7,10,11-hexacarboxylic acid |
| TT | tris(4-aminophenyl)triazine |
| TT-CHO | 4,4',4''-(1,3,5-triazine-2,4,6-triyl)tribenzaldehyde |
| TTI-COF | triazine triphenyl imine COF |
| TTT-COF | triazine triphenyl thiazole COF |
| UV-Vis | ultraviolet–visible spectroscopy |
| VP | pore volume |
| WHO | World Health Organization |
| XRPD | X-Ray powder diffraction |

## 8.2 *Supporting Information of Chapter 4.1 "Ionothermal Synthesis of Imide-Linked Covalent Organic Frameworks"*

### 8.2.1 *Experimental Details*

#### *FT-IR*

Infrared spectra were recorded on a PerkinElmer UATR Two in attenuated total reflection (ATR) geometry equipped with a diamond crystal.

#### *Diffuse Reflectance Spectroscopy*

Diffuse reflectance UV–visible absorption spectra were collected on a Cary 5000 spectrometer (referenced to barium sulphate). Absorption spectra were calculated from the reflectance data using the Kubelka-Munk function.

#### *Photoluminescence Spectroscopy*

Steady-state emission data was collected at room temperature using an Edinburgh FLS980 spectrometer. Samples were excited using light output from a housed 450 W Xe lamp passed through a single grating (1800 l/mm, 250 nm blaze) Czerny-Turner monochromator and finally a bandwidth slit. Emission from the sample was passed through a double grating (1200 l/mm, 500 nm blaze) Czerny-Turner monochromator (appropriate bandwidth) and finally detected by a cooled microchannel plate photomultipler tube (MCP-PMT) detector.

#### *SEM/EDX*

SEM SE (secondary electron) detector images were obtained on either a Zeiss Merlin or a VEGA TS 5130MM (TESCAN) with a SEM-EDX using a Si/Li detector (10 kV acceleration voltage, Oxford).

#### *Sorption*

Sorption measurements were performed on a Quantachrome Instruments Autosorb iQ MP with Argon at 87 K. The pore size distribution was determined from argon adsorption isotherms using the quenched solid-state density functional theory (QSDFT) for cylindrical pores in carbon model for argon at 87 K.

### *XRPD*

X-ray powder diffraction (XRPD) measurements were performed on a Stoe Stadi-P diffractometer in Debye-Scherrer geometry with Cu-$K_{\alpha 1}$ radiation equipped with a Ge(111) primary monochromator. The glass capillaries (0.7 mm in diameter) were spun during data collection for an improved particle statistics. Rietveld[1] refinements of the different COF structures were performed using TOPAS V5. Model structures created by Material Studio were used for the Rietveld refinements with fixed atomic coordinates. The peak profile of the XRPD patterns was described by applying the fundamental parameter[2] approach as implemented in TOPAS. Lattice parameter (*a*, *b*-axes) were freely refined. The *c*-axis was taken from the calculation, since no reliable information about stacking distance was obtained from XRPD patterns. The background was modeled by Chebychev polynomials. The microstructure of the different COFs was modeled using microstrain (Lorentzian and Gaussian components).

### *In situ XRPD*

*In situ* high temperature XRPD experiments were performed on a Bruker D8 diffractometer (Mo-$K_{\alpha 1}$ equipped with a primary Ge(220)-Johansson-type monochromator and a LynxEye position sensitive detector) in Debye-Scherrer geometry using a water cooled capillary furnace (mri Physikalische Geräte GmbH). The measurements were performed in the range of 2 – 25 ° $2\theta$ with 1 h exposure time. For better particle statistics, the quartz capillary was spun during data collection. XRPD patterns were measured at RT, 180, 210, 240, 270, 290, 300 with staying at 300 °C for 10 h and then cool down to RT again.

### *NMR*

Solid state nuclear magnetic resonance spectra (ssNMR) were recorded on a Bruker Avance III 400 MHz spectrometer (magnetic field 9.4 T). For ssNMR spectroscopy, the samples were packed in 4 mm $ZrO_2$ rotors, which were spun in a Bruker WVT BL4 double resonance MAS probe. Chemical shifts were referenced relative to tetramethylsilane. The spinning rate was 12-14 kHz and a standard cross-polarization sequence with a 2 ms ramped contact pulse was used for $^{13}C$ and a total of 4096-8192 scans were routinely accumulated. The measurements were performed under conditions of high-power broadband proton decoupling (SPINAL 64) with the spectral conditions being optimized for the shortest relaxation delay by measuring $^{1}H$ $T_1$ relaxation time.

### *TEM*

TEM was performed with a Philips CM30 ST (300kV, $LaB_6$ cathode). The samples were prepared dry onto a copper lacey carbon grid (Plano). The line scan analysis was done with ImageJ, version 1.52a.The simulation of the projected potential map was performedwith the jems package (Stadelmann).

### *Quantum-Chemical Calculations*

Atom positions and lattices of all periodic structures were optimized on RI-PBE-D3/def2-TZVP[3-6] level of theory using an acceleration scheme based on the resolution of the identity (RI) technique and the continuous fast multipole method (CFMM[7-9]) implemented[10] in Turbomole[11] version V7.3.

The CFMM uses multipole moments of maximum order 20, together with a well-separateness value of 3 and a basis function extent threshold of 10E-9 a.u. Grid 7 was used for the numerical integration of the exchange-correlation term. The norm of the gradient was converged to 10E-4 a.u. and the total energy to 10E-8 Hartree within the structure optimization using the gamma point approximation.

Structures for all investigated molecular compounds were optimized on PBE0-D3/def2-TZVP[3, 6, 12-13] level of theory. Subsequent frequency calculations were performed on the same level of theory to ensure all minima to be true minima on the potential energy hypersurface. Partial Charges were extracted from the summary of a subsequent Natural Population Analysis[14] on the same level of theory.

NMR chemical shifts were obtained on B97-2/pcSseg-2[15-16] level of theory using the FermiONs++ program package[17-18].

### *Scherrer Analysis*

To determine the mean size of the crystalline domains Scherrer analysis was performed using the Scherrer equation displayed below. All reflections of the COFs or phases of the *in situ* measurement without a significant overlap with other reflections were fitted using the Voigt function model. FWHM and Bragg angles were received from the corresponding fit function and inserted into the Scherrer equation together with the respective wavelength and the shape factor fixed at K = 0.9. To yield the most accurate crystallite sizes as many reflections as possible were considered for the final calculations. Since the quality of the synthesized COFs varies significantly, not every COF could be described with the same number of reflections.

Scherrer Equation:

$$\tau = \frac{K\lambda}{\beta \cos\theta}$$

$\tau$ = Mean size of the crystalline domains

K = Shape factor (K = 0.9)

$\lambda$ = X-ray wavelength (Cu-K$\alpha$1 = 1.540596 nm or Mo-K$\alpha$1 = 0.7107 nm)

$\beta$ = line broadening at half the maximum intensity (FWHM)

$\theta$ = Bragg angle

### *8.2.2 Materials and Synthetic Procedures*

#### *Materials*

Tris(4-aminophenyl)triazine was synthesized according to a literature procedure.[19] All other chemicals were obtained from commercial sources and were used as received.

#### *Ionothermal Synthesis of PI-COFs in $ZnCl_2$*

**Synthesis of TAPB-PMDA-COF.** Typically, pyromelltic dianhydride (21.8 mg, 0.1 mmol), 1,3,5-Tris(4-aminophenyl)benzene (25.2 mg, 0.67 mmol) and anhydrous zinc chloride (114 mg, 0.83 mmol) were ground thoroughly in a mortar under inert atmosphere and transferred into a quartz tube. The quartz tube was evacuated (< $10^{-2}$ mbar), flame sealed and heated to 300 °C for 48 h in a tube furnace. The ampoule was allowed to cool down to room temperature and opened. The crude product was ground carefully in a mortar and subsequently washed with 1M HCl, water and THF. Solvent exchange was carried out by Soxhlet extraction with methanol overnight. The solvent was removed via supercritical $CO_2$ drying to afford TAPB-PMDA-COF as a dark brown powder.

**Synthesis of TAPB-PTCDA-COF.** Typically, Perylene-3,4,9,10-tetracarboxylic dianhydride (31.2 mg, 0.08 mmol), 1,3,5-Tris(4-aminophenyl)benzene (20 mg, 0.053 mmol) and anhydrous zinc chloride (722 mg, 5.3 mmol) were ground thoroughly in a mortar under inert atmosphere and transferred into a quartz tube. The quartz tube was evacuated (< $10^{-2}$ mbar), flame sealed and heated to 300 °C for 48 h in a tube furnace. The ampoule was allowed to cool down to room temperature and opened. The crude product was ground carefully in a mortar and subsequently washed with 1M HCl, water and THF. Solvent exchange was carried out by Soxhlet extraction with methanol overnight. The solvent was removed via supercritical $CO_2$ drying to afford TAPB-PTCDA-COF as a dark brown powder.

### *Ionothermal Synthesis of PI-COFs in eutectic salt mixture*

**Synthesis of TT-PMDA-COF.** First, sodium chloride (12.4 mg, 0.21 mmol), potassium chloride (39.5 mg, 0.53 mmol) and anhydrous zinc chloride (114 mg, 0.83 mmol) were ground together thoroughly in a mortar under inert conditions. Then, pyromelltic dianhydride (21.8 mg, 0.1 mmol) and 1,3,5-Tris(4-aminophenyl)triazine (23.6 mg, 0.067 mmol) were added and the mixture was ground again to achieve homogeneity and transferred into a quartz tube. The quartz tube was evacuated (< $10^{-2}$ mbar), flame sealed and heated to 250 °C for 48 h in a tube furnace. The ampoule was allowed to cool down to room temperature and opened. The crude product was ground carefully in a mortar and subsequently washed with 1M HCl, water and THF. Solvent exchange was carried out by Soxhlet extraction with methanol overnight. The solvent was removed via supercritical $CO_2$ drying to afford TT-PMDA-COF as a light brown - yellow powder.

**Synthesis of TAPA-PMDA-COF.** First, sodium chloride (12.4 mg, 0.21 mmol), potassium chloride (39.5 mg, 0.53 mmol) and anhydrous zinc chloride (114 mg, 0.83 mmol) were ground together in a mortar thoroughly under inert conditions. Then, pyromellitic dianhydride (21.8 mg, 0.1 mmol) and Tris-(4-aminophenyl)amine (19.3 mg, 0.067 mmol) were added and the mixture was ground again to achieve homogeneity and transferred into a quartz tube. The quartz tube was evacuated (< $10^{-2}$ mbar), flame sealed and heated to 250 °C for 48 h in a tube furnace. The ampoule was allowed to cool down to room temperature and opened. The crude product was ground carefully in a mortar and subsequently washed with 1M HCl, water and THF. Solvent exchange was carried out by Soxhlet extraction with methanol overnight. The solvent was removed via supercritical $CO_2$ drying to afford TT-PMDA-COF as a brown powder.

### *8.2.3 Supplementary Figures*

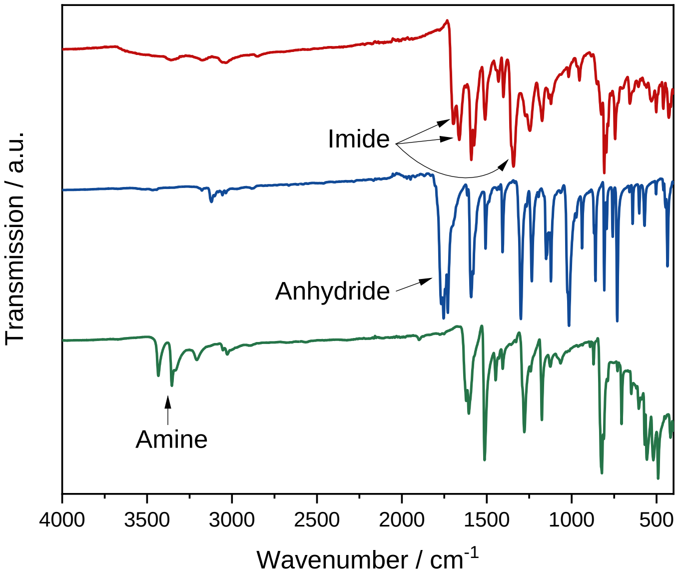

**Figure S8-1.** FT-IR spectra of **TAPB-PTCDA-COF** (red) and its precursor molecules PTCDA (blue) and TAPB (green). The absence of amine and anhydride vibrations in the COF indicate complete imide formation.

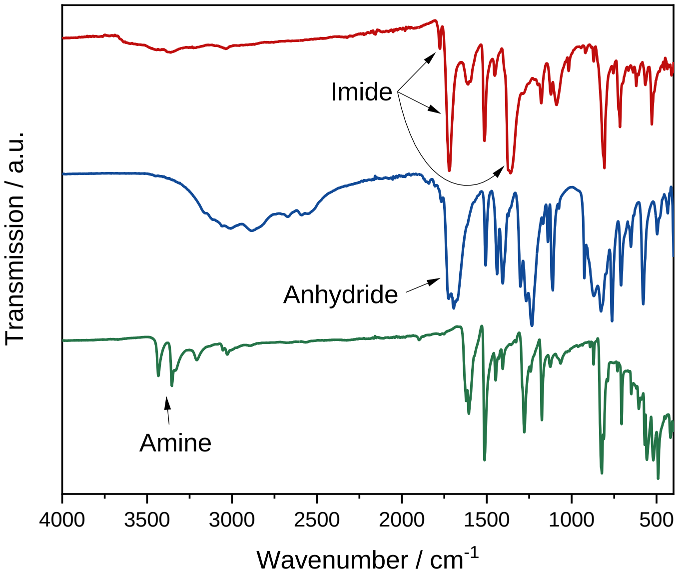

**Figure S8-2.** FT-IR spectra of TAPB-PMDA-COF (red) and its precursor molecules PMDA (blue) and TAPB (green). The absence of amine or anhydride vibrational bands in the COF indicate complete imide formation.

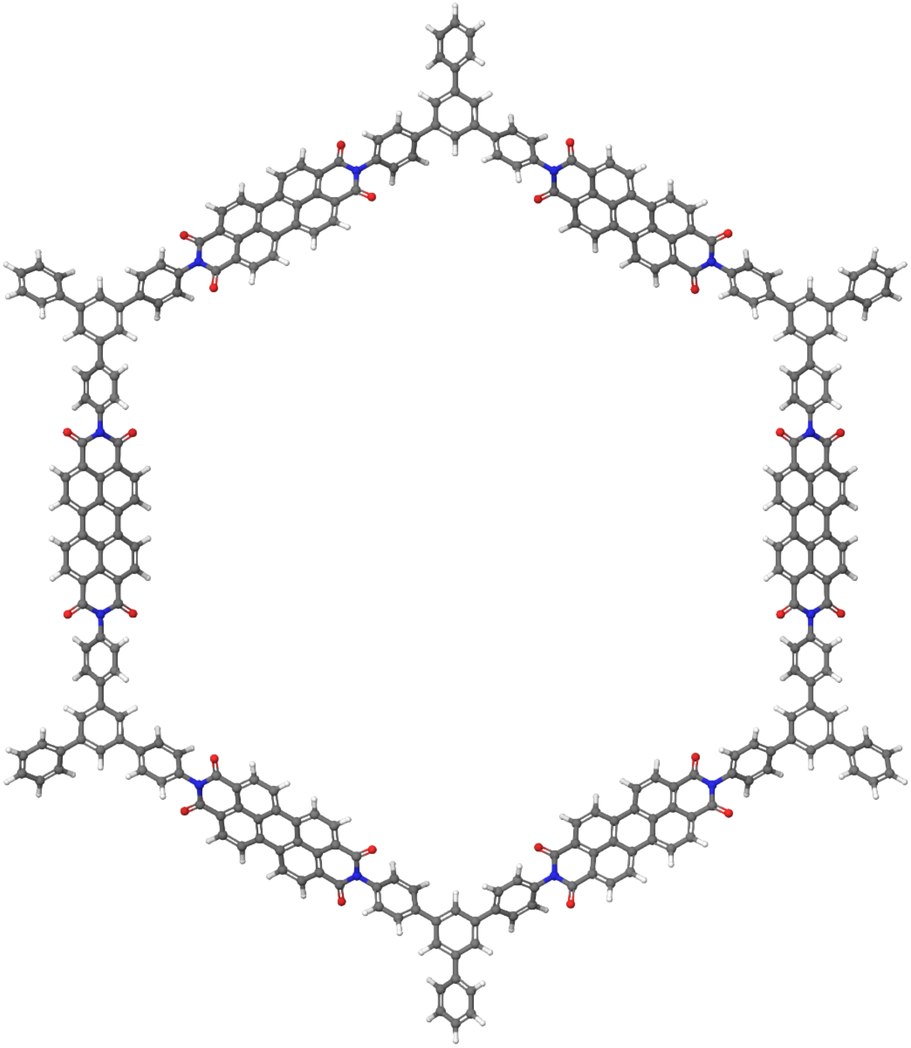

**Figure S8-3.** Structure of a single pore of the TAPB-PTCDA COF, obtained by composing a supercell from a 2D periodic geometry optimization of the corresponding asymmetric unit on RI-PBE-D3/def2-TZVP level of theory.

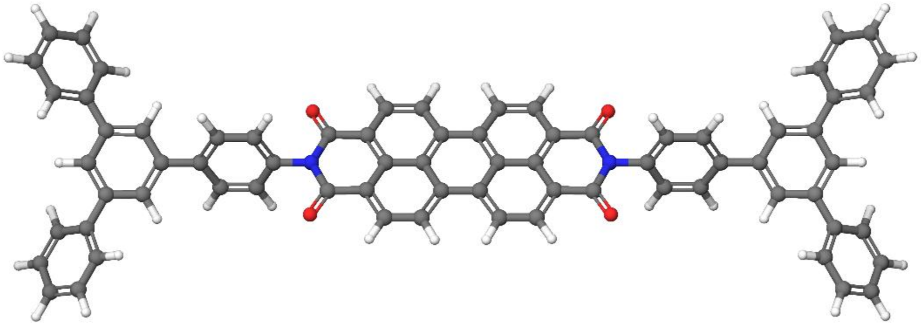

**Figure S8-4.** Structure of the TAPB-PTCDA NMR model, modeled by cutting the supercell obtained from the 2D optimized structure of the TAPB-PTCDA COF model.

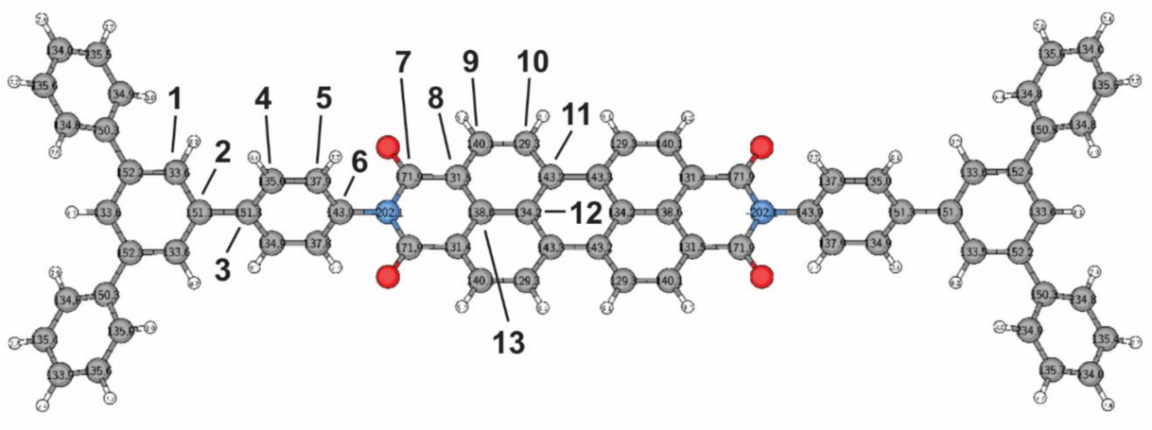

**Figure S8-5.** Calculated NMR chemical shifts for the TAPB-PTCDA NMR model, obtained on B97-2/pcsSeg-2 level of theory.

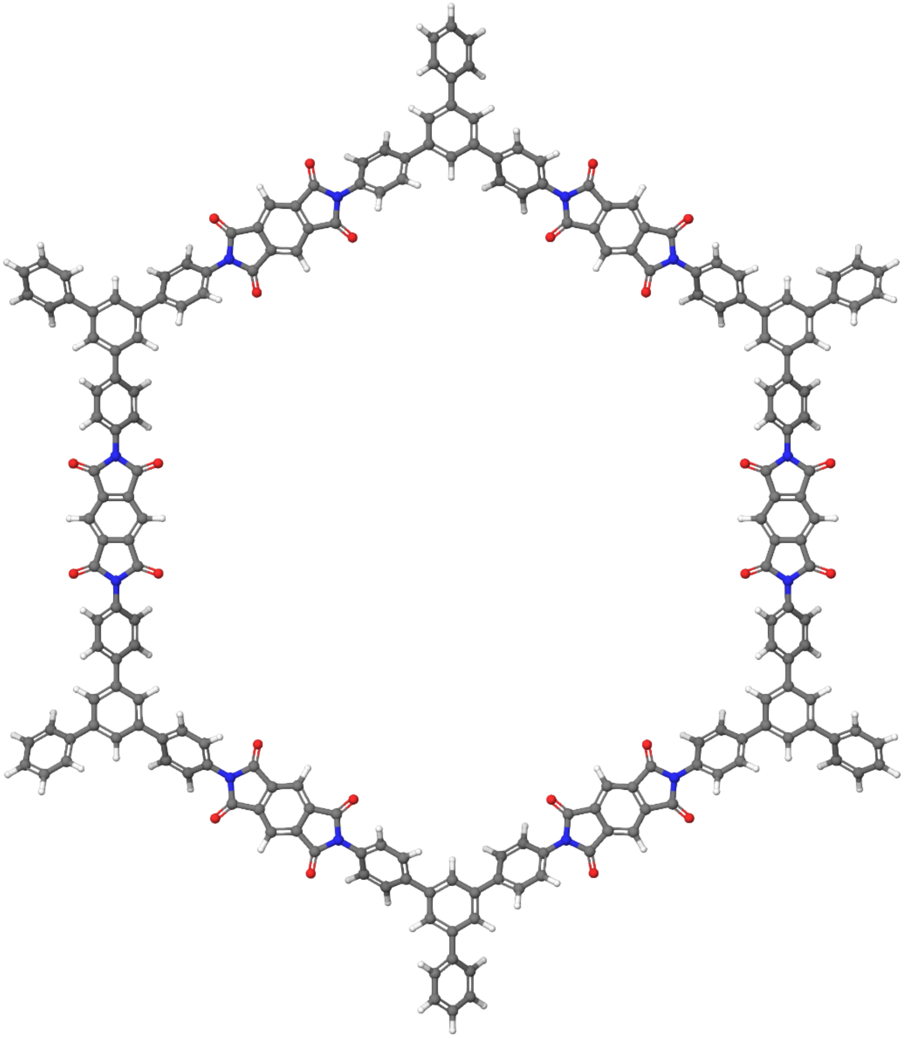

**Figure S8-6.** Structure of a single pore of the TAPB-PMDA COF, obtained by composing a supercell from a 2D periodic geometry optimization of the corresponding asymmetric unit on RI-PBE-D3/def2-TZVP level of theory.

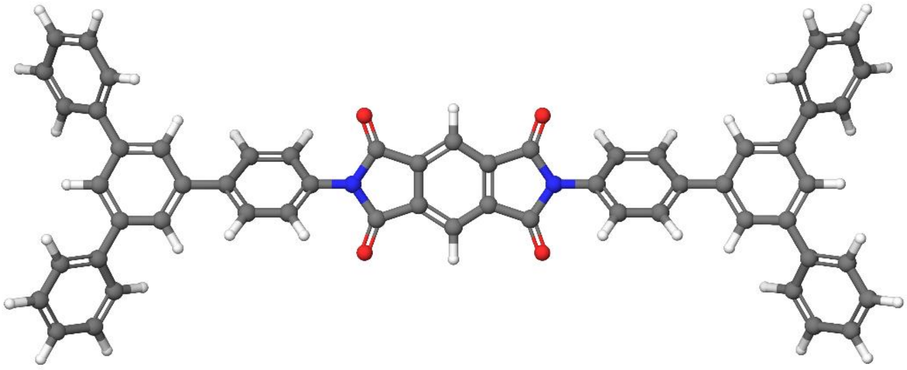

**Figure S8-7.** Structure of the TAPB-PMDA NMR model, modeled by cutting the supercell obtained from the 2D optimized structure of the TAPB-PMDA COF model.

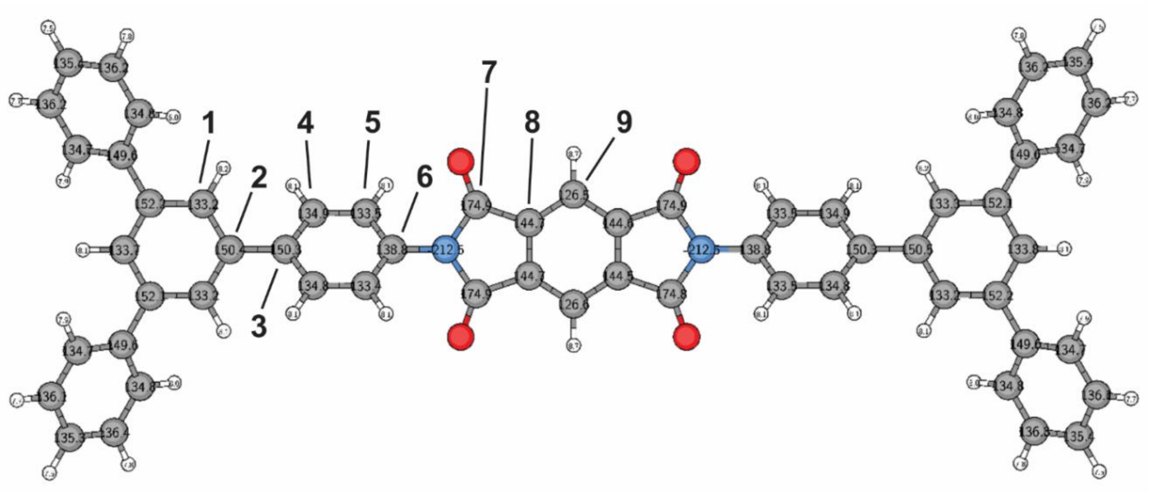

**Figure S8-8.** Calculated NMR chemical shifts for the TAPB-PMDA NMR model, obtained on B97-2/pcsSeg-2 level of theory.

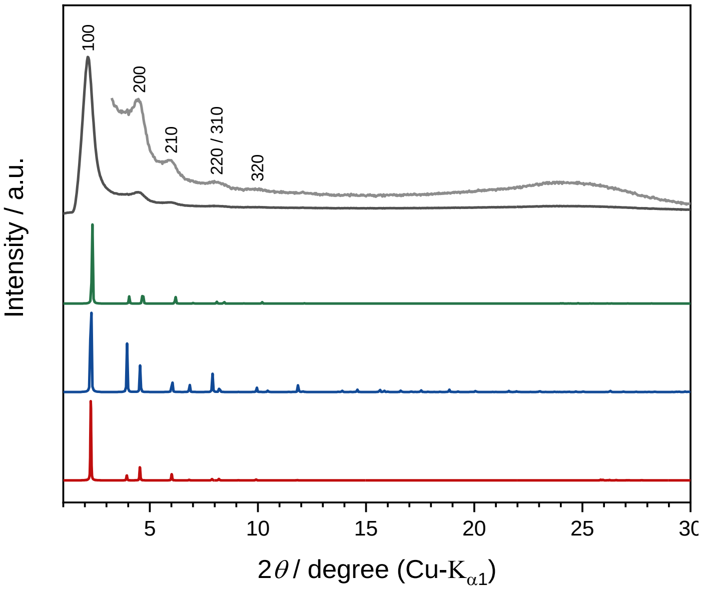

**Figure S8-9.** Experimental XRPD pattern (λ = Cu-K$_{\alpha 1}$) of TAPB-PTCDA-COF (black) compared to simulated patterns of the COF assuming $P\bar{3}1m$ symmetry (green), $P\bar{3}1c$ symmetry (blue) and Cmcm symmetry (red).

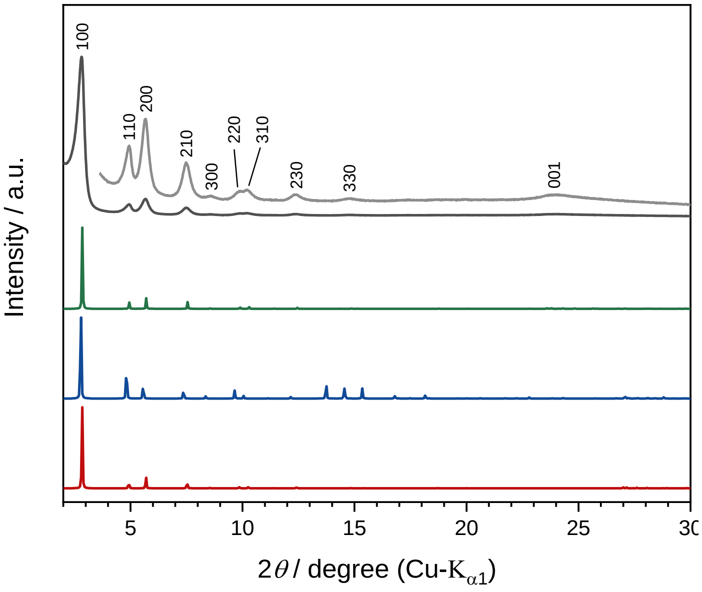

**Figure S8-10.** Experimental XRPD pattern (λ = Cu-K$_{\alpha 1}$) of TAPB-PMDA-COF (black) compared to simulated patterns of the COF assuming $P\bar{3}1m$ symmetry (green), $P\bar{3}1c$ symmetry (blue) and Cmcm symmetry (red).

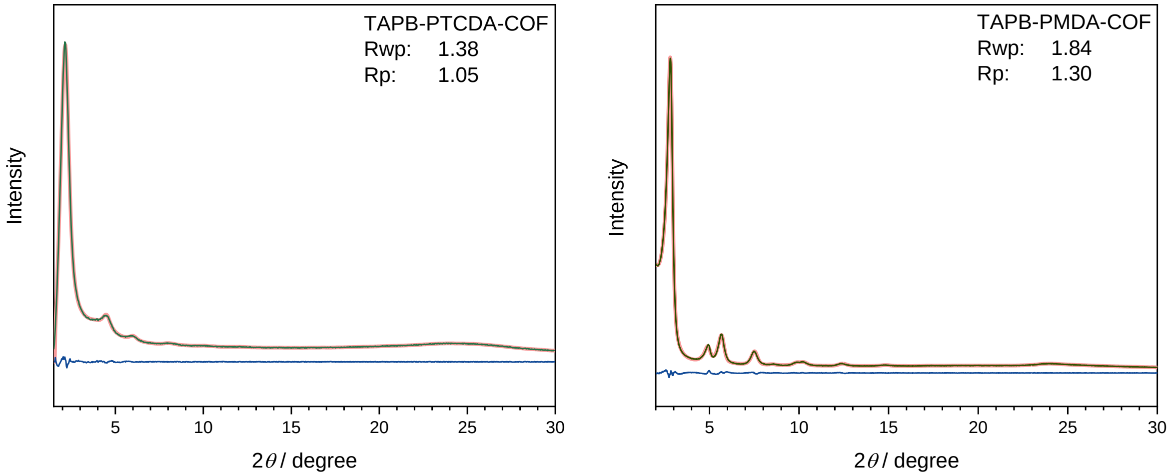

**Figure S8-11.** Pawley refinement of TAPB-PTCDA-COF (left) and TAPB-PMDA-COF (right) assuming $P\bar{3}1m$ symmetry with fixed lattice sizes and fit parameters obtained from Rietveld refinement.

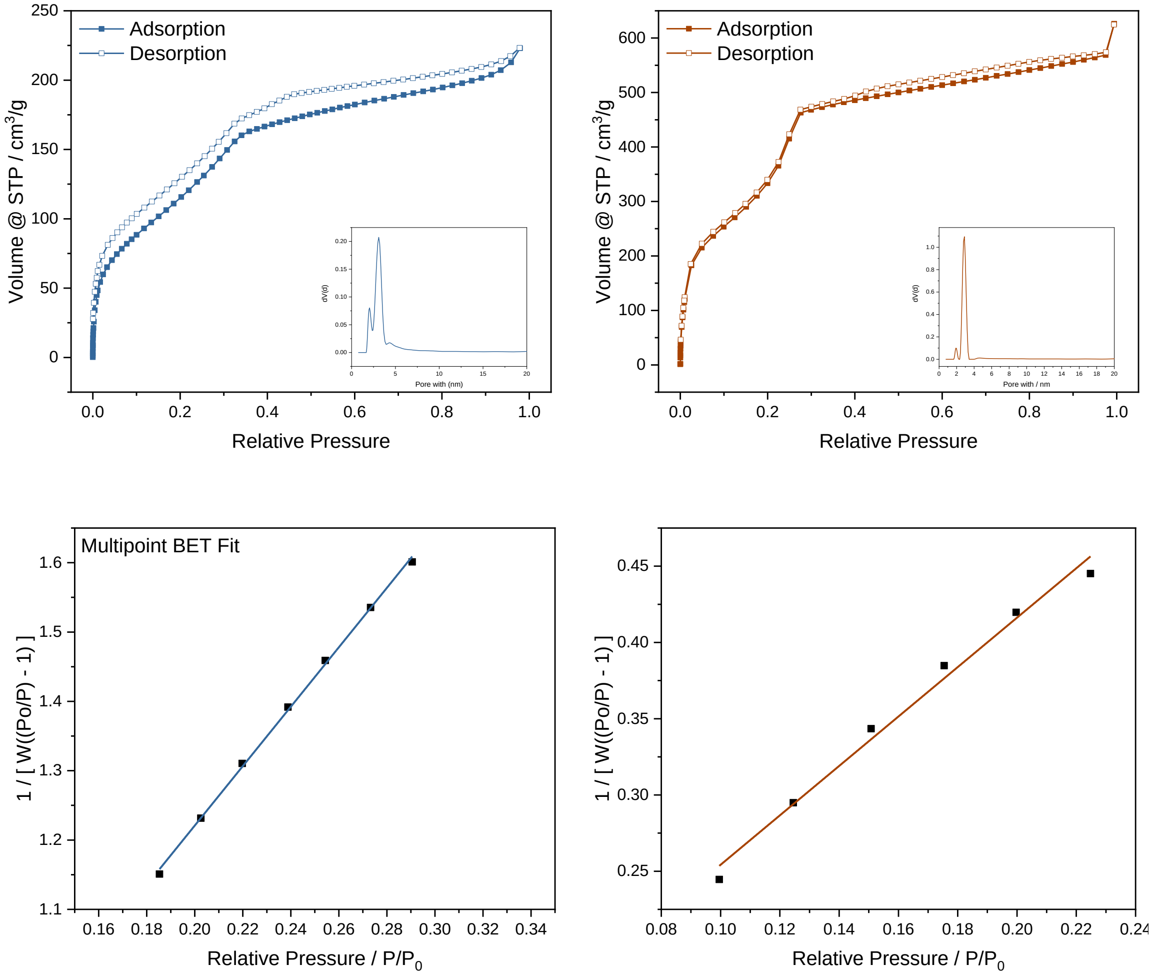

**Figure S8-12.** Top: Argon gas adsorption and desorption isotherms for TAPB-PTCDA (blue) and TAPB-PMDA-COF (brown). Insets: Respective calculated pore size distributions of PI-COFs from fitting the quenched solid-state density functional theory (QSDFT) model. Bottom: Multipoint BET fits of TAPB-PTCDA (blue) and TAPB-PMDA (brown).

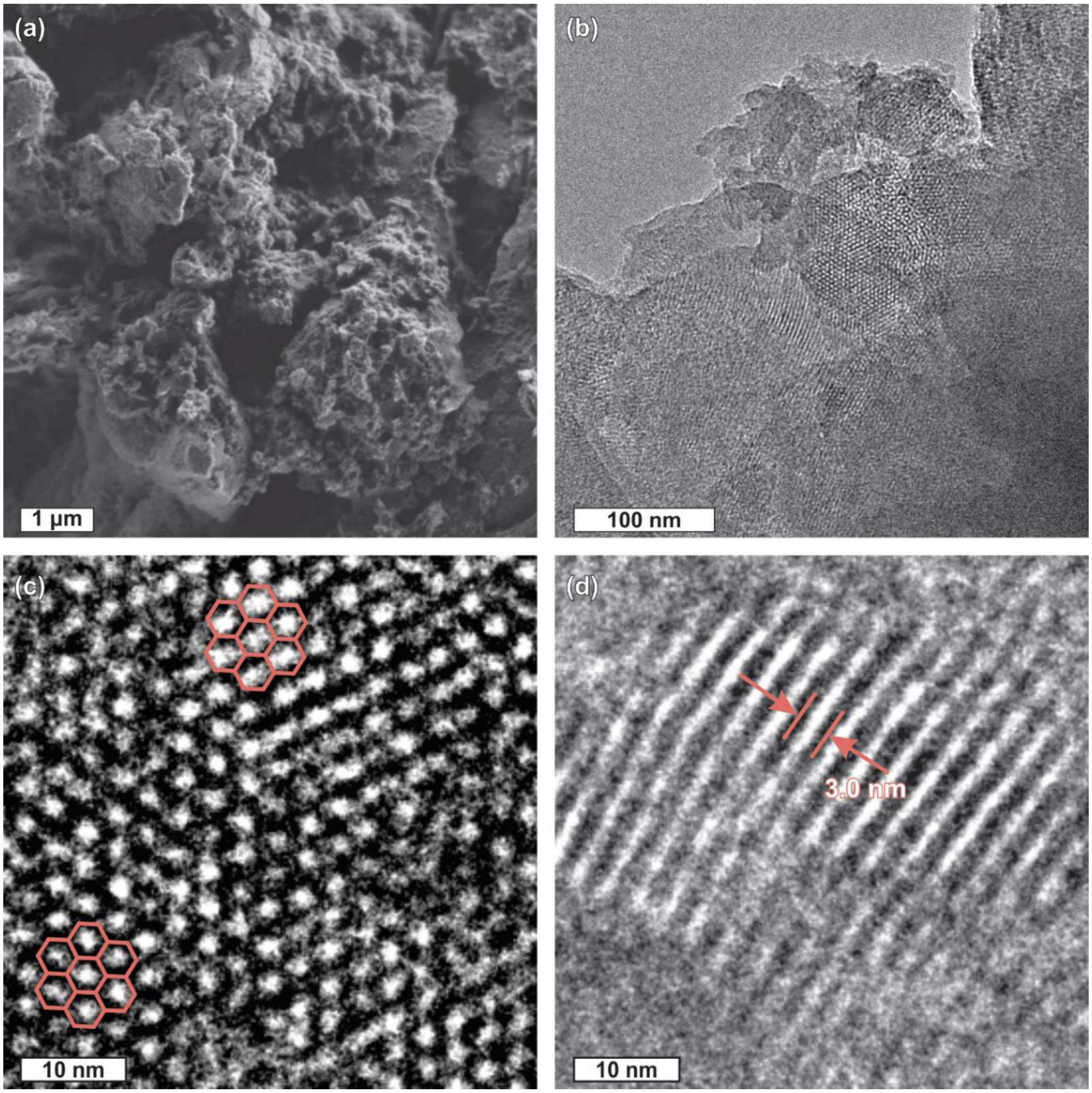

**Figure S8-13.** SEM image (a) and TEM images (b) – (d) of TAPB-PMDA-COF. (c) shows the hexagonal pores highlighted in red and (d) shows straight channels with a diameter of ≈ 3.0 nm.

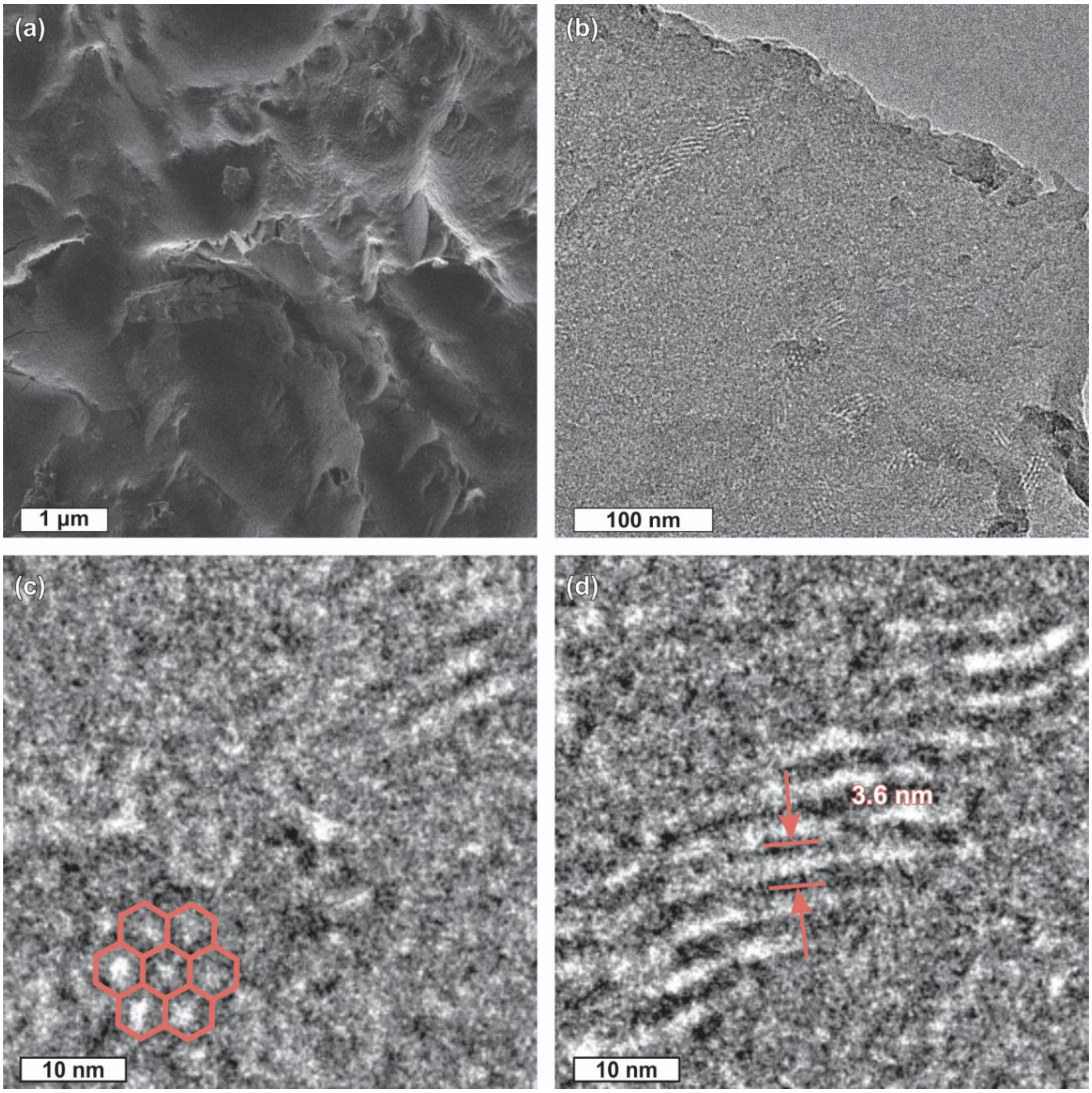

**Figure S8-14.** SEM image (a) and TEM images (b) – (d) of TAPB-PTCDA-COF. (c) shows the hexagonal pores highlighted in red and (d) shows straight pore channels with a diameter of ≈ 3.6 nm.

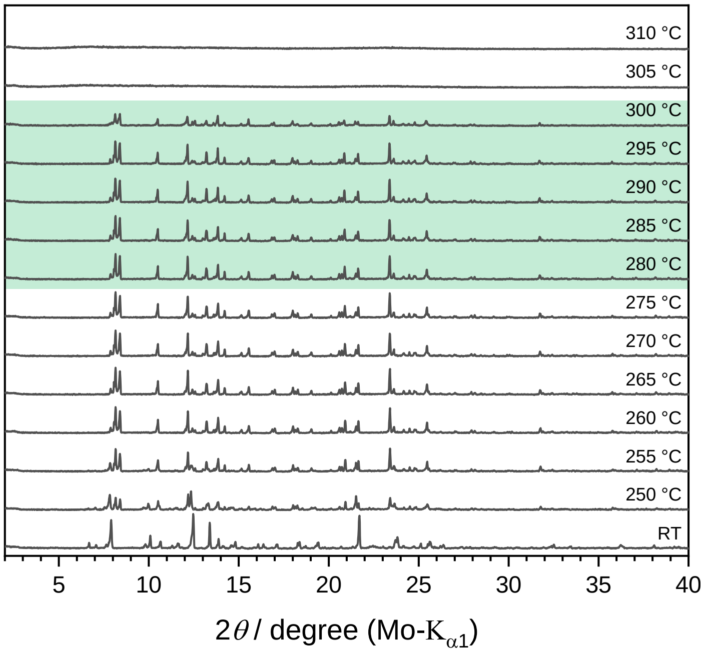

**Figure S8-15.** Melting point determination of $ZnCl_2$ via high-temperature XRPD. The melting point is indicated by the complete vanishing of the X-ray reflections between 300 and 305 °C. The green area shows the temperature window, in which the COF formation in pure $ZnCl_2$ takes place.

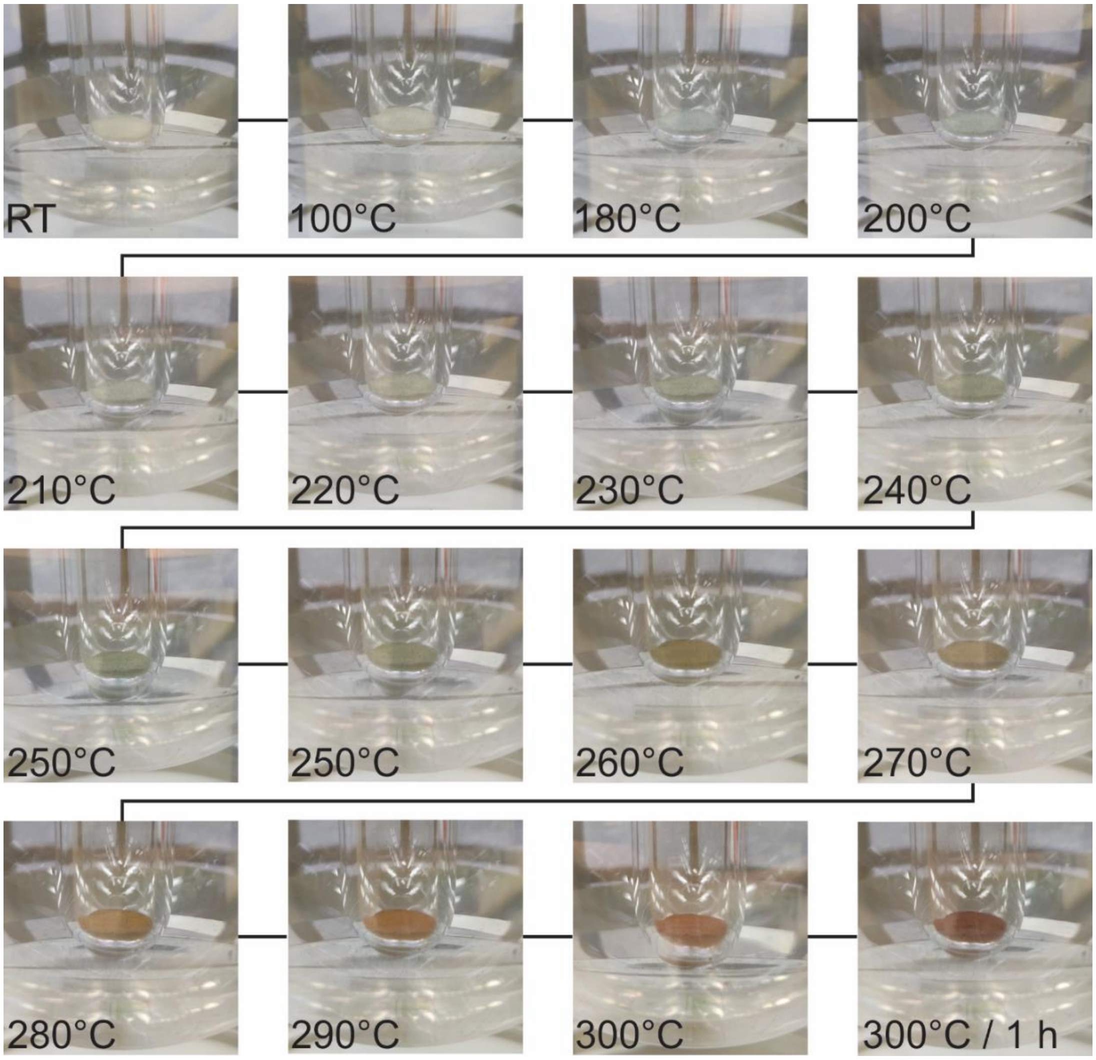

**Figure S8-16.** Visual observation of the TAPB-PMDA-COF formation reaction showing the absence of a solution or melt involved in the reaction process. The reaction mixture was heated stepwise to the respective temperatures. After reaching the respective temperatures, the system was allowed to equilibrate for 15 min before the pictures were taken.

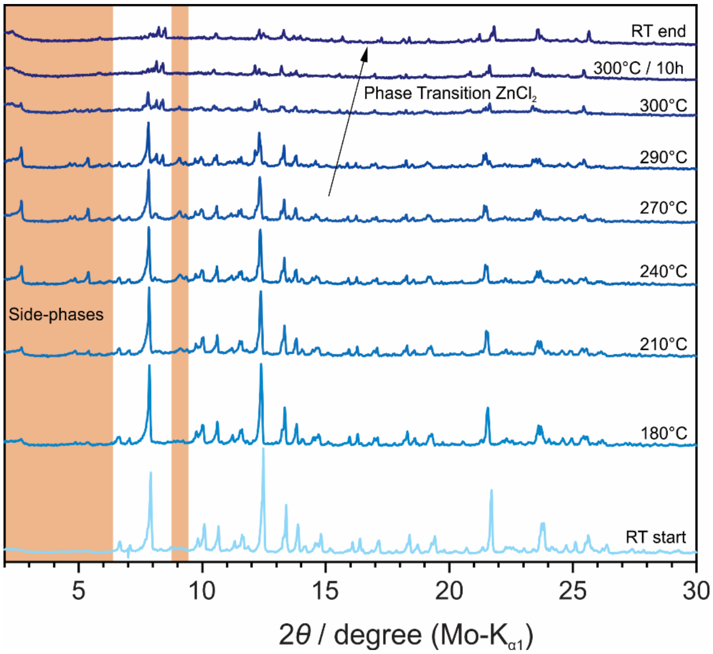

**Figure S8-17.** In situ HT-XRPD patterns (λ = Mo-K$_{\alpha1}$) of the COF precursor mixture (TAPB, PMDA, $ZnCl_2$) revealing a dramatic change of the appearing reflections over time and temperature. The pattern at room temperature is dominated by the reflections of zinc chloride, which undergoes a phase transition at elevated temperatures. Besides that side phases can be observed to appear at 180 °C, which get more prominent with increasing temperature till 290 °C. At 300 °C the side phases start vanishing again.

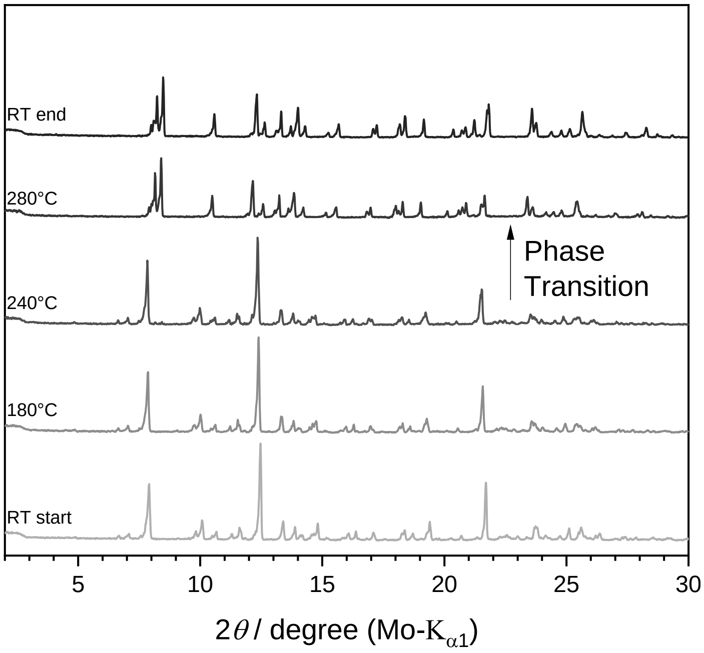

**Figure S8-18.** In situ HT-XRPD patterns (λ = Mo-K$_{\alpha1}$) of pure zinc chloride showing a phase transition from the monoclinic γ-form to the orthorhombic δ-form above 240 °C.

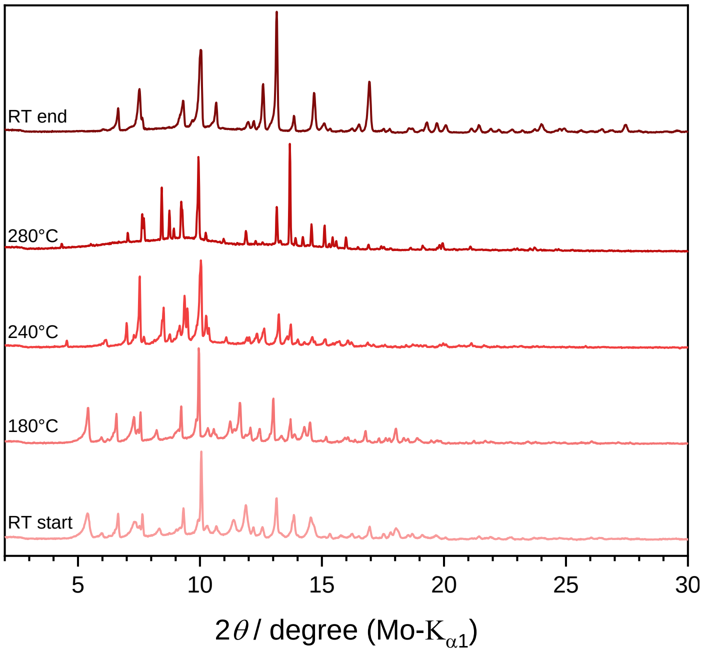

**Figure S8-19.** In situ HT-XRPD patterns (λ = Mo-$K_{\alpha1}$) of pure PMDA showing a row of structural changes with proceeding time and temperature.

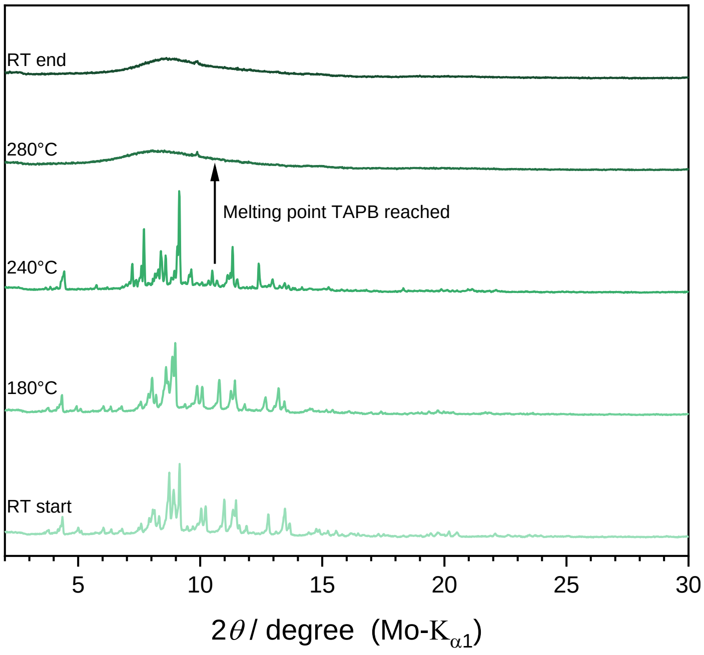

**Figure S8-20.** In situ HT-XRPD patterns (λ = Mo-$K_{\alpha1}$) of pure TAPB revealing the complete loss of reflections above 240 °C due to melting of the precursor.

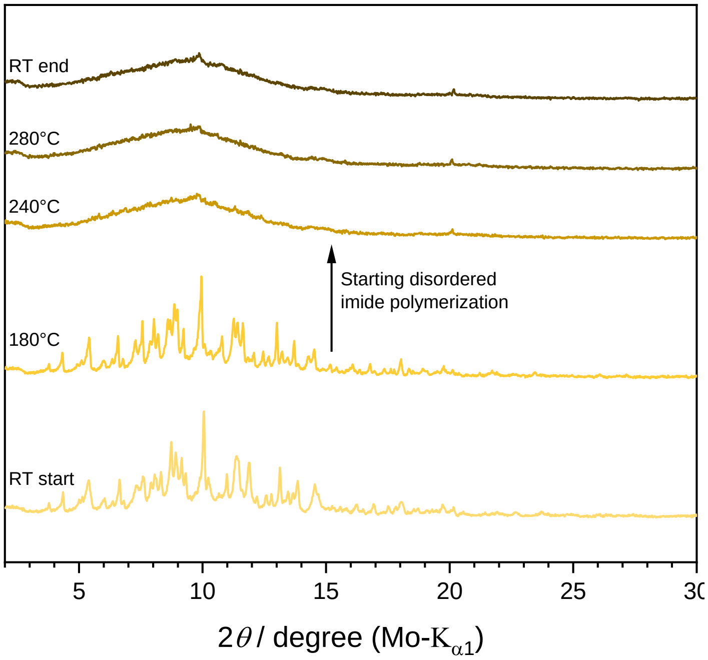

**Figure S8-21.** In situ HT-XRPD patterns (λ = Mo-$K_{\alpha1}$) of a mixture of TAPB and PMDA showing reflections of both precursor molecules up to 180 °C. In addition the patterns reveal a complete loss of all reflections between 180 and 240 °C. This is due to the starting disordered imide polymerization as evident from the screening experiments described in the main text.

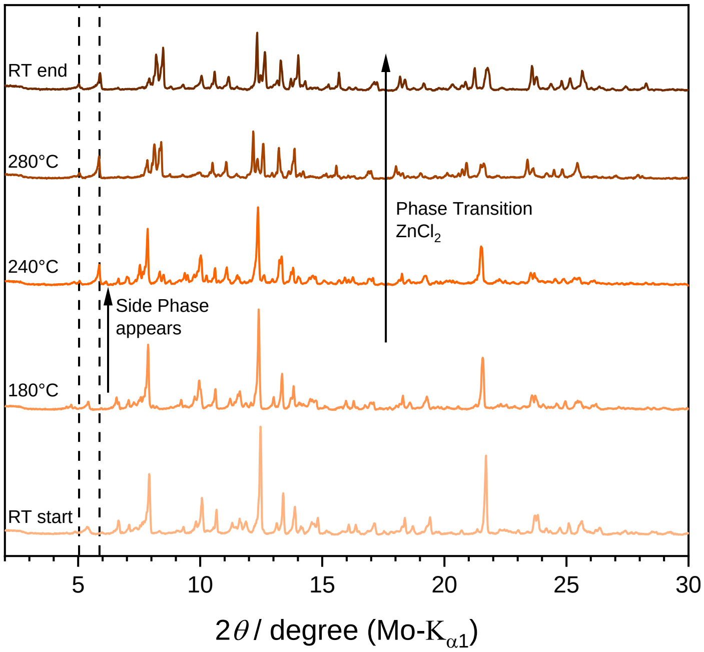

**Figure S8-22.** In situ HT-XRPD patterns (λ = Mo-$K_{\alpha1}$) of a mixture of PMDA and $ZnCl_2$. The patterns are dominated by the reflections of zinc chloride that undergoes phase transition from the monoclinic γ-form to the orthorhombic δ-form 240 °C upwards. An appearing side-phase can be identified, which were observed neither in the diffraction pattern of pure PMDA nor in the pattern of pure zinc chloride hinting towards a reaction between PMDA and $ZnCl_2$ to form an intermediate species.

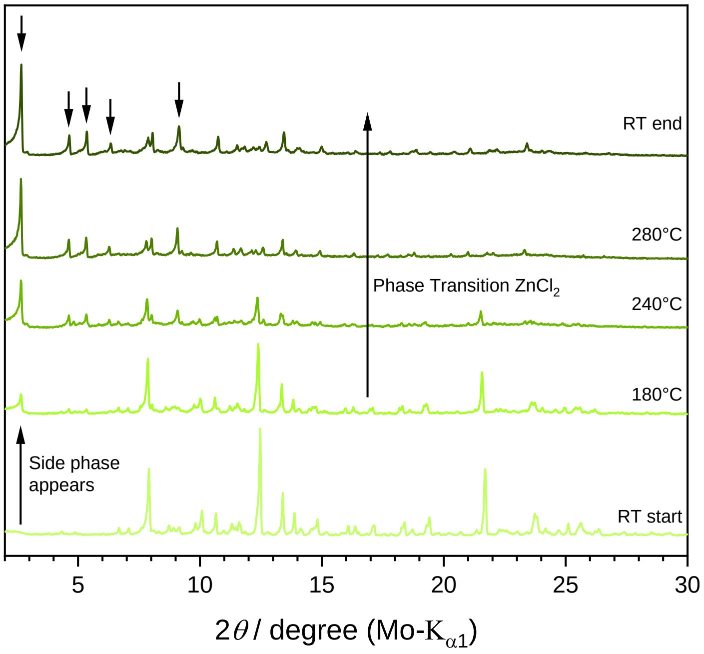

**Figure S8-23.** In situ HT-XRPD patterns (λ = Mo-K$_{\alpha1}$) of a mixture of TAPB and ZnCl$_2$. At room temperature, the patterns are dominated by the reflections of zinc chloride that undergoes phase transition from the monoclinic γ-form to the orthorhombic δ-form 240 °C upwards. At 180 °C, an appearing side-phase can be identified, which were observed neither in the diffraction pattern of pure TAPB nor in the pattern of pure zinc chloride hinting towards a reaction between TAPB and ZnCl$_2$ to form an intermediate species. With increasing temperature the reflections of the observed side-phase intensify and dominate the reflections of ZnCl$_2$ emphasizing the highly oriented structure of this species.

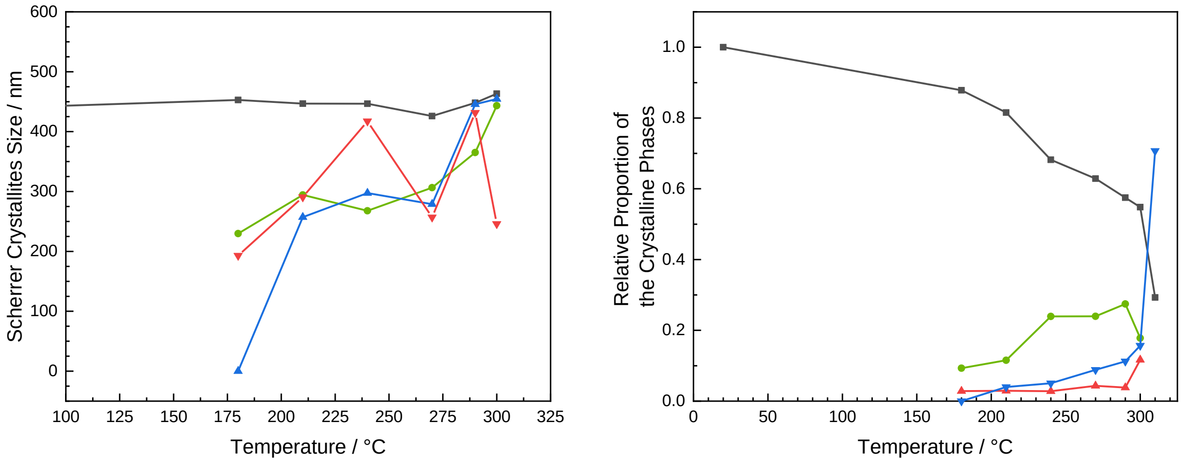

**Figure S8-24.** Calculated Scherrer crystallite sizes (left) and calculated relative amounts (right) of the individual crystalline domains (γ-ZnCl$_2$ (black), δ-ZnCl$_2$ (blue), TAPB-adduct (green), PMDA-adduct (red)) at different temperatures from the *in situ* high temperature XRD measurement. Scherrer analysis of the *in situ* measurement revealed that the crystallite size of the γ-ZnCl$_2$ (black) remains constant at 450 nm with increasing temperature, while the relative amount of γ-ZnCl$_2$ decreases. The constant crystallite size of this ZnCl$_2$ phase confirms that no melting takes place. In addition, a successive increase of the crystallite size and relative amounts of the intermediate phases with a maximum at the optimized reaction temperature (280 – 300 °C) can be observed. Two effects can explain the decreasing relative amount of the γ-ZnCl$_2$ phase: I) At 180°C and higher the ZnCl$_2$ reacts with the precursor molecules to form the ZnCl$_2$ – precursor adducts (green and red) resulting in a successive increase of the crystallite size and relative amount of the precursor adducts in the same temperature region. II) The phase transition from γ-$ZnCl_2$ to δ-$ZnCl_2$ proceeds quickly above 290 °C and results in an inversion of the relative amounts of the respective phase (blue vs. black).

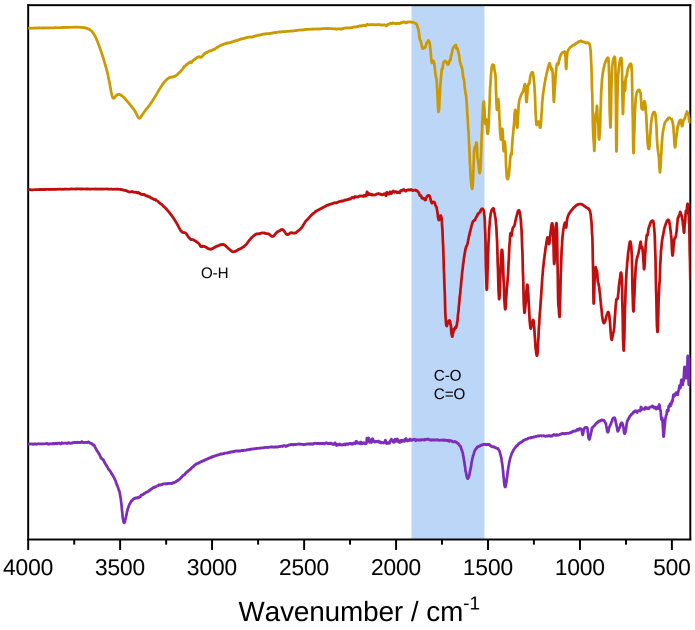

**Figure S8-25.** FT-IR spectra of $ZnCl_2$ (purple), PMDA (red) and the corresponding intermediate species (yellow), showing a shift of the C-O and C=O vibrational bands indicating the formation of an PMDA-$ZnCl_2$ adduct.

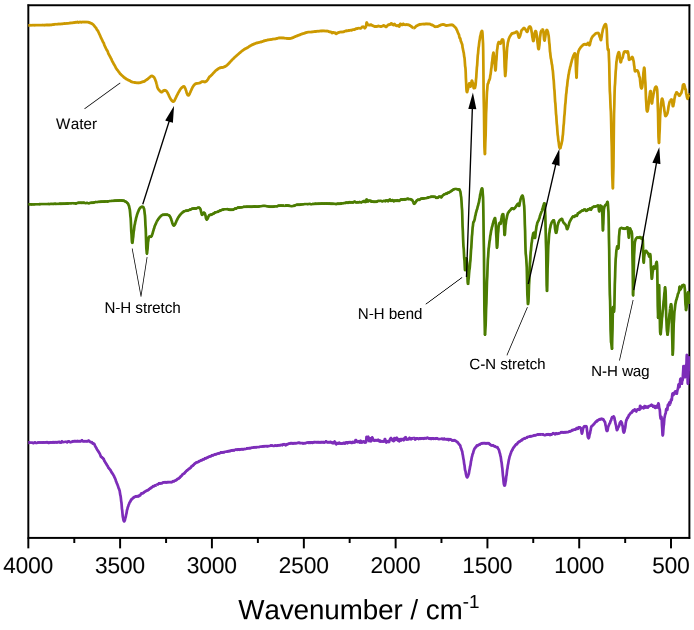

**Figure S8-26.** FT-IR spectra of $ZnCl_2$ (purple), PMDA (red) and the corresponding intermediate species (yellow), showing a shift of all amine-related vibrational bands towards lower wavenumber indicating the formation of an TAPB-$ZnCl_2$ adduct.

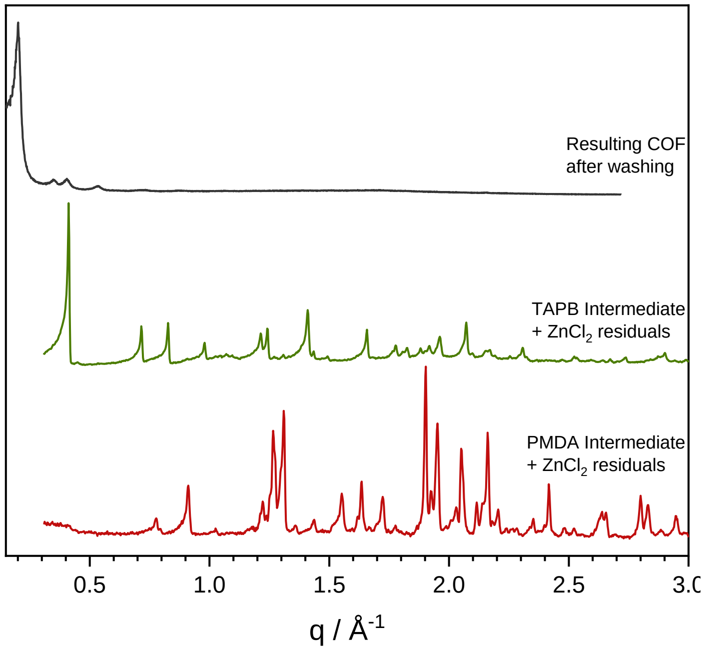

**Figure S8-27.** XRPD Patterns of the separately synthesized intermediate species of PMDA (red) and TAPB (green) and the resulting COF (black) after combining the intermediates and heating to 290 °C for 20 h.

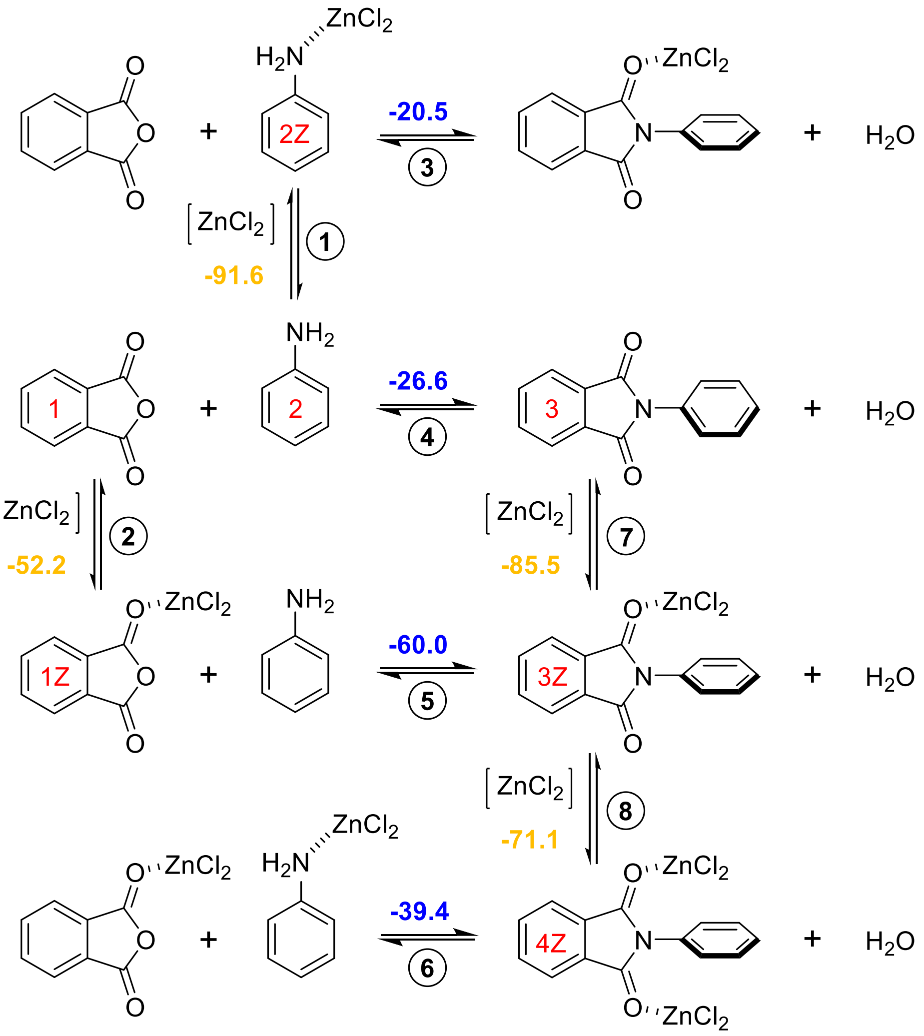

**Figure S8-28.** Summary of three individual polymerization reaction pathways, supplemented with calculated reaction enthalpies as total energy differences of the sum of reactants and products, obtained on PBE0-D3/def2-TZVP level of theory.

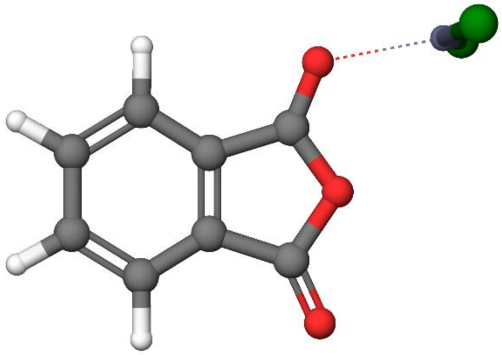

**Figure S8-29.** Optimized structure for the 1Z model system, obtained on PBE0-D3/def2-TZVP level of theory.

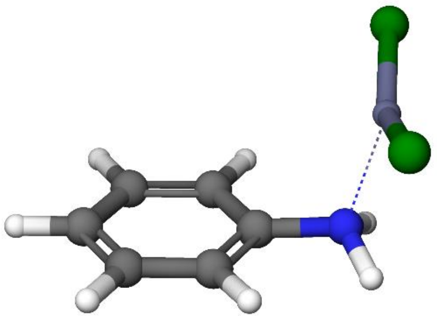

**Figure S8-30.** Optimized structure for the 2Z model system, obtained on PBE0-D3/def2-TZVP level of theory.

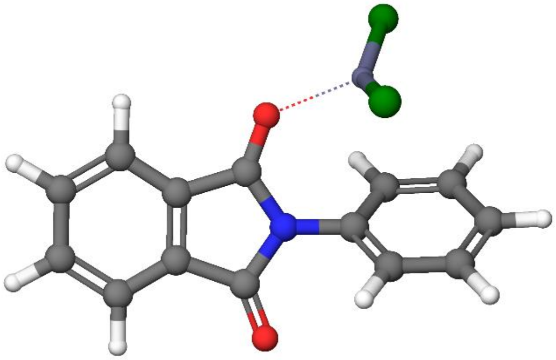

**Figure S8-31.** Optimized structure for the 3Z model system, obtained on PBE0-D3/def2-TZVP level of theory.

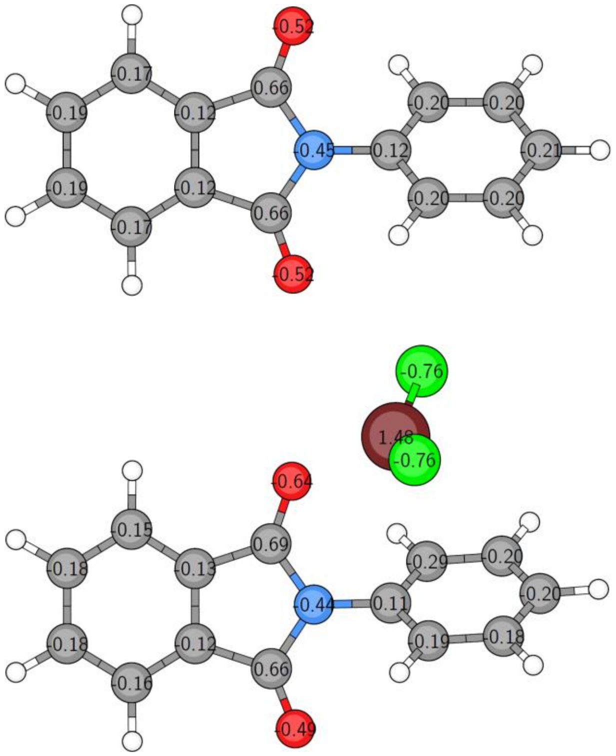

**Figure S8-32.** Comparison of partial charges, extracted from the summary of a Natural Population Analysis for the the **3** (top) and the **3Z** (bottom) model system.

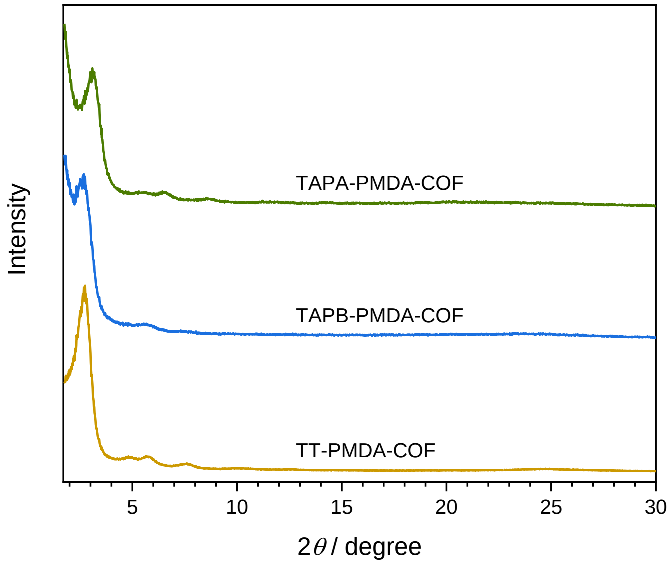

**Figure S8-33.** XRPD patterns of TAPA-PMDA-COF (green), TAPB-PMDA-COF (blue) and TT-PMDA-COF (yellow) synthesized according solvothermal literature procedure in NMP/Mesithylene/Isoquinoline.

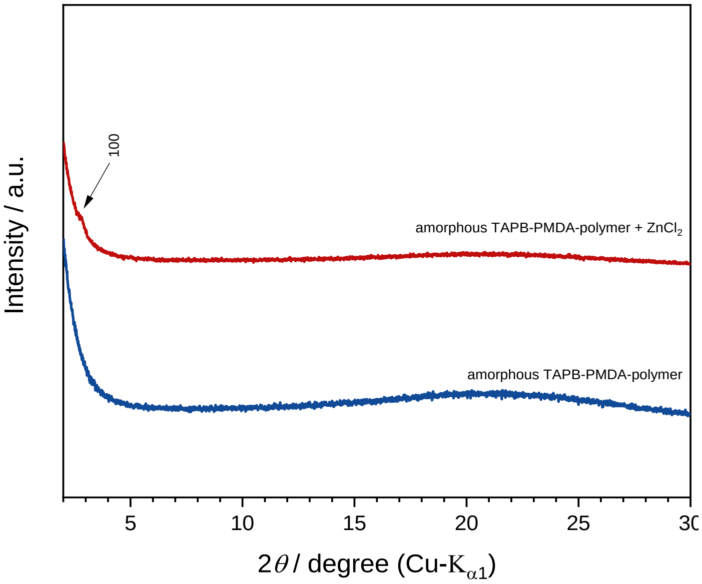

**Figure S8-34.** XRPD pattern of the amorphous TAPB-PMDA-polymer (blue) and the same polymer mixed with $ZnCl_2$ and heated to 300 °C for 48 h (red), showing a slight increase in structural orientation by the appearance of the (100) reflection of TAPB-PMDA-COF.

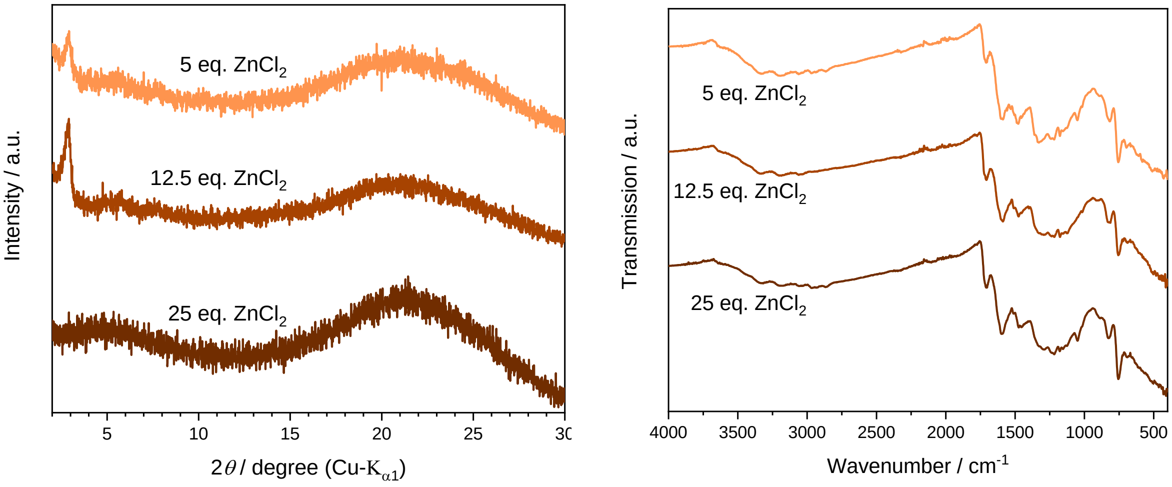

**Figure S8-35.** XRPD patterns ($\lambda$ = Cu-$K_{\alpha1}$) (left) and IR spectra (right) of screening experiments on **TT-PMDA-COF** in $ZnCl_2$, in which the zinc chloride ratio was varied between 5 and 25 equivalents with respect to PMDA, with reaction time and temperature kept constant at 20 h and 300 °C, respectively. XRPD reveals that no product with satisfactory crystallinity is formed. The IR spectra show that although in each case imide condensation took place, a significant broadening of the vibrational bands is observed, which indicates the loss of short-range order and therefore points towards partial decomposition of the linker molecules - most probably the amine linker is affected, since PMDA is stable under these conditions (see TAPB-PMDA-COF).

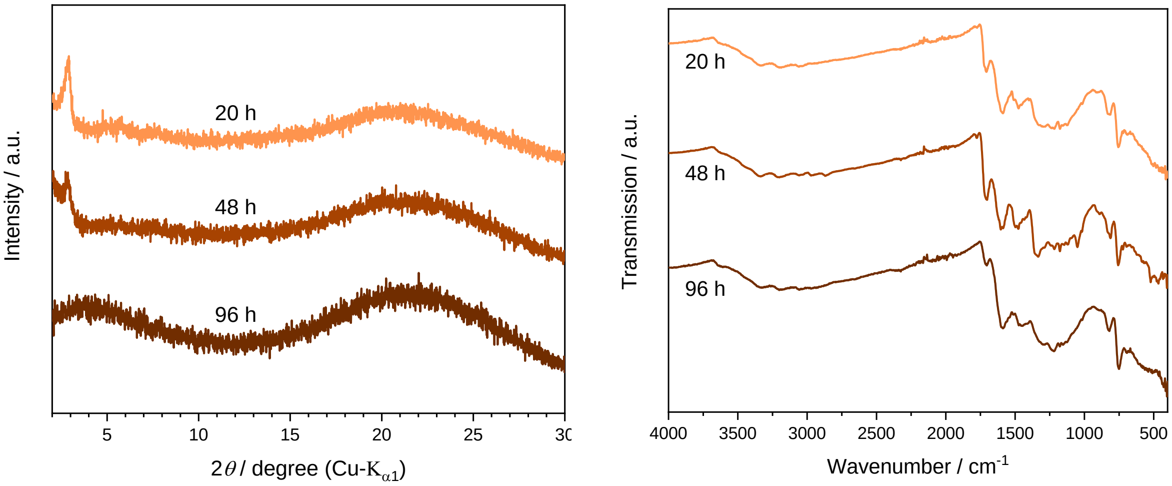

**Figure S8-36.** XRPD patterns (λ = Cu-Kα1) (left) and IR spectra (right) of screening experiments on **TT-PMDA-COF** in $ZnCl_2$, in which the reaction time was varied between 20 and 96 h with the zinc chloride portion and reaction temperature kept constant at 12.5 eq. w.r.t. PMDA and 300 °C, respectively. XRPD reveals that no product with satisfactory crystallinity is formed. The IR spectra again show a significant broadening of the vibrational bands, which indicates the loss of short-range order and therefore points towards partial decomposition of the amine linker.

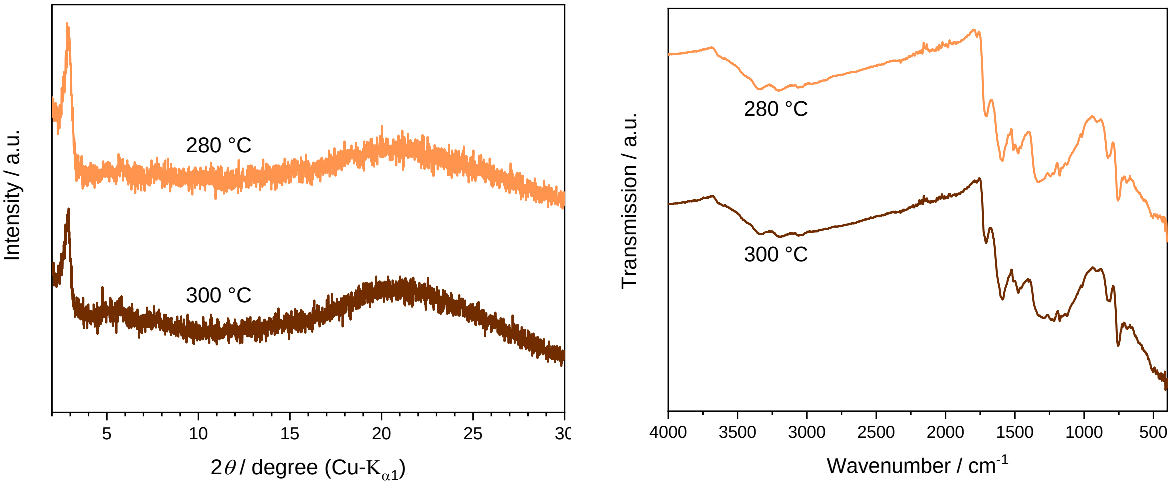

**Figure S8-37.** XRPD patterns (λ = Cu-Kα1) (left) and IR spectra (right) of screening experiments using **TT-PMDA-COF** in $ZnCl_2$, in which the reaction temperature was varied between 280 and 300 °C with the zinc chloride portion and reaction time kept constant at 12.5 eq. w.r.t. PMDA and 48 h, respectively. XRPD reveals that in neither case a product with satisfactory crystallinity is formed. The IR spectra again show a significant broadening of the vibrational bands, which indicates the loss of short-range order and therefore points towards partial decomposition of the amine linker.

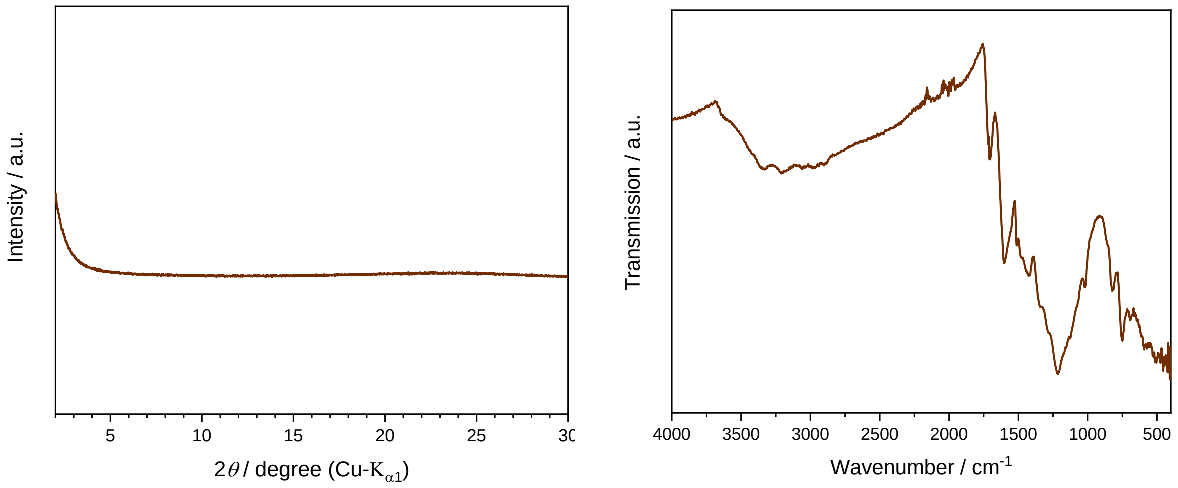

**Figure S8-38.** XRPD pattern (λ = Cu-K$_{\alpha1}$) (left) and IR spectrum (right) of **TAPA-PMDA-COF** synthesized in ZnCl$_2$ at 290 °C for 30 h. XRPD reveals that no crystalline product is formed. Although the imide-vibration can be identified at 1723 cm$^{-1}$ the IR spectrum shows a significant broadening of the vibrational bands, which indicates the loss of short range order and therefore points towards partial decomposition of the amine linker.

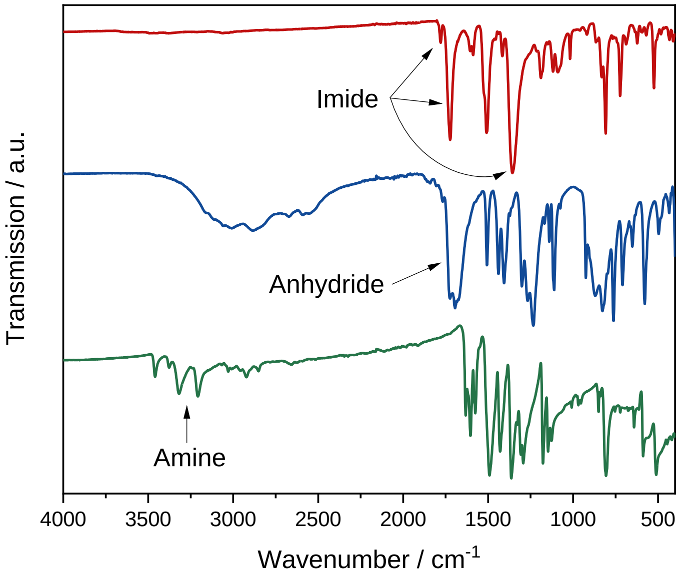

**Figure S8-39.** FT-IR spectra of **TT-PMDA-COF** (red) and its precursor molecules PMDA (blue) and TT (green). The absence of amine or anhydride vibrational bands in the COF indicate complete imide formation.

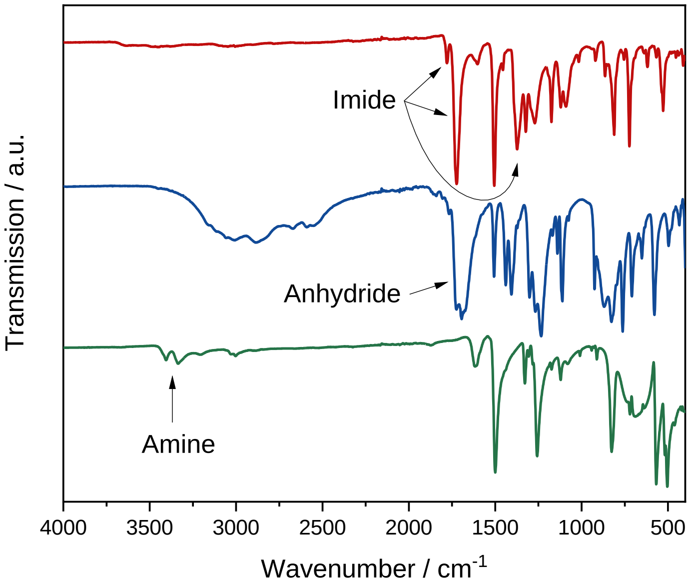

**Figure S8-40.** FT-IR spectra of **TAPA-PMDA-COF** (red) and its precursor molecules PMDA (blue) and TAPA (green). The absence of amine or anhydride vibrational bands in the COF indicate complete imide formation.

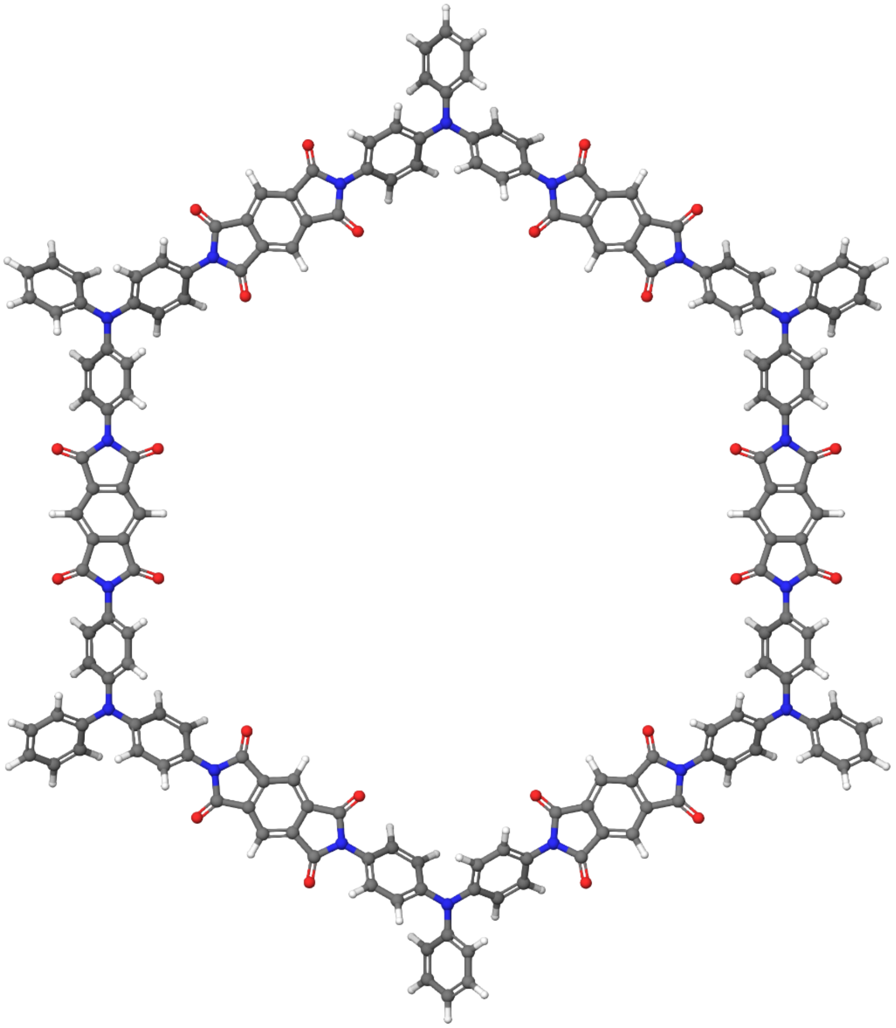

**Figure S8-41.** Structure of a single pore of the **TAPA-PMDA** COF, obtained by composing a supercell from a 2D periodic geometry optimization of the corresponding asymmetric unit on RI-PBE-D3/def2-TZVP level of theory.

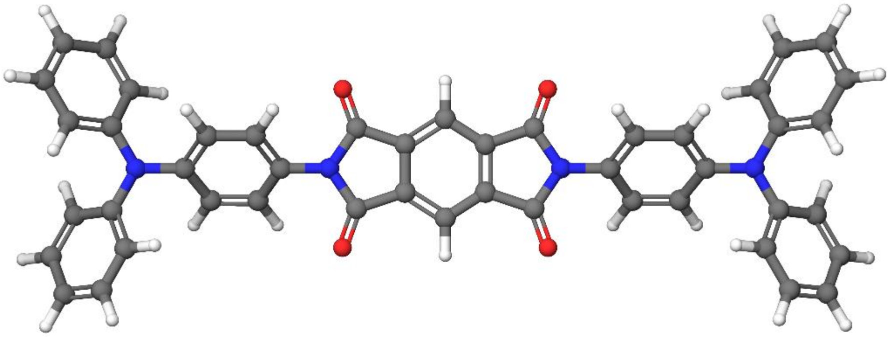

**Figure S8-42.** Structure of the **TAPA-PMDA** NMR model, modeled by cutting the supercell obtained from the 2D optimized structure of the TAPA-PMDA COF model.

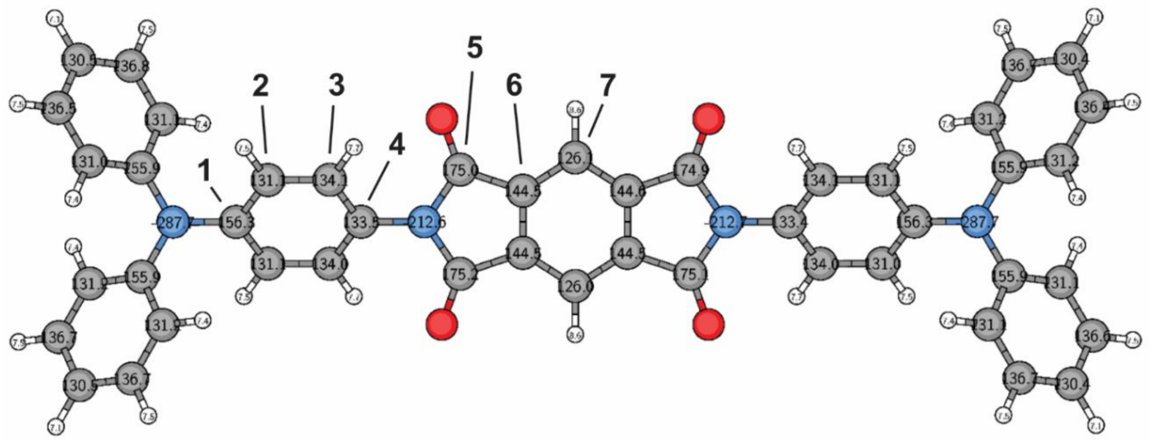

**Figure S8-43.** Calculated NMR chemical shifts for the **TAPA-PMDA** NMR model, obtained on B97-2/pcsSeg-2 level of theory.

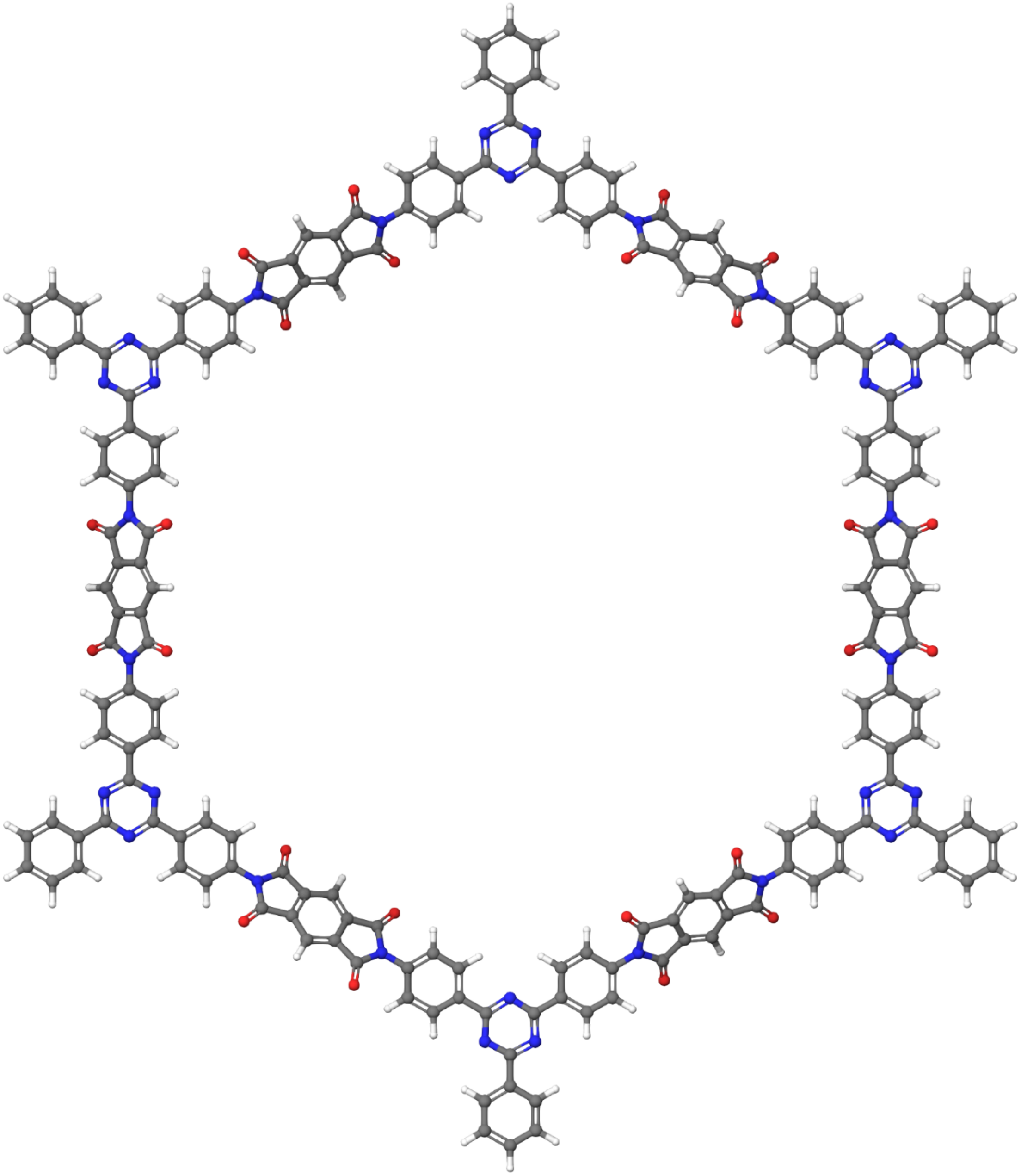

**Figure S8-44.** Structure of a single pore of the **TT-PMDA** COF, obtained by composing a supercell from a 2D periodic geometry optimization of the corresponding asymmetric unit on RI-PBE-D3/def2-TZVP level of theory.

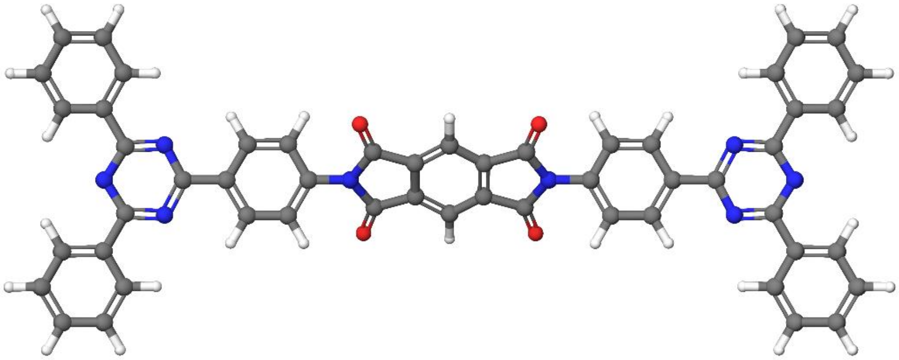

**Figure S8-45.** Structure of the **TT-PMDA** NMR model, modeled by cutting the supercell obtained from the 2D optimized structure of the TAPA-PMDA COF model.

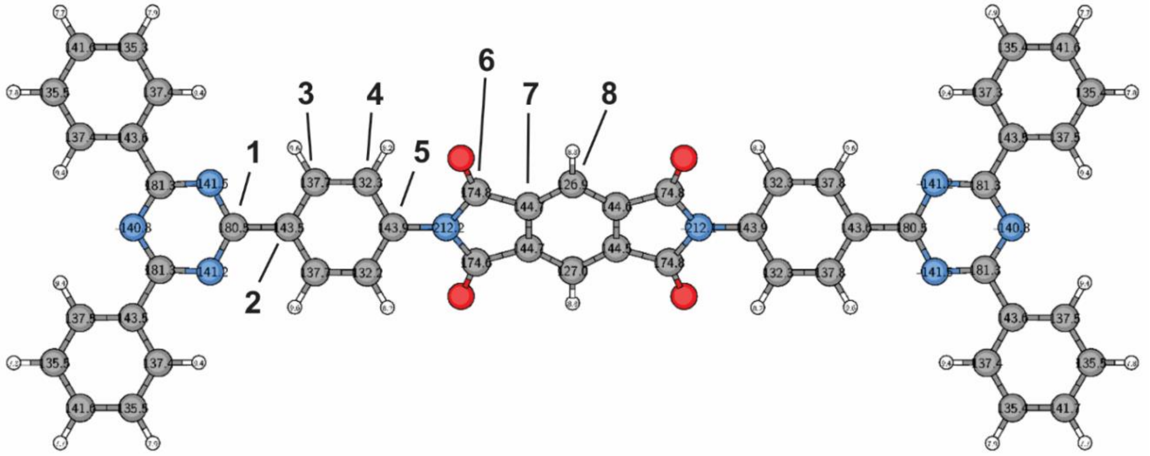

**Figure S8-46.** Calculated NMR chemical shifts for the **TT-PMDA** NMR model, obtained on B97-2/pcsSeg-2 level of theory.

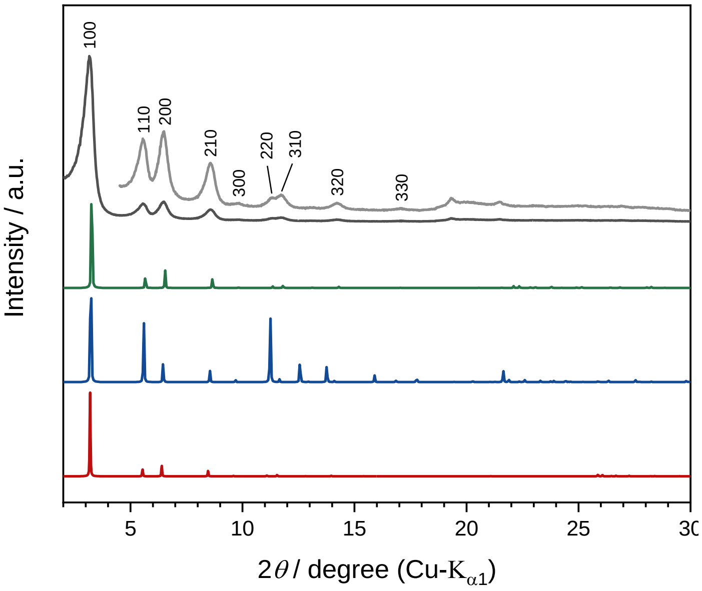

**Figure S8-47.** Experimental XRPD pattern (λ = Cu-Kα1) of **TAPA-PMDA-COF** (black) compared to simulated patterns of the COF assuming $P\bar{3}1m$ symmetry (green), $P\bar{3}1c$ symmetry (blue) and $Cmcm$ symmetry (red).

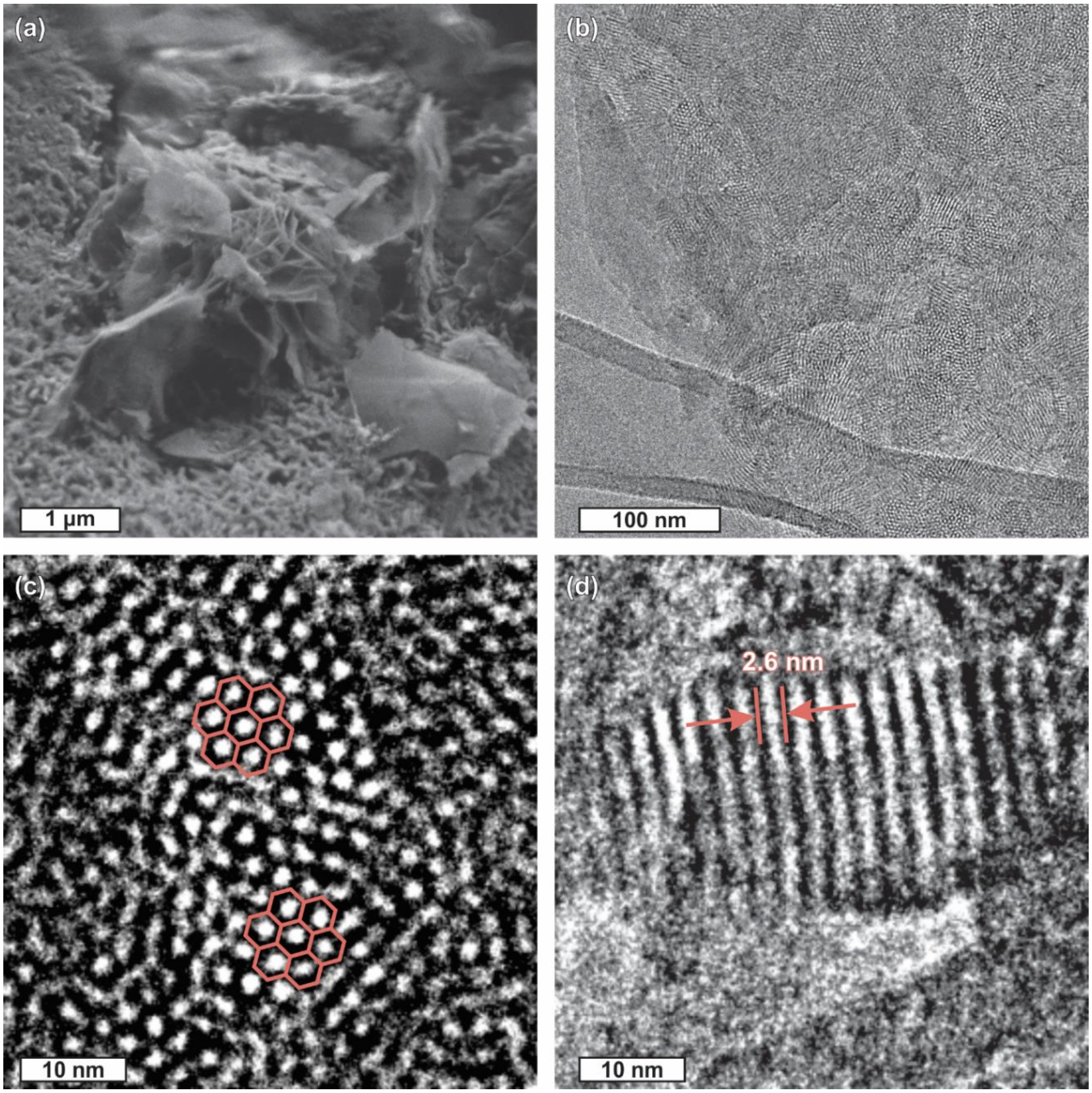

**Figure S8-48.** SEM image (a) and TEM images (b) – (d) of **TAPA-PMDA-COF**. (c) shows the hexagonal pores highlighted in red and (d) shows straight channels with a diameter of ≈ 2.6 nm.

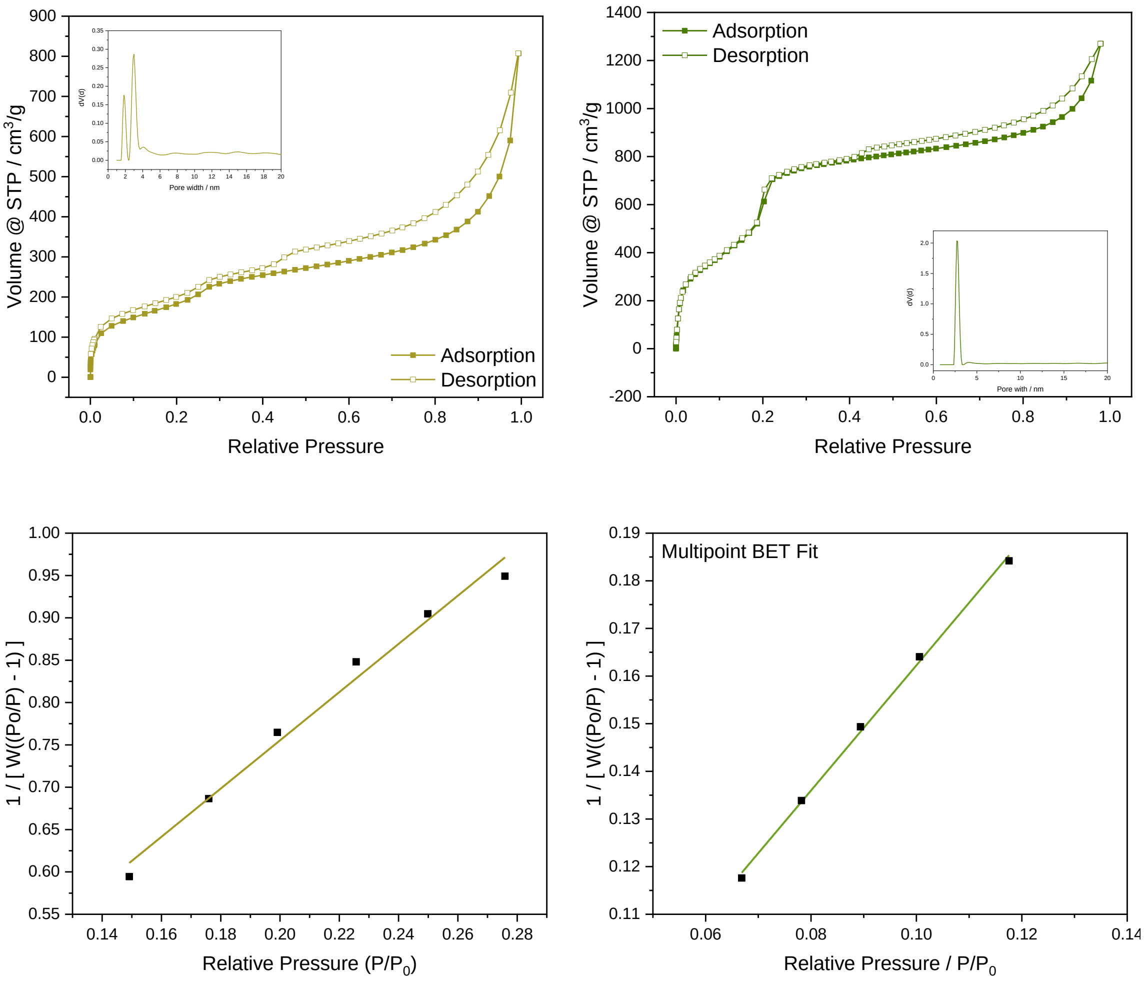

**Figure S8-49.** Top: Argon gas adsorption and desorption isotherms for **TT-PMDA** (yellow) and **TAPA-PMDA** (green). Insets: Respective calculated pore size distributions of PI-COFs from fitting the quenched solid-state density functional theory (QSDFT) model. Bottom: Multipoint BET fits of TT-PMDA (yellow) and TAPA-PMDA (green).

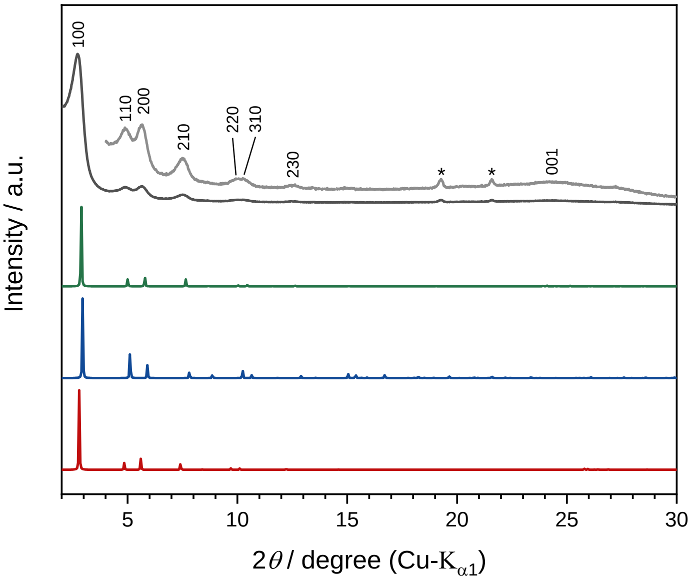

**Figure S8-50.** Experimental XRPD pattern (λ = Cu-$K_{\alpha1}$) of **TT-PMDA-COF** (black) compared to simulated patterns of the COF assuming $P\bar{3}1m$ symmetry (green), $P\bar{3}1c$ symmetry (blue) and $Cmcm$ symmetry (red). Reflections marked with an asterisk show minor impurities, which couldn't be eliminated.

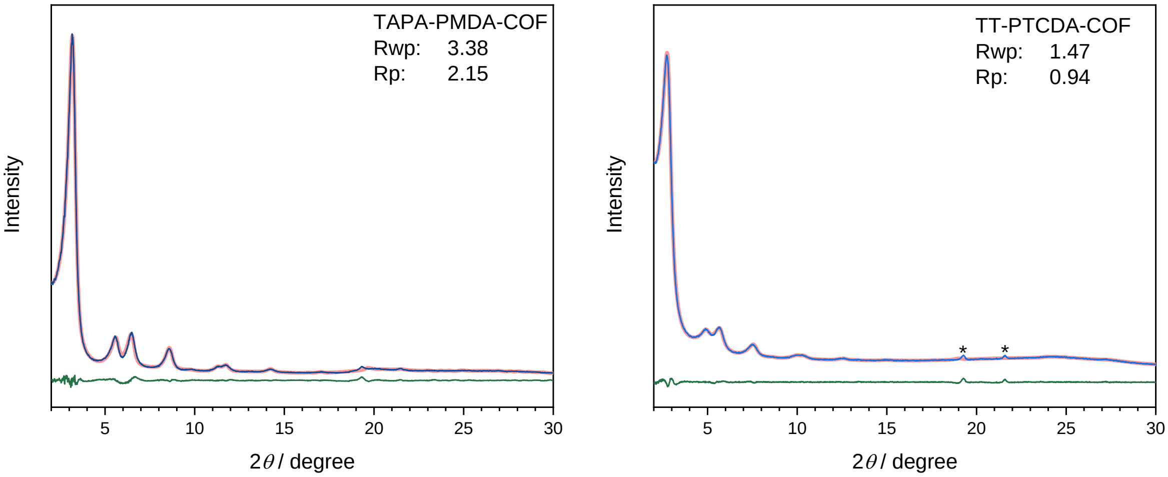

**Figure S8-51.** Pawley refinement of TAPA-PMDA-COF (left) and TT-PMDA-COF (right) with fixed lattice sizes and fit parameters obtained from Rietveld refinement. Reflections marked with an asterisk show minor impurities, which couldn't be eliminated.

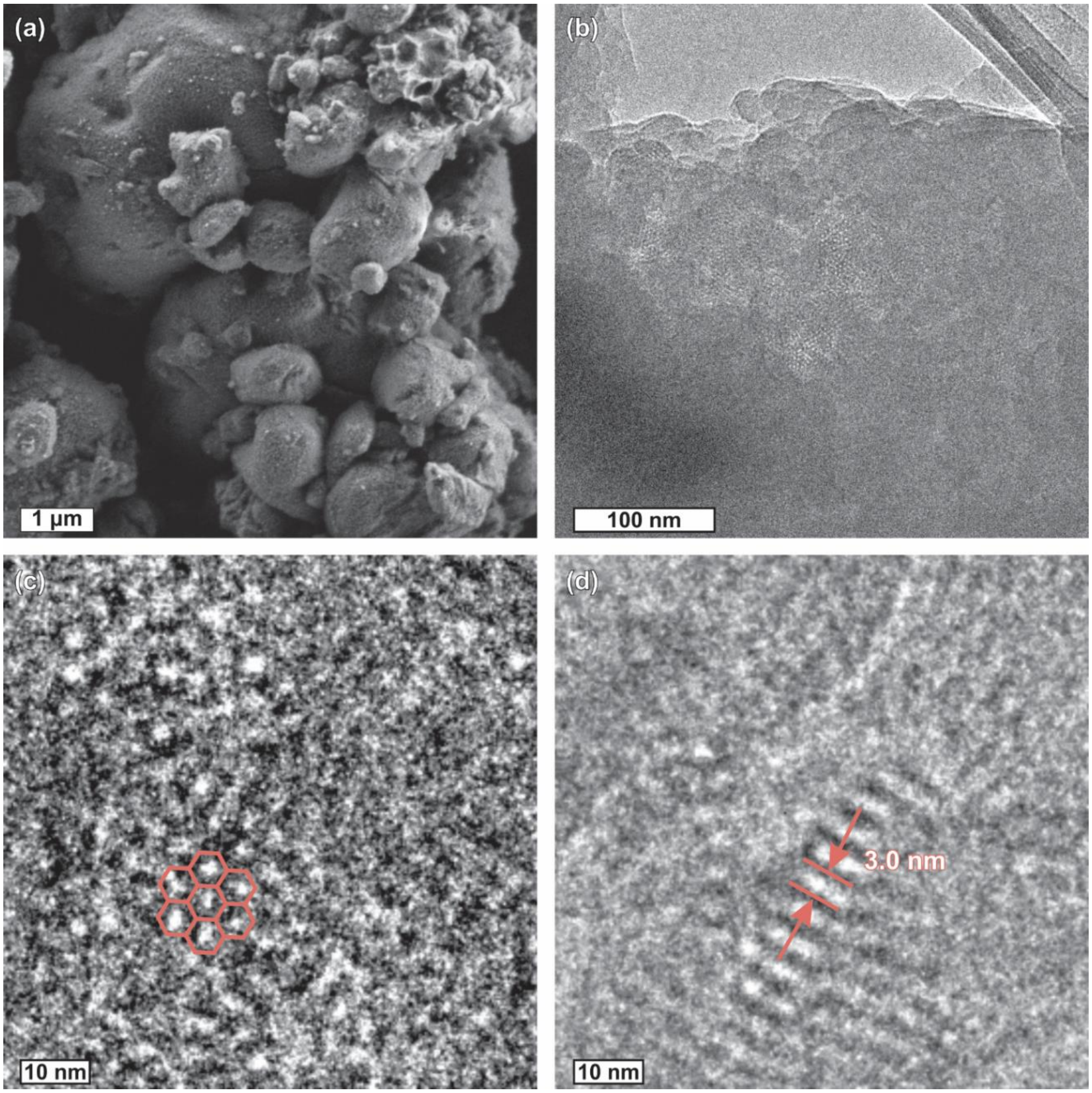

**Figure S8-52.** SEM image (a) and TEM images (b) – (e) of **TT-PMDA-COF**. (c) shows the hexagonal pores highlighted in red and (d) shows straight channels with a diameter of ≈ 3.0 nm and (e) shows straight channels with a diameter of ≈ 1.7 nm.

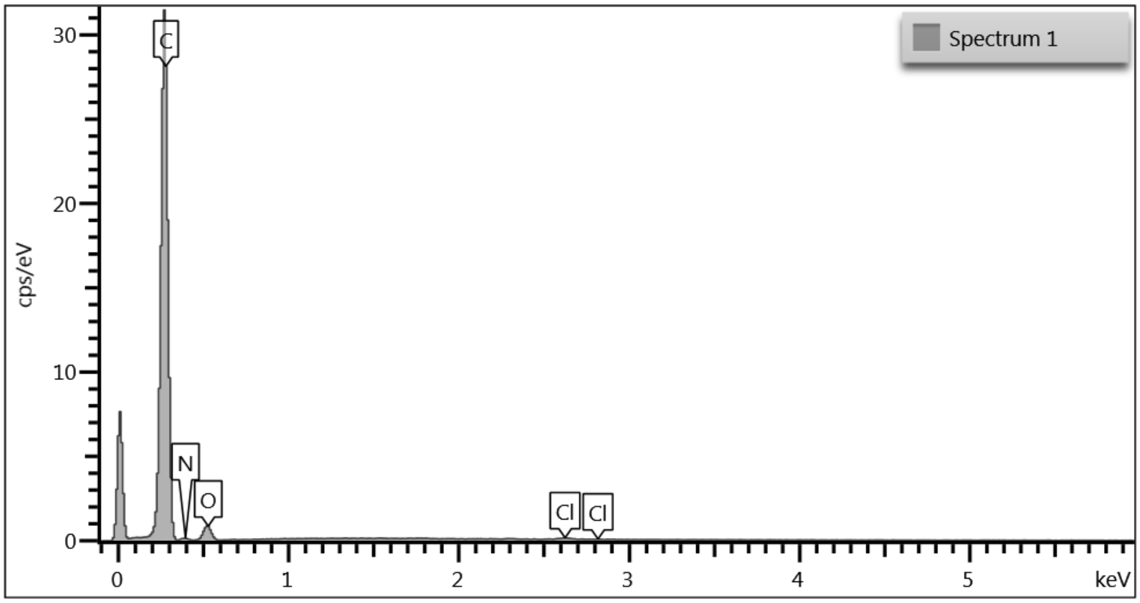

**Figure S8-53.** EDX spectrum of TAPB-PTCDA-COF showing only traces of chloride residuals in the COF.

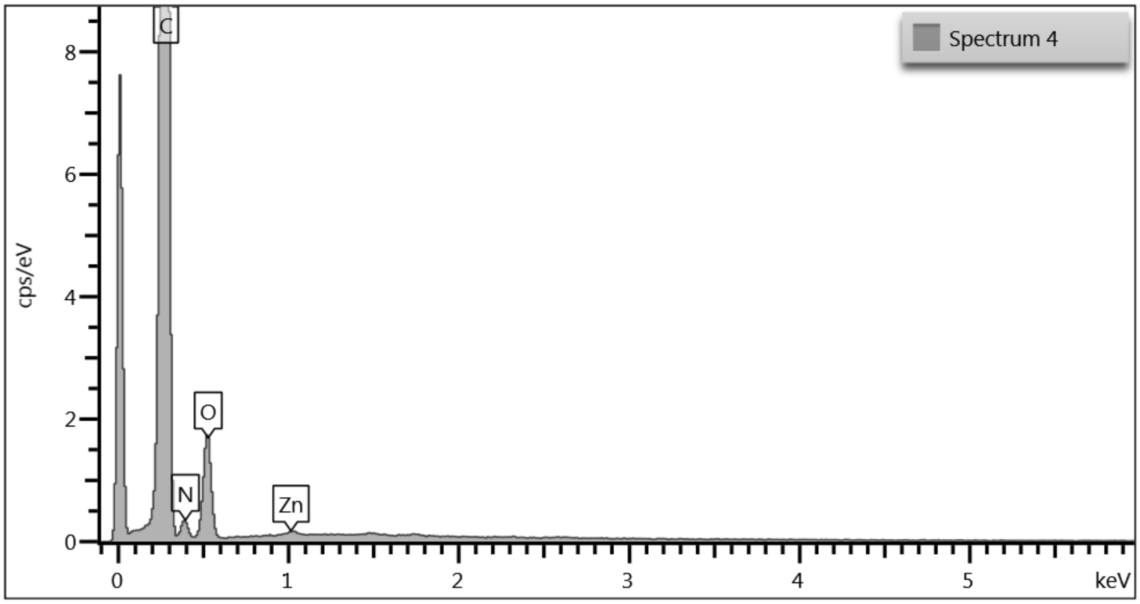

**Figure S8-54.** EDX spectrum of TAPB-PMDA-COF showing trace amounts of zinc residuals in the COF.

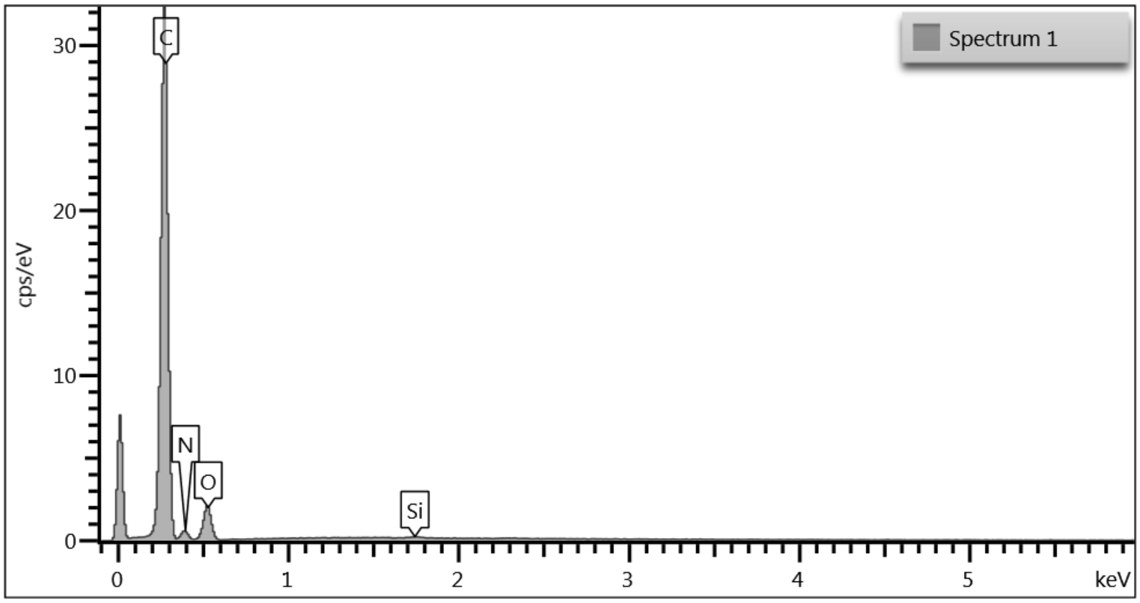

**Figure S8-55.** EDX spectrum of TT-PMDA-COF showing the absence of $ZnCl_2$ residuals in the COF.

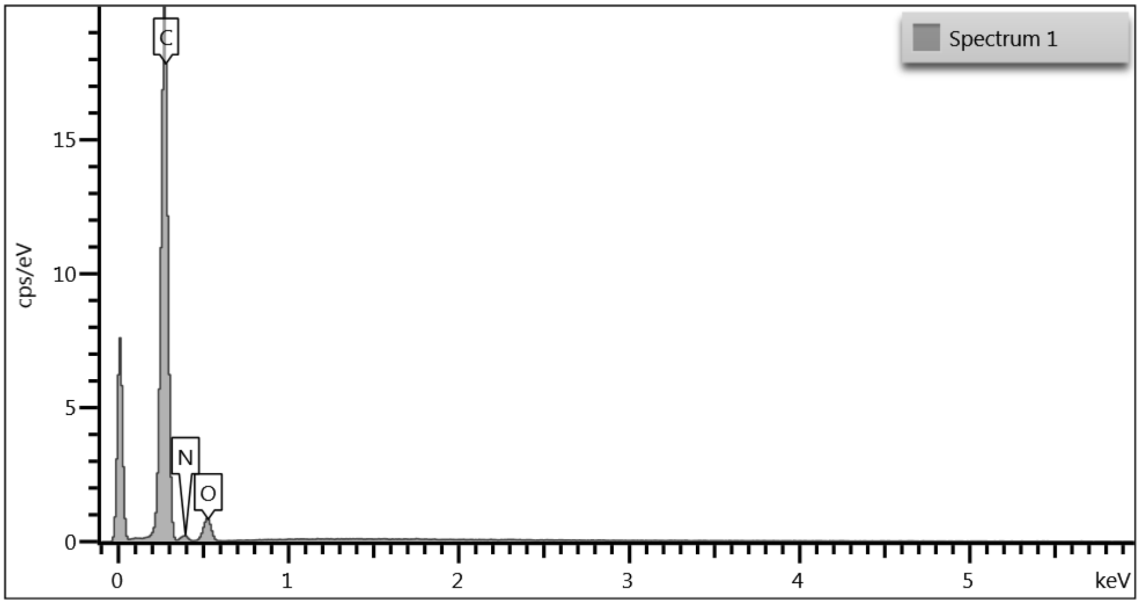

**Figure S8-56.** EDX spectrum of TAPA-PMDA-COF showing the absence of $ZnCl_2$ residuals in the COF.

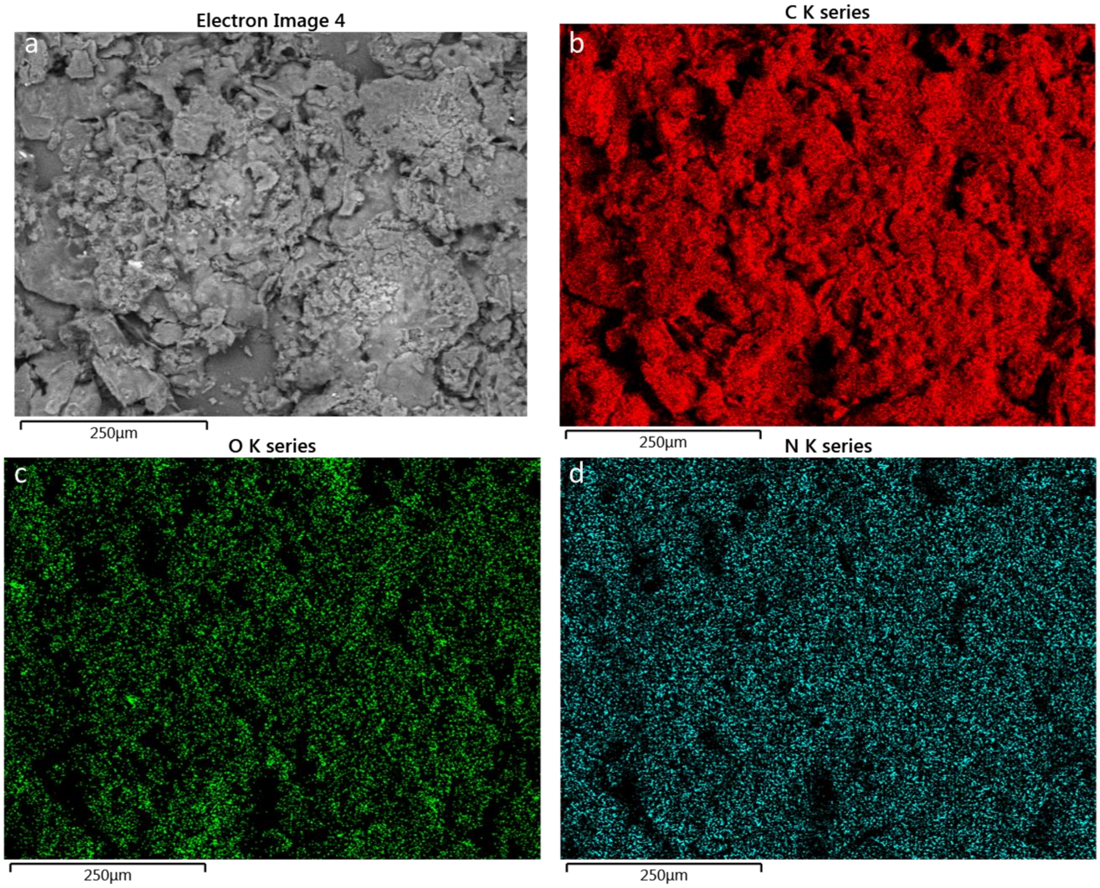

**Figure S8-57.** SEM image (a) and elemental mapping of carbon (b), oxygen (c) and nitrogen (d) of **TAPB-PTCDA-COF** showing a homogeneous distribution of the corresponding elements.

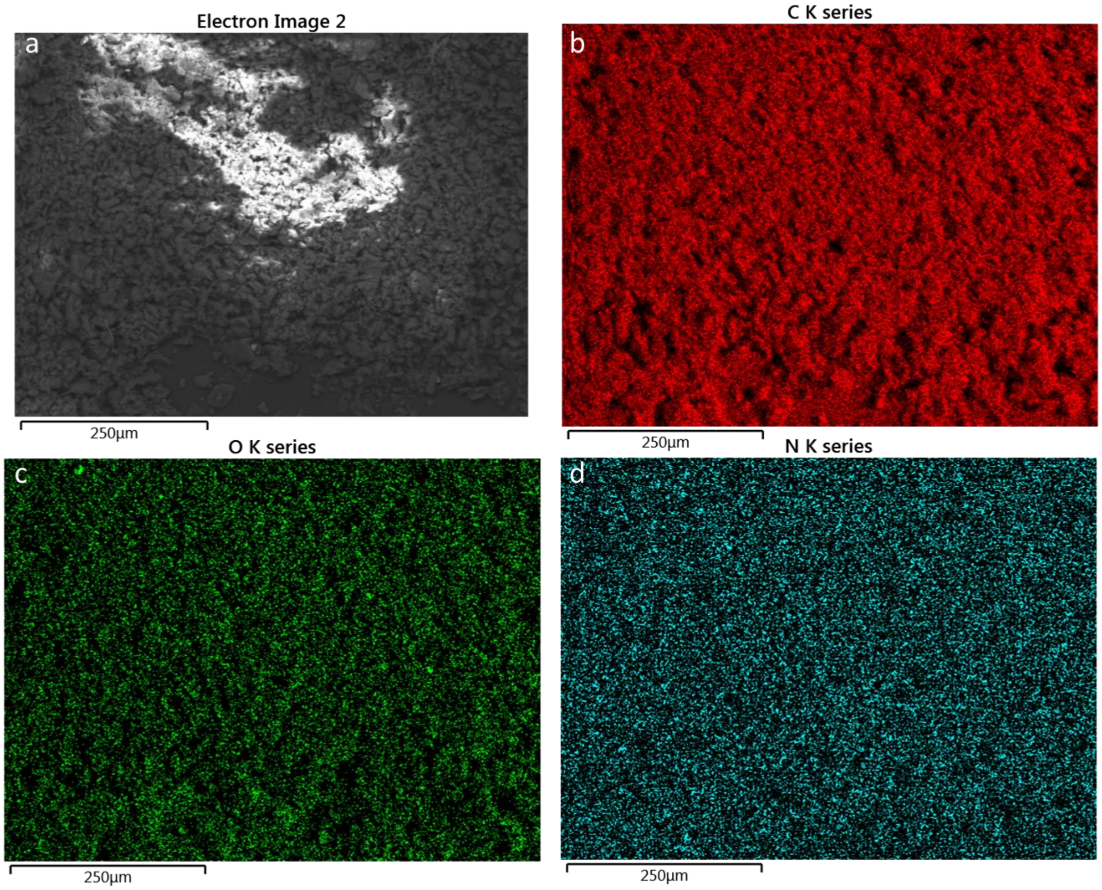

**Figure S8-58.** SEM image (a) and elemental mapping of carbon (b), oxygen (c) and nitrogen (d) of **TAPB-PMDA-COF** showing a homogeneous distribution of the corresponding elements.

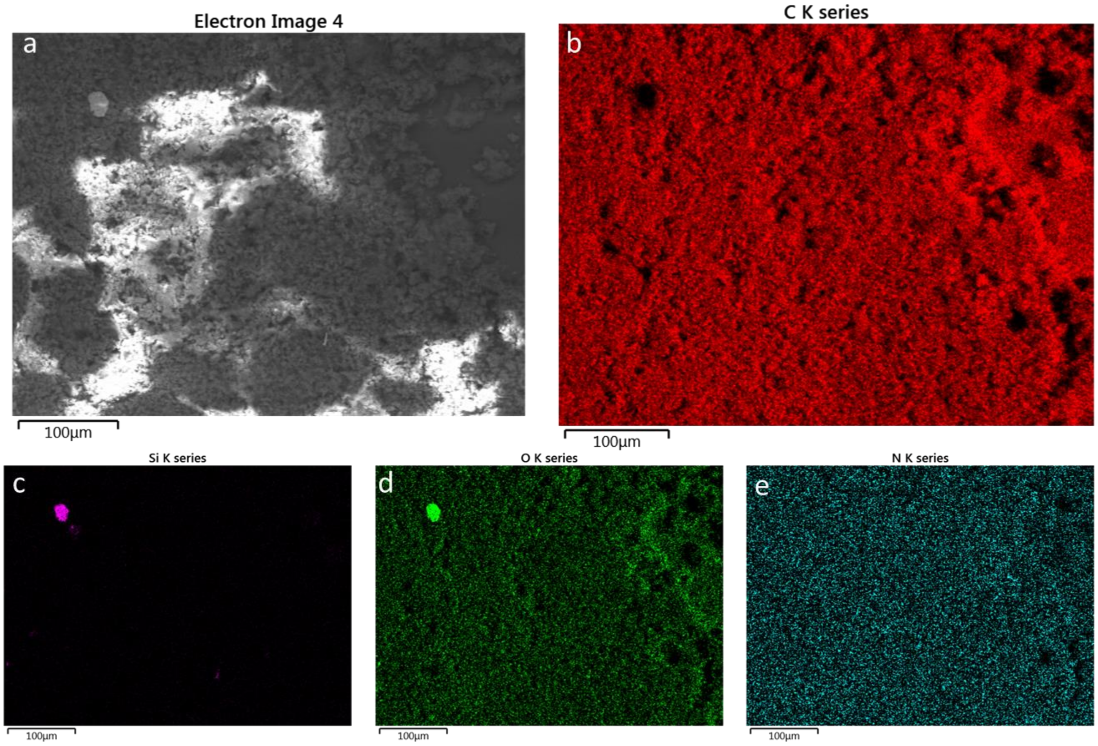

**Figure S8-59.** SEM image (a) and elemental mapping of carbon (b), silicon (c), oxygen (d) and nitrogen (e) of **TT-PMDA-COF** showing a homogeneous distribution of the corresponding elements. The silicon found in this sample corresponds to a quartz impurity.

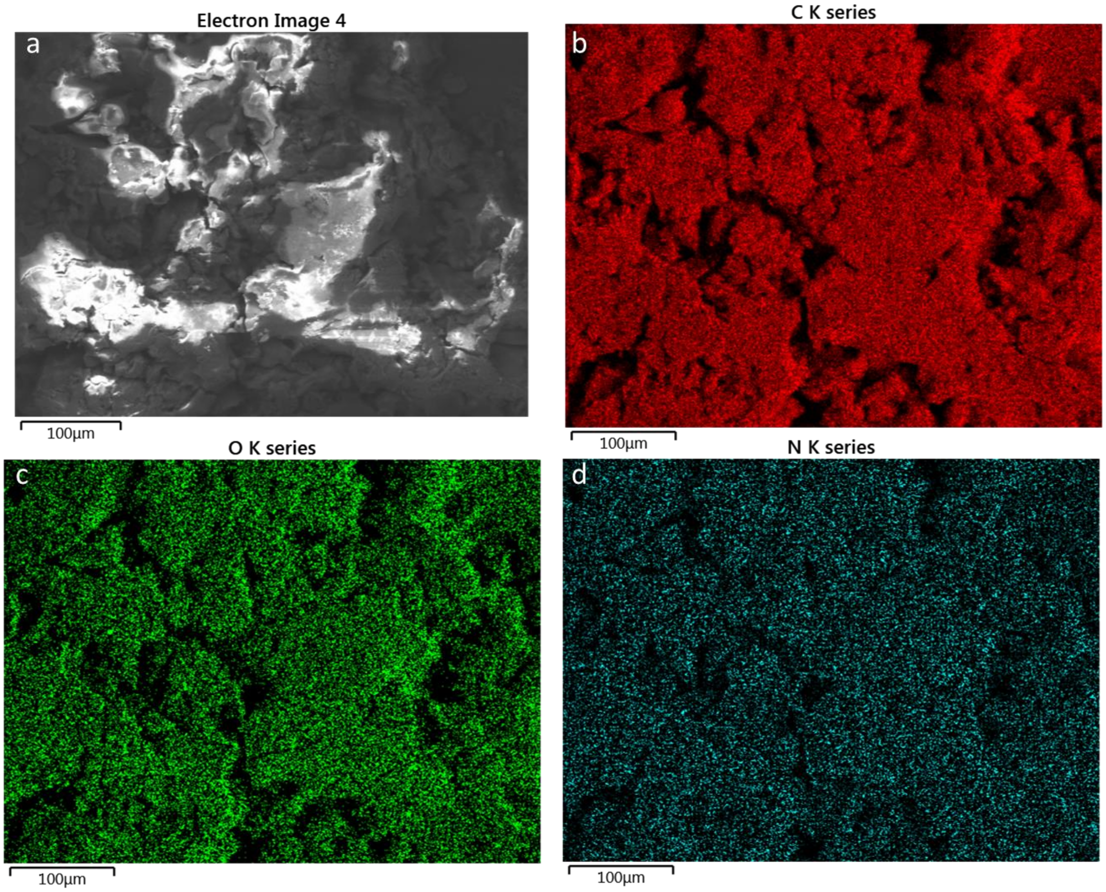

**Figure S8-60.** SEM image (a) and elemental mapping of carbon (b), silicon (c), oxygen (d) and nitrogen (e) of **TAPA-PMDA-COF** showing a homogeneous distribution of the corresponding elements.

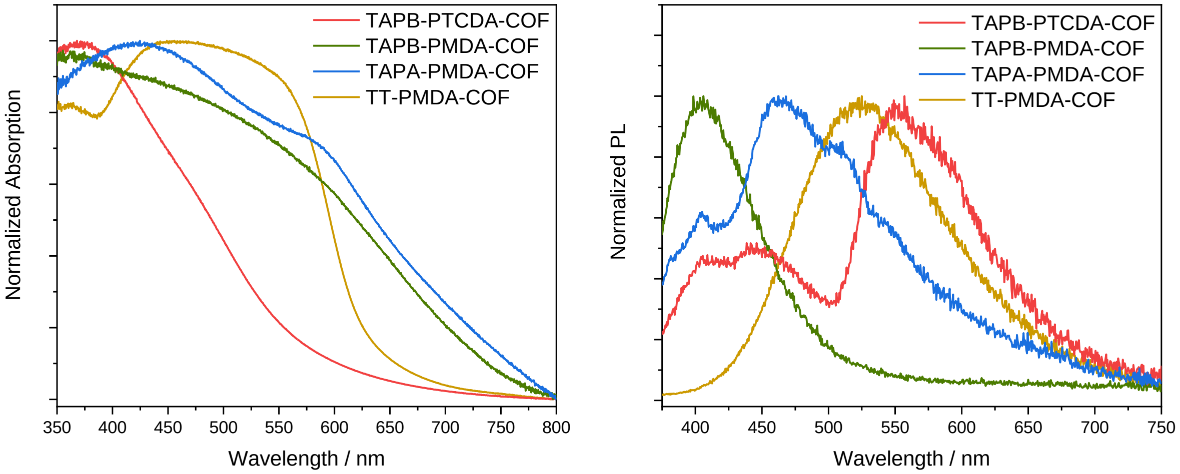

**Figure S8-61**. Diffuse reflectance spectra (left) and photoluminescence spectra (right) of the ionothermal imide-linked COFs TAPB-PTCDA (red), TAPB-PMDA (green), TAPA-PMDA (blue) and TT-PMDA (yellow).

### *8.2.4 Supplementary Tables*

**Table S8-1.** Calculated NMR chemical shifts for the **TAPB-PTCDA** NMR model, obtained on B97-2/pcsSeg-2 level of theory.

| Atom Label | Atom | NMR Chemical Shift [ppm] |
|---|---|---|
| 1 | C | 133.6 |
| 2 | C | 151.1 |
| 3 | C | 151.3 |
| 4 | C | 135.0 |
| 5 | C | 137.9 |
| 6 | C | 143.9 |
| 7 | C | 171.9 |
| 8 | C | 131.5 |
| 9 | C | 140.1 |
| 10 | C | 129.3 |
| 11 | C | 143.2 |
| 12 | C | 134.2 |
| 13 | C | 138.6 |

**Table S8-2.** Calculated NMR chemical shifts for the **TAPB-PMDA** NMR model, obtained on B97-2/pcsSeg-2 level of theory.

| Atom Label | Atom | NMR Chemical Shift [ppm] |
|---|---|---|
| 1 | C | 133.2 |
| 2 | C | 150.2 |
| 3 | C | 150.3 |
| 4 | C | 134.9 |
| 5 | C | 133.5 |
| 6 | C | 138.8 |
| 7 | C | 174.9 |
| 8 | C | 144.7 |
| 9 | C | 126.5 |

**Table S8-3.** Rietveld refinement of TAPB-PTCDA- and TAPB-PMDA-COF at room temperature.

| Fitted Pattern | TAPB-PTCDA-COF | TAPB-PMDA-COF |
|---|---|---|
| **Space group** | $P\bar{3}1m$ | $P\bar{3}1m$ |
| **Constraints** | *c* = fixed | - |
| **Rwp (%)** | 3.922 | 4.986 |
| **Cell Volume (Å³)** | 6100(3) | 4164(9) |
| **A (Å)** | 43.6(2) | 35.7(4) |
| **B (Å)** | 43.6(2) | 35.7(4) |
| **C (Å)** | 3.705 | 3.76(5) |
| **α (°)** | 90 | 90 |
| **β (°)** | 90 | 90 |
| **γ (°)** | 120 | 120 |

**Table S8-4.** Calculated total energies for investigated model compounds, obtained on PBE0-D3/def2-TZVP level of theory.

| Compound | Label | Total Energy [H] |
|---|---|---|
| Phthalic anhydride | 1 | -532.572907 |
| Phthalic anhydride · $ZnCl_2$ | 1Z | -3231.977974 |
| Aniline | 2 | -287.371607 |
| Aniline · $ZnCl_2$ | 2Z | -2986.791682 |
| N-Phenylphthalimide | 3 | -743.577316 |
| N-Phenylphthalimide · $ZnCl_2$ | 3Z | -3442.995082 |
| N-Phenylphthalimide· 2·$ZnCl_2$ | 4Z | -6142.407343 |
| Water | $H_2O$ | -76.377335 |
| $ZnCl_2$ | Z | -2699.385181 |

| Reactant | | | | Product | | | Reaction Enthalpy [kJ/mol] |
|---|---|---|---|---|---|---|---|
| 1 | + | 2Z | = | 3Z | + | $H_2O$ | -20.5 |
| 1 | + | 2 | = | 3 | + | $H_2O$ | -26.6 |
| 1Z | + | 2 | = | 3Z | + | $H_2O$ | -60.0 |
| 1Z | + | 2Z | = | 4Z | + | $H_2O$ | -39.4 |
| 1 | + | $ZnCl_2$ | = | 1Z | | | -52.2 |
| 2 | + | $ZnCl_2$ | = | 2Z | | | -91.6 |
| 3 | + | $ZnCl_2$ | = | 3Z | | | -85.5 |
| 3Z | + | $ZnCl_2$ | = | 4Z | | | -71.1 |

**Table S8-5.** List of data obtained from peak fittings using a Voigt function and the resulting calculated Scherrer crystallite sizes of the ionothermal TAPB-PTCDA-COF.

| **Ionothermal TAPB-PTCDA-COF** | | | | |
|---|---|---|---|---|
| **Bragg Peak** | **Peak Position [degree]** | **FWHM** | **Crystallite Size D [nm]** | **D [nm] Average** |
| 100 | 2.11298 | 0.60025 | 132.3718305 | **112.29** |
| 200 | 4.37692 | 0.86225 | 92.20141425 | |

**Table S8-6.** List of data obtained from peak fittings using a Voigt function and the resulting calculated Scherrer crystallite sizes of the ionothermal and solvothermal TAPB-PMDA-COF.

| **Ionothermal TAPB-PMDA-COF** | | | | |
|---|---|---|---|---|
| **Bragg Peak** | **Peak Position [degree]** | **FWHM** | **Crystallite Size D [nm]** | **D [nm] Average** |
| 100 | 2.77758 | 0.38474 | 206.5447495 | **193.51** |
| 110 | 4.91073 | 0.33593 | 236.7031444 | |
| 200 | 5.64845 | 0.42333 | 187.8895726 | |
| 210 | 7.49409 | 0.41563 | 191.5474646 | |
| 230 | 12.37508 | 0.55154 | 144.8819576 | |
| 001 | 24.16267 | 2.34523 | 34.641411 | **34.64** |
| **Solvothermal TAPB-PMDA-COF** | | | | |
| **Bragg Peak** | **Peak Position [degree]** | **FWHM** | **Crystallite Size D [nm]** | **D [nm] Average** |
| 100 | 2.72016 | 0.70723 | 112.3610022 | **112.36** |

**Table S8-7.** List of data obtained from peak fittings using a Voigt function and the resulting calculated Scherrer crystallite sizes of the ionothermal and solvothermal TAPA-PMDA-COF.

| **Ionothermal TAPA-PMDA-COF** | | | | |
|---|---|---|---|---|
| **Bragg Peak** | **Peak Position [degree]** | **FWHM** | **Crystallite Size D [nm]** | **D [nm] Average** |
| 100 | 3.22244 | 0.48247 | 164.7234143 | **155.01** |
| 110 | 5.62072 | 0.49822 | 159.6450274 | |
| 200 | 6.56218 | 0.50782 | 156.6955284 | |
| 210 | 8.6424 | 0.5585 | 142.6484469 | |
| 230 | 14.30553 | 0.52911 | 151.3216167 | |
| **Solvothermal TAPA-PMDA-COF** | | | | |
| **Bragg Peak** | **Peak Position [degree]** | **FWHM** | **Crystallite Size D [nm]** | **D [nm] Average** |
| 100 | 3.12165 | 0.79129 | 100.4336845 | **121.77** |
| 110 | - | - | - | |
| 200 | - | - | - | |
| 210 | 8.63151 | 0.55668 | 143.1137922 | |
| 230 | - | - | - | |

**Table S8-8.** List of data obtained from peak fittings using a Voigt function and the resulting calculated Scherrer crystallite sizes of the ionothermal and solvothermal TT-PMDA-COF.

| **Ionothermal TT-PMDA-COF** | | | | |
|---|---|---|---|---|
| **Bragg Peak** | **Peak Position [degree]** | **FWHM** | **Crystallite Size D [nm]** | **D [nm] Average** |
| 100 | 2.67318 | 0.74271 | 106.9923722 | **116.76** |
| 110 | 4.92101 | 0.74721 | 106.4171966 | |
| 210 | 7.44826 | 0.80717 | 98.62952516 | |
| 230 | 12.48957 | 0.51565 | 154.9828203 | |
| 001 | 24.47828 | 2.95726 | 27.48838668 | **27.49** |
| **Solvothermal TT-PMDA-COF** | | | | |
| **Bragg Peak** | **Peak Position [degree]** | **FWHM** | **Crystallite Size D [nm]** | **D [nm] Average** |
| 100 | 2.66297 | 0.83045 | 95.68804849 | **101.65** |
| 110 | 4.8814 | 0.84909 | 93.64710123 | |
| 210 | 7.57262 | 0.68849 | 115.6392463 | |
| 230 | - | - | - | |
| 001 | 25.07428 | 3.51016 | 23.1850474 | **23.19** |

**Table S8-9.** Calculated NMR chemical shifts for the **TAPA-PMDA** NMR model, obtained on B97-2/pcsSeg-2 level of theory.

| **Atom Label** | **Atom** | **NMR Chemical Shift [ppm]** |
|---|---|---|
| 1 | C | 156.3 |
| 2 | C | 131.1 |
| 3 | C | 134.1 |
| 4 | C | 133.5 |
| 5 | C | 175.0 |
| 6 | C | 144.5 |
| 7 | C | 126.1 |

**Table S8-10.** Calculated NMR chemical shifts for the **TT-PMDA** NMR model, obtained on B97-2/pcsSeg-2 level of theory.

| **Atom Label** | **Atom** | **NMR Chemical Shift [ppm]** |
|---|---|---|
| 1 | C | 180.5 |
| 2 | C | 143.5 |
| 3 | C | 137.7 |
| 4 | C | 132.3 |
| 5 | C | 143.9 |
| 6 | C | 174.8 |
| 7 | C | 144.7 |
| 8 | C | 126.9 |

**Table S8-11.** Rietveld refinement of **TAPA-PMDA-** and **TT-PMDA-COF** at room temperature.

| **Fitted Pattern** | **TAPA-PMDA-COF** | **TT-PMDA-COF** |
|---|---|---|
| **Space group** | $P\bar{3}1m$ | $P\bar{3}1m$ |
| **Constraints** | *c* = fixed | - |
| **Rwp (%)** | 9.031 | 2.220 |
| **Cell Volume (Å$^3$)** | 3379(6) | 3971(7) |
| **A (Å)** | 31.1(6) | 35.2(5) |
| **B (Å)** | 31.1(6) | 35.2(5) |
| **C (Å)** | 4.018 | 3.7(2) |
| **α (°)** | 90 | 90 |
| **β (°)** | 90 | 90 |
| **γ (°)** | 120 | 120 |

### 8.2.5 *Bibliography*

[1] H. M. Rietveld, *J. Appl. Crystallogr.* **1969**, *2*, 65-&.

[2] A. A. Coelho, *J. Appl. Crystallogr.* **2000**, *33*, 899-908.

[3] A. Schafer, C. Huber, R. Ahlrichs, *J. Chem. Phys.* **1994**, *100*, 5829-5835.

[4] J. P. Perdew, K. Burke, M. Ernzerhof, *Phys. Rev. Lett.* **1996**, *77*, 3865-3868.

[5] K. Eichkorn, F. Weigend, O. Treutler, R. Ahlrichs, *Theor. Chem. Acc.* **1997**, *97*, 119-124.

[6] S. Grimme, J. Antony, S. Ehrlich, H. Krieg, *J. Chem. Phys.* **2010**, *132*, 154104.

[7] A. M. Burow, M. Sierka, *J. Chem. Theory Comput.* **2011**, *7*, 3097-3104.

[8] A. M. Burow, M. Sierka, F. Mohamed, *J. Chem. Phys.* **2009**, *131*, 214101.

[9] L. Grajciar, *J. Comput. Chem.* **2015**, *36*, 1521-1535.

[10] R. Lazarski, A. M. Burow, M. Sierka, *J. Chem. Theory Comput.* **2015**, *11*, 3029-3041.

[11] TURBOMOLE V7.3 2018, a development of University of Karlsruhe and Forschungszentrum Karlsruhe GmbH, **1989-2007**, TURBOMOLE GmbH, since 2007; available from http://www.turbomole.com.

[12] C. Adamo, V. Barone, *J. Chem. Phys.* **1999**, *110*, 6158-6170.

[13] M. Ernzerhof, G. E. Scuseria, *J. Chem. Phys.* **1999**, *110*, 5029-5036.

[14] A. E. Reed, R. B. Weinstock, F. Weinhold, *J. Chem. Phys.* **1985**, *83*, 735-746.

[15] P. J. Wilson, T. J. Bradley, D. J. Tozer, *J. Chem. Phys.* **2001**, *115*, 9233-9242.

[16] F. Jensen, *J. Chem. Theory Comput.* **2015**, *11*, 132-138.

[17] J. Kussmann, C. Ochsenfeld, *J. Chem. Phys.* **2013**, *138*, 134114.

[18] J. Kussmann, C. Ochsenfeld, *J. Chem. Theory Comput.* **2015**, *11*, 918-922.

[19] D. Mullangi, S. Shalini, S. Nandi, B. Choksi, R. Vaidhyanathan, *J. Mater. Chem. A* **2017**, *5*, 8376-8384.

## 8.3 Supporting Information of Chapter 4.2 “Direct and Linker-Exchange Alcohol-Assisted Hydrothermal Synthesis of Imide-Linked COFs”

### 8.3.1 Experimental Details

*FT-IR*

Infrared spectra were recorded on a PerkinElmer UATR Two in attenuated total reflection (ATR) geometry equipped with a diamond crystal.

*TEM*

TEM was performed with a Philips CM30 ST (300kV, LaB6 cathode). The samples were prepared dry onto a copper lacey carbon grid (Plano). Images were recorded with a TVIPS TemCam-F216 CMOS camera. The program EM-Menu 4.0 Extended was used for analysis.

*Sorption*

Sorption measurements were performed on a Quantachrome Instruments Autosorb iQ MP with Argon at 87 K. The pore size distributions were determined from argon adsorption isotherms using the quenched solid-state density functional theory (QSDFT) for cylindrical pores in carbon model for argon at 87 K.

*XRPD*

X-ray powder diffraction (XRPD) measurements were performed on a Stoe Stadi-P diffractometer in Debye-Scherrer geometry with Cu-$K_{\alpha1}$ radiation equipped with a Ge(111) primary monochromator. The glass capillaries (1 mm in diameter) were spun during data collection for an improved particle statistics. Rietveld[1] refinements of the different COF structures were performed using TOPAS V6. Model structures created by Material Studio were used for the Rietveld refinements with fixed atomic coordinates. The peak profile of the XRPD patterns was described by applying the fundamental parameter[2] approach as implemented in TOPAS. The background was modeled by Chebychev polynomials. The microstructure of the different COFs was modeled using microstrain (Lorentzian and Gaussian components).

### *NMR*

Solid state nuclear magnetic resonance spectra (ssNMR) were recorded on a Bruker Avance III 400 MHz spectrometer (magnetic field 9.4 T). For ssNMR spectroscopy, the samples were packed in $ZrO_2$ rotors, and spun in a Bruker WVT BL4 double resonance MAS probe. The spinning rate was 12-14 kHz in $^{13}C$ measurements, and 6 kHz in $^{15}N$ experiments. A standard cross-polarization sequence with a ramped contact pulse was used for both nuclei. The duration of contact pulse was 2 ms for $^{13}C$ and 4 ms for $^{15}N$. A total of 4096-8192 scans were routinely accumulated in $^{13}C$ experiments, and 80000 scans in the experiments with $^{15}N$. All the measurements were performed under conditions of high-power broadband proton decoupling (SPINAL 64) with the spectral conditions being optimized for the shortest relaxation delay by measuring $^{1}H$ $T_1$ relaxation time. Chemical shifts were referenced relative to tetramethylsilane in $^{13}C$ ($\delta_{iso}$ = 0.0 ppm) and relative to nitromethane in $^{15}N$ ($\delta_{iso}$ = 0.0 ppm), with solid glycine as the secondary reference ($\delta_{iso}$ [$^{15}N$] = -347.54 ppm).

## *8.3.2 Materials and Synthetic Procedures*

4,4',4'',4'''-(pyrene-1,3,6,8-tetrayl)tetraaniline was synthesized according to literature procedures.[3,4] All other chemicals were obtained from commercial sources and were used as received.

All hydrothermal experiments were carried out in “Schlenk bombs”. Schlenk bombs are a subclass of Schlenk flasks of structurally sound shapes and heavy walls that have only one opening which is accessed by opening a Teflon plug valve. Due to the Teflon plug valve, Schlenk bombs can be sealed more completely than standard Schlenk flasks. This design allows reactions at elevated temperatures and pressures.

No unexpected or unusually high safety hazards were encountered.

### *Hydrothermal Synthesis of Imide-COFs*

**Synthesis of TAPA-PMDA-COF.** Typically, tris(4-aminophenyl)amine (TAPA, 0.067 mmol, 19.4 mg) and pyromellitic dianhydride (PMDA, 0.1 mmol, 21.8 mg) were placed in a Schlenk bomb and suspended in a mixture of 1.8 ml $H_2O$/0.2 ml n-hexanol/0.04 ml pyridine (or 1 ml $H_2O$/0.5 ml n-butanol/0.04 ml pyridine). The reaction mixture was sonicated for 10 min and degassed by four freeze-pump-thaw cycles. The Schlenk bombs were placed in an aluminum heating block and were heated to 180 °C (~12°bar) for four days. The resulting brown precipitate was isolated via filtration and washed with methanol and THF followed by Soxhlet extraction in methanol. Supercritical $CO_2$ drying yielded TAPA-PMDA-COF in 73 % yield.

**Synthesis of TAPB-PMDA-COF.** Typically, tris(4-aminophenyl)benzene (TAPB, 0.067 mmol, 23.4 mg) and pyromellitic dianhydride (PMDA, 0.1 mmol, 21.8 mg) were placed in a Schlenk bomb and suspended in a mixture of 1.2 ml $H_2O$/0.3 ml n-hexanol/0.04 ml pyridine. The reaction mixture was sonicated for 10 min and degassed by four freeze-pump-thaw cycles. The Schlenk bombs were placed in an aluminum heating block and were heated to 200 °C (~16 bar) for 6 days. The resulting brown precipitate was isolated via filtration and washed with methanol and THF followed by Soxhlet extraction in methanol. Supercritical $CO_2$ drying yielded TAPB-PMDA-COF in 63 % yield.

**Synthesis of TAPE-PMDA-COF.** Typically, 1,1,2,2-tetrakis(4aminophenyl)ethylene (TAPE, 0.05 mmol, 19.6 mg) and pyromellitic dianhydride (PMDA, 0.1 mmol, 21.8 mg) were placed in a Schlenk bomb and suspended in a mixture of 1 ml $H_2O$/0.5 ml n-butanol/0.04 ml pyridine. The reaction mixture was sonicated for 10 min and degassed by four freeze-pump-thaw cycles. The Schlenk bombs were placed in an aluminum heating block and were heated to 190 °C (~13 bar) for 4 days. The resulting brown precipitate was isolated via filtration and washed with methanol and THF followed by Soxhlet extraction in methanol. Supercritical $CO_2$ drying yielded TAPB-PMDA-COF in 56 % yield.

### *COF-to-COF Transformation*

**Synthesis of Py1P-COF.** Py1P-COF was synthesized according to a literature procedure[1]: 4,4',4'',4'''-(pyrene-1,3,6,8-tetrayl)tetraaniline (0.06 mmol, 34 mg) and terephthal aldehyde (0.114 mmol, 15.6 mg) were placed in a microwave vial and suspended in a mixture of 2 ml mesitylene/1 ml 1,4-dioxane and 0.3 ml 6M AcOH. The reaction vessel was closed and heated to 120 °C for four days. The bright orange Py1P-COF was isolated via filtration and washed with THF and DCM, followed by Soxhlet extraction with methanol. Supercritical $CO_2$ drying yielded Py1P-COF in 79.7 % yield.

**Transformation of Py1P-COF into Py-imide-COF.** Typically, Py1P-COF (0.04 mmol, 30 mg) and pyromellitic dianhydride (0.16 mmol, 34.9 mg) were placed in a Schlenk bomb and suspended in a mixture of 1.0 ml $H_2O$/0.5 ml n-butanol/0.04 ml pyridine. The reaction mixture was sonicated for 10 min and degassed by four freeze-pump-thaw cycles. The Schlenk bombs were placed in an aluminum heating block and were heated to 200 °C (~16 bar) for 4 days. The resulting brown orange precipitate was isolated via filtration and washed with methanol, THF and ethanol. Still wet, the solid was suspended in a mixture of ethanol and formic acid (1:1) at 60 °C for 18 h to remove potential unreacted Py1P-COF. The solid was filtered and washed again with THF and methanol, followed by Soxhlet extraction with methanol. Supercritical $CO_2$ drying yielded Py-Imide COF in 92 % yield.

### 8.3.3 *Supplementary Figures*

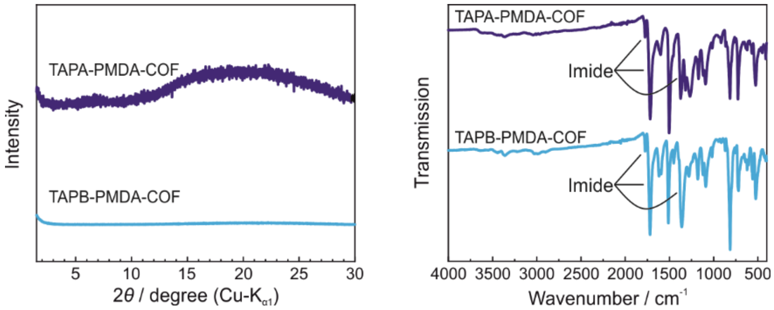

**Figure S8-62**. XRPD pattern (left) and FT-IR spectra (right) of the amorphous PI polymers TAPA-PMDA (violet) and TAPB-PMDA (blue) received from the synthesis in pure water at 200 °C.

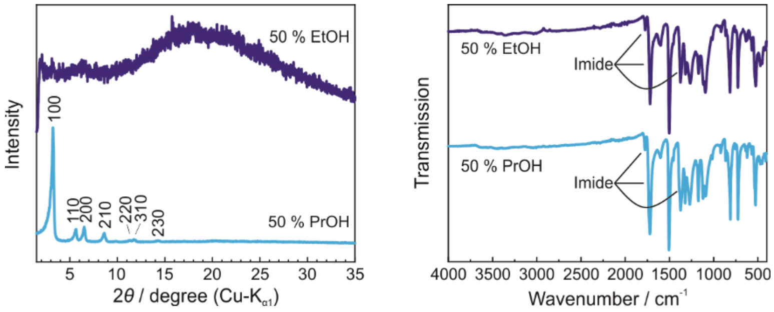

**Figure S8-63**. XRPD pattern (left) and FT-IR spectra (right) of TAPA-PMDA-COF samples synthesized in a mixture of 1 ml $H_2O$/1 ml ethanol/0.04 ml pyridine (violet) and 1 ml $H_2O$/1 ml n-propanol/0.04 ml pyridine (blue).

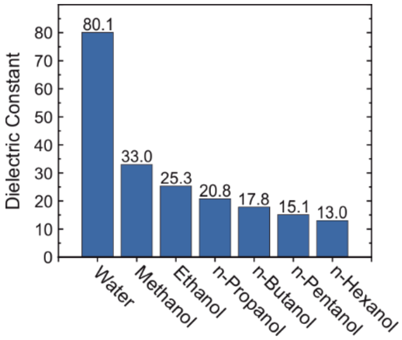

**Figure S8-64**. Dielectric constants of water compared to a row of n-alcohols from methanol to n-hexanol.[5]

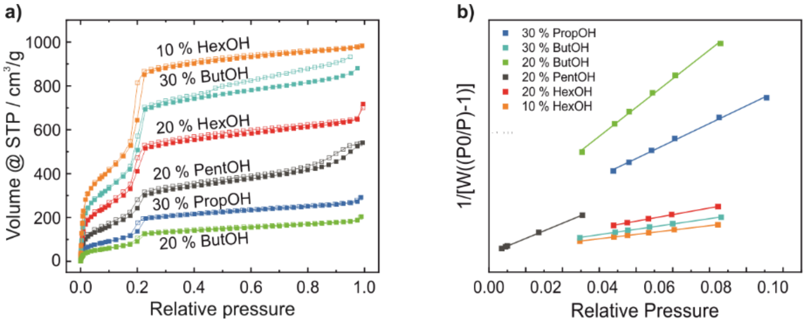

c)

| Solvent | BET Surface Area |
|---|---|
| 10 % HexOH | 1619 m$^2$/g |
| 20 % HexOH | 1062 m$^2$/g |
| 20 % PentOH | 726 m$^2$/g |
| 20 % ButOH | 244 m$^2$/g |
| 30 % ButOH | 1327 m$^2$/g |
| 30 % PropOH | 397 m$^2$/g |

**Figure S8-65**. a) Ar sorption and desorption isotherms of TAPA-PMDA-COF synthesized in $H_2O$/n-alcohol/pyridine mixtures with varying alcohols and alcohol concentrations together with b) the corresponding BET plots and c) the calculated BET surface areas.

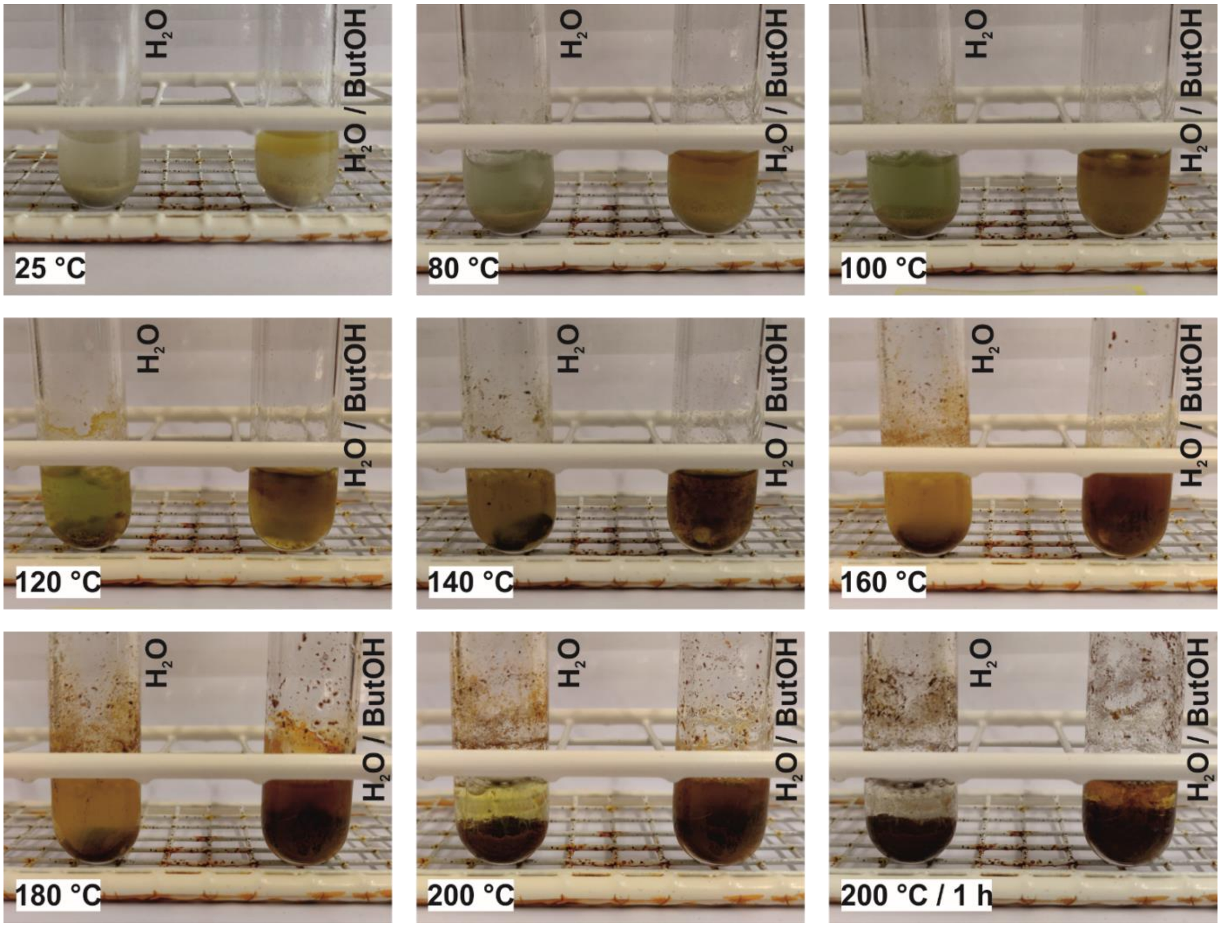

**Figure S8-66**. Pictures taken during the heating process of the TAPA-PMDA-COF reaction in 1.5 ml $H_2O$/0.04 ml pyridine (left tube) and 1.0 ml $H_2O$/0.5 ml n-butanol/0.04 ml pyridine (right tube).

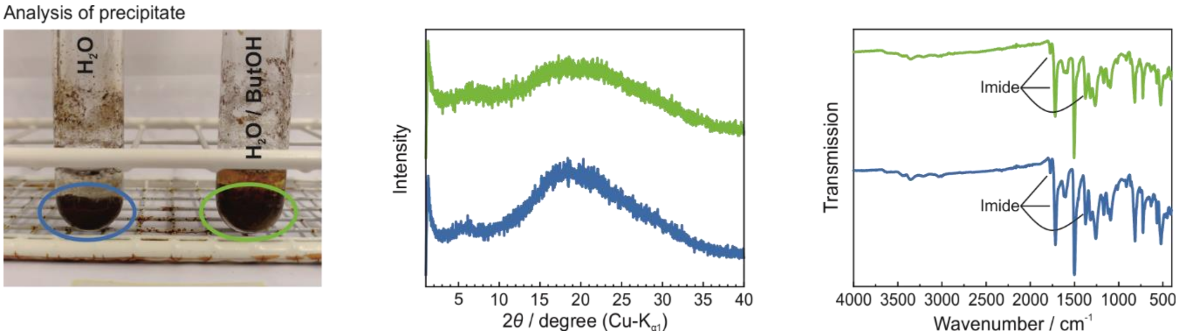

**Figure S8-67**. XRPD patterns (middle) and FT-IR spectra (right) of the precipitate of the TAPA-PMDA-COF reactions obtained from the reaction observation experiment in Figure S8-66 after 1 h at 200 °C (left). The analysis revealed that imide formation occurs rapidly already during the heating process in both cases, but in an amorphous fashion.

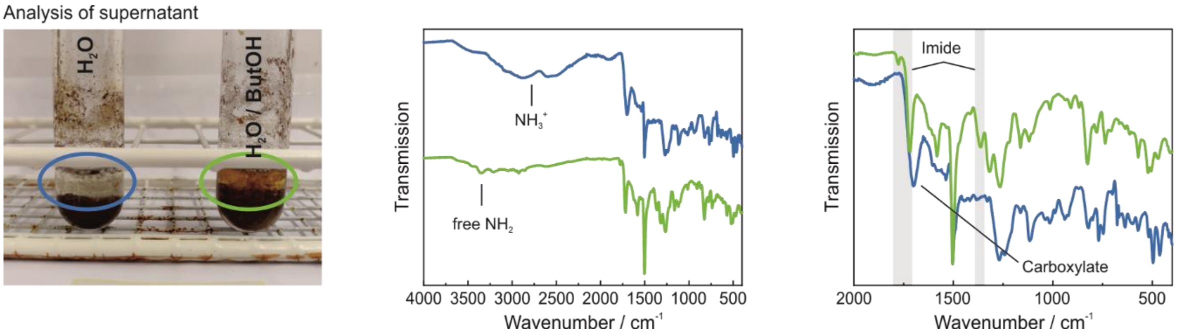

**Figure S8-68**. FT-IR spectra (middle) and close-up (right) of the supernatant of the TAPA-PMDA-COF reactions obtained from the reaction observation experiment in Figure S8-66 after 1 h at 200 °C (left). While in the supernatant of the alcohol containing reaction mixture (green) imide species could be detected, the supernatant of the water reaction mixture (blue) contains protonated amine and deprotonated pyromellitic acid linker molecules.

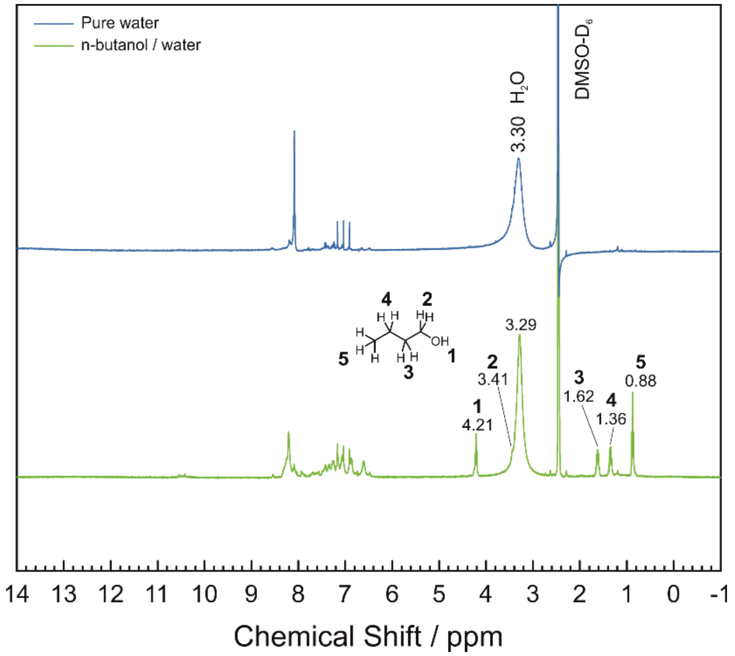

**Figure S8-69**. $^1$H NMR spectra of the in the supernatant dissolved species of the TAPA-PMDA-COF reactions obtained from the reaction observation experiment in Figure S8-66 after 1 h at 200 °C revealing n-butanol residuals.

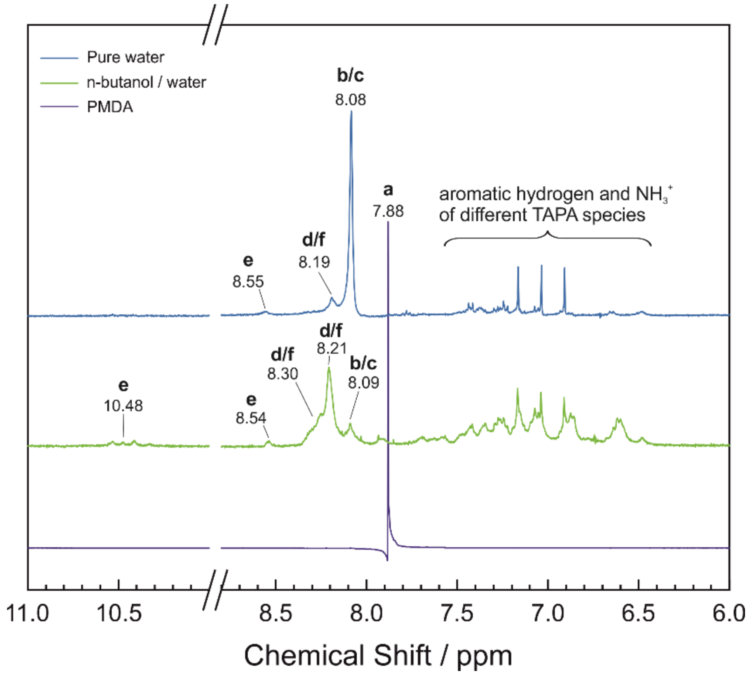

**Figure S8-70**. Close-up of the $^1$H NMR spectra of the in the supernatant dissolved species of the TAPA-PMDA-COF reactions obtained from the reaction observation experiment in Figure S8-66 after 1 h at 200 °C together with the $^1$H NMR spectrum of PMDA. While in the supernatant of the alcohol containing reaction mixture (green) imide (marked blue) and amic acid (marked red) species could be detected, the supernatant of the water reaction mixture (blue) contains predominantly deprotonated pyromellitic acid linker molecules (marked purple).

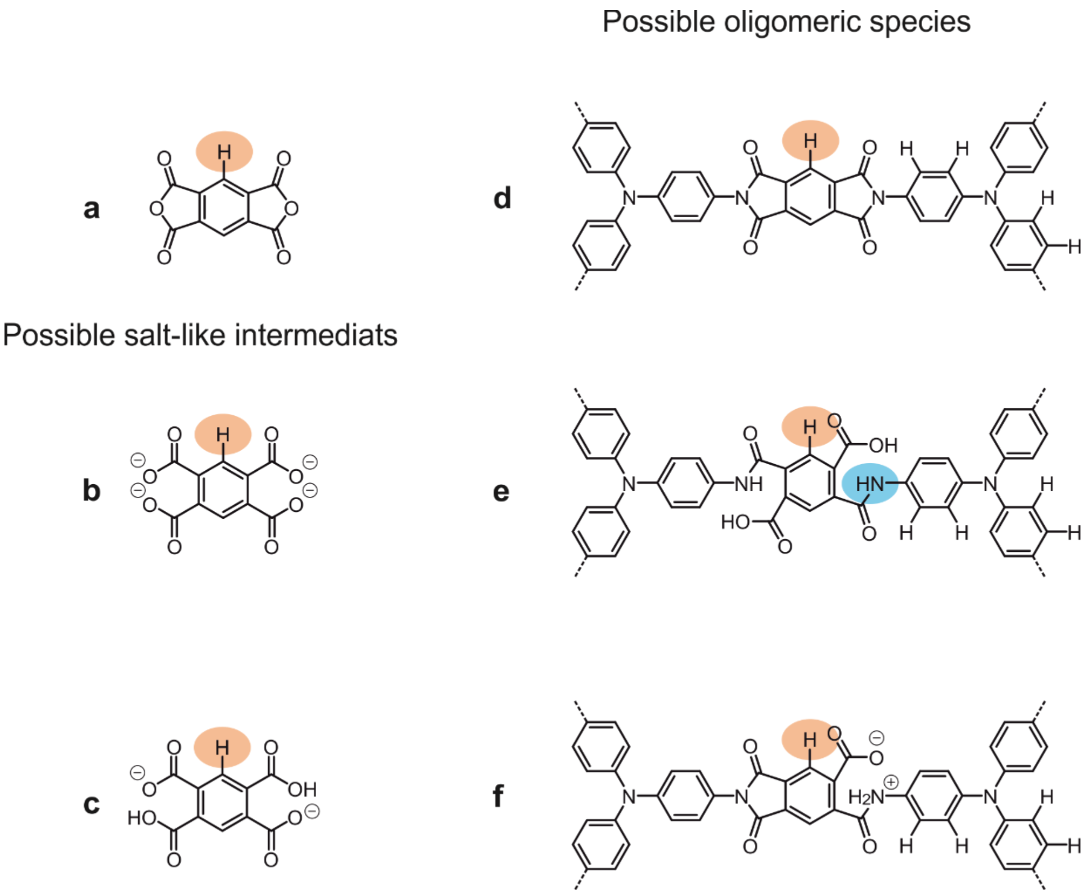

**Figure S8-71**. Chemical structures of species possibly present in the supernatant of the TAPA-PMDA-COF reactions obtained from the reaction observation experiment in Figure S8-66 after 1 h at 200 °C.

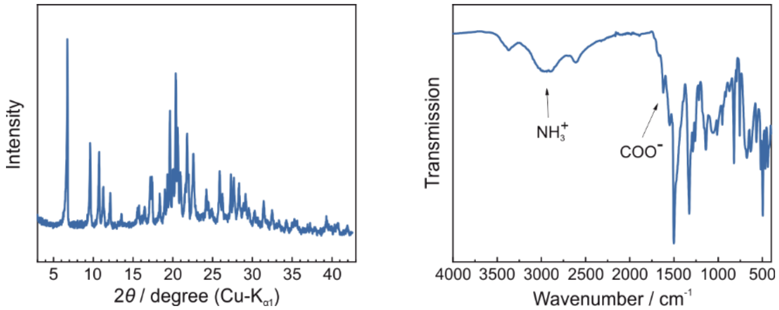

**Figure S8-72**. XRPD pattern (left) and FT-IR spectrum (right) of the isolated monomer-salt consisting of protonated TAPA and deprotonated pyromellitic acid linker molecules.

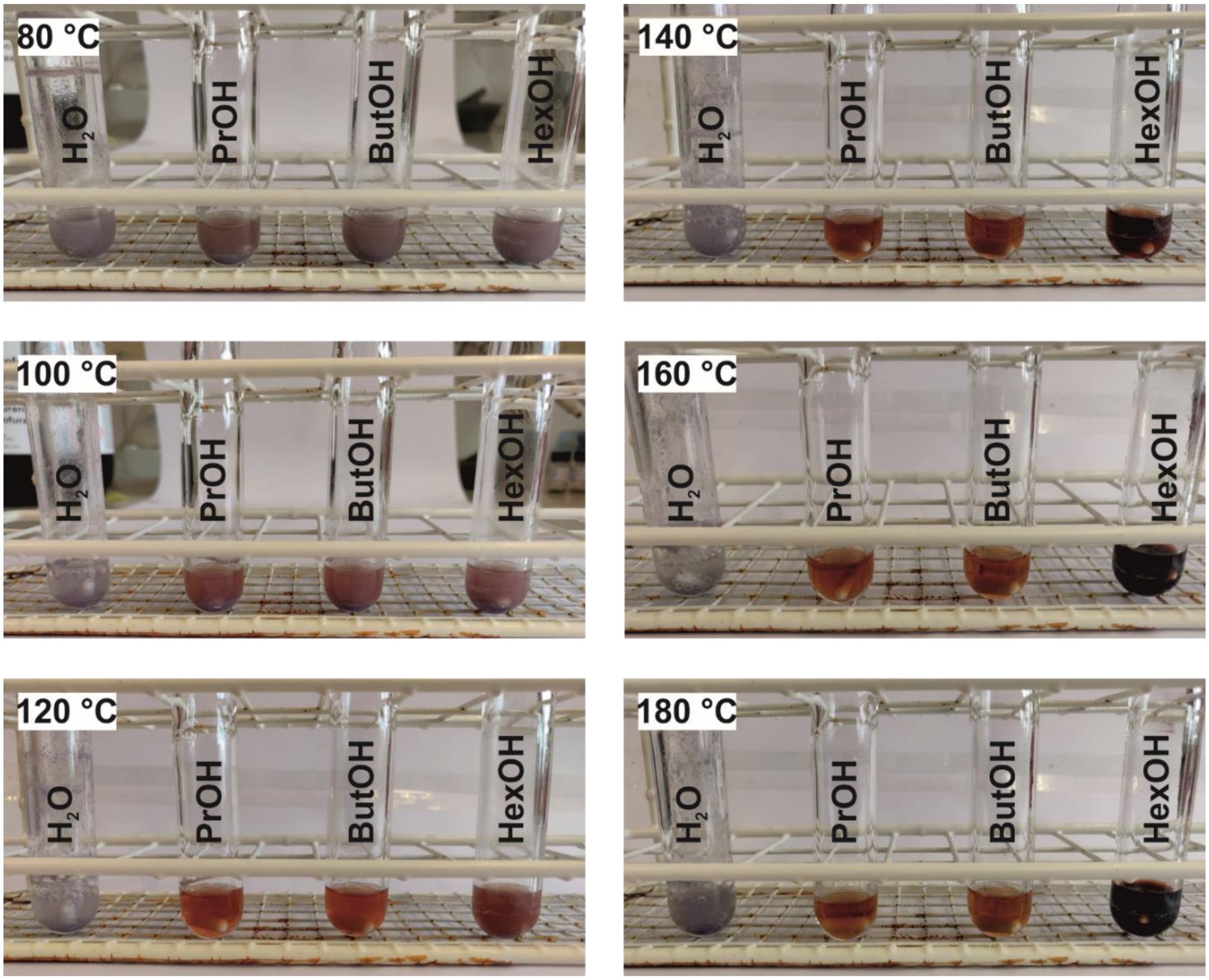

**Figure S8-73**. Solubility tests of TAPA in $H_2O$ and different n-alcohols revealing poor solubility of TAPA in $H_2O$ and good solubility in all the tested n-alcohols.

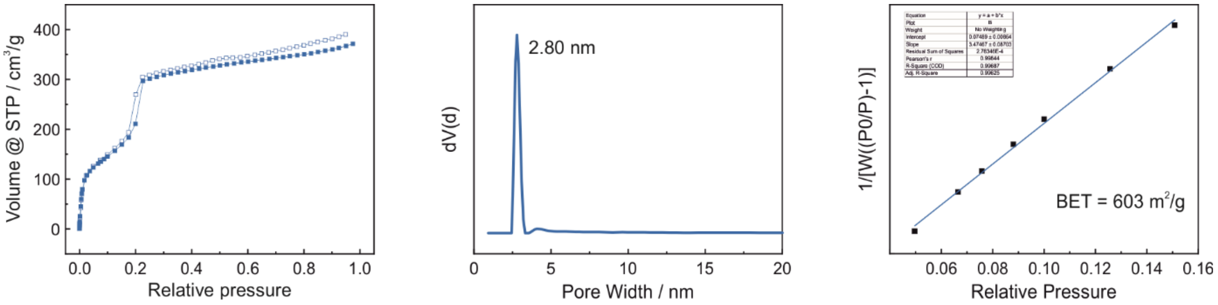

**Figure S8-74**. Ar sorption and desorption isotherm (left), calculated pore size distribution (center) and BET plot (right) of TAPA-PMDA-COF synthesized in 1.2 ml $H_2O$/0.3 ml n-hexanol/0.04 ml pyridine at 180 °C for 24 h.

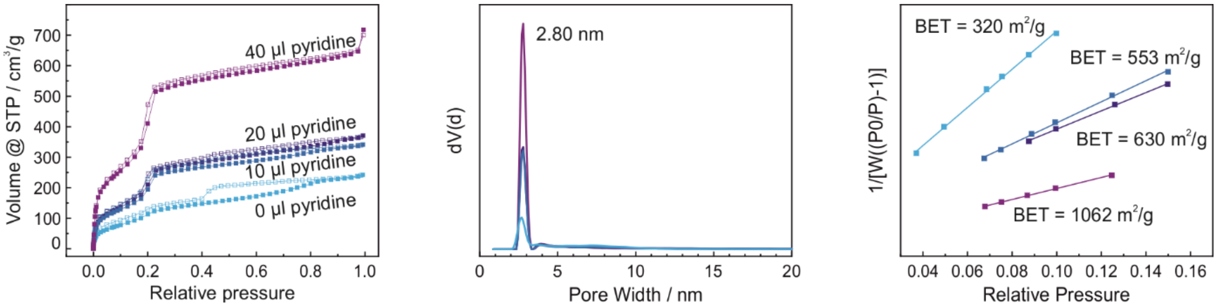

**Figure S8-75**. Ar sorption and desorption isotherms (left), calculated pore size distributions (center) and BET plots (right) of TAPA-PMDA-COF synthesized in 1.2 ml $H_2O$/0.3 ml n-hexanol with varying pyridine contents at 180 °C for 4 days.

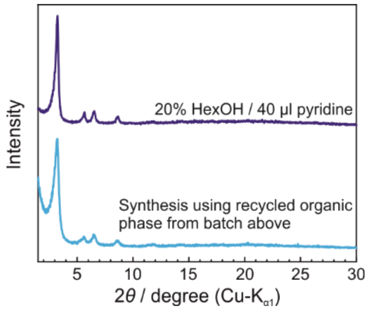

**Figure S8-76**. XRPD pattern of TAPA-PMDA-COF synthesized using fresh solvents (violet) and using the recycled organic phase (blue).

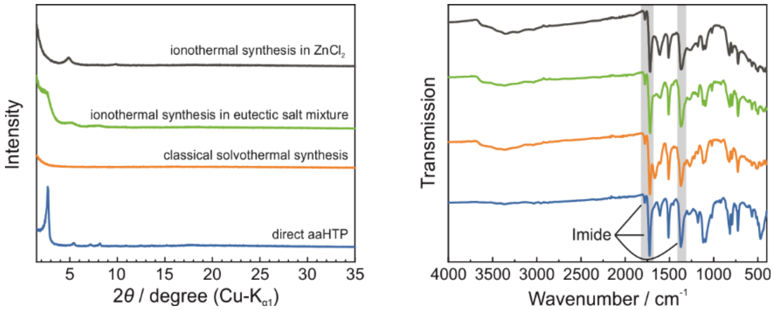

**Figure S8-77**. XRPD patterns (left) and FT-IR spectra (right) of the attempts to synthesize TAPE-PMDA-COF using different published synthetic procedures and the direct aaHTP.[6-7]

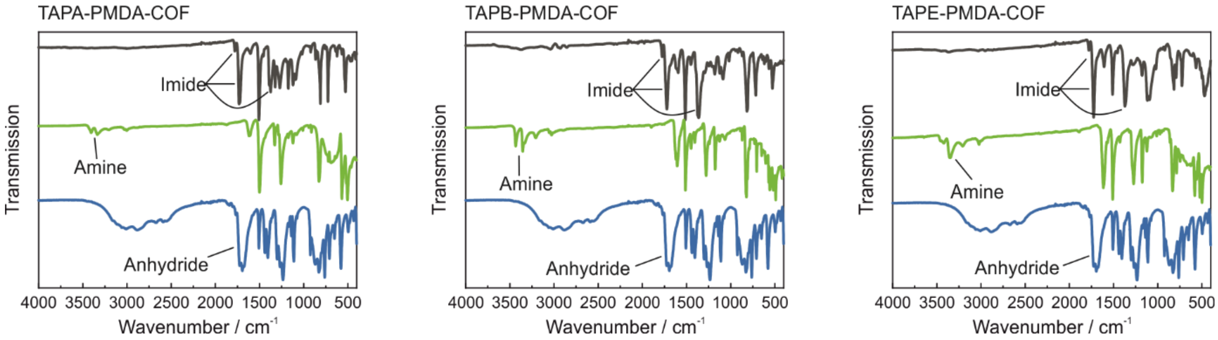

**Figure S8-78**. FT-IR spectra of TAPA-PMDA-, TAPB-PMDA- and TAPE-PMDA-COF (black) synthesized in optimized reaction conditions together with FT-IR spectra of their respective precursor molecules TAPA/TAPB/TAPE (green) and PMDA (blue). The absence of amine vibrational bands at 3367 cm$^{-1}$ and anhydride vibrational bands at 1700 cm$^{-1}$ in the COFs spectra indicate complete imide formation.

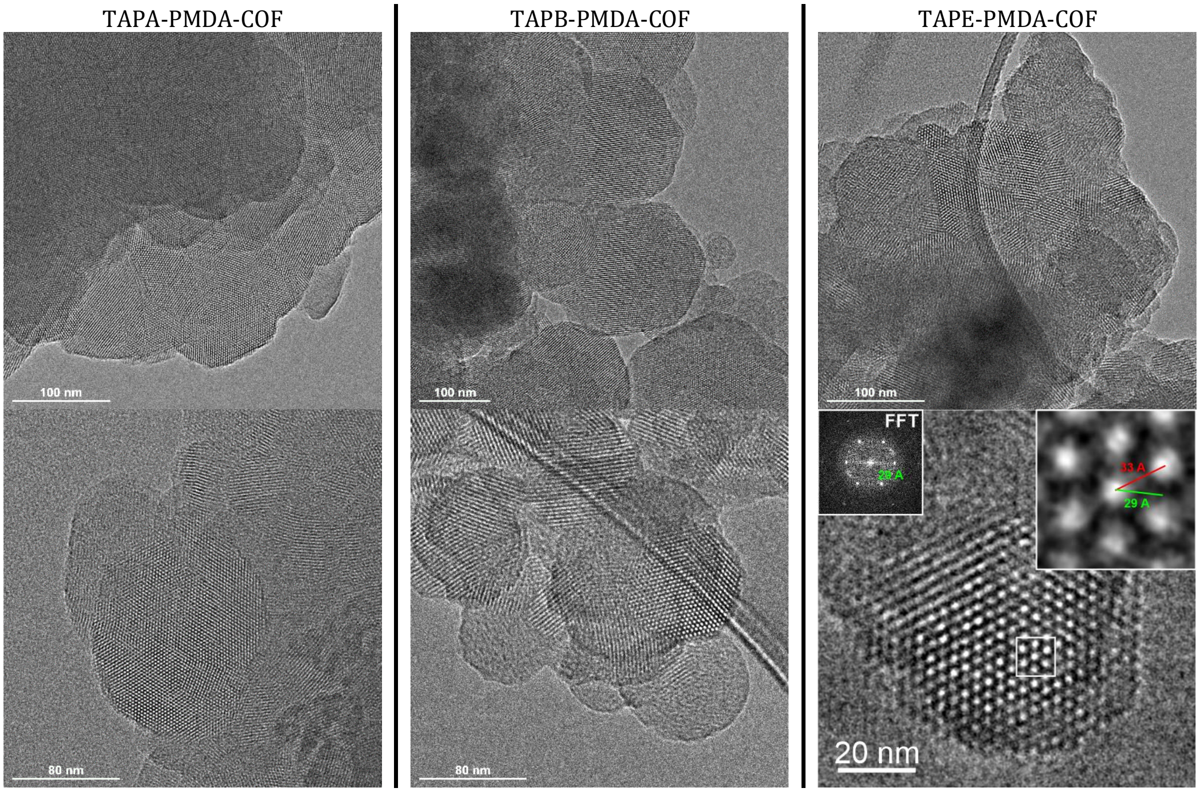

**Figure S8-79**. TEM images of TAPA-PMDA-COF (left), TAPB-PMDA-COF (center) and TAPE-PMDA-COF (right).

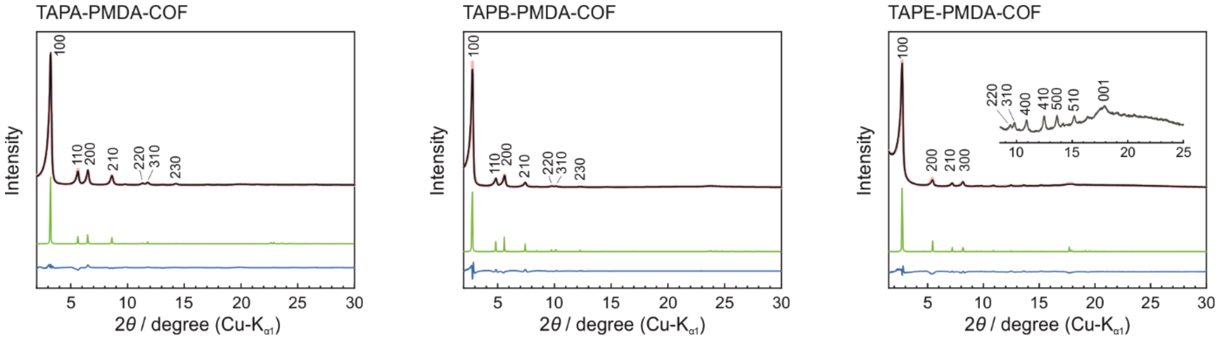

**Figure S8-80**. Experimental XRPD patterns of TAPA-PMDA-, TAPB-PMDA- and TAPE-PMDA-COF (black) together with the Rietveld fits (red), simulated patterns (green) and difference curves (blue). Simulations of the three COFs were performed based on the $P622$ space group for TAPA-PMDA-COF, $P\bar{3}1m$ space group for TAPB-PMDA-COF, and $P622$ space group for TAPE-PMDA-COF.

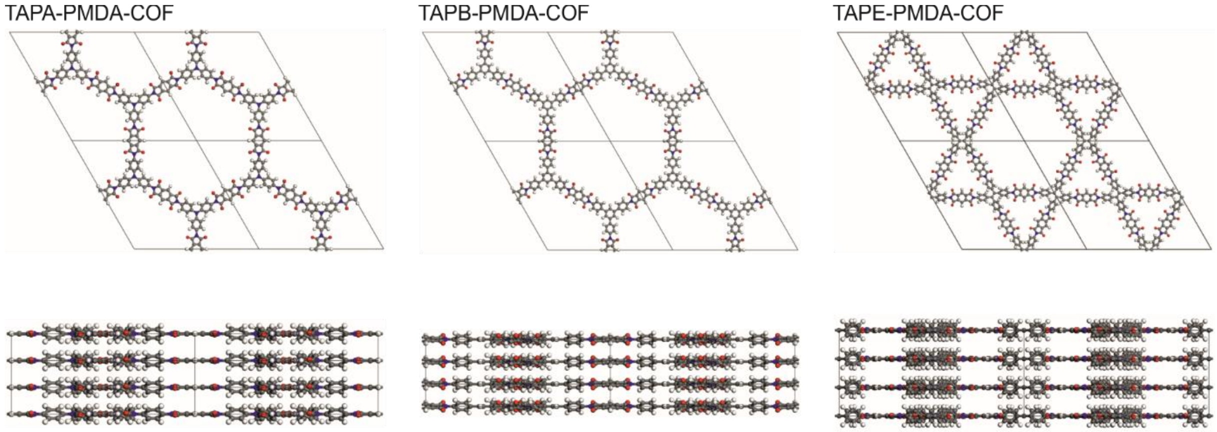

**Figure S8-81**. Simulated structures of the TAPA-PMDA-COF, TAPB-PMDA-COF and TAPE-PMDA-COF based on the space groups $P622$, $P\bar{3}1m$ and $P622$, respectively.

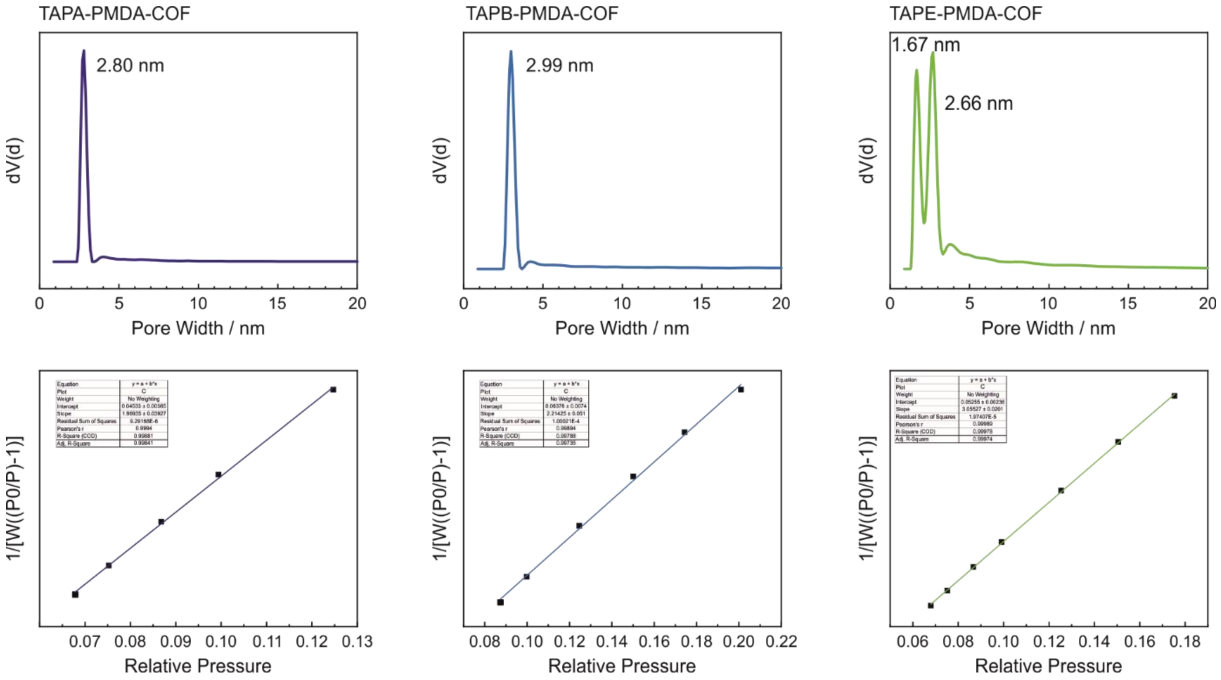

**Figure S8-82**. Calculated pore size distribution of TAPA-PMDA-COF (violet), TAPB-PMDA-COF (blue) and TAPE-PMDA-COF (green) together with their respective BET plots.

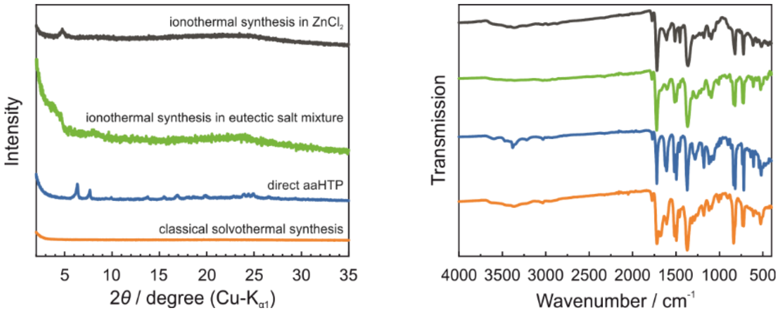

**Figure S8-83**. XRPD patterns (left) and FT-IR spectra (right) of the attempts to synthesize Py-imide COF directly from the precursor molecules using different published synthetic procedures.[6-7]

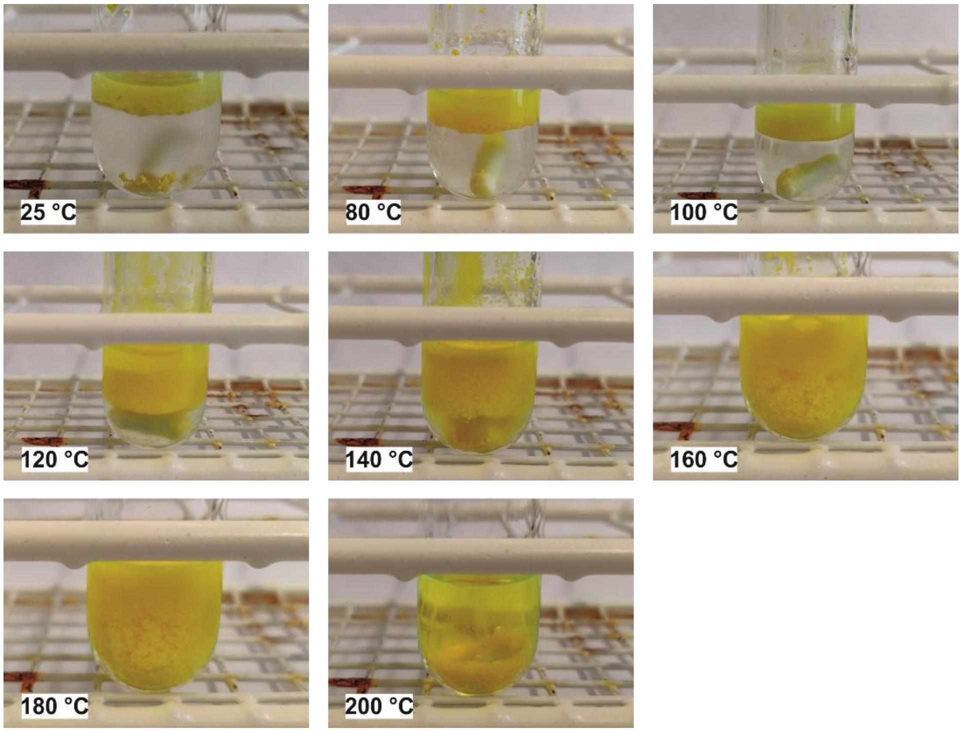

**Figure S8-84**. Solubility test of PyTTA in a mixture of 30 % n-butanol/$H_2O$ revealing poor solubility of PyTTA up to 200 °C.

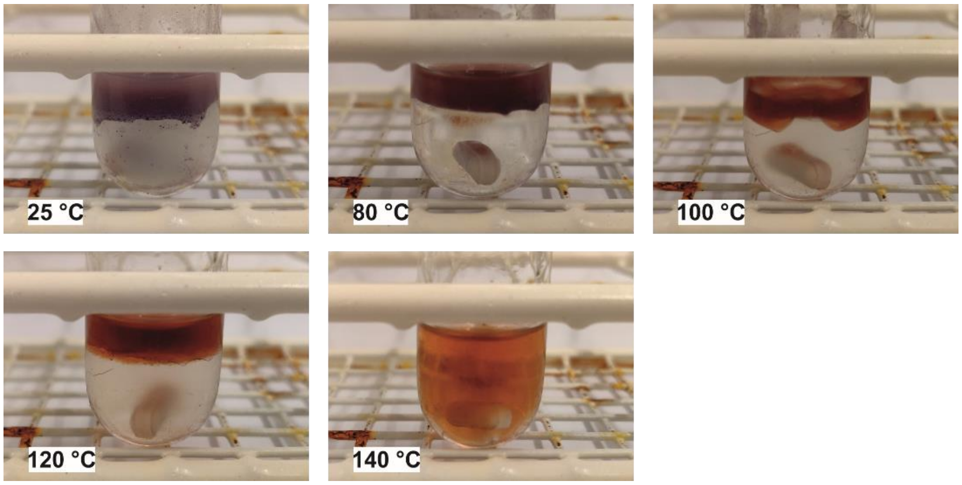

**Figure S8-85**. Solubility test of TAPA in a mixture of 30 % n-butanol/$H_2O$ revealing complete dissolution of TAPA at 140 C.

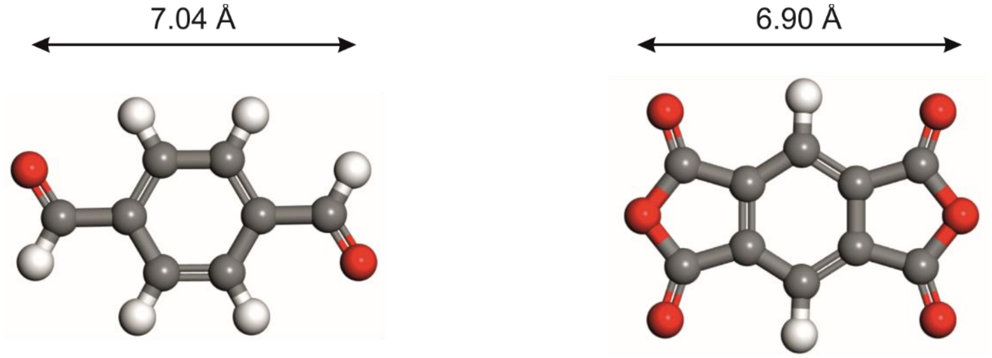

**Figure S8-86**. Calculated size of the linker molecules terephthaldehyde (left) and PMDA (right).

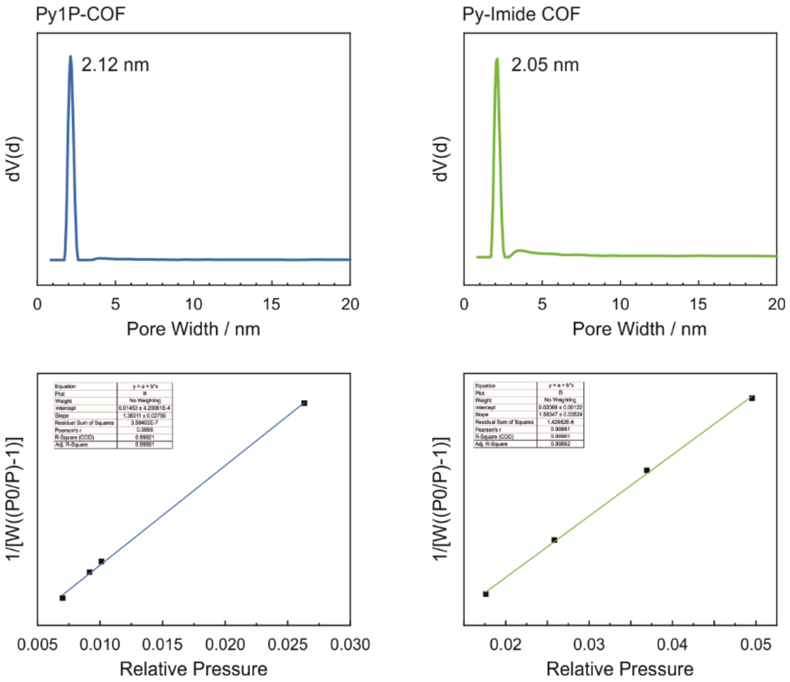

| | |
|---|---|
| Equation | y = a + b*x |
| Plot | B |
| Weight | No Weighting |
| Intercept | 0.01453 ± 4.20061E-4 |
| Slope | 1.38311 ± 0.02756 |
| Residual Sum of Squares | 3.59403E-7 |
| Pearson's r | 0.9996 |
| R-Square (COD) | 0.99921 |
| Adj. R-Square | 0.99881 |

| | |
|---|---|
| Equation | y = a + b*x |
| Plot | B |
| Weight | No Weighting |
| Intercept | 0.02069 ± 0.00122 |
| Slope | 1.58347 ± 0.03524 |
| Residual Sum of Squares | 1.42982E-6 |
| Pearson's r | 0.99951 |
| R-Square (COD) | 0.99901 |
| Adj. R-Square | 0.99852 |

**Figure S8-87**. Calculated pore size distribution of Py1P-COF (blue) and Py-imide COF (green) together with their respective BET plots.

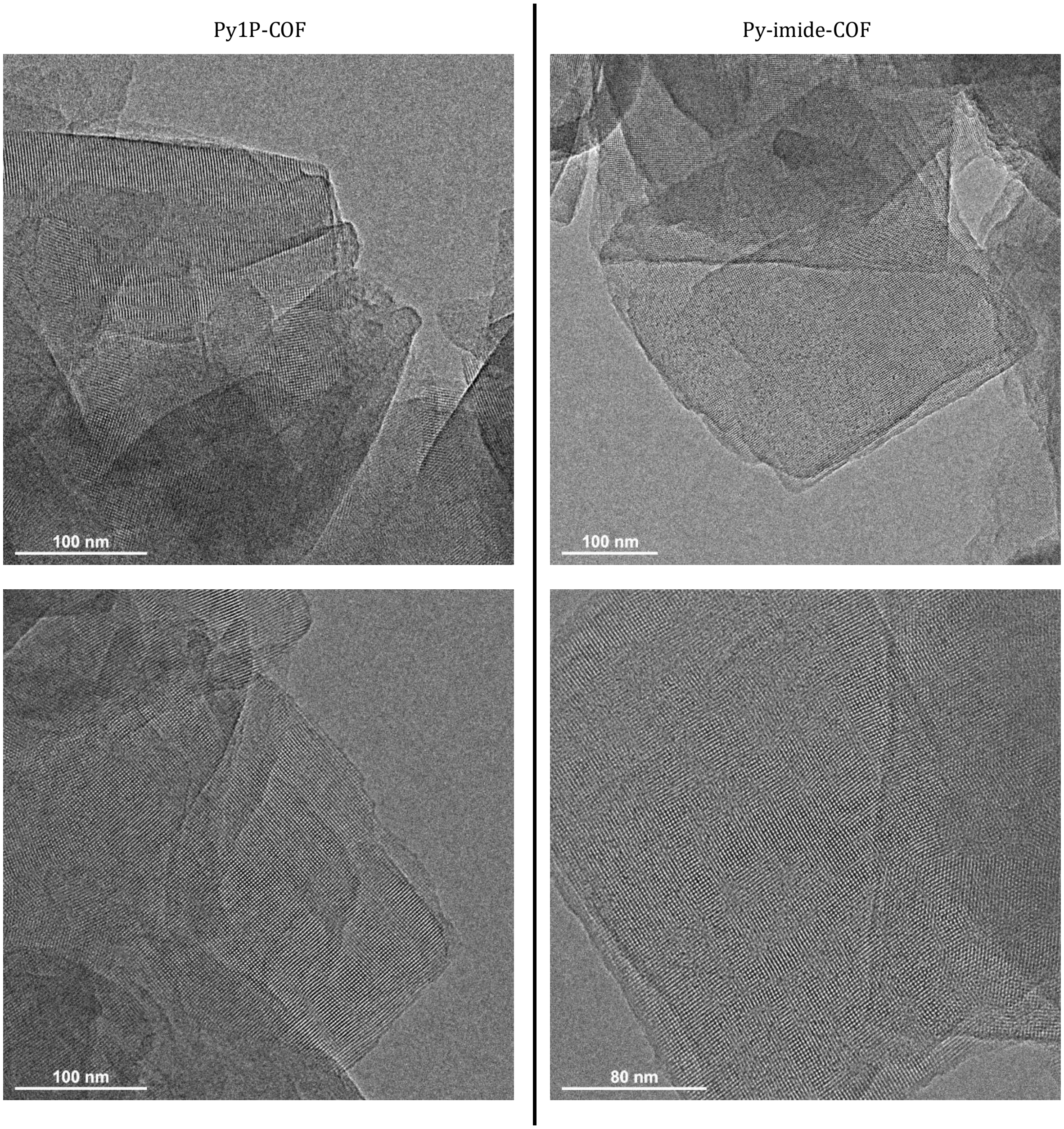

**Figure S8-88**. TEM images of Py1P-COF (left) and Py-imide COF (right).

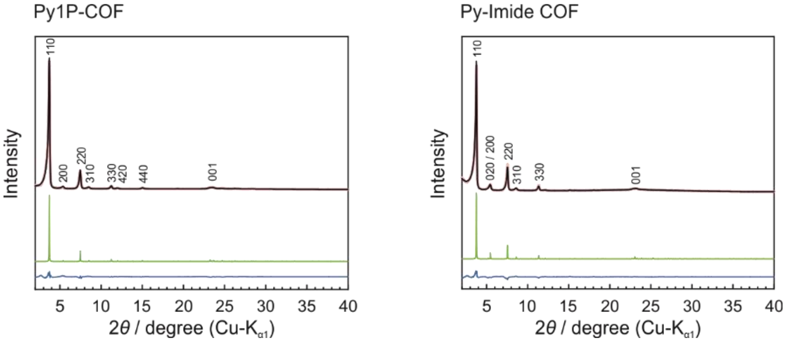

**Figure S8-89**. Experimental XRPD pattern of the imine-linked Py1P-COF and the imide-linked Py-imide COF (black) together with the Rietveld fits (red), simulated patterns (green) and difference curves (blue). Both COFs were simulated based on the $C2/m$ space group.

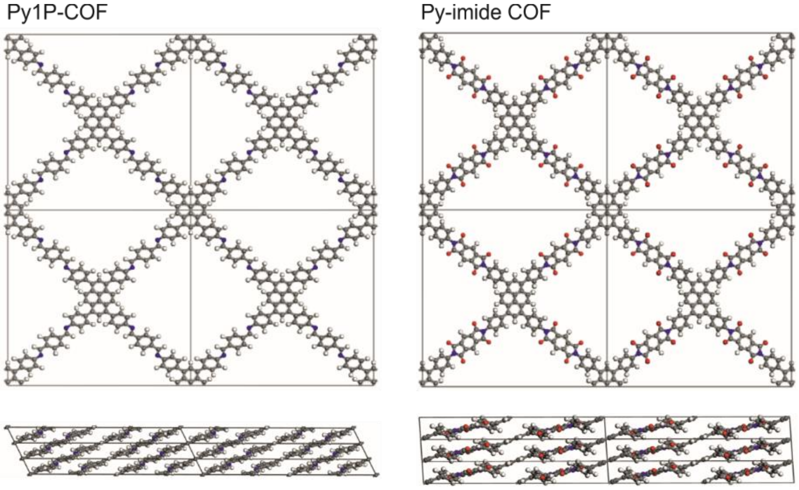

**Figure S8-90**. Simulated structures of the Py1P-COF and Py-imide COF based on the space group $C/2m$.

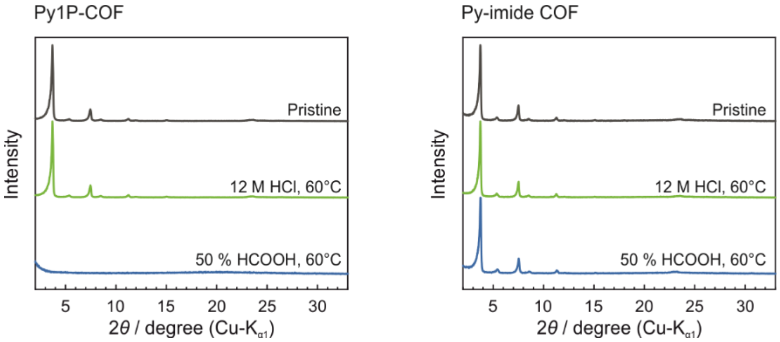

**Figure S8-91.** Comparison of the XRPD patterns of Py1P-COF and Py-imide COF pristine (black) and after treatment with concentrated hydrochloric acid (green) and formic acid (blue).

### *8.3.4 Supplementary Tables*

**Table S8-12.** Rietveld refinement of TAPA-PMDA-COF**,** TAPB-PMDA-COF and TAPE-PMDA-COF at room temperature.

| **Fitted Pattern** | **TAPA-PMDA-COF** | **TAPB-PMDA-COF** | **TAPE-PMDA-COF** |
|---|---|---|---|
| **Space group** | $P622$ | $P\bar{3}1m$ | $P622$ |
| **Rwp (%)** | 7.63 | 9.37 | 5.47 |
| **Cell Volume (Å$^3$)** | 3268 | 4225 | 6081 |
| ***a* (Å)** | 31.06(9) | 36.0(4) | 37.4(6) |
| ***b* (Å)** | 31.06(9) | 36.0(4) | 37.4(6) |
| ***c* (Å)** | 3.9(1) | 3.75(6) | 5.00(4) |
| **α (°)** | 90 | 90 | 90 |
| **β (°)** | 90 | 90 | 90 |
| **γ (°)** | 120 | 120 | 120 |

**Table S8-13.** Rietveld refinement of Py1P-COF- and Py-imide COF at room temperature.

| **Fitted Pattern** | **Py1P-COF** | **Py-imide COF** |
|---|---|---|
| **Space group** | $C2/m$ | $C2/m$ |
| **Rwp (%)** | 7.4 | 5.3 |
| **Cell Volume (Å$^3$)** | 4225 | 4252 |
| ***a* (Å)** | 38.0(1) | 33.8(1) |
| ***b* (Å)** | 32.5(1) | 32.1(7) |
| ***c* (Å)** | 3.82(3) | 3.91(6) |
| **α (°)** | 90 | 90 |
| **β (°)** | 63.4(2) | 86.(8) |
| **γ (°)** | 90 | 90 |

### *8.3.5 Bibliography*

[1] H. M. Rietveld, *J. Appl. Crystallogr.* **1969**, *2*, 65-&.

[2] Coelho, A., *J. Appl. Crystallogr.* **2000,** *33* (3 Part 2), 899-908.

[3] F. Auras, L. Ascherl, A. H. Hakimioun, J. T. Margraf, F. C. Hanusch, S. Reuter, D. Bessinger, M. Döblinger, C. Hettstedt, K. Karaghiosoff, S. Herbert, P. Knochel, T. Clark, T. Bein, *J. Am. Chem. Soc.* **2016**, *138*, 16703-16710.

[4] L. Grunenberg, G. Savasci, M. W. Terban, V. Duppel, I. Moudrakovski, M. Etter, R. E. Dinnebier, C. Ochsenfeld, B. V. Lotsch, *J. Am. Chem. Soc.* **2021**, *143*, 3430-3438.

[5] D. R. Lide, CRC Handbook of Chemistry and Physics, 86 ed., Boca Raton : CRC Press, **2005**.

[6] Q. Fang, Z. Zhuang, S. Gu, R. B. Kaspar, J. Zheng, J. Wang, S. Qiu, Y. Yan, *Nat. Commun.* **2014**, *5*; 4503.

[7] J. Maschita, T. Banerjee, G. Savasci, F. Haase, C. Ochsenfeld, B. V. Lotsch, *Angew. Chem. Int. Ed*. **2020**, *59*, 15750-15758.

## 8.4 *Supporting Information of Chapter 5 "NO as a Reagent for Topochemical Framework Transformation and Controlled Nitric Oxide Release in Covalent Organic Frameworks"*

### 8.4.1 *Experimental Details*

#### *Fourier-Transform Infrared Spectroscopy*

Fourier-transform infrared (FT-IR) spectra were recorded on a PerkinElmer UATR Two in attenuated total reflection (ATR) geometry equipped with a diamond crystal.

#### *Transmission Electron Microscopy*

Transmission electron microscopy (TEM) was performed with a Philips CM30 ST (300kV, $LaB_6$ cathode). The samples were prepared dry onto a copper lacey carbon grid (Plano). Images were recorded with a TVIPS TemCam-F216 CMOS camera. The program EM-Menu 4.0 Extended was used for analysis.

#### *X-ray Powder Diffraction*

X-ray powder diffraction (PXRD) measurements were performed on a Stoe Stadi-P diffractometer in Debye-Scherrer geometry with Cu-$K_{\alpha 1}$ radiation equipped with a Ge(111) primary monochromator. The glass capillaries (1 mm in diameter) were spun during data collection for an improved particle statistics. Pawley refinements of the different COF structures were performed using TOPAS V6. Model structures created by Material Studio were used for the Pawley refinements with fixed atomic coordinates. The peak profile of the XRPD patterns was described by applying the fundamental parameter approach as implemented in TOPAS. The background was modeled by Chebychev polynomials. The microstructure of the different COFs was modeled using microstrain (Lorentzian and Gaussian components).

#### *Nuclear Magnetic Resonance Spectroscopy*

Solid state nuclear magnetic resonance spectra (ssNMR) were recorded on a Bruker Avance III 400 MHz spectrometer (magnetic field 9.4 T). For ssNMR spectroscopy, the samples were packed in $ZrO_2$ rotors, and spun in a Bruker WVT BL4 double resonance MAS probe. The spinning rate was 12-14 kHz in $^{13}C$ measurements, and 6 kHz in $^{15}N$ experiments. A standard cross-polarization sequence with a ramped contact pulse was used for both nuclei. The duration of contact pulse was 2 ms for $^{13}C$ and 4 ms for $^{15}N$. A total of 4096-8192 scans were routinely accumulated in $^{13}C$ experiments, and 80000 scans in the experiments with $^{15}N$. All the measurements were performed under conditions of high-power broadband proton decoupling (SPINAL 64) with the spectral conditions being optimized for the shortest relaxation delay by measuring $^{1}H$ $T_1$ relaxation time. Chemical shifts were referenced relative to tetramethylsilane in $^{13}C$ ($\delta_{iso}$ = 0.0 ppm) and relative to nitromethane in $^{15}N$ ($\delta_{iso}$ = 0.0 ppm), with solid glycine as the secondary reference ($\delta_{iso}$ [$^{15}N$] = -347.54 ppm).

### *UV/VIS Spectroscopy*

Diffuse reflectance UV-Vis spectra were collected on a Cary 5000 spectrometer referenced to barium sulfate as reference.

### *Sorption*

Sorption measurements were performed on a Quantachrome Instruments Autosorb iQ MP. BET suface areas and pore size distributions were calculated from argon isotherms recorded at 87 K using the quenched solid-state density functional theory (QSDFT) for cylindrical pores in carbon model for argon at 87 K. $CO_2$ and NO isotherms were measured at 273, 288 and 298 K.[1]

### *Explanation of fittings and selectivity calculations based on ideal adsorption solution theory (IAST)*

The NO and $CO_2$ isotherms were fitted with a dual-site Langmuir-Freundlich model (Figure S36 and S37). $n$ is the adsorbed gas amount (mmol $g^{-1}$), $p$ is the pressure in the bulk gas phase (bar), $q_{sat}$ is the saturation amount (mmol $g^{-1}$), $b$ is the Langmuir-Freundlich parameter (bar), $\alpha$ is the Langmuir-Freundlich exponent (dimensionless) for two adsorption sites A and B.[2]

$$n = \frac{q_{sat,A} b_A p^{\alpha_A}}{1 + b_A p^{\alpha_A}} + \frac{q_{sat,B} b_B p^{\alpha_B}}{1 + b_B p^{\alpha_B}}$$

The IAST selectivities $S_{IAST}$ were calculated with the IAST equation. SIAST is the selectivity (dimensionless), $q$ is the adsorbed amount (mmol $g^{-1}$), and $p$ is the partial pressure (bar).[2]

$$S_{IAST} = \frac{q_1/q_2}{p_1/p_2}$$

### *8.4.2 Materials and Synthetic Procedures*

#### *Chemicals*

All starting materials, unless otherwise specified, were obtained from Sigma-Aldrich Chemicals, and used without further purification. All solvents, unless otherwise specified, were obtained from Acros Organics, and used without further purification. $^{15}$N-Ammonium Chloride was purchased from Sigma Aldrich. 2,4,6-Tris(4-aminophenyl)-1,3,5-triazine and 4,4',4''-(1,3,5-triazine-2,4,6-triyl)tribenzaldehyde were prepared according to a literature procedure.[3]

#### *Synthesis of 4,4',4''-(1,3,5-triazine-2,4,6-triyl)trianiline-$^{15}$N.*

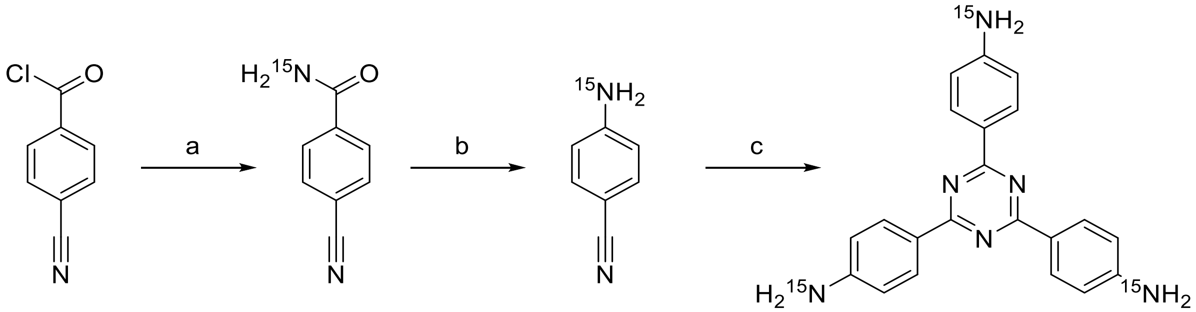

**Scheme S8-1.** Synthesis of 15N-4,4',4''-(1,3,5-triazine-2,4,6-triyl)trianiline linker.

**4-Cyanobenzamide-$^{15}$*N*.** Ammonium chloride-$^{15}$*N* (1.81 g, 33.2 mmol) was dissolved in 12.5 mL water and the solution cooled to 0 °C. 20 mL diethyl ether was added followed by 4-cyanobenzoyl chloride (5.0 g, 20.2 mmol). After 5 minutes 5 mL aqueous sodium hydroxide (10 M) was added and the mixture stirred for 30 minutes. The white precipitate was collected by filtrations and washed with small amounts of ice cooled water. After drying the solid under air and *in vacuo*, 3.75 g (30.2 mmol, 85 %) of 4-cyanobenzamide-$^{15}$*N* was obtained.

$^{1}$H NMR (400 MHz, DMSO-*D*6) $\delta$ 8.04 – 7.99 (m, 2H), 7.97 – 7.91 (m, 2H), 7.56 (s, 2H). $^{13}$C NMR (101 MHz, DMSO-*D*6) $\delta$ 166.57, 166.40, 138.36, 138.28, 132.41, 128.29, 118.41, 113.67. $^{15}$N NMR (41 MHz, DMSO-*D*6) $\delta$ -273.21.

**4-(Amino-$^{15}$*N*)benzonitrile**. Bromine (1.58 mL, 30.9 mmol) was added dropwise to 125 mL aqueous sodium hydroxide solution (1 M) at 0 °C. 4-cyanobenzamide-$^{15}$*N* (3.0 g, 20.6 mmol) was added and the mixture stirred until fully dissolved. The solution was quickly heated to 70 °C with a pre-heated oil bath and stirred for 15 minutes before cooling to room temperature. The aqueous solution was extracted three times with dichloromethane, the combined organic phases washed with brine, dried with sodium sulfate and the solvent removed under reduced pressure. The resulting residue of 0.726 g (6.15 mmol, 30 %) 4-(amino-$^{15}$*N*)benzonitrile was used without further purification.

$^{1}$H NMR (400 MHz, CHLOROFORM-*D*) $\delta$ 7.50 – 7.36 (m, 2H), 6.76 – 6.61 (m, 2H), 4.18 (d, J = 56.0 Hz, 2H). $^{13}$C NMR (101 MHz, CHLOROFORM-*D*) $\delta$ 150.60, 150.46, 133.92, 120.26, 114.56, 114.53, 100.28. $^{15}$N NMR (41 MHz, CHLOROFORM-*D*) $\delta$ -315.30.

**4,4',4''-(1,3,5-Triazine-2,4,6-triyl)trianiline-$^{15}$*N***. Under argon 4-(amino-$^{15}$*N*)benzonitrile (0.57 g, 4.82 mmol) was dissolved in 2 mL chloroform and trifluoromethanesulfonic acid (1.69 mL, 19.3 mmol) was added. The reaction mixture was stirred for 16 h at room temperature before 10 mL of water was carefully added and the mixture was neutralized with sodium hydroxide (1 M) to pH = 7. The precipitate was filtered off and washed with water, isopropanol, and dichloromethane. The solid was dried *in vacuo* to obtain 0.28 g (1.59 mmol, 49 %) 4,4',4''-(1,3,5-triazine-2,4,6-triyl)trianiline-$^{15}$*N*.

$^{1}$H NMR (400 MHz, DMSO-*D*6) $\delta$ 8.35 (d, J = 8.6 Hz, 2H), 6.69 (dd, J = 8.7, 1.7 Hz, 2H), 5.90 (d, J = 85.8 Hz, 2H). $^{13}$C NMR (101 MHz, DMSO-*D*6) $\delta$ 169.57, 153.03, 152.90, 130.14, 122.91, 113.09, 39.52. $^{15}$N NMR (41 MHz, DMSO-*D*6) $\delta$ -308.66.

### *Synthesis of $^{15}$N Enriched TTI-COF*

TTI-COF was synthesized following a literature procedure.[3] Into a 10 mL *Biotage* microwave vial, 4,4',4''-(1,3,5-triazine-2,4,6-triyl)trianiline-$^{15}$N (9 mg, 0.025 mmol), 4,4',4''-(1,3,5-triazine-2,4,6-triyl)trianiline (36 mg, 0.102 mmol) and 4,4',4''-(1,3,5-triazine-2,4,6-triyl)tribenzaldehyde (50 mg, 0.127) were placed. Mesitlyene (2.5 mL), 1,4-dioxane (2.5 mL), and 6M AcOH (0.125 mL) was added. The vial was capped and placed in an aluminum heating block that was preheated to 120°C. Under stirring at 500 rpm the mixture was kept at 120°C for 72h. After cooling to room temperature the solid was isolated by filtration, washed with acetone, isopropanol, and methanol before subjecting it to a Soxhlet extraction with MeOH for 24h. The MeOH soaked solid was then activated by scCO2 drying to obtain TTI-COF (67.6 mg, 77 %).

### *Synthesis of $^{15}$N Enriched rTTI-COF*

rTTI-COF was synthesized following a literature procedure.[4] $^{15}$N enriched TTI-COF (90 mg, 0.203 mmol) was suspended in mesitylene (6 mL) and 1,4-dioxane (3 mL). Formic acid (97%, 59.0 µL) was added and the suspension was heated at 120°C for 48 h. The solid was isolated by filtration, washed with methanol and subjected to a Soxhlet extraction with MeOH for 24h. The MeOH soaked solid was then activated by scCO2 drying to obtain TTI-COF (84 mg, 93 %).

### *Synthesis of $^{15}$N Enriched TTT-COF*

TTT-COF was synthesized following a literature procedure.[5] $^{15}$N enriched TTI-COF (80 mg, 0.203 mmol) was thoroughly mixed with sulfur (1.2 g, 37.4 mmol) in a mortar and the homogeneous mixture was transferred to an aluminum oxide boat in a horizontal tubular furnace. Under constant argon flow, the tube was purged at 60 °C for 1 h followed by a temperature increase to 155 °C (1 K min$^{-1}$ heating rate) for 3 h and a further increase to 350 °C (1.5 K min$^{-1}$ heating rate) for another 3 h. After cooling to room temperature, the solid was subjected to Soxhlet extractions with $CS_2$ and methanol (24 h each). The MeOH soaked solid was then activated by scCO2 drying to obtain TTT-COF (72.2 mg, 80 %).

### *Synthesis of $^{15}$N Enriched TT-Imide-COF*

TT-Imide-COF was synthesized following a literature procedure.[6] A Schlenk tube was charged with the precursor molecules pyromellitic dianhydride (PMDA, 32.7 mg, 0.15 mmol) and $^{15}$N enriched 2,4,6-tris(4-aminophenyl)-1,3,5-triazine (TT, 35.4 mg, 0.1 mmol) together with a mixture of 0.5 ml N-methyl-2-pyrrolidone, 0.5 ml mesitylene and 0.05 ml isoquinoline. The reaction mixture was degassed by four freeze-pump-thaw cycles and subsequently heated to 180 °C for 5 days. A yellow precipitate was formed, isolated by filtration and subjecting it to Soxhlet extractions with THF and methanol (24 h each). The MeOH soaked solid was then activated by scCO2 drying to obtain TT-Imide-COF (40.8 mg, 65 %).

### *Exposure of COFs to NO*

The COFs were exposed to nitric oxide via the NO adsorption measurements on the Quantachrom Autosorb IQ3 system. All analytics on the post-NO materials were performed after the performance of all NO sorption experiments, including seven succeeding NO adsorption/desorption isotherms at 298 K and three isotherms at 298 K, 288 K and 273 K, respectively, to ensure full reaction of the frameworks with the gas.

### *NO release experiments*

The NO release experiment was conducted by suspending 10 mg rTTI-COF-*NO* in 5 ml 0.1 M PBS buffer solution. The temperature was kept constant at 37 °C during the observation period and the mixture was shaken permanently to avoid precipitation of the COF. To determine the concentration of NO in the mixture, a Griess reagent kit for nitrite determination (G-7921) produced by *Probes* has been used. The conversion of the released nitric oxide to nitrite appears *in situ* by atmospheric oxygen:

$$2\,NO + O_2 \longrightarrow 2\,NO_2$$

$$2\,NO + 2\,NO_2 \longrightarrow 2\,N_2O_3$$

$$2\,N_2O_3 + 2\,H_2O \longrightarrow 4\,NO_2^- + 4\,H^+$$

**Scheme S8-2.** Conversion of the released nitric oxide to nitrite by atmospheric oxygen.

The formed nitrite is detected by using the Griess reagent through the formation of an azo-dye following the reaction:

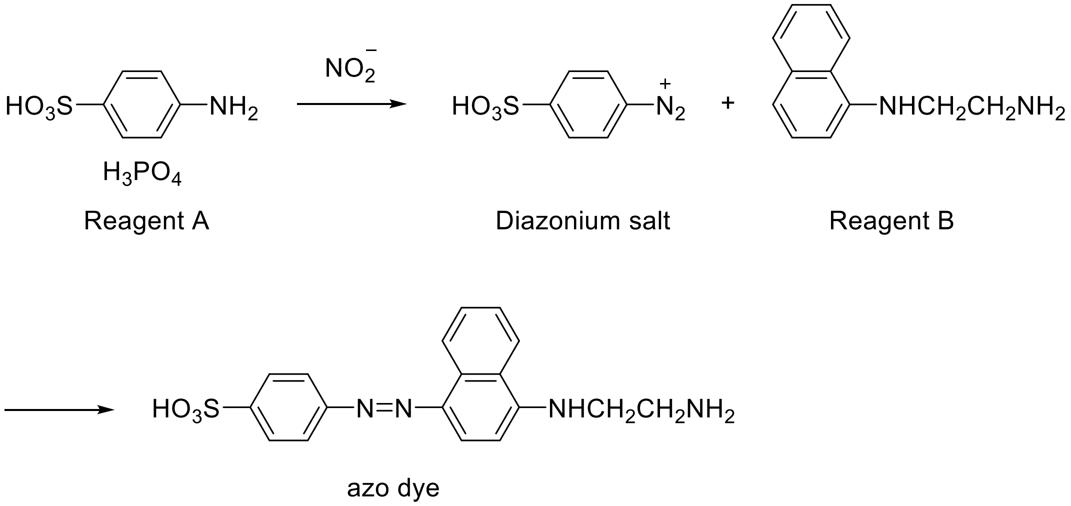

**Scheme S8-3.** Reaction of the formed nitrite with the Griess reagent forming an azo-dye.

For each measurement, 500 µl sample were taken and centrifuged. 300 µl of the supernatant were mixed with 100 µl Griess reagent and diluted with 2.6 ml water. After 30 min dwelling time, the nitrite concentration was measured by UV/VIS spectroscopy using a serial dilution as reference. The remaining 200 µl supernatant together with the centrifuged COF were subsequently combined with the initial NO-release mixture again. Unavoidable volume changes through the sample withdrawal during the long-term experiment (300 µl) have been considered in the NO release calculations.

### *8.4.3 Supplementary Figures*

### *Supplementary PXRD Data*

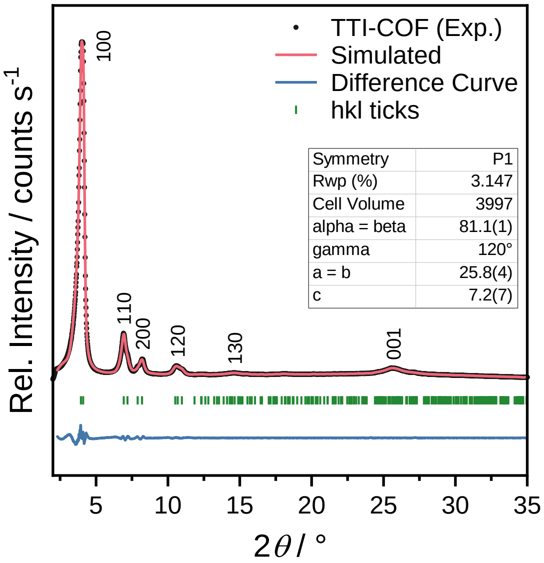

| | |
|---|---|
| Symmetry | P1 |
| Rwp (%) | 3.147 |
| Cell Volume | 3997 |
| alpha = beta | 81.1(1) |
| gamma | 120° |
| a = b | 25.8(4) |
| c | 7.2(7) |

**Figure S8-92.** Experimental PXRD pattern of TTI-COF (black) together with the Pawley fit (red), calculated reflection positions, (green) and difference curves (blue).

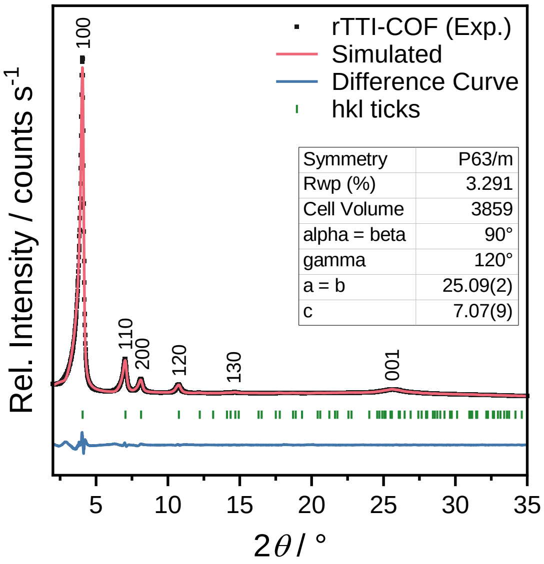

| | |
|---|---|
| Symmetry | P63/m |
| Rwp (%) | 3.291 |
| Cell Volume | 3859 |
| alpha = beta | 90° |
| gamma | 120° |
| a = b | 25.09(2) |
| c | 7.07(9) |

**Figure S8-93.** Experimental PXRD pattern of rTTI-COF (black) together with the Pawley fit (red), calculated reflection positions, (green) and difference curves (blue).

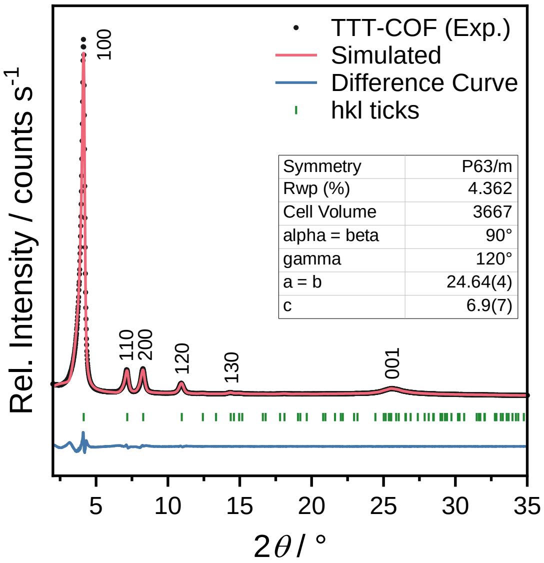

**Figure S8-94.** Experimental PXRD pattern of TTT-COF (black) together with the Pawley fit (red), calculated reflection positions, (green) and difference curves (blue).

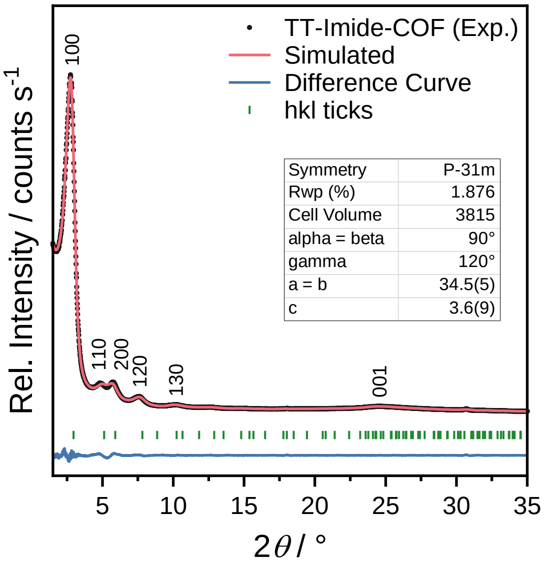

**Figure S8-95.** Experimental PXRD pattern of TT-Imide-COF (black) together with the Pawley fit (red), calculated reflection positions (green), and difference curves (blue).

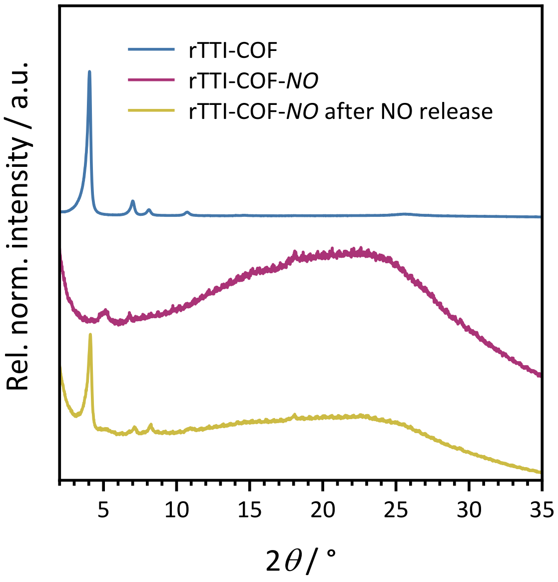

**Figure S8-96.** Comparison of experimental PXRD patterns of rTTI-COF (blue), rTTI-COF-*NO*, and rTTI-COF-*NO* after NO release.

## *Supplementary FT-IR Spectra*

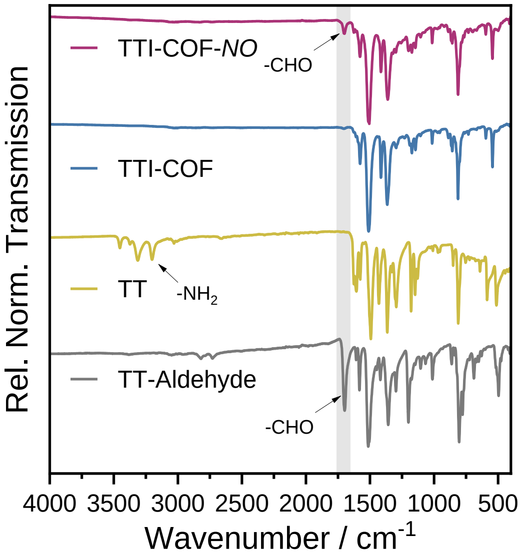

**Figure S8-97.** FT-IR spectra of TTI-COF before (blue) and after NO sorption experiments (red) together with FT-IR spectra of the precursor molecules TT-Aldehyde (black) and TT (yellow). The absence of amine vibrational bands at 3367 $cm^{-1}$ and aldehyde vibrational bands at 1698 $cm^{-1}$ in the COF spectrum indicate complete imine formation. After NO treatment the aldehyde vibrational band at 1698 $cm^{-1}$ of the precursor TT-Aldehyde appears again, indicating imine bond breaking.

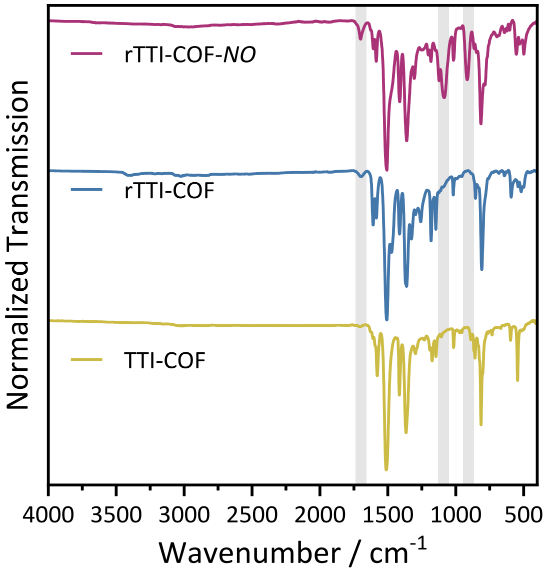

**Figure S8-98.** FT-IR spectra of rTTI-COF before (blue) and after NO adsorption experiments (red) together with the FT-IR spectrum of the precursor TTI-COF (yellow). After NO treatment three additional vibrational bands at 1700 cm$^{-1}$, 1084 cm$^{-1}$, and 916 cm$^{-1}$ appear, indicating the formation of the NONOate.

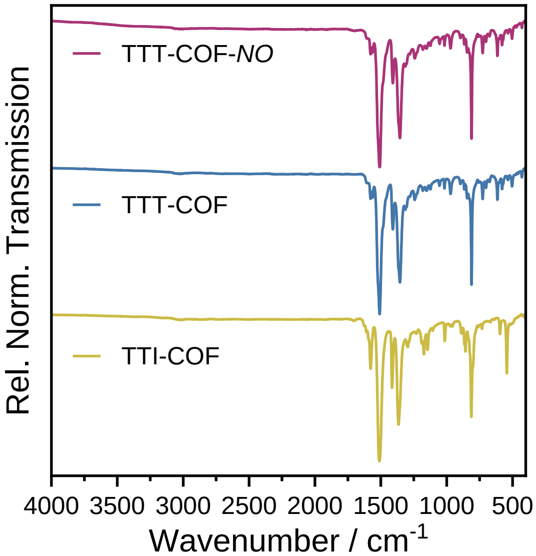

**Figure S8-99.** FT-IR spectra of TTT-COF before (blue) and after NO adsorption experiments (red) together with the FT-IR spectrum of the precursor TTI-COF (yellow). No changes can be observed in the spectrum of TTT-COF after NO treatment, indicating inertness of the system against NO.

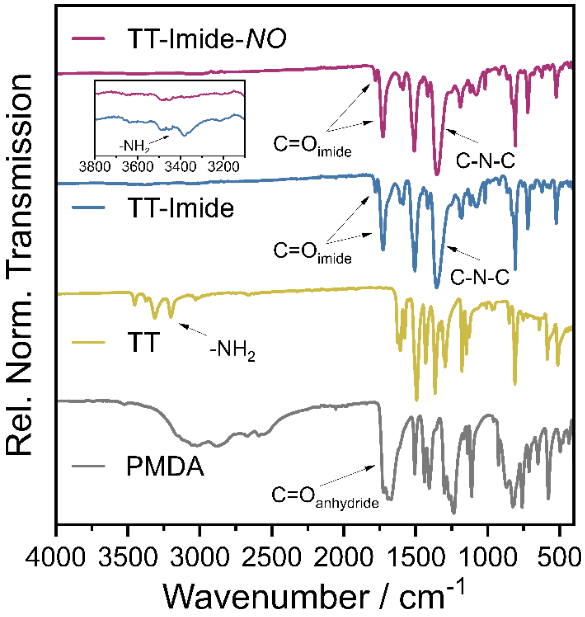

**Figure S8-100.** FT-IR spectra of TT-Imide-COF before (blue) and after NO adsorption experiments (red) together with FT-IR spectra of the precursor molecules PMDA (black) and TT (yellow). The absence of amine vibrational bands at 3367 cm$^{-1}$ and anhydride vibrational bands at 1700 cm$^{-1}$ in the COFs spectrum indicate complete imide formation. No strong changes can be observed in the spectrum after NO treatment, indicating strong inertness of the system towards NO. Inset shows the disappearance of faint amine vibrational bands at 3367 cm$^{-1}$ after the NO-treatment, which are in good agreement to the findings of by $^{15}$N CP-MAS ssNMR.

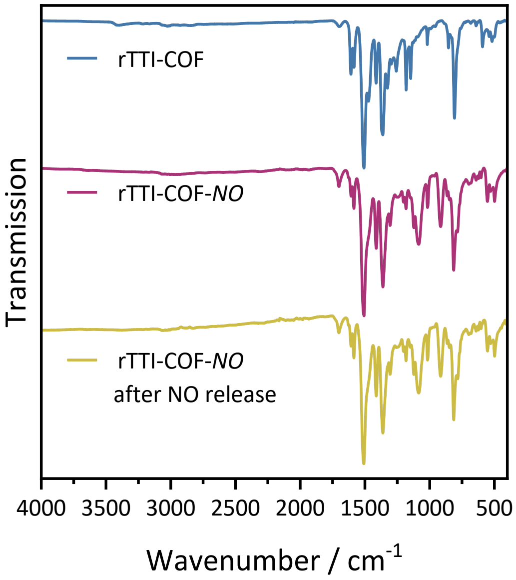

**Figure S8-101.** FT-IR spectra of rTTI-COF before (blue) and after NO adsorption experiments (red) as well as after the NO release (yellow), which show no significant changes.

## *Supplementary NMR Spectra*

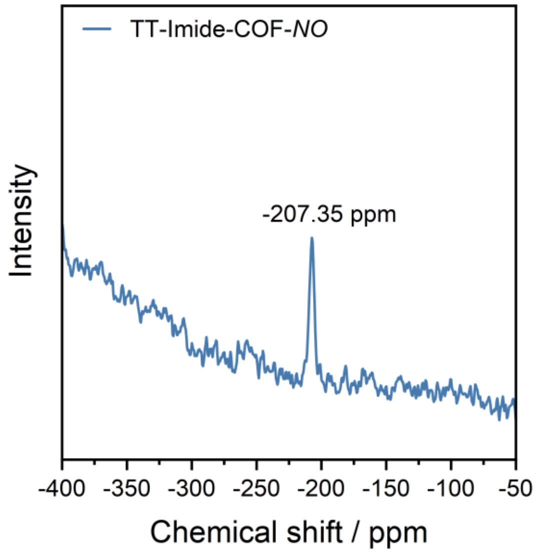

**Figure S8-102.** $^{15}N$ direct excitation NMR spectrum of TT-Imide COF showing one signal corresponding to the imide nitrogen at -207.35 ppm.

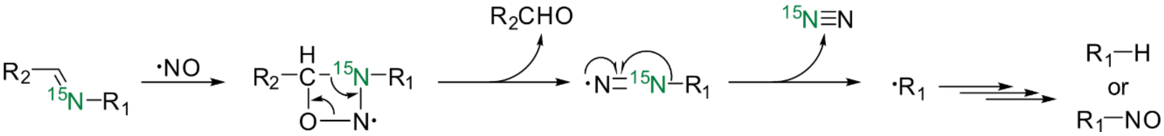

**Scheme S8-4.** Mechanism of imine linkage degradation by a [2+2] cycloaddition of NO to the imine bond, proposed by Hrabie et al.[7]

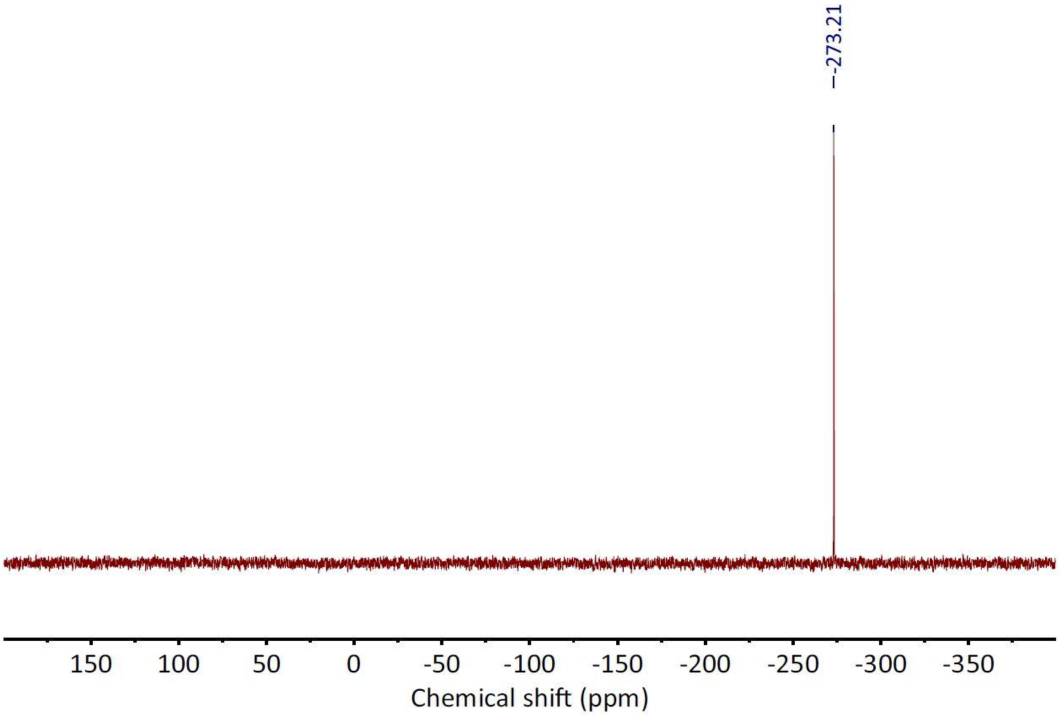

**Figure S8-103.** $^{15}$N NMR of **4-cyanobenzamide-$^{15}$*N*** in DMSO-*D6*.

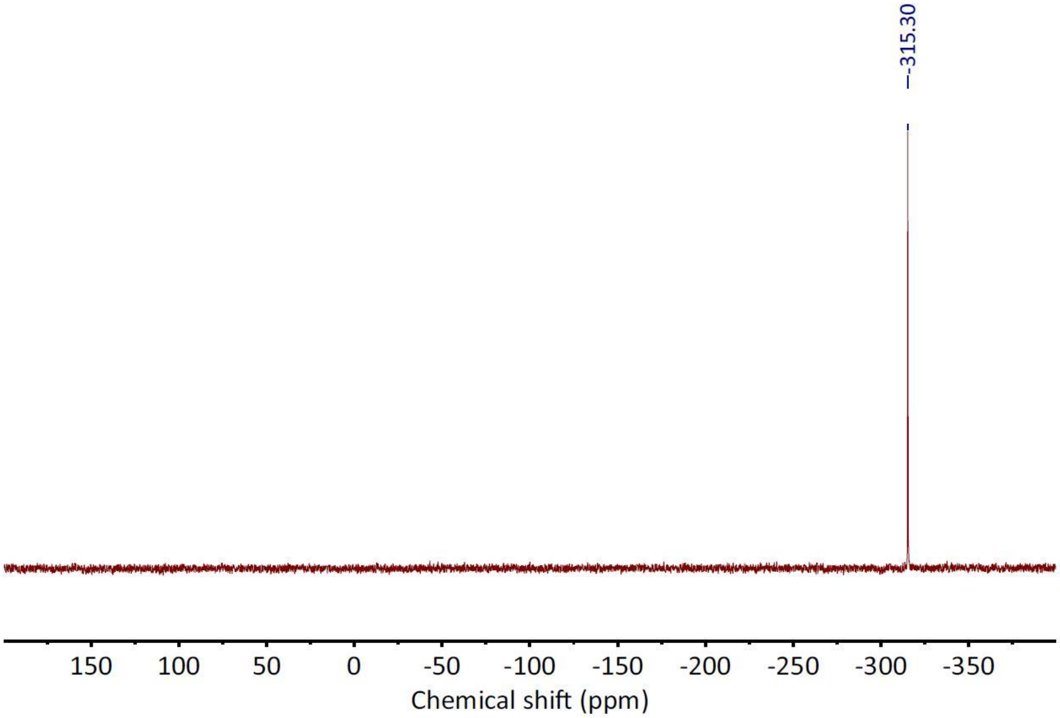

**Figure S8-104.** $^{15}$N NMR of **4-(amino-$^{15}$*N*)benzonitrile** in $CDCl_3$.

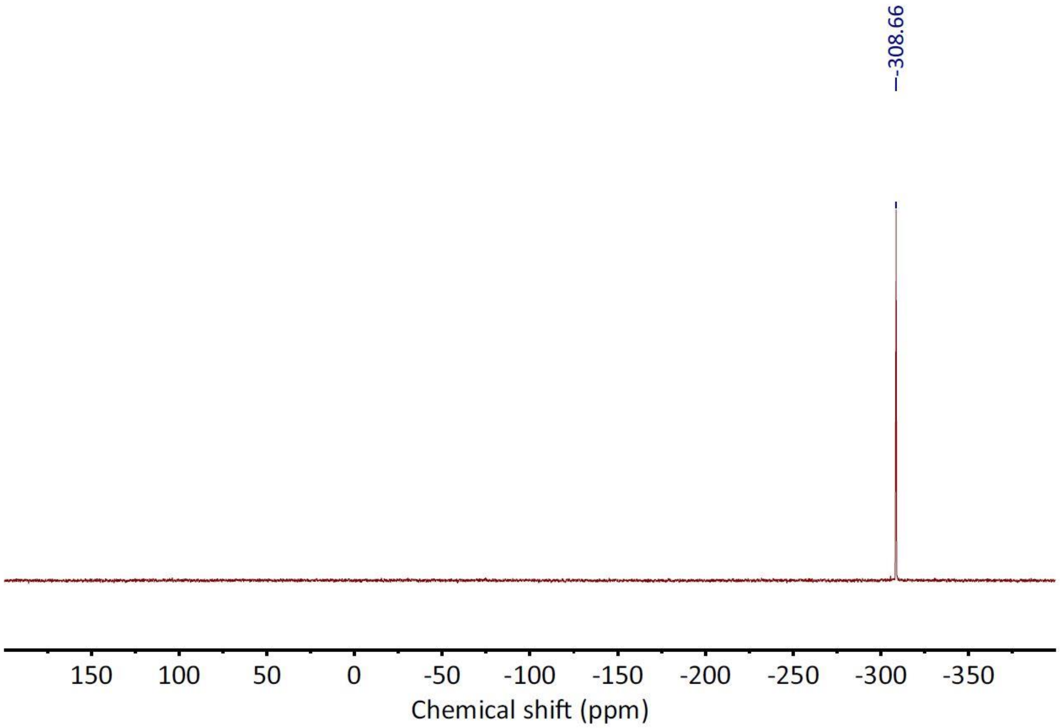

**Figure S8-105.** $^{15}$N NMR of **4,4',4''-(1,3,5-triazine-2,4,6-triyl)trianiline-$^{15}$*N*** in DMSO-*D*6.

## *Supplementary TEM Images*

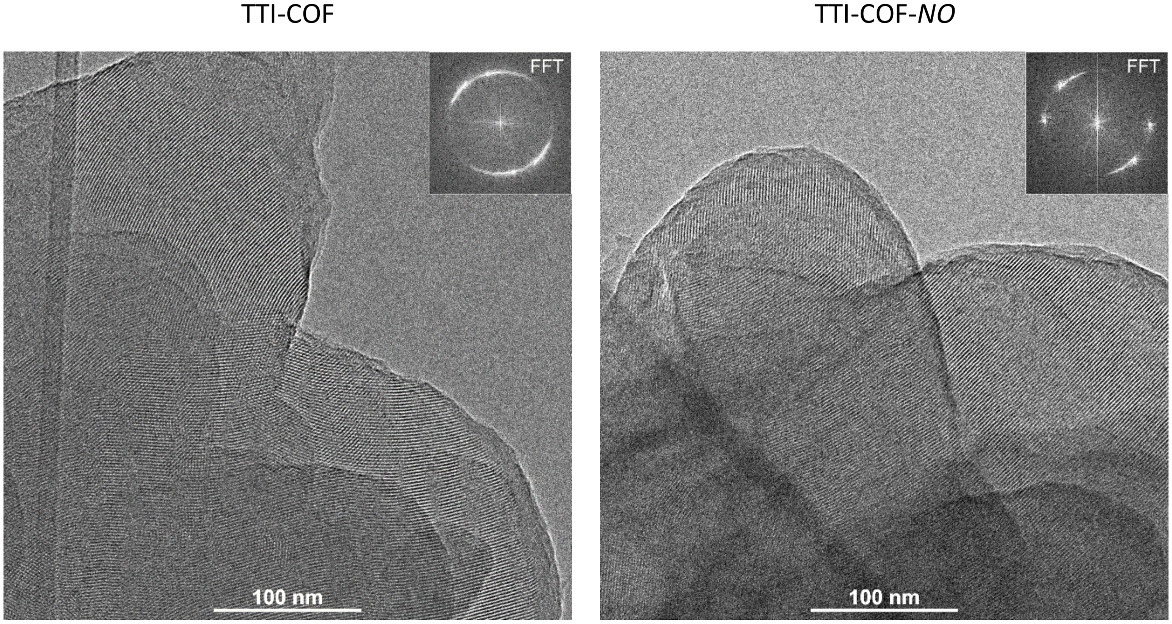
TTI-COF

TTI-COF-*NO*

**Figure S8-106.** TEM images of TTI-COF before (left) and after NO sorption measurements (right) showing retention of the crystalline structure.

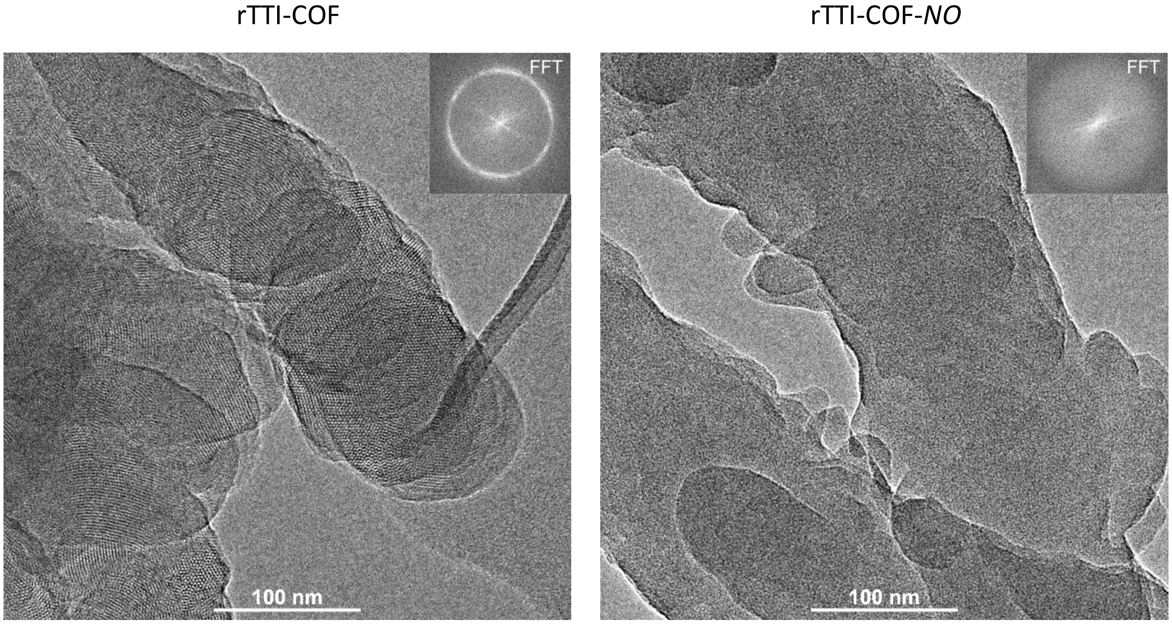
rTTI-COF

rTTI-COF-*NO*

**Figure S8-107.** TEM images of rTTI-COF before (left) and after NO sorption measurements (right) revealing a collapse of the crystalline structure.

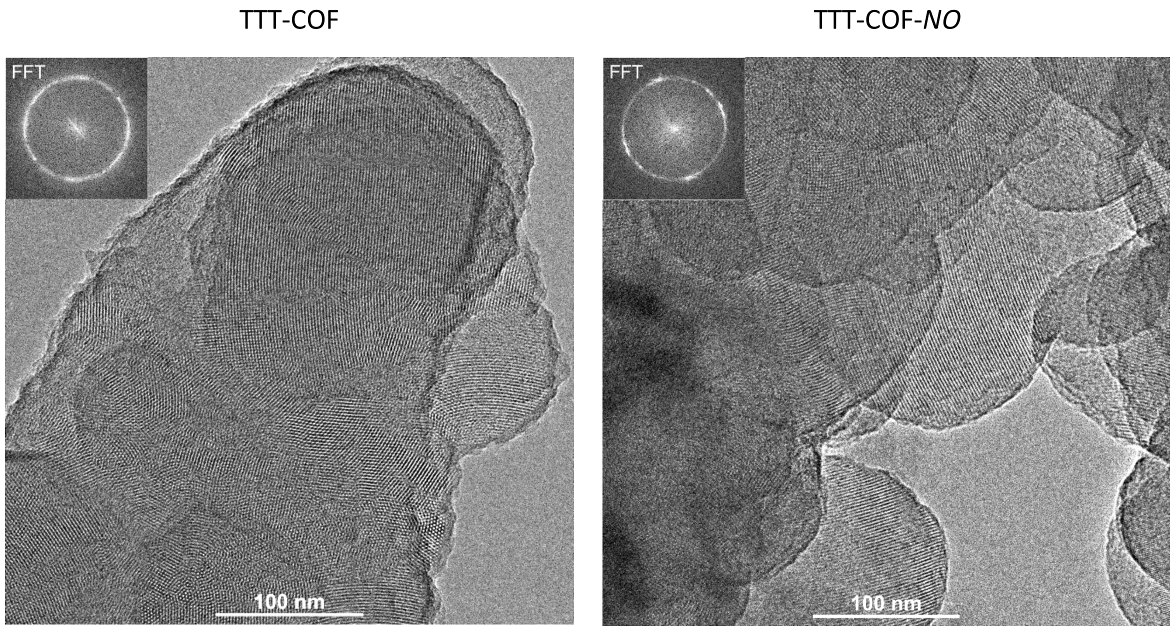

TTT-COF

TTT-COF-*NO*

**Figure S8-108.** TEM images of TTT-COF before (left) and after NO sorption measurements (right) showing retention of the crystalline structure.

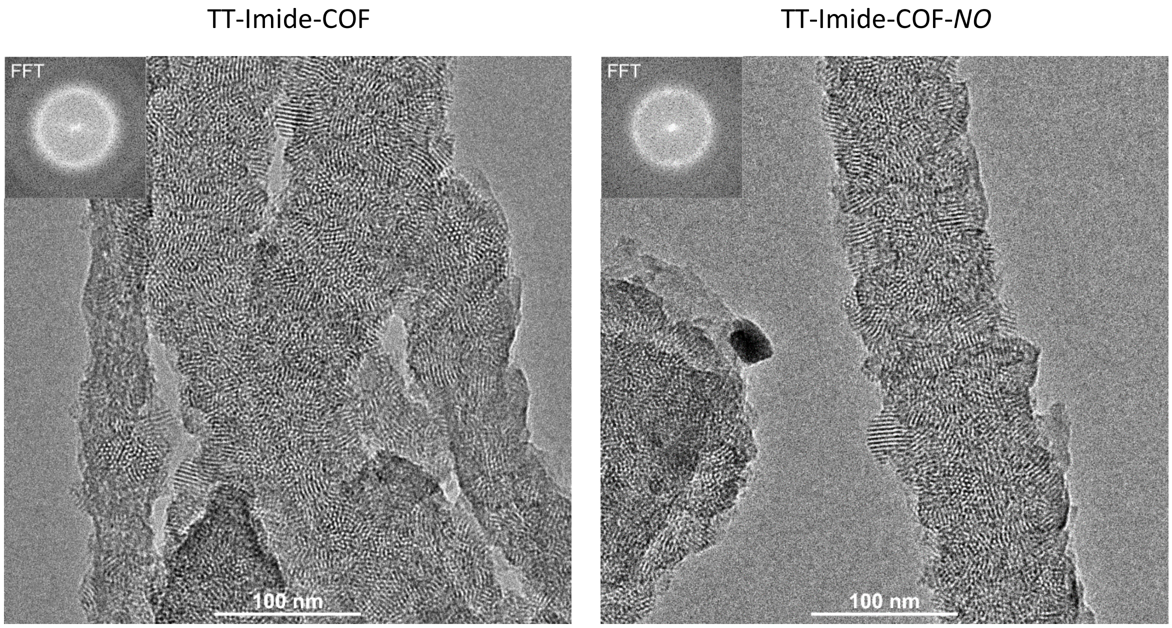

TT-Imide-COF

TT-Imide-COF-*NO*

**Figure S8-109.** TEM images of TT-Imide-COF before (left) and after NO sorption measurements (right) showing retention of the crystalline structure.

### *Supplementary UV/VIS Spectra*

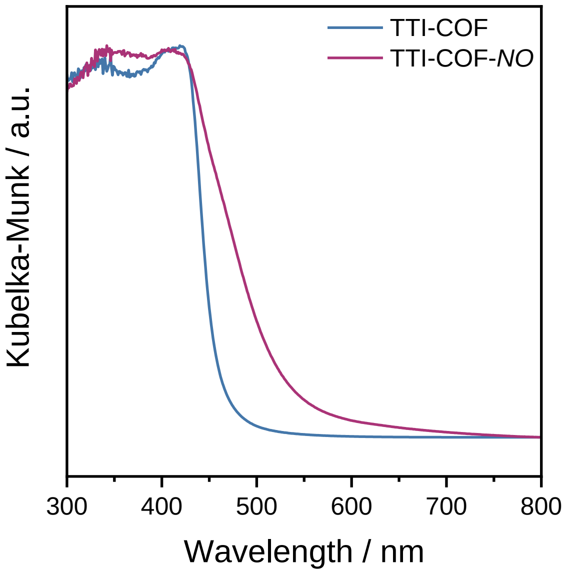

**Figure S8-110.** Diffuse reflectance spectra of TTI-COF before (blue) and after NO sorption experiments (red) revealing a shift of the absorption towards higher wavelengths, along with broadening/tailing of the absorption edge.

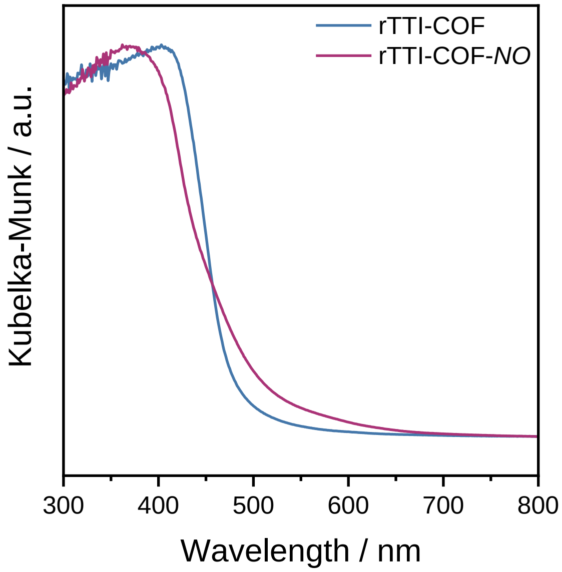

**Figure S8-111.** Diffuse reflectance spectra of rTTI-COF before (blue) and after NO sorption experiments (red) revealing a slight blueshift in the absorption edge, along with broadening/tailing.

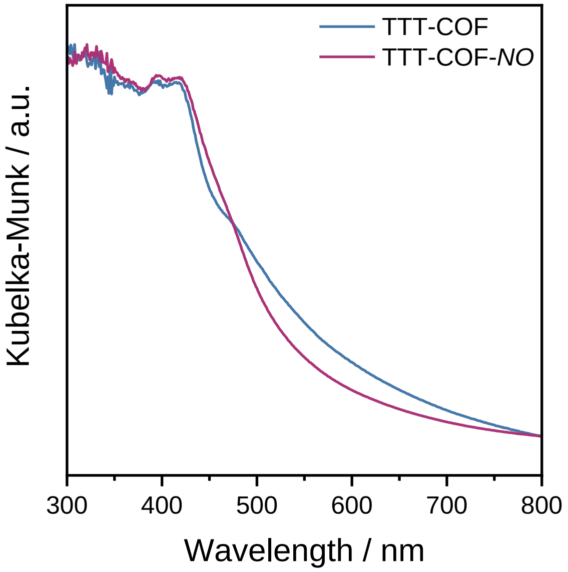

**Figure S8-112.** Diffuse reflectance spectra of TTT-COF before (blue) and after NO sorption experiments (red) showing slight changes in the structure of the absorption edge.

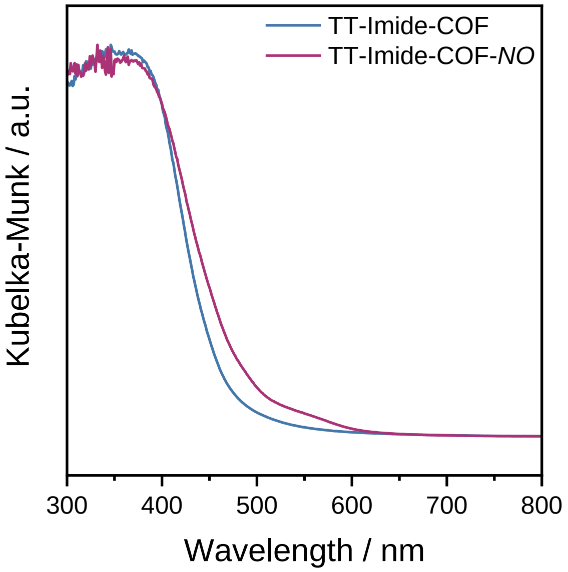

**Figure S8-113.** Diffuse reflectance spectra of TT-Imide-COF before (blue) and after NO sorption experiments (red), suggesting that the optical properties are largely retained.

## *Supplementary Sorption Data*

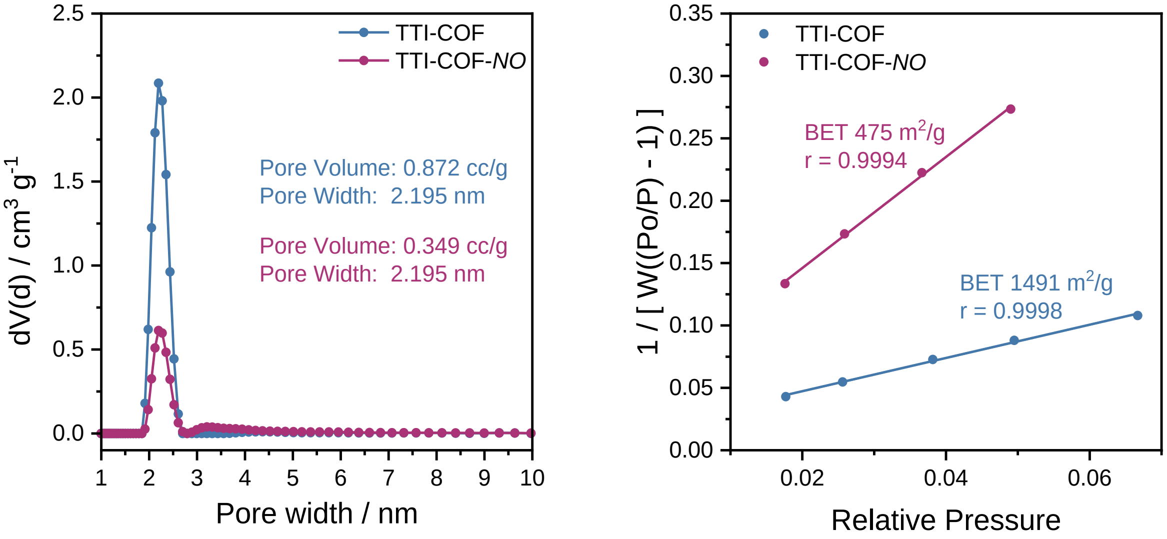

**Figure S8-114.** Calculated pore size distributions (left) and BET plots (right) of TTI-COF before (blue) and after NO sorption experiments (red), revealing a significant decrease in the surface area and pore volume after NO treatment.

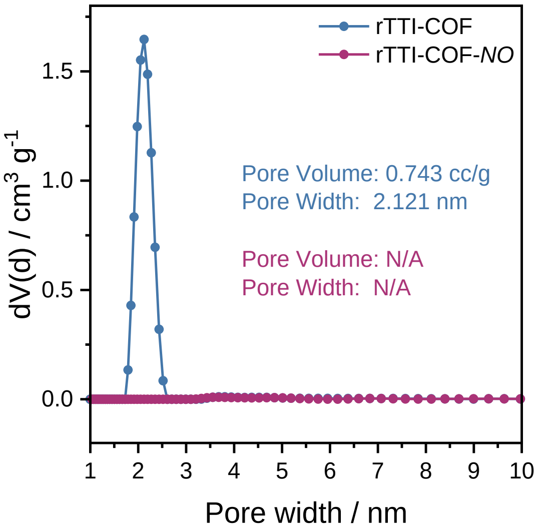

**Figure S8-115.** Calculated pore size distributions of rTTI-COF before (blue) and after NO sorption experiments (red), revealing a complete loss of structural porosity after NO treatment.

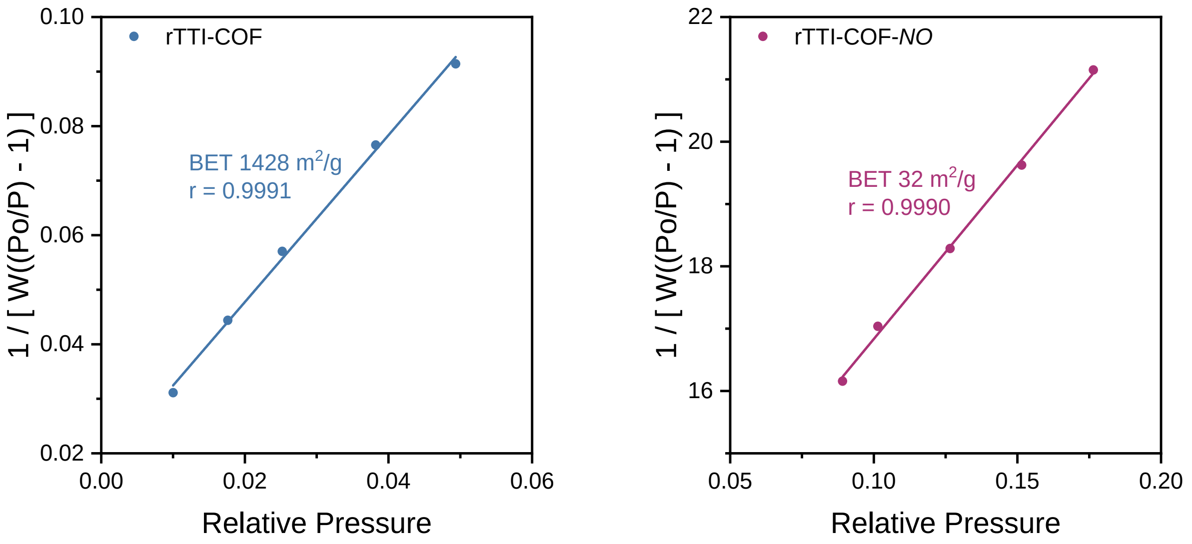

**Figure S8-116.** BET plots of rTTI-COF before (blue) and after NO sorption experiments (red), revealing an essentially complete loss of surface area after NO treatment.

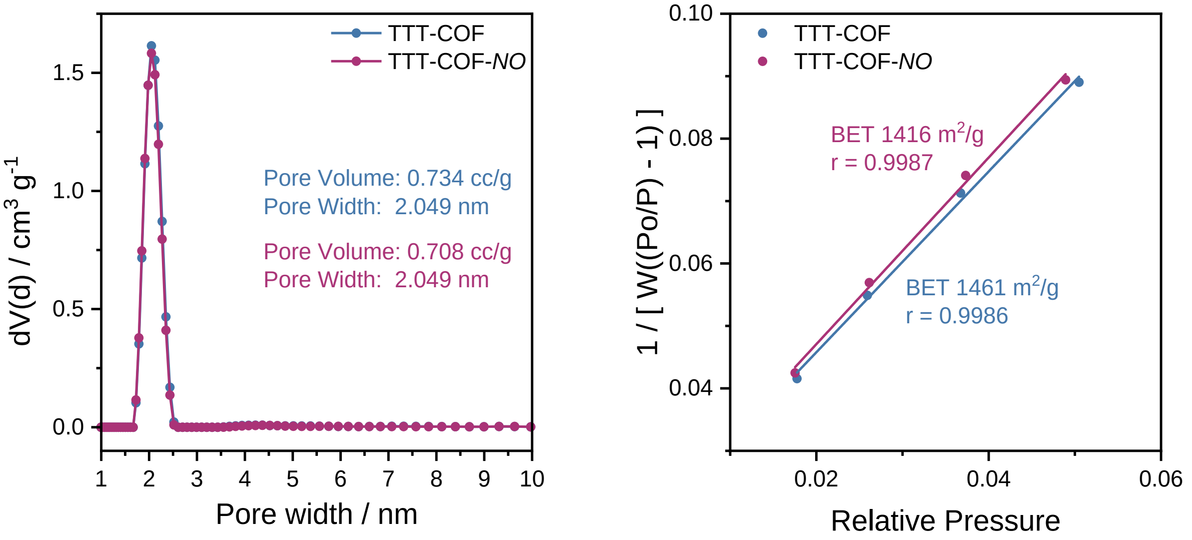

**Figure S8-117.** Calculated pore size distributions (left) and BET plots (right) of TTT-COF before (blue) and after NO sorption experiments (red), showing retention of its surface area and pore volume upon NO treatment indicating a strong robustness of the framework against NO.

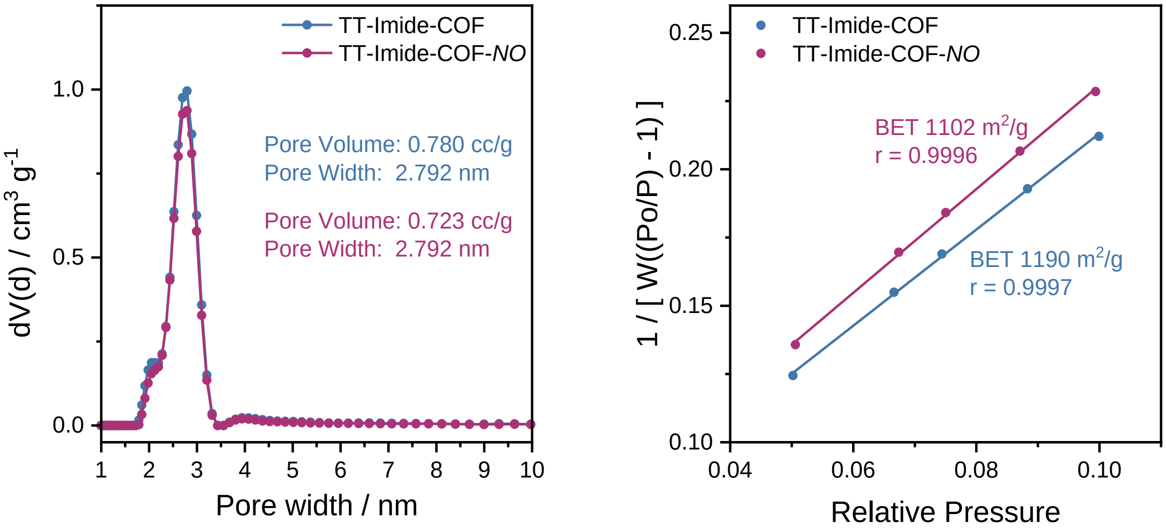

**Figure S8-118.** Calculated pore size distributions (left) and BET plots (right) of TT-Imide-COF before (blue) and after NO sorption experiments (red), showing retention of its surface area and pore volume upon NO treatment, indicating that the framework is robust against NO.

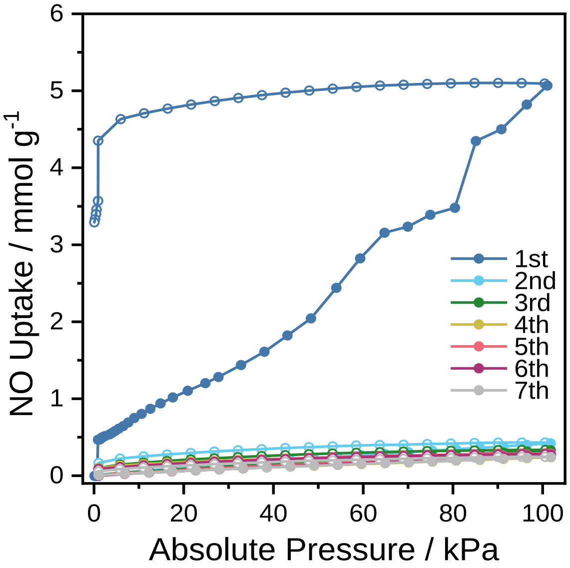

**Figure S8-119.** First seven NO adsorption and desorption isotherms of TTI-COF showing an unusual increased NO uptake within the first cycle. After the first cycle, the total uptake decreases until it stabilizes after three cycles.

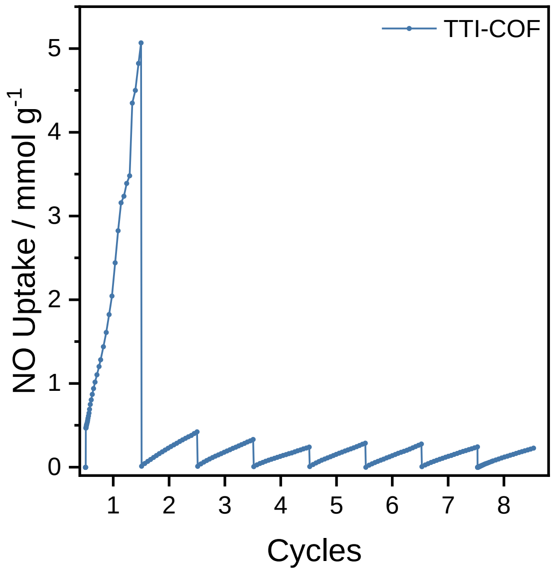

**Figure S8-120.** NO adsorption isotherms of TTI-COF plotted in a row, demonstrating the stabilization in NO uptake behavior after two to three cycles.

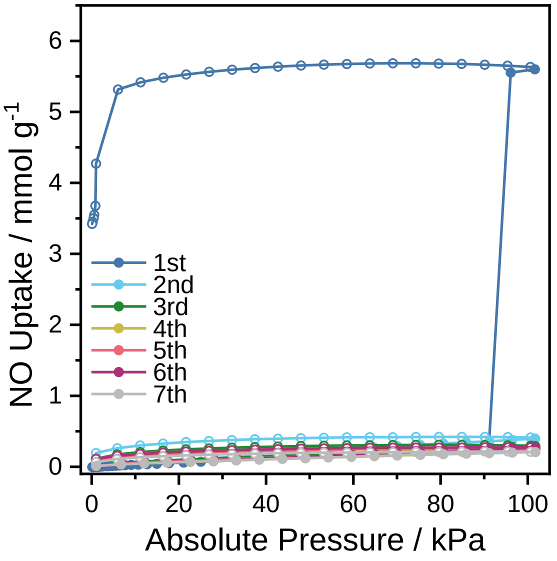

**Figure S8-121.** First seven NO adsorption and desorption isotherms of rTTI-COF showing an unusual increased NO uptake within the first cycle. After the first cycle, the total uptake decreases until it stabilizes after three cycles.

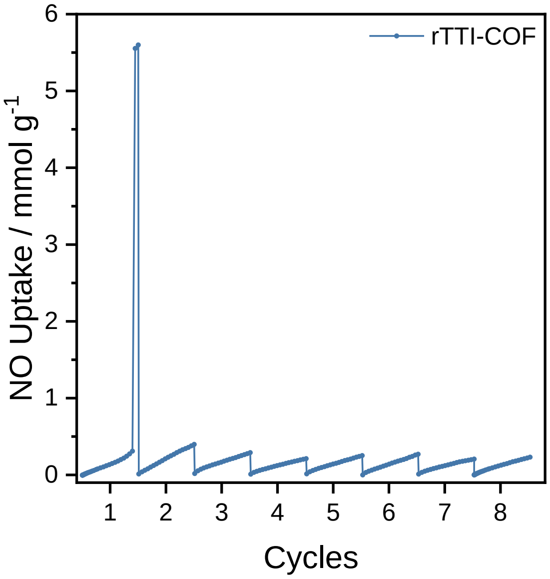

**Figure S8-122.** NO adsorption isotherms of rTTI-COF plotted in a row demonstrating the stabilization of NO uptake behavior after two to three cycles.

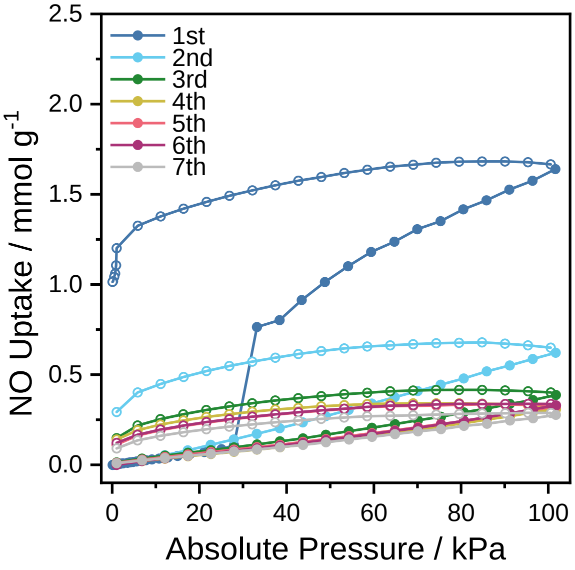

**Figure S8-123.** First seven NO adsorption and desorption isotherms of TTT-COF showing an unusual increased NO uptake within the first two cycles. Over the first and second cycle, the total uptake decreases until it stabilizes after three cycles.

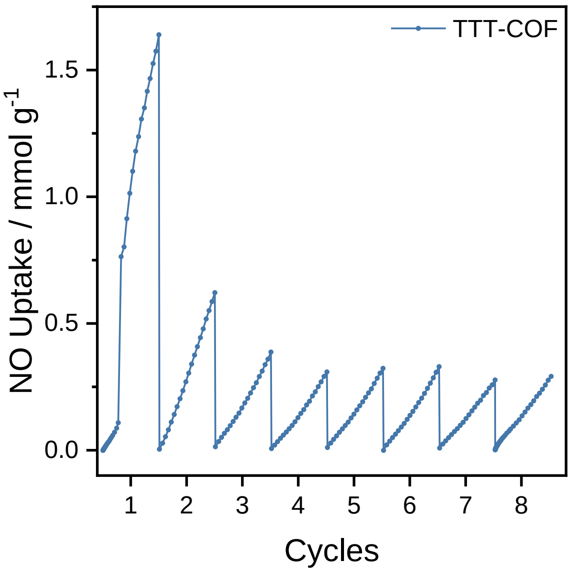

**Figure S8-124.** NO adsorption isotherms of TTT-COF plotted in a row demonstrating stabilization of the NO uptake behavior after three cycles.

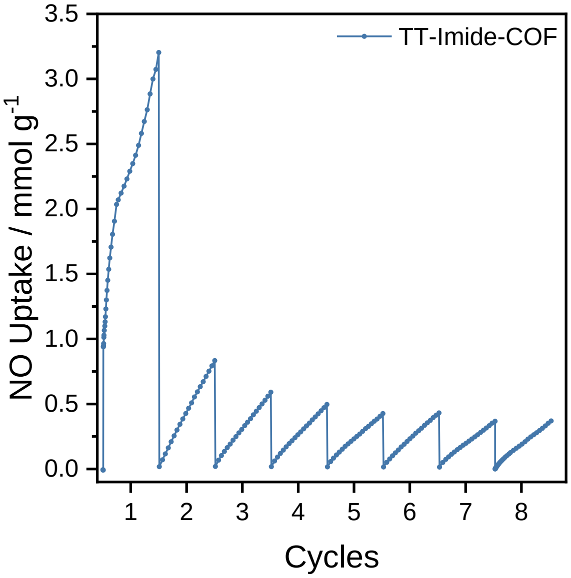

**Figure S8-125.** NO adsorption isotherms of TT-Imide-COF plotted in a row, demonstrating stabilization of the NO uptake behavior after two to four cycles.

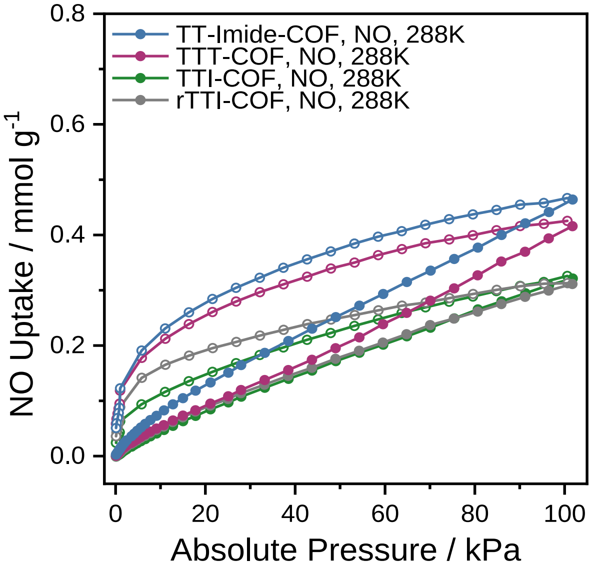

**Figure S8-126.** NO adsorption and desorption isotherms of TTI-, rTTI-, TTT-, and TT-Imide-COF at 288 K, after the cycling experiments. The reversibility of the isotherms indicates a process that can be described by physisorption.

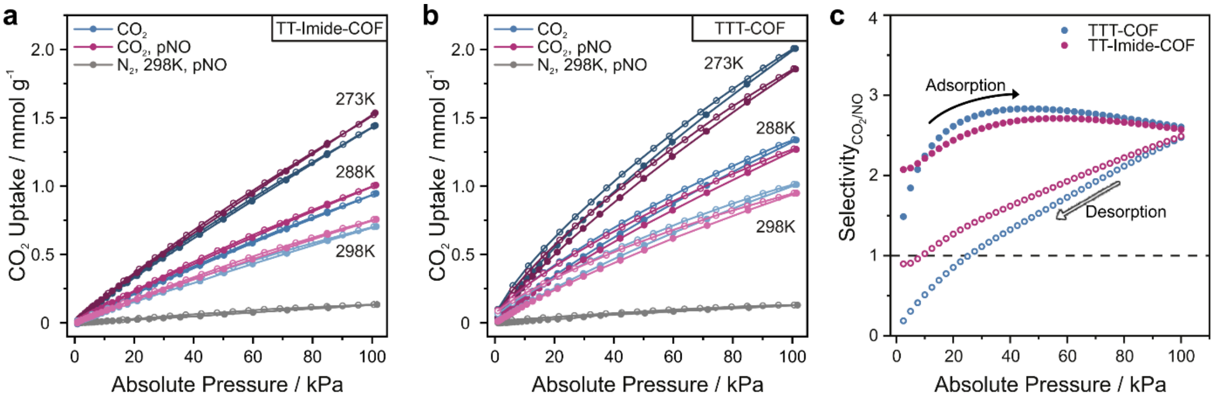

**Figure S8-127.** $CO_2$ isotherms of (a) TT-Imide-COF and (b) TTT-COF before (blue) and after NO exposure (red). Filled circles represent adsorption and empty circles desorption isotherms. (c) IAST selectivity of TTT-COF-NO and TT-Imide-COF-NO for a binary $CO_2$/NO (50/50) gas mixture during adsorption (filled circles) and desorption (empty circles). For a binary $CO_2$/NO (50/50) gas mixture, we found a selectivity towards $CO_2$ over the whole pressure range during adsorption up to 100 kPa for both COFs. The selectivities first increase until around 50 kPa before slightly declining to an almost identical value of 2.5 at 100 kPa. However, applying IAST to the desorption instead of the adsorption branch, in both COFs, the selectivity changes in favor of NO for low pressures below 30 kPa. In our opinion, this practice is a better representation of the thermodynamic equilibrium state due to the unusual and broad hysteresis of the pure NO isotherm.

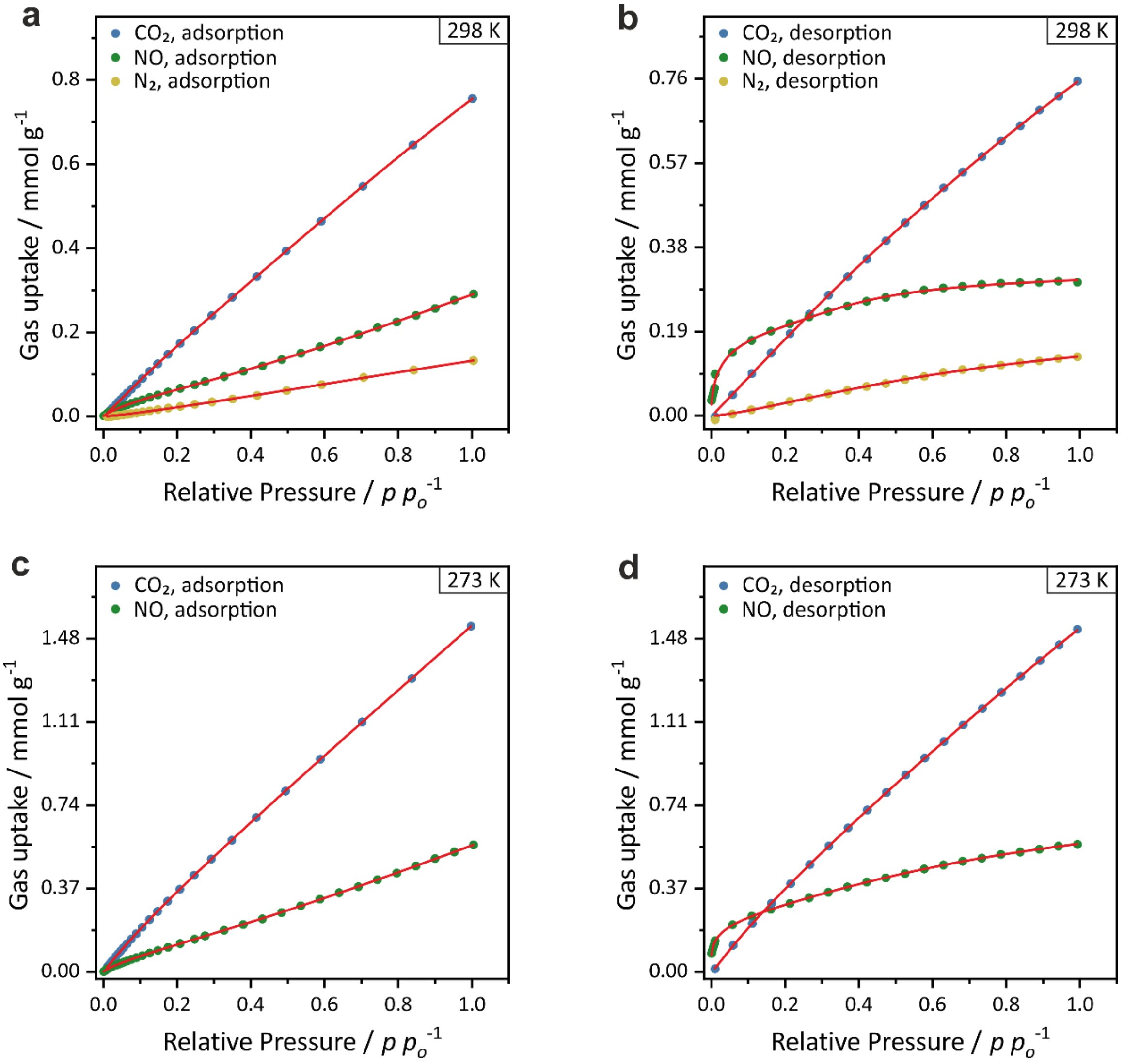

**Figure S8-128.** Fitting curves of **a** the adsorption isotherms at 298 K, **b** the desorption isotherms at 298 K, **c** the adsorption isotherms at 273 K and **d** the desorption isotherms at 273 K of TTT-COF.

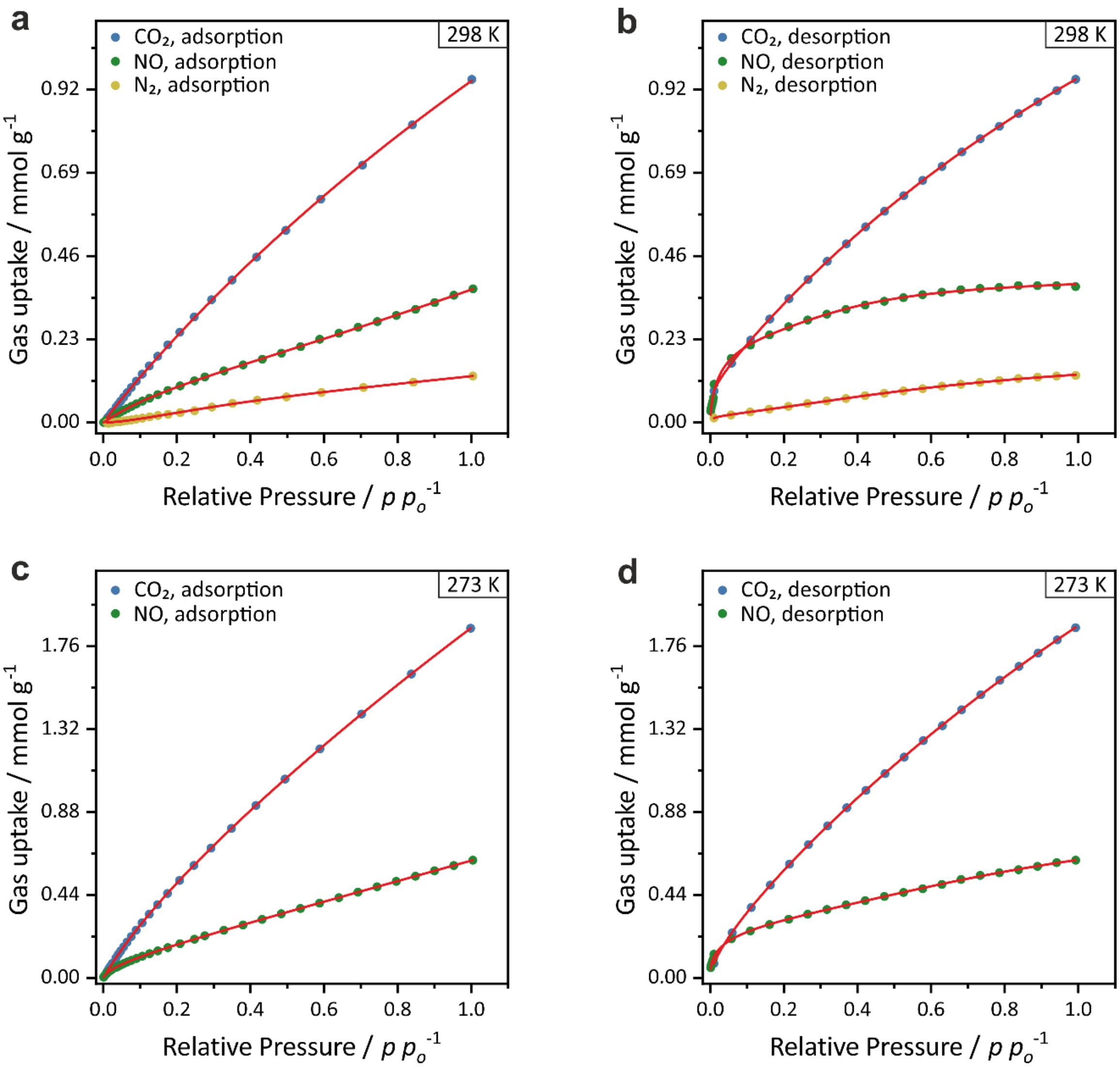

**Figure S8-129.** Fitting curves of **a** the adsorption isotherms at 298 K, **b** the desorption isotherms at 298 K, **c** the adsorption isotherms at 273 K and **d** the desorption isotherms at 273 K of TT-Imide-COF.

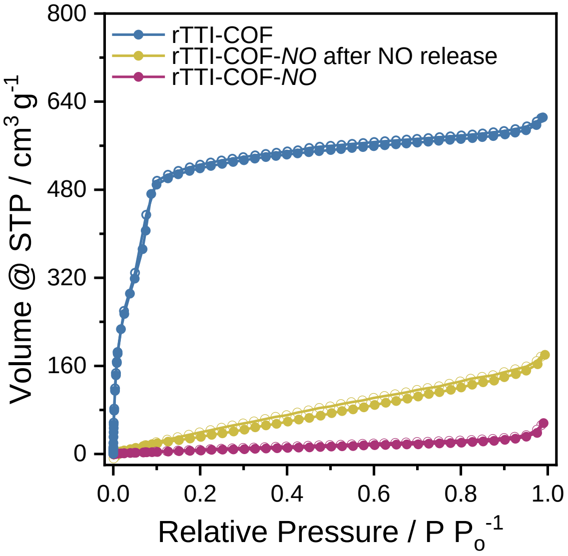

**Figure S8-130.** Argon adsorption isotherms at 87 K of rTTI-COF-*NO* (blue), rTTI-COF-*NO* (red) and rTTI-COF-*NO* after NO release (yellow).

### 8.4.4 *Supplementary Tables*

**Table S8-14.** Calculated heats of adsorption, $CO_2$ and NO adsorption capacities and IAST selectivities for TT-Imide-COF-NO and TTT-COF-NO.

| | Initial $Q_{st}$ $CO_2$ (kJ $mol^{-1}$) | $CO_2$ capacity (mmol $g^{-1}$) | | Selectivity[a] $CO_2/N_2$ (IAST) | Initial $Q_{st}$ NO (kJ $mol^{-1}$) | NO capacity (mmol $g^{-1}$) | | Selectivity[b] $NO/N_2$ (IAST) |
|---|---|---|---|---|---|---|---|---|
| | | 273K | 298K | | | 273K | 298K | |
| TT-Imide-COF-*NO* | 26.6-20.5 | 1.86 | 0.944 | 9.22 | 35.7-16.9 | 0.623 | 0.367 | 5.55 |
| TTT-COF-*NO* | 23.8-20.8 | 1.54 | 0.755 | 6.44 | 21.6-17.0 | 0.562 | 0.290 | 3.95 |

[a] Selectivity was calculated for 15/85 gas mixtures at 1 bar and 298 K for $CO_2/N_2$

[b] Selectivity was calculated for 3/97 gas mixtures at 1 bar and 298 K for $NO/N_2$

### *8.4.5 Bibliography*

[1] J. W. M. Osterrieth, D. Fairen-Jimenez et al., *Adv. Mater* **2022**, *34*, 2201502

[2] J. Dong, Y. Wang, G. Liu, Y. Cheng, D. Zhao, *CrystEngComm* **2017**, *19*, 4899–4904.

[3] F. Haase, K. Gottschling, L. Stegbauer, L. S. Germann, R. Gutzler, V. Duppel, V. S. Vyas, K. Kern, R. E. Dinnebier, B. V. Lotsch, *Mater. Chem. Front.* **2017**, *1*, 1354–1361.

[4] L. Grunenberg, G. Savasci, M. W. Terban, V. Duppel, I. Moudrakovski, M. Etter, R. E. Dinnebier, C. Ochsenfeld, B. V. Lotsch, *J. Am. Chem. Soc.* **2021**, *143*, 3430–3438.

[5] F. Haase, E. Troschke, G. Savasci, T. Banerjee, V. Duppel, S. Dörfler, M. M. J. Grundei, A. M. Burow, C. Ochsenfeld, S. Kaskel, B. V. Lotsch, *Nat. Commun.* **2018**, *9*, 1–10.

[6] X. Zhu, S. An, Y. Liu, J. Hu, H. Liu, C. Tian, S. Dai, X. Yang, H. Wang, C. W. Abney, S. Dai, *AIChE J.* **2017**, *63*, 3470–3478.

[7] J. A. Hrabie, A. Srinivasan, C. George, L. K. Keefer, *Tetrahedron Lett.* **1998**, *39*, 5933–5936.

## 8.5 List of Publications

### 8.5.1 Publications that are part of this thesis

*Ionothermal Synthesis of Imide-Linked Covalent Organic Frameworks*
Johannes Maschita, Tanmay Banerjee, Gökcen Savasci, Frederik Haase, Christian Ochsenfeld, Bettina V. Lotsch
*Angew. Chem. Int. Ed.* **2020**, *59*, 15750. DOI: 10.1002/anie.202007372

*Direct and Linker-Exchange Alcohol-Assisted Hydrothermal Synthesis of Imide-Linked Covalent Organic Frameworks*
Johannes Maschita, Tanmay Banerjee, Bettina V. Lotsch
*Chem. Mater.*, **2022**, *34*, 2249-2258. DOI: 10.1021/acs.chemmater.1c04051

*NO as a Reagent for Topochemical Framework Transformation and Controlled Nitric Oxide Release in Covalent Organic Frameworks*
Sebastian T. Emmerling,⊥ Johannes Maschita,⊥ Bettina V. Lotsch
⊥ S.E. and J.M. contributed equally to this work.
*ChemRxiv*. Cambridge: Cambridge Open Engage; **2022**; This content is a preprint and has not been peer-reviewed. DOI: 10.26434/chemrxiv-2022-czptr

### 8.5.2 Publications that are not part of this thesis

*Stickstoffhaltige Kohlenstoffe für hochkapazitive zyklenstabile Lithium-Schwefel-Kathoden: Schlussbericht des Max-Planck-Instituts für Festkörperforschung, Stuttgart*
Johannes Maschita, Hendrik Schlomberg, Frederik Haase and Bettina V. Lotsch
*German National Library of Science and Technology*, **2019**, Catalogue-ID: 1687020841. DOI: 10.2314/KXP:1688798692

*Scalable Production of Nitrogen-Doped Carbons for Multilayer Lithium-Sulfur Battery Cells*
Christian Kensy, Paul Härtel, Johannes Maschita, Susanne Dörfler, Benjamin Schumm, Thomas Abendroth, Holger Althues, Bettina V. Lotsch, Stefan Kaskel
*Carbon*, **2020**, *161*, 190-197. DOI: 10.1016/j.carbon.2020.01.037

*In Situ Generation of Electrolyte inside Pyridine-Based Covalent Triazine Frameworks for Direct Supercapacitor Integration*
Erik Troschke, Desirée Leistenschneider, Tilo Rensch, Sven Grätz, Johannes Maschita, Sebastian Ehrling, Benjamin Klemmed, Bettina V. Lotsch, Alexander Eychmüller, Lars Borchardt, and Stefan Kaskel
*ChemSusChem*, **2020**, *13*, 3192 –3198. DOI: 10.1002/cssc.202000518

*Protocol for the Analysis of Real-Time XRD Data of Intercalation Processes in Thin Films Demonstrated for Amine Intercalation in* $H_3Sb_3P_2O_{14}$ *Thin Films*
Marie Däntl, Johannes Maschita, Peter Wochner, Alberto Jiménez-Solano, Hugo Vignolo-Gonzalez, D. Putzky, Robert E. Dinnebier, Sebastian Bette, Bettina V. Lotsch
*Submitted to Chemistry of Materials*